

UNCLASSIFIED

AD NUMBER	
AD387211	
CLASSIFICATION CHANGES	
TO:	UNCLASSIFIED
FROM:	CONFIDENTIAL
LIMITATION CHANGES	
TO: Approved for public release; distribution is unlimited.	
FROM: Distribution authorized to DoD only; Administrative/Operational Use; OCT 1967. Other requests shall be referred to U.S. Army Aviation Materiel Laboratories, Fort Eustis, VA 23604.	
AUTHORITY	
USAAMRDL notice 29 Dec 1972 ; USAAMRDL notice 29 Dec 1972	

THIS PAGE IS UNCLASSIFIED

GENERAL DECLASSIFICATION SCHEDULE

**IN ACCORDANCE WITH
DOD 5200.1-R & EXECUTIVE ORDER 11652**

THIS DOCUMENT IS:

CLASSIFIED BY DDC

**Subject to General Declassification Schedule of
Executive Order 11652-Automatically Downgraded at
2 Years Intervals- DECLASSIFIED ON DECEMBER 31, 73.**

BY

**Defense Documentation Center
Defense Supply Agency
Cameron Station
Alexandria, Virginia 22314**

SECURITY

MARKING

The classified or limited status of this report applies to each page, unless otherwise marked.

Separate page printouts MUST be marked accordingly.

THIS DOCUMENT CONTAINS INFORMATION AFFECTING THE NATIONAL DEFENSE OF THE UNITED STATES WITHIN THE MEANING OF THE ESPIONAGE LAWS, TITLE 18, U.S.C., SECTIONS 793 AND 794. THE TRANSMISSION OR THE REVELATION OF ITS CONTENTS IN ANY MANNER TO AN UNAUTHORIZED PERSON IS PROHIBITED BY LAW.

NOTICE: When government or other drawings, specifications or other data are used for any purpose other than in connection with a definitely related government procurement operation, the U. S. Government thereby incurs no responsibility, nor any obligation whatsoever; and the fact that the Government may have formulated, furnished, or in any way supplied the said drawings, specifications, or other data is not to be regarded by implication or otherwise as in any manner licensing the holder or any other person or corporation, or conveying any rights or permission to manufacture, use or sell any patented invention that may in any way be related thereto.

CONFIDENTIAL

CMF - R - 15487

AD

AD 387211

USAAVLABS TECHNICAL REPORT 67-34
SMALL GAS TURBINE ENGINE COMPONENT TECHNOLOGY
REGENERATOR DEVELOPMENT (U)
PHASE 1, PRELIMINARY COMPONENT TESTING
AND REGENERATOR DESIGN (U)

By

H. A. Spaight

H. J. Selfors

October 1967

U. S. ARMY AVIATION MATERIEL LABORATORIES
FORT EUSTIS, VIRGINIA

CONTRACT DA 44-177-AMC-181(T)
PRATT & WHITNEY AIRCRAFT DIVISION
UNITED AIRCRAFT CORPORATION
EAST HARTFORD, CONNECTICUT

Downgraded at 3 year intervals;
declassified after 12 years.
DOD DIR 5, 200, 10

Each transmittal of this document outside
the Department of Defense must have
prior approval of U. S. Army Aviation
Materiel Laboratories, Fort Eustis,
Virginia 23604.



This material contains information affecting
the national defense of the United States
within the meaning of the Espionage Laws
(18 U. S. C. 793 and 794), the transmission
or revelation of which in any manner to an
unauthorized person is prohibited by law.

Copy 1 of 87 Copies

CONFIDENTIAL

Disclaimers

The findings in this report are not to be construed as an official Department of the Army position unless so designated by other authorized documents.

When Government drawings, specifications, or other data are used for any purpose other than in connection with a definitely related Government procurement operation, the United States Government thereby incurs no responsibility nor any obligation whatsoever; and the fact that the Government may have formulated, furnished, or in any way supplied the said drawings, specifications, or other data is not to be regarded by implication or otherwise as in any manner licensing the holder or any other person or corporation, or conveying any rights or permission, to manufacture, use, or sell any patented invention that may in any way be related thereto.

Trade names cited in this report do not constitute an official endorsement or approval of the use of such commercial hardware or software.

Disposition Instructions

When this report is no longer needed, Department of the Army organizations will destroy it in accordance with the procedures given in AR 380-5.

CONFIDENTIAL



DEPARTMENT OF THE ARMY
U. S. ARMY AVIATION MATERIEL LABORATORIES
FORT EUSTIS, VIRGINIA 23604

(U) This program was undertaken to demonstrate an advancement in lightweight, compact, high-effectiveness rotary regenerator technology and to demonstrate combined rotary regenerator and experimental T74 engine performance.

(U) The U.S. Army Aviation Materiel Laboratories has reviewed this report and concurs in the findings contained herein. The report is recommended for use in planning future rotary regenerator and regenerative engine programs.

This report is classified **CONFIDENTIAL** because of the compilation of information. Individual pages are **UNCLASSIFIED** when separated from the report.

CONFIDENTIAL

CONFIDENTIAL

Task 1M121401D14413
Contract DA 44-177-AMC-181(T)
USAAVLABS Technical Report 67-34
October 1967

**SMALL GAS TURBINE ENGINE COMPONENT TECHNOLOGY
REGENERATOR DEVELOPMENT (U)**

**PHASE I, PRELIMINARY COMPONENT TESTING
AND REGENERATOR DESIGN (U)**

PWA-2942

by

H. A. Spaight and H. J. Selfors

Prepared by

Pratt & Whitney Aircraft Division
United Aircraft Corporation
East Hartford, Connecticut

U. S. ARMY AVIATION MATERIEL LABORATORIES
FORT EUSTIS, VIRGINIA

Each transmittal of this document outside the Department of Defense must have prior approval of U.S. Army Aviation Materiel Laboratories, Fort Eustis, Virginia 23604.

DOWNGRADED AT 3 YEAR INTERVALS:
DECLASSIFIED AFTER 12 YEARS.
DOD DIR 5,200 10

THIS DOCUMENT CONTAINS INFORMATION AFFECTING THE NATIONAL DEFENSE OF THE UNITED STATES WITHIN THE MEANING OF THE ESPIONAGE LAWS, TITLE 18 U. S. C., SECTIONS 793 AND 794. ITS TRANSMISSION OR REVELATION OF ITS CONTENTS IN ANY MANNER TO AN UNAUTHORIZED PERSON IS PROHIBITED BY LAW.

CONFIDENTIAL

(U) SUMMARY

This report describes the work accomplished during the 12-month Phase I portion of a 32-month program for the advancement of toroidal rotary regenerator technology for small gas turbine engines. The regenerator component work included analytical and experimental evaluation of candidate heat transfer surfaces where previous data did not exist; experimental determination of matrix airflow distribution and corrective measures; and refinement of seal system components, including all-metal inner diameter seals. The optimum matrix and seal configurations determined from these component tests were evaluated in an existing regenerator which was run at conditions simulating small gas turbine operation. As a result of these component investigations, major improvements in regenerator technology were made and were incorporated into the design of a flightweight high-effectiveness toroidal rotary regenerator designed during Phase I.

(U) FOREWORD

The subject of this report is the work performed by Pratt & Whitney Aircraft Division of United Aircraft Corporation, East Hartford, Connecticut, on preliminary component testing and regenerator design, which is the Phase I portion of the program for small gas turbine engine component technology, regenerator development. The work was performed in accordance with Contract No. DA 44-177-AMC-181(T), Task 1M121401D14413, during the period 7 May 1964 through 7 May 1965. The report was submitted in January 1967 in compliance with part 2, Statement of Work, paragraph c. (4) of the contract schedule.

Under the same contract, a second report, USAAVLABS Technical Report 67-35 (contractor's report PWA-3008), covers Phase II, full-scale regenerator fabrication and engine-regenerator testing.

The technical representatives for the U.S. Army Aviation Materiel Laboratories were Messrs. J. W. White and N. C. Kailos.

(U) CONTENTS

	<u>Page</u>
SUMMARY	iii
FOREWORD	v
LIST OF ILLUSTRATIONS	viii
LIST OF TABLES	xxiii
LIST OF SYMBOLS	xxiv
INTRODUCTION	1
ANALYTICAL STUDY OF MATRIX CANDIDATES	4
MATRIX EXPERIMENTAL INVESTIGATION	14
MATRIX TESTS IN REGENERATOR	58
INNER DIAMETER SEAL TESTS	84
FULL SCALE REGENERATOR DESIGN	113
SUPPORTING STUDIES	127
CONCLUSIONS	153
BIBLIOGRAPHY	154
APPENDIX. REGENERATOR MATRIX CONFIGURATIONS TESTED IN THE MATRIX AIRFLOW RIG	155
DISTRIBUTION.	165

(U) ILLUSTRATIONS

<u>Figure</u>		<u>Page</u>
1	Predicted Friction Factor Vs. Reynolds Number for 10 x 10 x 0.0377 Wire Screen Matrix	6
2	Predicted Friction Factor Vs. Reynolds Number for 24 x 24 x 0.0135 Wire Screen Matrix	6
3	Predicted Friction Factor Vs. Reynolds Number for 40 x 40 x 0.0088 Wire Screen Matrix	7
4	Predicted Friction Factor Vs. Reynolds Number for 60 x 60 x 0.0059 Wire Screen Matrix	7
5	Predicted Friction Factor Vs. Reynolds Number for 80 x 80 x 0.004 Wire Screen Matrix	8
6	Predicted Friction Factor Vs. Reynolds Number for 24 x 24 x 0.0093 Wire Screen Matrix	8
7	Predicted Friction Factor Vs. Reynolds Number for 60 x 60 x 0.004 Wire Screen Matrix	9
8	Predicted Colburn Factor Vs. Reynolds Number	9
9	Periodic-Flow Matrix Heat Transfer Test Rig Flow Diagram	15
10	Matrix Holder With Screens	16
11	Exploded View of Matrix Assembly	17
12	Periodic-Flow Matrix Heat Transfer Rig	18
13	Typical Time-Temperature Response for 42-Layer, 24 x 24 x 0.010 Wire Screen Matrix	18
14	Stanton-Prandtl Number and Friction Factor Corre- lation for 24 x 24 x 0.0135 Wire Screen Matrix	21

(U) ILLUSTRATIONS (Cont'd)

<u>Figure</u>		<u>Page</u>
15	Stanton-Prandtl Number and Friction Factor Correlation for 100 x 100 x 0.0045 Wire Screen Matrix	22
16	Stanton-Prandtl Number and Friction Factor Correlation for 60 x 60 x 0.0075 Sintered Wire Screen Matrix.	23
17	Stanton-Prandtl Number and Friction Factor Correlation for 40 x 40 x 0.0085 Wire Screen Matrix	24
18	Stanton-Prandtl Number and Friction Factor Correlation for 24 x 24 x 0.0075 Wire Screen Matrix	25
19	Stanton-Prandtl Number and Friction Factor Correlation for 60 x 60 x 0.0040 Wire Screen Matrix	26
20	Stanton-Prandtl Number and Friction Factor Correlation for 60 x 60 x 0.0065 Wire Screen Matrix	27
21	Stanton-Prandtl Number and Friction Factor Correlation for 24 x 24 x 0.0145 Wire Screen Matrix	28
22	Stanton-Prandtl Number and Friction Factor Correlation for 60 x 60 x 0.0069 Wire Screen Matrix	29
23	Stanton-Prandtl Number and Friction Factor Correlation for 80 x 80 x 0.0037 Wire Screen Matrix	30
24	Stanton-Prandtl Number and Friction Factor Correlation for 60 x 60 x 0.0058 Wire Screen Matrix	31
25	Stanton-Prandtl Number and Friction Factor Correlation for 10 x 10 x 0.0350 Wire Screen Matrix	32
26	Stanton-Prandtl Number and Friction Factor Correlation for T-20-38 CERCOR Matrix	33
27	Stanton-Prandtl Number and Friction Factor Correlation for 60 x 60 x 0.0018 Wire Screen Matrix	34

(U) ILLUSTRATIONS (Cont'd)

<u>Figure</u>		<u>Page</u>
28	Stanton-Prandtl Number and Friction Factor Correlation for TC-20-38 Impregnated CERCOR Matrix	35
29	Stanton-Prandtl Number and Friction Factor Correlation for 60 x 60 x 0.0061 Sintered Wire Screen Matrix	36
30	Local Flow Distortion of Early Matrices, Cross Section Through Torus	37
31	Schematics of Reoperated Vee Matrices	38
32	Matrix Airflow Rig Schematic	39
33	Matrix Airflow Rig	40
34	Oil-Graphite Traces on the 35° Vee Matrix	41
35	Oil-Graphite Traces and Flow Streamlines Around a Tube	42
36	Oil-Graphite Traces and Flow Streamlines Around a Flat Plate	42
37	Oil-Graphite Traces and Flow Streamlines Entering Vee Matrix	43
38	Oil-Graphite Traces and Flow Streamlines Leaving a 35° Vee Matrix	44
39	Mass Velocity Leaving Matrix Face Vs. Distance Across Channels (Flow Into the Vee)	45
40	Mass Velocity Leaving Matrix Face Vs. Distance Along Matrix (Flow Into the Vee).	46
41	Mass Velocity Leaving Matrix Face Vs. Distance Along Matrix (Flow Over the Vee)	46

(U) ILLUSTRATIONS (Cont'd)

<u>Figure</u>		<u>Page</u>
42	Hot-Wire Anemometer and 60 x 60 x 0.0058 Wire Screen Matrix, Airflow Rig	47
43	View of 24 x 24 x 0.0135 Matrix Package (1-Inch-Thick Screen)	48
44	Normalized Mass Velocity Leaving Matrix Vs. Distance Along Matrix Face for Flow Into Vee, Configurations 1, 2, 3, 7, 8, 11, 12, 13, 19, and 20	50
45	Normalized Mass Velocity Leaving Matrix Vs. Distance Along Matrix Face for Flow Over Vee, Configurations 4, 5, 6, 9, 10, 14, 15, and 16	51
46	Normalized Mass Velocity Leaving Matrix Vs. Distance Along Matrix Face for Flow Into Vee, Configurations 3, 25, 27, and 29	52
47	Normalized Mass Velocity Leaving Matrix Vs. Distance Along Matrix Face for Flow Over Vee, Configurations 16, 26, 28, and 30	52
48	Normalized Mass Velocity Leaving Matrix Vs. Distance Along Matrix Face for Flow Into Vee, Configurations 3 and 31	53
49	Normalized Mass Velocity Leaving Matrix Vs. Distance Along Matrix Face for Flow Over Vee, Configurations 16 and 32	53
50	Normalized Mass Velocity Leaving Matrix Vs. Distance Along Matrix Face for Flow Into Vee, Configurations 27 and 33	54
51	Normalized Mass Velocity Leaving Matrix Vs. Distance Along Matrix Face for Flow Over Vee, Matrix Configurations 28 and 34	54

(U) ILLUSTRATIONS (Cont'd)

<u>Figure</u>		<u>Page</u>
52	Normalized Mass Velocity Leaving Matrix Vs. Distance Along Matrix Face for Flow Into Vee, Matrix Configurations 8 and 35	55
53	Normalized Mass Velocity Leaving Matrix Vs. Distance Along Matrix Face for Flow Over Vee, Matrix Configurations 10 and 36	55
54	Normalized Mass Velocity Leaving Matrix Vs. Distance Along Matrix Face for Flow Into Vee, Matrix Configurations 8 and 37	56
55	Normalized Mass Velocity Leaving Matrix Vs. Distance Along Matrix Face for Flow Over Vee, Matrix Configurations 10 and 38	56
56	Mass Velocity Leaving Matrix Face Vs. Distance Along Matrix Face, Configurations 21 Through 24.	57
57	View Showing Cold Side of Rotor Assembly	59
58	Regenerator Rotor Subassembly	59
59	Regenerator Bearing Housing and Integral Seal Plate	60
60	Hot Side of Regenerator Housing	61
61	Cold Side of Regenerator Housing	61
62	Regenerator Rotor Assembly	62
63	Hot Side Inlet View of Straight Radial Vee Matrix	64
64	Cold Side Inlet View of Straight Radial Vee Matrix	64
65	View of Regenerator Rig (Hot Side) With Blanking Plates Installed	65

(U) ILLUSTRATIONS (Cont'd)

<u>Figure</u>		<u>Page</u>
66	View of Regenerator Rig (Cold Side) With Pressurizing Boss on Blanking Plate; Rig Drive Motor Visible	65
67	Baseline Calibration, Total Rotary Regenerator Leakage and Carryover	66
68	Temperature Effectiveness Vs. Airflow for Build 1 Regenerator With 24 x 24 Wire Screen Matrix; Prediction Based on 1.73 Square Feet of Frontal Area.	67
69	Temperature Effectiveness Vs. Airflow for Build 1 Regenerator Test Rig With 24 x 24 Wire Screen Matrix; Prediction Based on 2.23 Square Feet of Frontal Area	67
70	Temperature Effectiveness Vs. Rotor Speed for Build 1 Regenerator Test Rig	68
71	Pressure Loss Vs. Flow Parameter for Build 1, High-Pressure Side	69
72	Pressure Loss Vs. Flow Parameter for Build 1, Low-Pressure Side	69
73	Build 2 Rotary Regenerator Circumferential Matrix Assembly With Integrated Rub Strip at Top of Matrix Package	71
74	Build 2 Rotary Regenerator Circumferential Matrix Assembly Viewed From Cold Side of Vee Matrix; Screen Incorporates 24-Mesh, 0.0135-Inch-Diameter Wire	71
75	Build 2 Rotary Regenerator Circumferential Matrix Assembly Viewed From Hot Side of Vee Matrix; Screen Incorporates 24-Mesh, 0.0135-Inch-Diameter Wire	72
76	Leakage Calibration, Total Rotary Regenerator Leakage and Carryover	72

(U) ILLUSTRATIONS (Cont'd)

<u>Figure</u>		<u>Page</u>
77	Rotary Regenerator Build 2 Viewed From Cold Side Showing Circumferential Vee Matrix Assemblies and Hydraulic Drive	73
78	Temperature Effectiveness Vs. Airflow for Build 2 With 24 x 24 x 0.0135 Wire Screen Matrix and With Rotor Speeds of 40 and 45 R. P. M.	75
79	Temperature Effectiveness Vs. Airflow for Build 2 With 24 x 24 x 0.0135 Wire Screen Matrix and With Rotor Speeds of 50 and 55 R. P. M.	75
80	Temperature Effectiveness Vs. Rotor Speed for Builds 2 and 3 (1.0 and 1.5 Pounds per Second Airflow)	76
81	Temperature Effectiveness Vs. Rotor Speed for Build 2 (2.0 and 2.5 Pounds per Second Airflow)	76
82	Pressure Loss Vs. Flow Parameter for Builds 2 and 3 (High-Pressure Side)	77
83	Pressure Loss Vs. Flow Parameter for Builds 2 and 3 (Low-Pressure Side)	78
84	Mass Velocity Leaving Matrix Face Vs. Distance Along Matrix Face for Build 2	78
85	Predicted Ideal Regenerator Performance Vs. Regenerator Total Pressure Loss for 80 x 80 x 0.0037 Wire Screen Matrix (Frontal Area 1.73 Square Feet)	79
86	Predicted Ideal Regenerator Performance Vs. Regenerator Total Pressure Loss for 60 x 60 x 0.004 Wire Screen Matrix (Frontal Area 1.73 Square Feet)	80
87	Build 3 Rotary Regenerator Total Mass Loss Vs. Seal Cavity Pressure Drop	82

(U) ILLUSTRATIONS (Cont'd)

<u>Figure</u>		<u>Page</u>
88	Torus Inner Diameter (I.D.) Ring Seal Rig Schematic	86
89	Regenerator I.D. Ring Seal Test Installation Showing (1) Air Supply to Seal, (2) Pressure Sensing Line, (3) Seal Bleed, (4) Air Temperature Probes, (5) Rig Oil Scavenge Line, and (6) 3.4-to-1 Gearbox	86
90	Regenerator I.D. Ring Seal, Segmented Carbon, With Axial and Radial Spring Loading	87
91	Regenerator I.D. Seal Leakage Calibration, Segmented Single-Ring Carbon Seal With Uncompensated Seal Plate and Liner	87
92	Regenerator I.D. Seal Leakage Calibration, Single- Ring Segmented Carbon Seal With Compensated Plate and Liner (Ambient Air Temperature)	88
93	Regenerator I.D. Seal, Split One-Piece Conically Sprung Ring Seals Disassembled, Showing (1) Untapered Seal Plate, (2) Conical Carbons, (3) Wavy Spring Washer, and (4) Thrust Plates	89
94	Regenerator I.D. Seal, Split One-Piece Conically Sprung Ring Seals Assembled, Showing (1) Hub, (2) Tapered Seal Plate, (3) Conical Carbons, (4) Untapered Seal Plate, (5) Locking Nut, and (6) Wavy Spring Washer.	90
95	Regenerator I.D. Seal Leakage Calibration, Split One- Piece Conically Sprung Ring Seals (Ambient Air Tem- perature)	91
96	Regenerator I.D. Seal Leakage Calibration, Single- Ring Segmented Carbon Seal (Ambient Air Temperature) . .	91
97	Regenerator I.D. Seal Leakage Calibration, Single- Ring Segmented Carbon With Outer Diameter (O.D.) Seal Taper No. 1 and Compensated Plate and Uncom- pensated Plate and Uncompensated Liner; 500°F Air Temperature	93

(U) ILLUSTRATIONS (Cont'd)

<u>Figure</u>		<u>Page</u>
98	Regenerator I.D. Seal Leakage Calibration, Single-Ring Segmented Carbon With O.D. Seal Taper No. 1 and Compensated Plate and Uncompensated Liner; Ambient Air Temperature	93
99	Regenerator I.D. Seal Leakage Calibration, Single-Ring Segmented Carbon With O.D. Seal Taper No. 2 and Compensated Plate and Uncompensated Liner; 500°F Air Temperature	94
100	Regenerator I.D. Seal Leakage Calibration, Single-Ring Segmented Carbon With O.D. Seal Taper No. 2 and Compensated Plate and Uncompensated Liner; Ambient Air Temperature	94
101	Regenerator I.D. Seal Leakage Calibration, Split One-Piece Conically Sprung Ring Seals With Three Levels of Seal Plate Thickness	95
102	Leakage Area Vs. Seal Pressure Drop	95
103	Regenerator I.D. Seal Plate Showing Weight Reduction Scheme	96
104	Regenerator I.D. Seal Leakage Calibration, Conically Sprung One-Piece Carbon Ring Seal, Ambient Air Temperature, 15-Pound Spring Load (Seal Plate 0.75 Inch Thick at Inner Diameter, 0.5 Inch Thick at Outer Diameter)	96
105	Regenerator I.D. Seal Leakage Calibration, Conically Sprung One-Piece Carbon Ring Seal, 500°F Air Temperature, 15-Pound Spring Load (Seal Plate 0.75 Inch Thick at Inner Diameter, 0.5 Inch Thick at Outer Diameter)	97

(U) ILLUSTRATIONS (Cont'd)

<u>Figure</u>		<u>Page</u>
106	Regenerator I.D. Seal Leakage Calibration, Conically Sprung One-Piece Carbon Seal Ring, Ambient Air Temperature, 28-Pound Spring Load (Seal Plate 0.75 Inch Thick at Inner Diameter, 0.5 Inch Thick at Outer Diameter)	98
107	Regenerator I.D. Seal Leakage Calibration, Conically Sprung One-Piece Carbon Ring Seal, 500°F Air Temperature, 28-Pound Spring Load (Seal Plate 0.75 Inch Thick at Inner Diameter, 0.5 Inch Thick at Outer Diameter)	98
108	Axial View of Regenerator I.D. Ring Seal, Back-to-Back Segmented Carbon Seal	99
109	Edge View of Regenerator I.D. Ring Seal, Back-to-Back Segmented Carbon Seal, Showing (1) Carbon Segments, (2) Thrust Plates, (3) Step Joint, (4) Damaged Step Joint, and (5) Sealing Lips, Axial and Radial	100
110	Regenerator I.D. Seal Leakage Calibration, Back-to-Back Segmented Carbon Seal With Uncompensated Seal Plate and Liner; Ambient Air Temperature	100
111	Regenerator I.D. Seal Leakage Calibration, Back-to-Back Segmented Carbon Seal With Uncompensated Seal Plate and Liner; 500°F. Air Temperature	101
112	Regenerator I.D. Seal Leakage Calibration, Back-to-Back Segmented Carbon Seal With Compensated Seal Plate and Uncompensated Liner; Ambient Air Temperature	101
113	Regenerator I.D. Seal Leakage Calibration, Back to-Back Segmented Carbon Seal With Compensated Seal Plate and Uncompensated Liner; 500°F. Air Temperature	102

(U) ILLUSTRATIONS (Cont'd)

<u>Figure</u>		<u>Page</u>
114	Regenerator I.D. Seal Leakage Vs. Endurance Time, Segmented Single-Ring Carbon Seal With Compensated Seal Plate and Uncompensated Liner	103
115	Edge View of Regenerator I.D. Ring Seal, Back-to-Back Segmented Carbon Seal, Showing (1) Carbon Segments, (2) Thrust Plates, (3) Step Joint, (4) Damaged Step Joint, and (5) Sealing Lips, Axial and Radial	104
116	Regenerator I.D. Ring Seal, All-Metal Simplex Seal	104
117	Regenerator I.D. Ring Seal, All-Metal Simplex Seal Showing Axial and Radial Sealing Lips, Piston Ring End Gap and Beam Spring	105
118	Regenerator I.D. Ring Seal, All-Metal Split Ring Seal Showing (1) Sealing Lips and (2) Staggered Joints	105
119	Regenerator I.D. Ring Seal, All-Metal Split Ring Seal Showing (1) Wave Washer Spring, (2) Groove for Wave Washer, and (3) Sealing Lip	106
120	Regenerator I.D. Ring Seal, All-Metal Split Ring Seal With Radial Springing Showing Staggered Gaps at A and C and Retaining Ring B	107
121	Regenerator I.D. Seal Leakage Calibration, All-Metal Split Ring Seal (Ambient Air Temperature)	108
122	Regenerator I.D. Seal Leakage Calibration, All-Metal Split Ring Seal With Reduced Web Thickness and Uncompensated Seal Plate and Liner (Ambient Air Temperature)	108
123	Regenerator I.D. Seal Leakage Calibration, All-Metal Split Ring Seal With Reduced Web Thickness and Uncompensated Seal Plate and Liner (Ambient Air Temperature)	109

(U) ILLUSTRATIONS (Cont'd)

<u>Figure</u>		<u>Page</u>
124	Regenerator I. D. Seal Leakage Calibration, All-Metal Split Ring Wave Spring Seal With Compensated Seal Plate and Uncompensated Liner	110
125	Regenerator I. D. Seal Leakage Calibration, All-Metal Simplex Seal With Compensated Seal Plate and Uncompensated Liner	110
126	Radial Vee Matrix Arrangement	115
127	Circumferential Vee Matrix Arrangement	115
128	Circumferential Z-Matrix Arrangement	116
129	Circumferential W-Matrix Arrangement	116
130	Model of Regenerator Section, Cold Side	118
131	Model of Regenerator Section, Hot Side	119
132	Model of Regenerator Section, Tunnel Area Showing (1) Tunnel Lead-In Chamfer and (2) Piston Ring O. D. Guide Surface	119
133	Model of Regenerator Section, Bulkhead and Seal Area	120
134	Regenerator on T74 Test Bed	122
135	Regenerator Test-Bed Mockup, Engine Inlet Three-Quarter View	123
136	Regenerator Test-Bed Mockup, Regenerator Exhaust Three-Quarter View	123
137	Regenerator Test-Bed Mockup, Side View	124
138	Toroidal Rotary Regenerator Leakage Flow System Schematic	128

(U) ILLUSTRATIONS (Cont'd)

<u>Figure</u>		<u>Page</u>
139	Regenerator Effectiveness Ratio Vs. Percent Leakage for Axial Leakage	129
140	Regenerator Effectiveness Ratio Vs. Percent Leakage for Tangential Leakage Bypassing Matrix, Burner, and Turbine	129
141	Regenerator Effectiveness Ratio Vs. Percent Leakage for Tangential Leakage Bypassing Burner and Turbine	130
142	Predicted Design-Point SFC Performance, Gas Turbine Powerplants With Toroidal Rotary Regenerators	131
143	Predicted Design-Point Specific Power Performance, Gas Turbine Powerplants With Toroidal Rotary Re- generators	132
144	Predicted Specific Fuel Consumption, Regenerative T74 Powerplant	132
145	Predicted Compressor Airflow and Compressor Pres- sure Ratio, Regenerative T74 Powerplant	133
146	Predicted Compressor Efficiency and Compressor Speed, Regenerative T74 Powerplant	133
147	Compressor Operating Line, Regenerative T74 Power- plant	134
148	Predicted Turbine Efficiency and Turbine Pressure Ratio, Regenerative T74 Powerplant	134
149	Predicted Turbine Inlet Temperature, Regenerative T74 Powerplant	135
150	Predicted Regenerator Performance, Regenerative T74 Powerplant	135

(U) ILLUSTRATIONS (Cont'd)

<u>Figure</u>		<u>Page</u>
151	Predicted Fuel Flow and Flow System Pressure Loss, Regenerative T74 Powerplant	136
152	Predicted Design Point Trades, Regenerative T74 Powerplant	138
153	Predicted Design Point Trades, Regenerative T74 Powerplant	138
154	Predicted Design Point Trades, Regenerative T74 Powerplant	139
155	Predicted Design Point Trades, Regenerative T74 Powerplant	139
156	Matrix Clogging Loop Schematic	140
157	Matrix Clogging Loop Rig	141
158	Hot Side of Regenerator Matrix Clogging Test Specimen (Screen 60 x 60 x 0.0044) After 100 Hours of Hot- and Cold-Air Cycling (1800 Pounds per Hour Airflow and 1200°F. Air Temperature)	142
159	Cold Side of Regenerator Matrix Clogging Test Specimen (Screen 60 x 60 x 0.0044) After 100 Hours of Hot- and Cold-Air Cycling (1800 Pounds per Hour Airflow and 1200°F. Air Temperature)	143
160	Hot Side of Regenerator Matrix Clogging Test Specimen (Screen 80 x 80 x 0.0044) After 100 Hours of Hot- and Cold-Air Cycling (1800 Pounds per Hour Airflow and 1200°F. Air Temperature)	144
161	Cold Side of Regenerator Matrix Clogging Test Specimen (Screen 80 x 80 x 0.0044) After 100 Hours of Hot- and Cold-Air Cycling (1800 Pounds per Hour Airflow and 1200°F. Air Temperature)	145

(U) ILLUSTRATIONS (Cont'd)

<u>Figure</u>		<u>Page</u>
162	Hot Side of Regenerator Matrix Clogging Test Specimen (Screen 60 x 60 x 0.0065) After 100 Hours of Hot- and Cold-Air Cycling Endurance Test (1800 Pounds per Hour Airflow and 1200°F. Air Temperature).	146
163	Hot Side of Regenerator Matrix Clogging Test Specimen (Screen 60 x 60 x 0.0065) After 100 Hours of Unidirectional Operation at 1800 Pounds per Hour Airflow and 1200°F. Air Temperature	147
164	Cold Side of Regenerator Matrix Clogging Test Specimen (Screen 60 x 60 x 0.0065) After 100 Hours of Unidirectional Operation at 1800 Pounds per Hour Airflow and 1200°F. Air Temperature	148
165	Hot Side of Regenerator Matrix Clogging Test Specimen (Screen 80 x 80 x 0.0044) After 100 Hours of Unidirectional Operation at 1745 Pounds per Hour Airflow and 1200°F. Air Temperature	149
166	Cold Side of Regenerator Matrix Clogging Test Specimen (Screen 80 x 80 x 0.0044) After 100 Hours of Unidirectional Operation at 1745 Pounds per Hour Airflow and 1200°F. Air Temperature	150
167	Hot Side of Regenerator Matrix Clogging Test Specimen (Screen 60 x 60 x 0.0044) After 100 Hours of Unidirectional Operation at 1745 Pounds per Hour Airflow and 1200°F. Air Temperature	151
168	Cold Side of Regenerator Matrix Clogging Test Specimen (Screen 60 x 60 x 0.0044) After 100 Hours of Unidirectional Operation at 1745 Pounds per Hour Airflow and 1200°F. Air Temperature	152

(U) TABLES

<u>Table</u>		<u>Page</u>
I	Preliminary T74 Regenerator Performance	10
II	Matrix Requirements	11
III	Wire Screen Matrices Selected for Testing	12
IV	Wire Screen Matrices Selected for Testing in Expanded Program	19
V	Plate Fin Matrices Selected for Testing	20
VI	Rotary Regenerator Effectiveness Calibration Program . .	74
VII	Predicted Ideal Heat Transfer Core Requirements and Associated Regenerator Performance for a 6-Percent Total Pressure Loss on Build 3	80
VIII	Comparison of Inner Diameter Seal Test Results	92
IX	All-Metal Seal Spring Load Tests	111

(U) SYMBOLS

C_r/C_c	heat capacity ratio of rotor to cold stream
ϵ	temperature effectiveness, $\epsilon = \Delta T_{\text{actual}} / \Delta T_{\text{ideal}}$
f	fanning friction factor
G/G_{avg}	local-to-average flow per unit area
J	Colburn factor, $J = N_{\text{st}}(N_{\text{pr}})^{2/3}$
N_{pr}	Prandtl number, $N_{\text{pr}} = \mu C_p / K$
N_{Re}	Reynolds number, $N_{\text{Re}} = W D_e / \mu p A_{\text{fr}}$
N_{st}	Stanton number, $N_{\text{st}} = h / G C_p$
p	porosity, $p = \text{void volume} / \text{total volume}$
$\Delta P / P$	pressure loss coefficient
X / L	relative distance along matrix face from apex of fold
A_c	matrix free flow area, ft. ²
A	total matrix surface area, ft. ²
A_{fr}	matrix face area, ft. ²
A / V	surface area density, ft. ² / ft. ³
C_c	air side heat capacity, B.t.u./sec.-°F.,
	$C_c = C_{\text{pa}} W$
C_p	specific heat at constant pressure, B.t.u./lb.-°F.
C_r	rotor heat capacity, B.t.u./sec.-°F.,
	$C_r = C_{\text{pm}} M_m N$

(U) SYMBOLS (Cont'd)

D_e	hydraulic diameter, ft., $D_e = 4pV/A$
G	stream mass velocity, lb./ft. ² -sec., $G = W/A_c$
h	coefficient of heat transfer, B.t.u./hr.-ft. ² -°F.
K	thermal conductivity of fluid, B.t.u./hr.-ft.-°F.
M	rotor mass, lb.
N	rotor speed, revolutions/min.
P	total pressure, lb./in. ²
P_{T1}	inlet total pressure, lb./in. ² abs. (p. s. i. a.)
SCFM	standard cubic feet per minute, ft. ³ /min.
SFC	specific fuel consumption, lb./hp.-hr.
SHP	shaft horsepower, hp.
T	temperature, °R.
T_{T1}	inlet total temperature, °R.
W	mass flow rate, lb./sec.
$W\sqrt{T}/P$	flow parameter, lb.-(°R.) ^{0.5} /sec.-p. s. i. a.
μ	absolute fluid viscosity, lb./ft.-hr.
a	air (as an additional subscript to above symbols)
g	gas (as an additional subscript to above symbols)
m	metal (as an additional subscript to above symbols)

CONFIDENTIAL

INTRODUCTION

Current gas turbine engine component efficiencies have been developed to a high level over a period of years. Future major improvement in engine performance is most likely to result from lightweight high-effectiveness regenerators, higher turbine inlet temperature, and higher compressor ratio. The purpose of this program is to advance the technology of regenerators for small gas turbine engines, not only for future aircraft propulsion but also for future ground vehicle and stationary power units.

Three basic types of heat exchangers have been used for regenerative gas turbine engines: direct gas-to-air transfer, indirect transfer using a liquid medium, and the rotary (rotating matrix) system.

The direct transfer, or stationary type, is generally of shell-on-tube or plate-fin construction in which the tubes or plates act as heat transfer surfaces and also as structural elements separating the air and gas flows. As a result of many years of experience with these heat exchangers, their performance is well understood. Therefore, they can be designed for a selected effectiveness with confidence. Where very high effectiveness is required in a reasonable size and weight, a design having very small tube diameter (or plate spacing), very thin materials, and thousands of brazed or welded joints is required. The fabrication and inspection of such a construction becomes difficult; there is limited practical experience with the use of fine-grain heat exchangers on regenerative gas turbines. A failure of a tube or plate, either from fatigue of a thin wall or a failure of a brazed joint, results in a direct leak of high-pressure air causing decay or loss of engine power.

The indirect type of heat exchanger offers certain advantages in arrangement of the engine and in fabrication of the heat exchanger, but it has the drawback of adding a new system (the heat transfer fluid circuit) to the engine. This system requires pumps and associated plumbing and must be kept leak-tight. In addition, the heat transfer fluid (usually a combination of sodium and potassium) requires special handling and logistics due to its unstable and corrosive properties.

The highest effectiveness levels for the lowest core weights can be achieved with the rotary heat exchanger. In this type, porous matrix elements are alternately heated and cooled by the hot gas and cool airstreams. Thus, thermal energy is transported from the exhaust gas to the compressed air before entering the combustor. One type of rotary heat exchanger is constructed in the form of a rotating disk or drum, which carries the matrix elements from one stream to the other. Sealing the passage between the hot and cold regions is

CONFIDENTIAL

a major problem with this type of rotary heat exchanger. This problem has inhibited the use of disk- and drum-type designs except in low-compression-ratio engines.

The toroidal rotary regenerator incorporates three design features which obviate the problems inherent in the drum and disk rotary regenerators. First, the matrix is folded so that the effective matrix frontal area is two to four times the torus frontal area. This feature allows compact packaging so that low pressure loss and high effectiveness are possible in a small overall package. The void volume mass carryover inherent with this type packaging causes a small performance loss, but this is more than offset by the advantages of increased frontal area. For comparison, the outer diameter of a toroidal regenerator is approximately one-half that of a comparable disk regenerator.

Second, the critical high-pressure seals in the toroidal regenerator have fundamentally superior durability and leakage characteristics. This is possible because the packaging of the matrix permits exclusive use of conventional rubbing seals. The primary considerations in the design of satisfactory rubbing seals are the nature of the rubbing surface and the ability of the seal to adapt to distortions in the surface that result from machining, thermal distortion, and wear. The circular piston ring and carbon ring seals used in this design are inherently flexible and readily adapt to such distortions. The machined flame-plated surfaces of the stationary tunnel provide durable, relatively distortion-free rubbing surfaces for the piston ring seals. In contrast, the flat seals required in the drum and disk regenerators must be segmented with uniform spring loading and a rigid support in order to obtain the necessary flexibility. It is difficult to provide an adequate rubbing surface in these designs because the matrix carries structural loads. Additional advantages of the sealing system used in the toroidal design are the relatively short length of the seals and the elimination of leakage at sharp corners.

The third advantage of the toroidal design is that the matrix is not a structural member. The complete loss of one or more matrix packages would result in a slight increase in fuel consumption but would not affect cycle leakage and power or the structural integrity of the engine. This feature permits the selection of highly efficient heat transfer surfaces without structural restrictions. Any rotor failure which may cause the rotor to jam would result in the loss of regenerator effectiveness, but it would not affect the power output.

The toroidal rotary regenerator has a good potential for meeting performance, leakage, weight, and structural integrity requirements of aircraft, ground vehicles, and stationary power applications.

CONFIDENTIAL

CONFIDENTIAL

The feasibility of this concept, which was developed at Pratt & Whitney Aircraft, was demonstrated under U. S. Navy Contract NOw 62-0636-f during the period 1962-1963. This work demonstrated:

- Design point leakage in component rigs,
- Nonclogging principle of cyclic flow matrix,
- Seal overhaul life equal to engine requirements,
- No performance deterioration due to seal wear, and
- Potential to operate at 1400°F. gas inlet temperature.

This early program made evident the technical areas where improvements, additional optimizations, and weight reduction were possible. The component work accomplished during Phase I of this program was aimed at all of the above items. In addition, the design of a new high-effectiveness lightweight rotary regenerator sized for the T74 engine cycle was completed.

The overall objective of this program, which consists of two phases, is to demonstrate the feasibility of a high-effectiveness, lightweight toroidal regenerator which will be capable of providing a potential for engine specific fuel consumption of less than 0.40 pound of fuel per horsepower-hour with a 50-percent reduction in part-load specific fuel consumption relative to current gas turbine engines. The following sections discuss the accomplishments of the five contract items of work in Phase I of the program.

CONFIDENTIAL

ANALYTICAL STUDY OF MATRIX CANDIDATES

The toroidal rotary regenerator inherently permits a wide latitude in choice of heat exchanger surface and material because the matrix does not serve as a separator between high- and low-pressure streams (bulkheads are incorporated for this purpose). Therefore, the matrix does not carry a large mechanical load. For this reason, packed screens and other surfaces with optimum thermodynamic, rather than mechanical, characteristics can be considered for this type heat exchanger. The regenerator matrix should have the following characteristics:

- High thermal capacity to minimize rotational speed and thus carryover leakage and seal wear.
- High heat transfer per unit pressure drop.
- Low frontal area and thickness to minimize regenerator size.

The regenerator constructed and tested under the previous contract (NOw 62-0636-f) used a 24-mesh, 0.0135-inch-wire-diameter screen pack for the matrix (24 wires per inch by 24 wires per inch, each wire 0.0135 inch in diameter; also specified in this report as 24 x 24 x 0.0135 without dimensions--other sizes expressed similarly). This was at that time the optimum matrix for which design data were available. Studies completed since then indicated that significant improvements in both regenerator weight and performance can be realized with matrices of high porosity and fine mesh. However, these matrix geometries had been neither fabricated nor tested prior to the present contract. The lack of basic heat transfer, friction factor, and packaging loss data limited the design of more efficient regenerators.

The object of Phase I of the program was to determine analytically the optimum matrix configuration with respect to effectiveness, weight, carryover, and pressure loss for a T74-size regenerator. The specific goals of the analytical study of matrix candidates (Contract Item 1 of Phase I) were (1) to evaluate candidate matrices, including theoretical matrices, for which data did not exist, and (2) to select a minimum of eight matrices for experimental evaluation under Item 2.

CONFIDENTIAL

METHOD OF ACCOMPLISHMENT

In order to select matrix candidates for testing in a transient heat transfer rig, an analytical study was conducted in the following phases.

- Literature survey to update our prediction system.
- Prediction of heat transfer and friction characteristics of new matrices.
- Comparative studies of regenerator frontal area, matrix thickness, matrix weight, carryover leakage, and rotational speed to meet the T74 cycle conditions and to give an overall SFC of 0.40 pound per horsepower-hour.

Each of these steps is described in the following paragraphs.

A literature survey to update the file of friction and heat transfer data for potentially attractive surfaces was completed. A bibliography of the pertinent literature reviewed is on page 154.

The work by L. S. Tong and A. L. London (reference 9) represents the best available correlation of wire screen heat transfer and pressure loss characteristics. These characteristics are represented as the Colburn factor, J , and the Fanning friction factor, f , as functions of Reynolds number. The primary variables of this correlation are matrix porosity and screen mesh density.

The predicted Colburn and friction factors obtained from the correlation were compared to the data obtained by J. E. Coppage (reference 2). This comparison indicates an accuracy of ± 10 percent for Colburn factors and from ± 10 percent (large meshes) to as large as -35 percent (fine meshes) for friction factors.

In order to determine the effects of mesh density and porosity, various representative screens were investigated using Tong and London's correlation. The predicted friction and factor variation with Reynolds number for these screens is shown in Figures 1 through 7, and the predicted Colburn factor variation with Reynolds number is shown in Figure 8.

Relative regenerator matrix frontal area, thickness, weight, carryover, and rotational speed resulting from predicted characteristics were evaluated at the T74 engine operating conditions (Table I). The matrix requirements (Table II) are related to the $24 \times 24 \times 0.0135$ mesh because more data are available for this mesh than any other under consideration. Also, our previous regenerator used this matrix.

CONFIDENTIAL

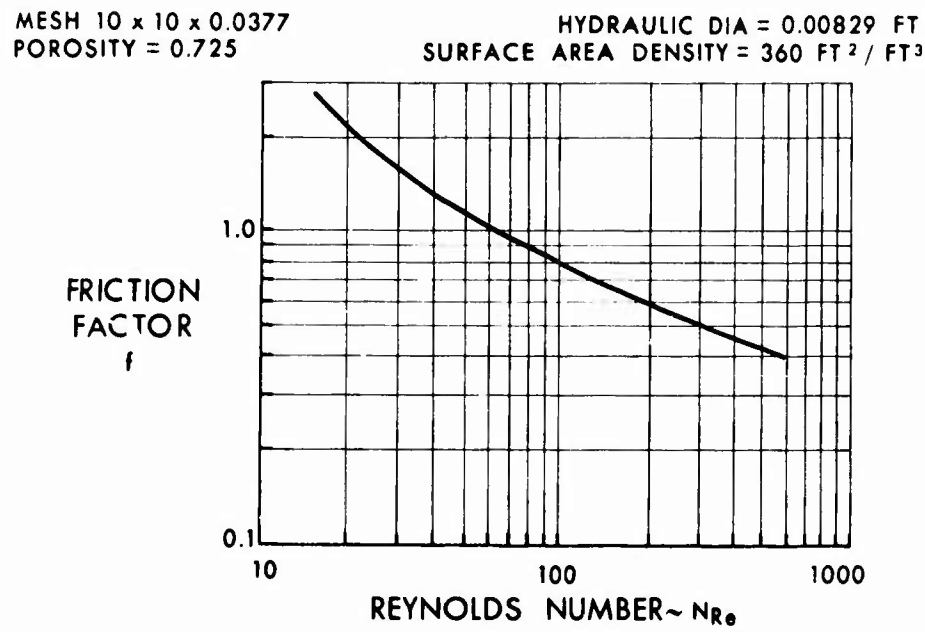


Figure 1. Predicted Friction Factor Vs. Reynolds Number for 10 x 10 x 0.0377 Wire Screen Matrix.

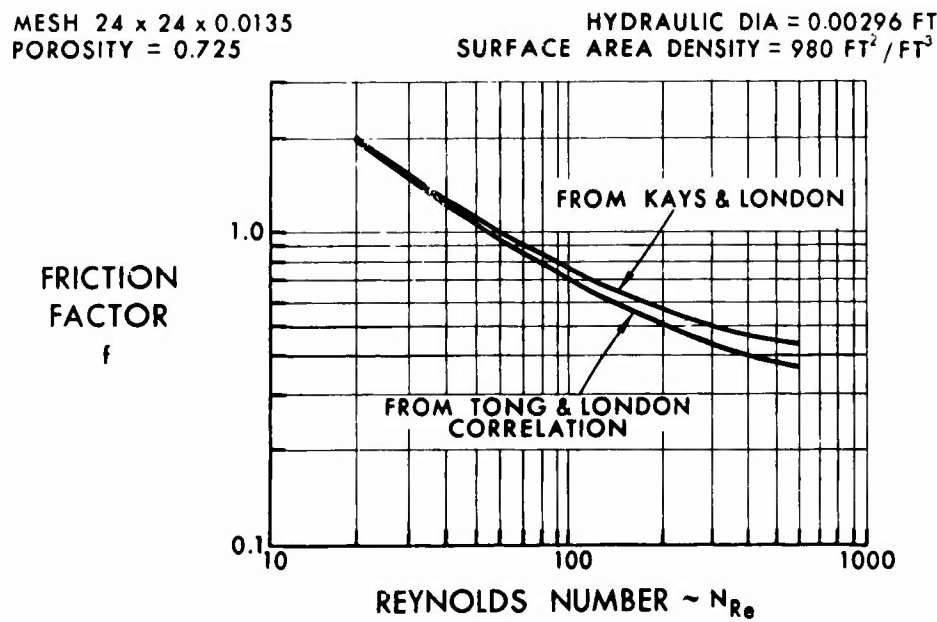


Figure 2. Predicted Friction Factor Vs. Reynolds Number for 24 x 24 x 0.0135 Wire Screen Matrix.

CONFIDENTIAL

CONFIDENTIAL

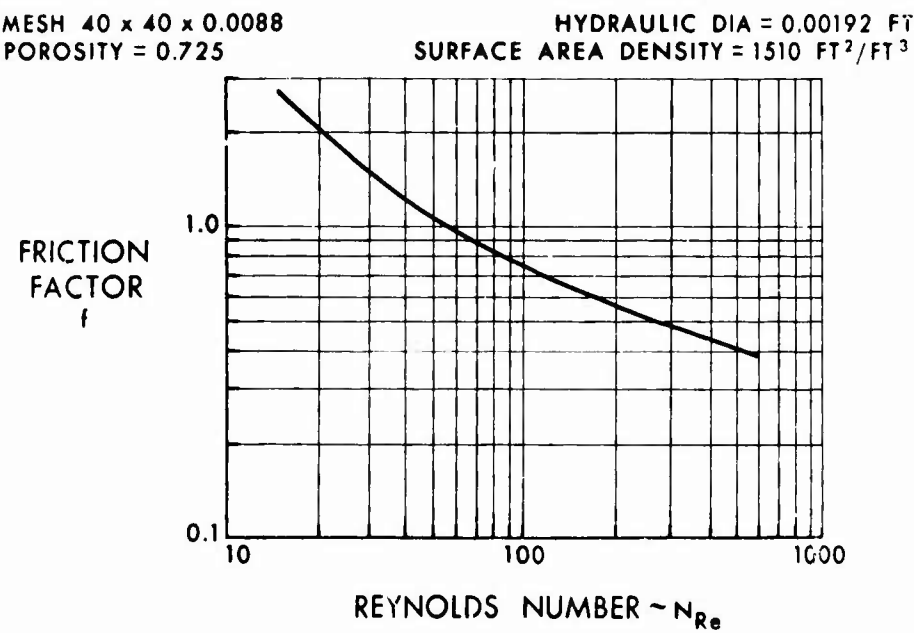


Figure 3. Predicted Friction Factor Vs. Reynolds Number for 40 x 40 x 0.0088 Wire Screen Matrix.

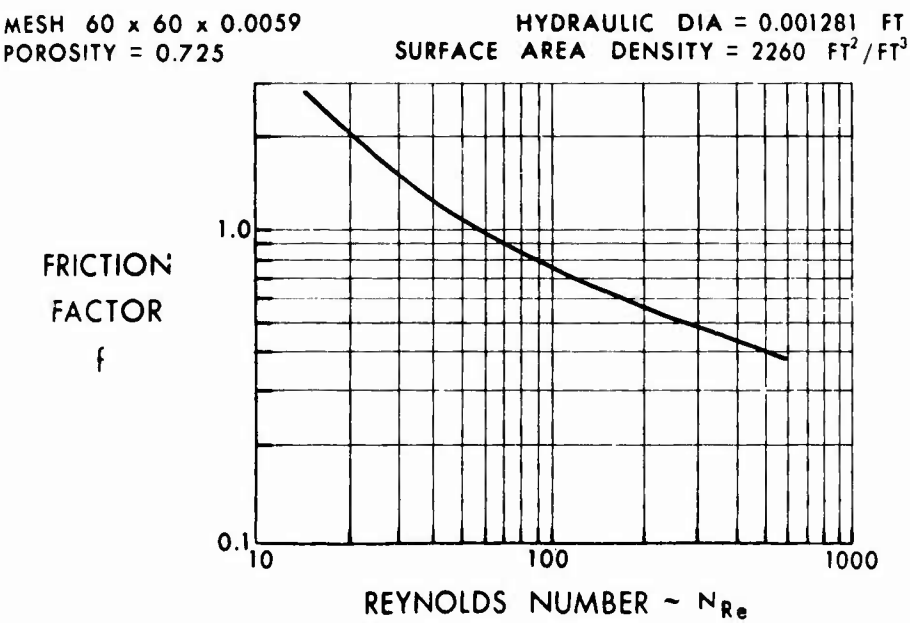


Figure 4. Predicted Friction Factor Vs. Reynolds Number for 60 x 60 x 0.0059 Wire Screen Matrix.

CONFIDENTIAL

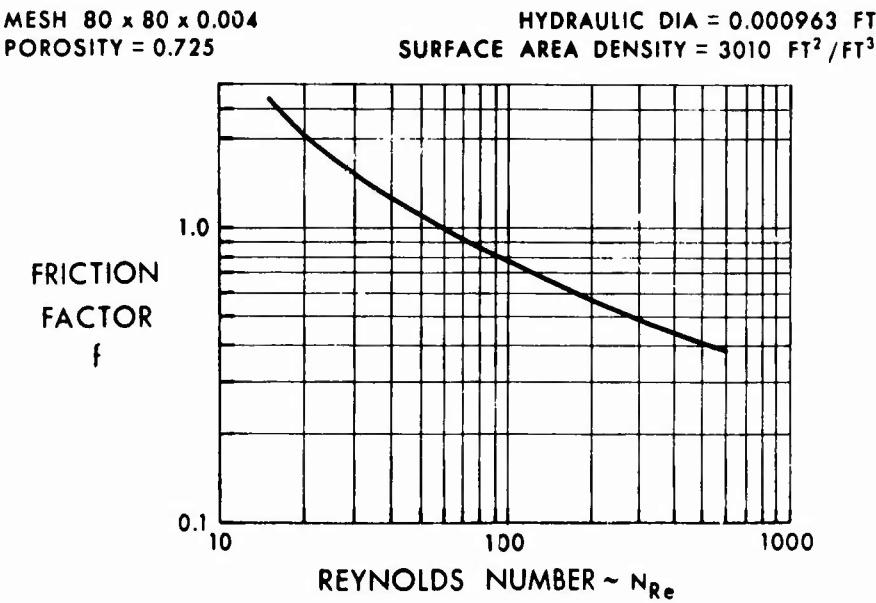


Figure 5. Predicted Friction Factor Vs. Reynolds Number for 80 x 80 x 0.004 Wire Screen Matrix.

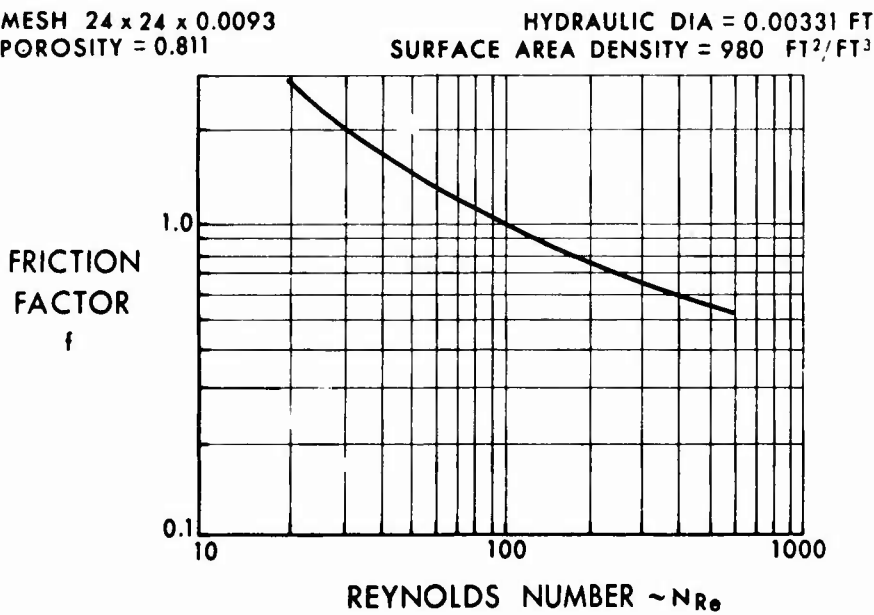


Figure 6. Predicted Friction Factor Vs. Reynolds Number for 24 x 24 x 0.0093 Wire Screen Matrix.

CONFIDENTIAL

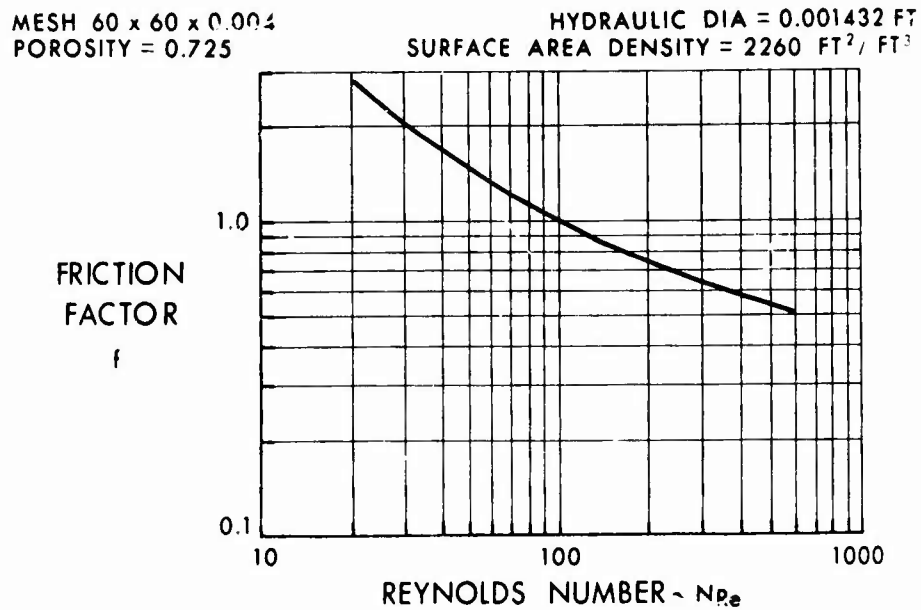


Figure 7. Predicted Friction Factor Vs. Reynolds Number for 60 x 60 x 0.004 Wire Screen Matrix.

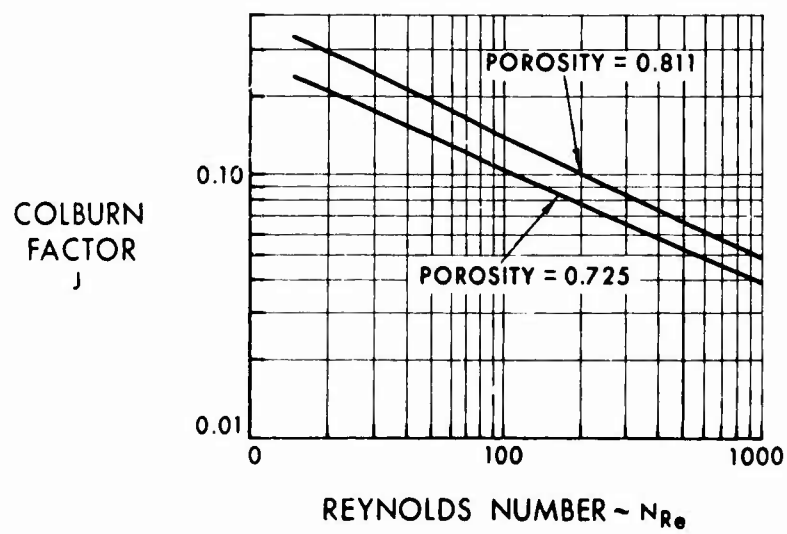


Figure 8. Predicted Colburn Factor Vs. Reynolds Number.

CONFIDENTIAL

TABLE I
PRELIMINARY T74 REGENERATOR PERFORMANCE

Engine airflow	4.7 lb./sec.
Net regenerator effectiveness	85%
Regenerator pressure loss	6%
Air-side-in temperature and pressure	435°F., 75.5 p.s.i.a.
Gas-side-in temperature and pressure	1236°F., 16.5 p.s.i.a.

From this comparison, it can be seen that, for constant-porosity wire screen matrices, the matrix thickness and weight are substantially reduced as mesh density increases, while rotational speed tends to increase significantly. Increased porosity moderately reduces matrix frontal area, thickness, and weight, while it significantly increases the required rotational speed and therefore the matrix carryover leakage.

Two corrugated types of matrix having relatively high surface area densities are also compared in Table II. These surfaces have been compared to others of a similar type by C. P. Howard (reference 3) and were found to demonstrate excellent heat transfer capability per unit of pressure loss. These matrices require smaller matrix frontal area than the wire screens. However, the thickness of matrix required makes the packaging of such matrices difficult in a lightweight toroidal configuration. The net effect is that torous frontal area and weight will be larger than with screen-type matrices.

From an overall point of view, the higher mesh, highly porous screens define the most compact torus with lowest weight. However, the relative carryover given in Table II is for the matrix only. The torus void volume, the void space outside the matrix, also contributes to carryover. This void space carryover varies directly with rotational speed; this results in a substantial carryover loss for the high-mesh-density, high-porosity matrices which require high rotational speeds. A study of this trade indicates that the performance losses associated with the higher carryover do not offset the improvement gained in reduced torus size and weight.

CONFIDENTIAL

TABLE II
MATRIX REQUIREMENTS

Matrix Size	Matrix Porosity	Matrix Surface Area Density (ft. 2/ft. 3)	Matrix Requirements Relative to 24 x 24 x 0.0135			
			Frontal Area (ft. /ft.)	Thickness (in. /in.)	Weight (lb./lb.)	Carry-over Ratio
10 x 10 x 0.0377	0.725	350	0.955	4.68	4.44	1.0
24 x 24 x 0.0135	0.725	980	1.000	1.000	1.000	1.0
40 x 40 x 0.0088	0.725	1510	1.04	0.582	0.60	1.0
60 x 60 x 0.0059	0.725	2260	1.05	0.32	0.327	1.0
80 x 80 x 0.0044	0.725	3010	1.07	0.221	0.231	1.0
24 x 24 x 0.0093	0.811	980	0.941	0.93	0.62	1.63
60 x 60 x 0.0040	0.811	2260	0.95	0.262	0.156	1.63
Corrugated	0.866	3219	0.833	1.43	0.625	2.45
CERCOR	0.650	1500	0.988	1.82	0.476	2.35

CONFIDENTIAL

RESULTS

As a result of the comparison shown in Table II, the wire screen matrices listed in Table III were chosen for testing in the transient-type heat transfer rig to determine actual heat transfer and friction loss characteristics.

TABLE III
WIRE SCREEN MATRICES SELECTED FOR TESTING

Mesh (wires/inch)	Wire Diameter (inch)	Porosity	Surface Area Density (ft. 2/ft. 3)
10 x 10	.0377	.725	350
24 x 24	.0135	.725	980
40 x 40	.0088	.725	1510
60 x 60	.0059	.725	2260
80 x 80	.0044	.725	3010
24 x 24	.0093	.811	980
60 x 60	.004	.811	2260
60 x 60	min.	max.	max.

Limits as to the highest mesh and finest wire diameter have been set at this time by the following considerations:

1. Previous matrix clogging data indicate that meshes of 100 x 100 or finer will gradually clog, even with cyclic flow.
2. Minimum wire diameter currently available is larger than 0.003 inch.

The selection of these wire screens for testing is based on the following:

1. Fine-mesh wire screens potentially offer significant reduction in matrix volume and weight. The 80 x 80 x 0.0044 screens, however, represent the practical limit from the standpoint of carryover loss and potential matrix clogging.
2. The wire screens selected for test represent a range of the two major parameters, porosity and surface-to-volume ratio, which are of prime interest not only in this program but also in future regenerator designs.
3. The 24 x 24 x 0.0135 matrix provides a basis for comparison to the test data obtained by other investigators.

CONFIDENTIAL

CONFIDENTIAL

4. Other types of available matrices, such as corrugated steel and CERCOR,* have been tested by other investigators.

* Trademark of Corning Glass Works, Corning, New York

CONFIDENTIAL

CONFIDENTIAL

MATRIX EXPERIMENTAL INVESTIGATION

The object of Contract Item 2 of Phase I was to conduct a matrix experimental investigation, which, for purposes of this report, is divided into periodic-flow heat transfer tests and matrix configuration and flow distribution tests.

PERIODIC-FLOW HEAT TRANSFER TESTS

The goal of this program was to obtain sufficient design data so that the optimum matrix package configuration could be selected for the T74 regenerator. At least eight matrices were experimentally evaluated in a transient-type heat transfer rig to obtain design data where none previously existed.

Method of Accomplishment

To evaluate the heat transfer and frictional characteristics of the matrices, a periodic-flow heat transfer test rig was designed and constructed; it is shown schematically in Figure 9. The test rig is similar in principle to the experimental apparatus used by G. L. Locke at Stanford University. The matrix was first cooled to a uniform low temperature and then, by switching the air through a valving arrangement, was heated by a stream of air which entered at a constant higher temperature. The time-temperature response of the fluid leaving the matrix was recorded. This response was compared with that predicted by the Schumann analysis; the method developed by G. L. Locke, which involves determining slope of the response curve to determine the heat transfer coefficient, was used in making the comparison.

Description of Test Rig. The test rig consists of a compressed-air source, an indirect gas-fired heater, a quick-change air valve arrangement, a test matrix, an orifice, a pressure measuring system, and a temperature measuring system. A 4-inch-diameter test matrix was selected to provide test data over the range of Reynolds numbers from 50 to 2000 with the available air supply of 1.2 pounds per second.

Air is supplied intermittently to the test core from two sources at different temperature levels. The first system supplies cool air so that the matrix temperature may be reduced to a uniform low temperature before the "hot blow". The cool air enters a transition section (located between the matrix and the main-stream switch valve), passes through the matrix, and is exhausted in the main discharge duct.

The cold-air flow is not measured, since its function is only to cool the matrix to a uniform low temperature. The transition section is constructed of a low-conductivity material to minimize heat losses. The section is made as short as possible,

CONFIDENTIAL

CONFIDENTIAL

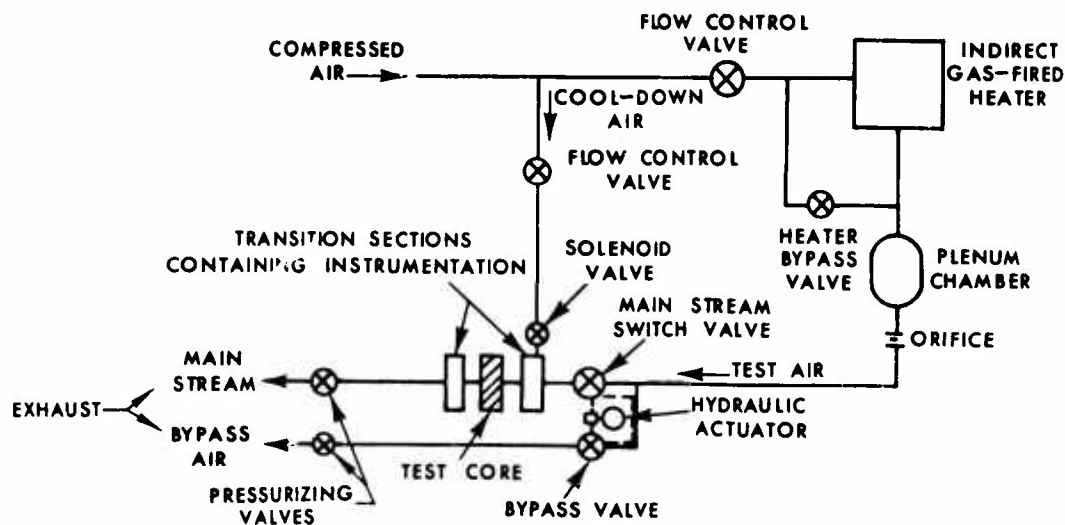


Figure 9. Periodic-Flow Matrix Heat Transfer Test Rig Flow Diagram.

approximately 1 inch, to minimize the volume of cool air passing through the matrix at the onset of the "hot blow". The hot-air system supplies air to the test section through an indirect gas-fired heater in which the air is heated to 300°F. A bypass around the heater is provided for mixing of cooler air with the hot air for further temperature control of the air to the test section. A test air temperature range of 130° to 190°F. was selected.

The hot air flows continually at the desired flow rate to the quick-change valve system. During the matrix cool-down period, the hot air is continuously short-circuited before reaching the matrix through holes provided in the main-stream switch ball valve body. This air is passed around the main valve body to maintain the valve at the hot airstream temperature so that air temperature changes during the "hot blow" can be kept to an absolute minimum. After the matrix has reached a uniform temperature, the cooling air is turned off and the main switch valve and bypass valve are actuated. As the bypass valve closes, the main stream switch valve opens and allows hot air to flow instantly through the matrix test core. The two switch ball valve stems are arranged back-to-back and are actuated from a common lever so that they are 180° out of phase. Ball valves were selected for the air switching system because of the uniform flow profiles and the low-pressure loss characteristics of this type of valve.

CONFIDENTIAL

Control of the airflow rate is achieved with a pressure regulating valve located upstream of the indirect-fired heater, a flow control valve, and an air choking device not shown in Figure 9 but located just downstream of the orifice. Flow is measured with a VDI* standard orifice; orifice plates of different throat diameters are used to meter the flow over the desired range. To ensure uniform flow entering the matrix, a flow straightener and approximately 5 feet of 4-inch pipe are used ahead of the matrix. The test section shown in Figure 10 is comprised of a 4-inch-inside-diameter wooden duct of length equal to the matrix thickness. The matrix is held between two slightly larger diameter screens sandwiched between support rings on each side of the matrix duct. Instrumentation rings of the same diameter as the matrix and approximately 1 inch in length are provided immediately upstream and downstream of the test section. Both matrix upstream and downstream temperatures are measured with 0.0017-inch-diameter thermocouple probes during test. These thermocouples are mounted in the instrumentation ring and are equally spaced 45° apart. An exploded view of the matrix assembly is shown in Figure 11. Amplifiers are provided for each thermocouple

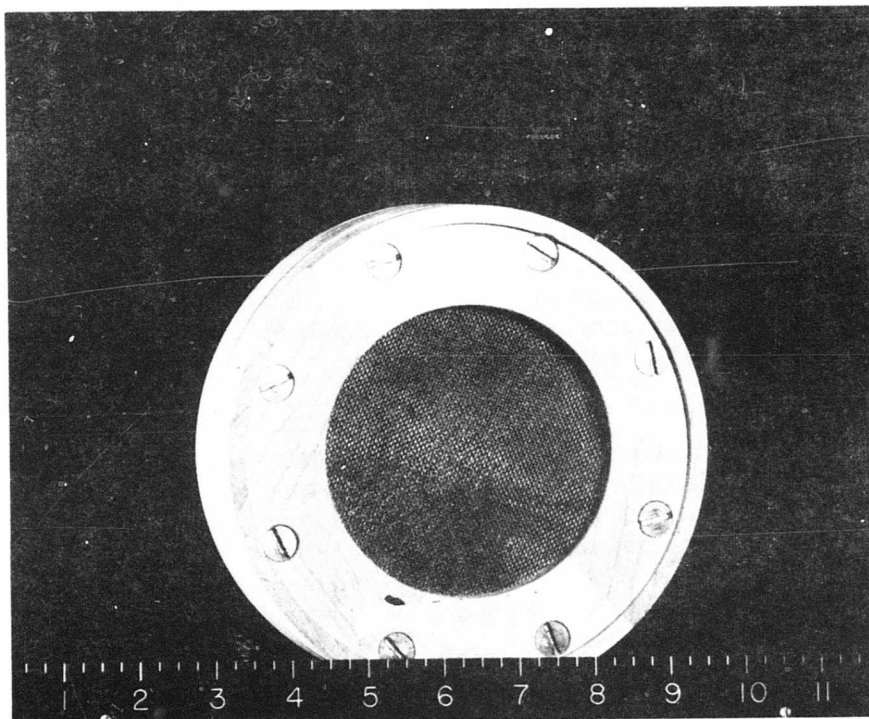


Figure 10. Matrix Holder With Screens.

* Verein deutscher Ingenieure (Association of German Engineers)

CONFIDENTIAL

CONFIDENTIAL

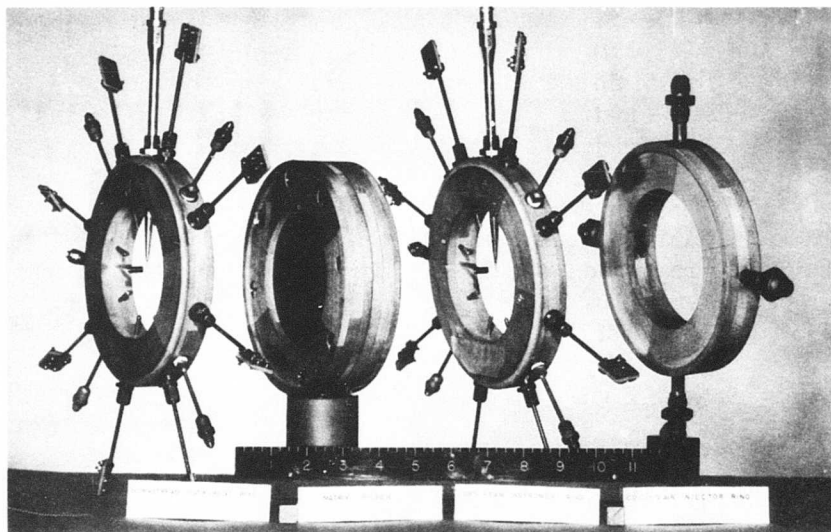


Figure 11. Exploded View of Matrix Assembly.

circuit to minimize errors due to impedance changes. Four equally spaced static pressure taps are provided on each side of the matrix in the transition sections. Kiel probes on each side of the matrix are used to measure total pressure. The time-temperature responses are recorded on a recording oscillograph. A photograph of the rig containing the matrix assembly is shown in Figure 12.

Test Program. Since the method of data analysis described earlier required a step change in the upstream temperature, shakedown tests were conducted to insure this change and to insure rapid flow establishment. The tests showed that the two valves could be actuated in 0.09 second. Tests conducted with a hot wire anemometer probe showed that the flow was established within 0.1 second. A typical recorder trace showing time-temperature traces and flow establishment time is shown in Figure 13. From these traces it was concluded that the performance of the rig was satisfactory and that good data could be obtained.

As a result of the analytical study of matrix candidates, the wire screen matrices listed in Table III were chosen for testing to determine the actual heat transfer and friction loss characteristics.

Orders were placed with two manufacturers (A and B) for the screen material because the thickness per layer varied between the two companies for the same mesh and wire diameter. The thickness of the screen is a function of the

CONFIDENTIAL

CONFIDENTIAL

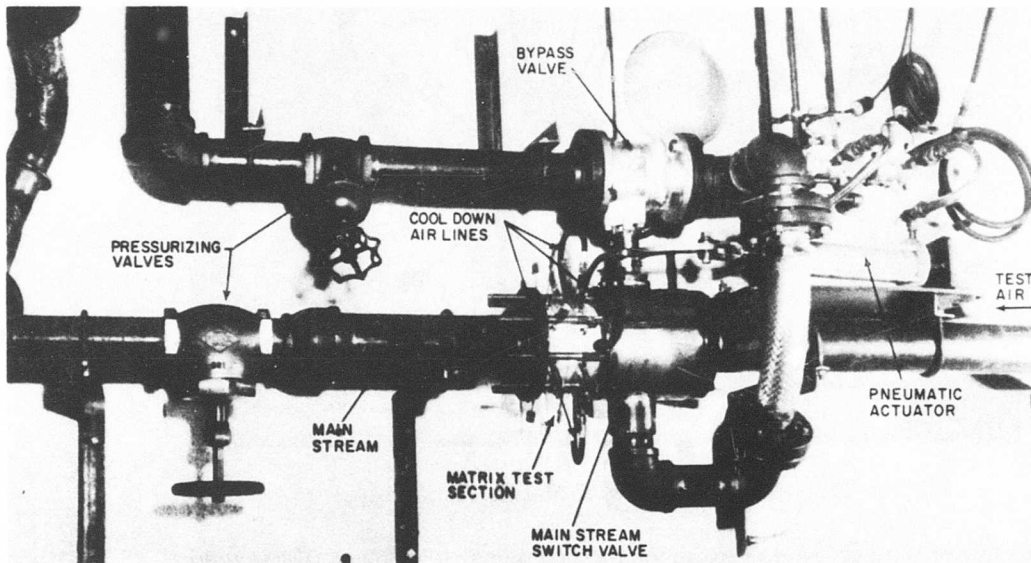


Figure 12. Periodic-Flow Matrix Heat Transfer Rig.

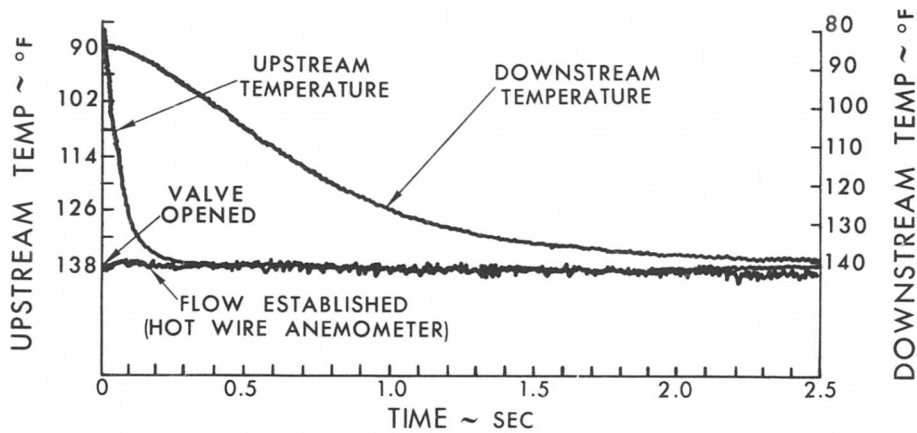


Figure 13. Typical Time-Temperature Response for 42-Layer, 24 x 24 x 0.010 Wire Screen Matrix.

CONFIDENTIAL

CONFIDENTIAL

weaving process. Screen layer thickness manufactured by B was approximately twice the wire diameter; the screen layer thickness manufactured by A was approximately 2.5 times the wire diameter. Since porosity is also a function of screen thickness, this factor was evaluated later in this part of the program.

Inquiries were also sent to various plate-fin manufacturers who might possibly produce matrices containing heat transfer surface-to-volume ratios of 3000 to 5000 square feet per cubic foot.

The matrices which were obtained for testing are listed in Tables IV and V. These tables include wire screens, CERCORS, sintered screens, and a plate-fin matrix.

TABLE IV
WIRE SCREEN MATRICES SELECTED FOR TESTING IN EXPANDED PROGRAM

Mesh (wire/in.)	Wire Dia. (in.)	Manu- facturer	Porosity	Surface Area Density (ft. ² /ft. ³)
1. 10 x 10 *	0.035	A	0.748	346
2. 24 x 24 *	0.0075	A	0.854	984
3. 24 x 24 *	0.015	A	0.757	805
1. 40 x 40 *	0.0085	A	0.723	1640
5. 60 x 60 *	0.004	A	0.802	2654
6. 60 x 60 *	0.0065	A	0.711	2131
7. 80 x 80 *	0.0037	A	0.790	2720
8. 100 x 100 *	0.0045	A	0.682	3394
9. 10 x 10 (sintered)	0.0035	A	0.976	329
10. 10 x 10	0.0035	B	0.976	329
11. 24 x 24	0.011	B	0.818	794
12. 24 x 24 *	0.0135	B	0.746	902
13. 24 x 24 (sintered)	0.0135	B	0.746	902
14. 60 x 60 *	0.0018	B	0.902	2240
15. 60 x 60 *	0.0058	B	0.755	2024
16. 60 x 60 *	0.0069	B	0.675	2259
17. 60 x 60 (sintered)*	0.0075	B	0.667	2130
18. 60 x 60 (edge sintered)*	0.006	B	0.675	2259
19. 80 x 80	0.0037	B	0.795	2660
* Tests completed				

CONFIDENTIAL

TABLE V
PLATE FIN MATRICES SELECTED FOR TESTING

Matrix	Cells/in. ²	Manu- facturer	Porosity	Surface Area Density (ft. ² /ft. ³)
1. T-20-38 CERCOR*	1000	A	0.60	1400
2. T-40-75 CERCOR	360	A	0.68	900
3. TC-20-38 CERCOR *	1000	A	0.60	1400
4. TC-20-38 Imp. CERCOR	1000	A	0.60	1400
5. TC-40-75 CERCOR	360	A	0.68	900
6. P-WF-1 (Stainless Steel)	588	B	0.761	2860

* Tests completed

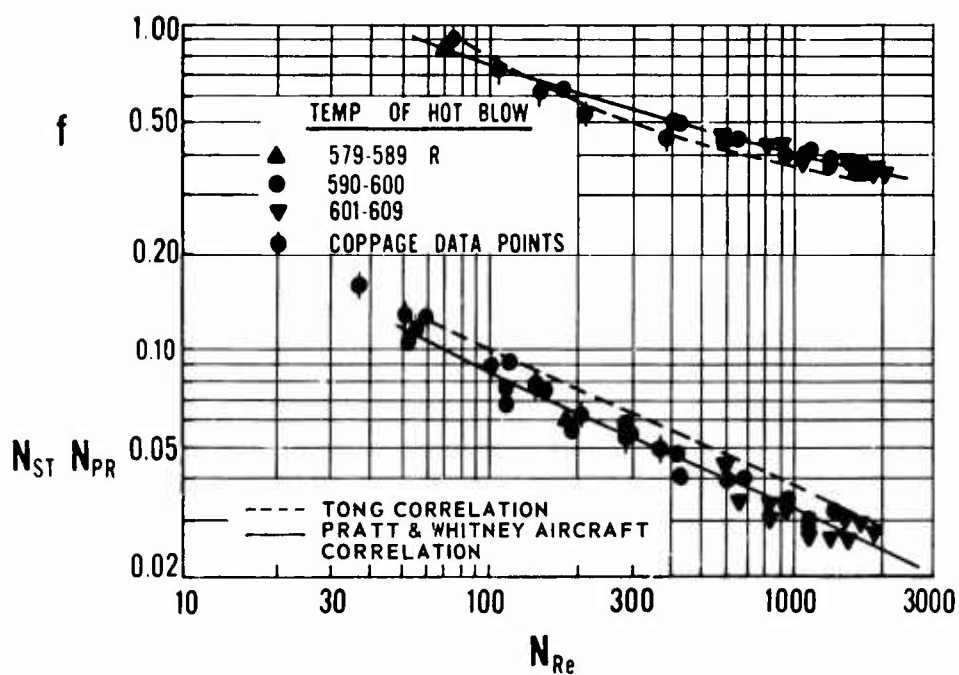
Results

Sixteen matrices were tested and are indicated with asterisks in Tables IV and V. The results of these tests are shown in Figures 14 through 29 in the form of Fanning friction factor and the product of Stanton and Prandtl numbers versus Reynolds number. Where direct comparison could be made with other experimenters' findings, data were in good agreement.

From these test results, the 60-mesh, 0.0040-inch-wire-diameter screen was selected as the optimum matrix for the high-effectiveness, lightweight regenerator.

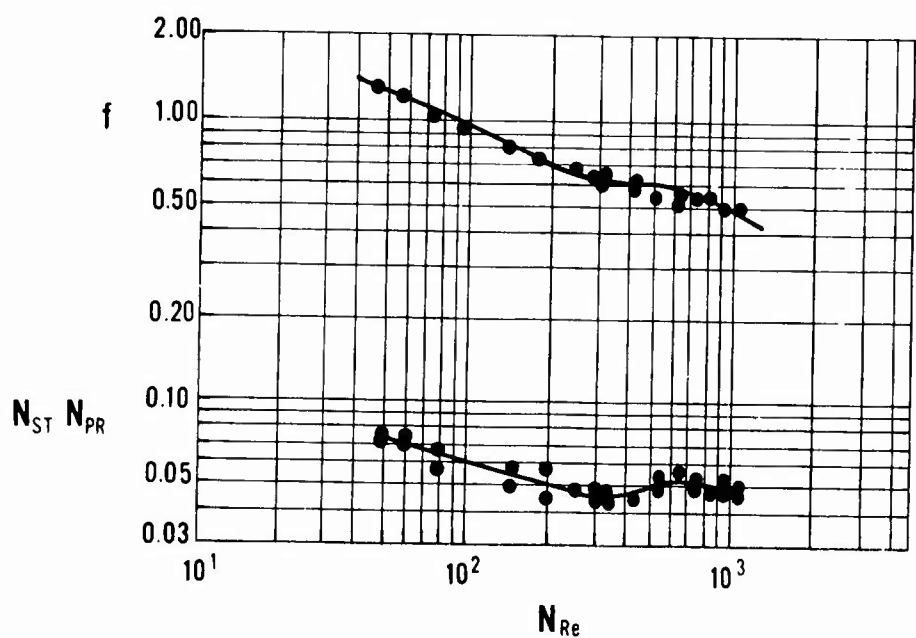
MATRIX CONFIGURATION AND FLOW DISTRIBUTION TESTS

Performance tests of the existing toroidal regenerator in the previous program (Contract NOw 62-0636-f), which contained radial V-shaped packages having blunt ends, resulted in low regenerator effectiveness. The low effectiveness was attributed to poor flow distribution through the matrix. A simple flow test was conducted on a matrix package, with smoke being used to examine visually the nature of the flow approaching the matrix. The test showed flow reduction in the portion of matrix adjacent to the blockage which increased mass velocity through the remaining portion of the matrix. The flow pattern observed in the test is shown schematically in Figure 30. The nonflow portion of the matrix for the cold flow is not the same area which is bypassed by the hot flow. Since the regenerator is a counterflow heat exchanger device, the hot and cold gases flow in opposite directions and see different blockage areas. The only portion of the matrix which feels cycling flow and exchanges heat between the hot and cold streams is that area which both flows utilize. Thus, the flow distribution pattern described provided a bypass path for both the hot and the cold streams through noncommon portions of the matrix.



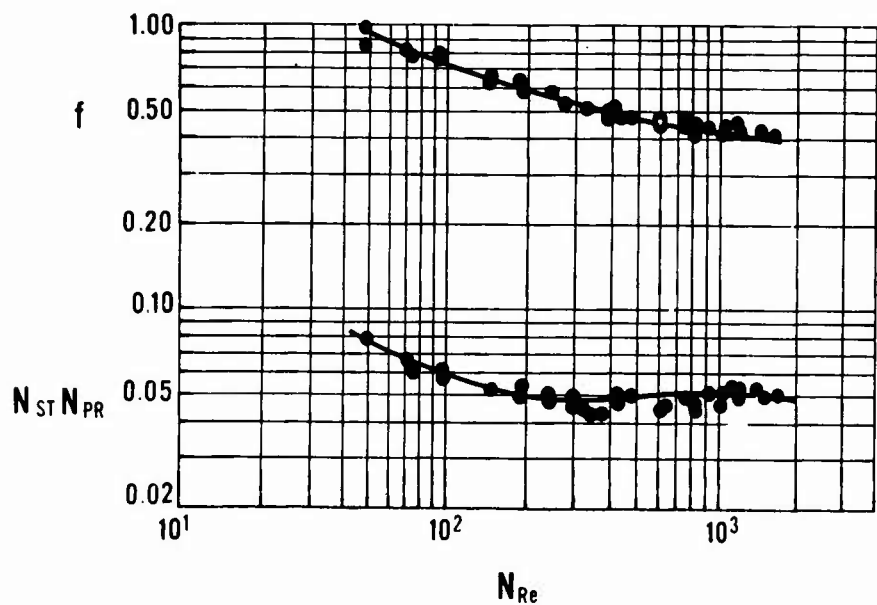
Frontal area	0.08726 ft. ²
Package thickness	1.752 in.
Mass of matrix	1.574 lb.
Number of screens	60
Screen material	Type 304 stainless steel
Porosity of matrix	0.748
Surface area/total volume	896 ft. ² /ft. ³
Layer thickness	0.029 in.
Density of screen material	490 lb./ft. ³
Screen specific heat	0.12 B.t.u./lb. - °F.
Hydraulic diameter	0.00334 ft.

Figure 14. Stanton-Prandtl Number and Friction Factor Correlation for 24 x 24 x 0.0135 Wire Screen Matrix.



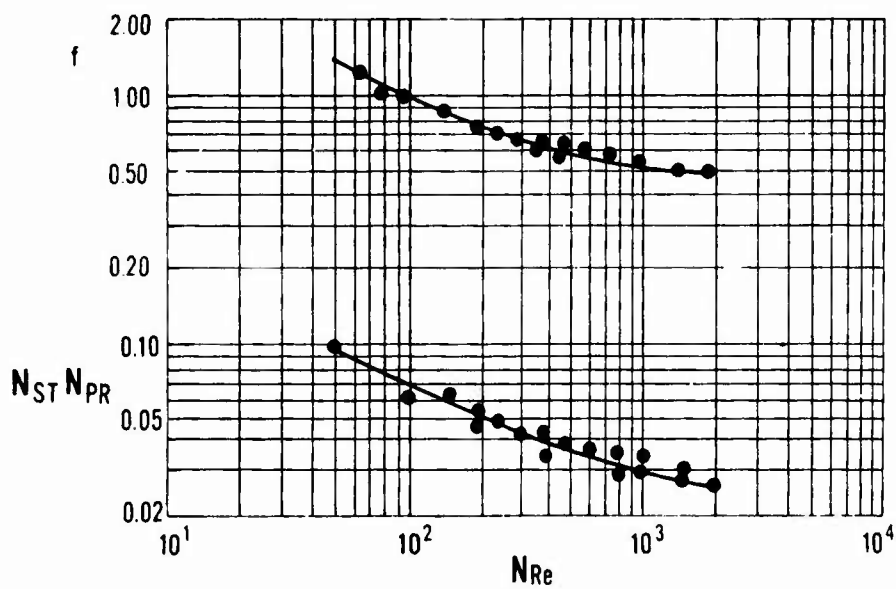
Frontal area	0.08726 ft. ²
Package thickness	0.446 in.
Mass of matrix	0.514 lb.
Number of screens	44
Screen material	Type 304 stainless steel
Porosity of matrix	0.677
Surface area/total volume	3,450 ft. ² /ft. ³
Layer thickness	0.011 in.
Density of screen material	490 lb. /ft. ³
Screen specific heat	0.12 B.t.u. /lb. - °F.
Hydraulic diameter	0.000785 ft.

Figure 15. Stanton-Prandtl Number and Friction Factor Correlation for 100 x 100 x 0.0045 Wire Screen Matrix.



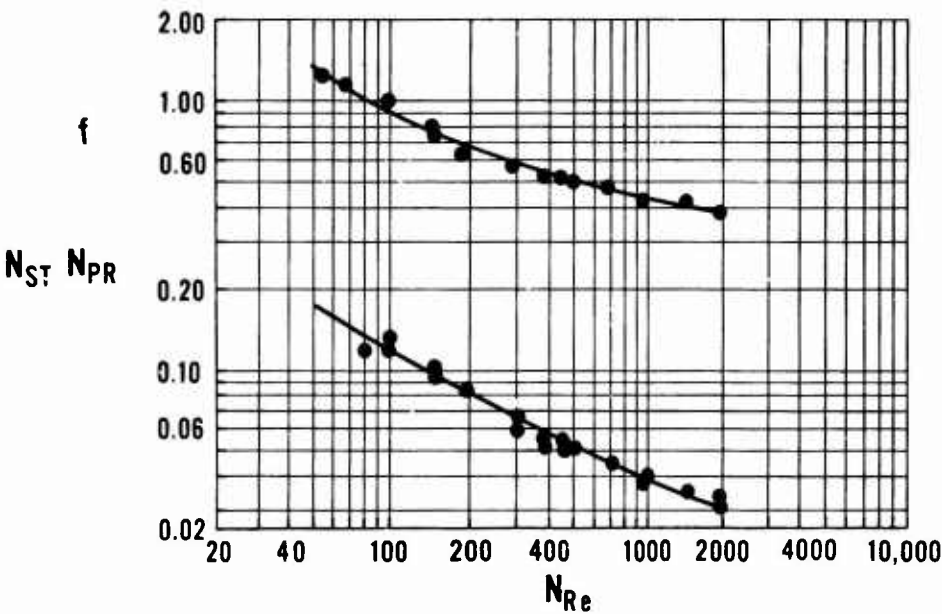
Frontal area	0.08726 ft. ²
Package thickness	0.936 in.
Mass of matrix	1.24 lb.
Number of screens	69
Screen material	Type 304 stainless steel
Porosity of matrix	0.632
Surface area/total volume	2,370 ft. ² /ft. ³
Layer thickness	0.016 in.
Density of screen material	490 lb./ft. ³
Screen specific heat	0.12 B.t.u./lb. - °F.
Hydraulic diameter	0.001065 ft.

Figure 16. Stanton-Prandtl Number and Friction Factor Correlation for 60 x 60 x 0.0075 Sintered Wire Screen Matrix.



Frontal area	0.08726 ft. ²
Package thickness	0.887 in.
Mass of matrix	0.83 lb.
Number of screens	52
Screen material	Type 304 stainless steel
Porosity of matrix	0.737
Surface area/total volume	1,485 ft. ² /ft. ³
Layer thickness	0.0185 in.
Density of screen material	490 lb./ft. ³
Screen specific heat	0.12 B.t.u./lb. - °F.
Hydraulic diameter	0.001985 ft.

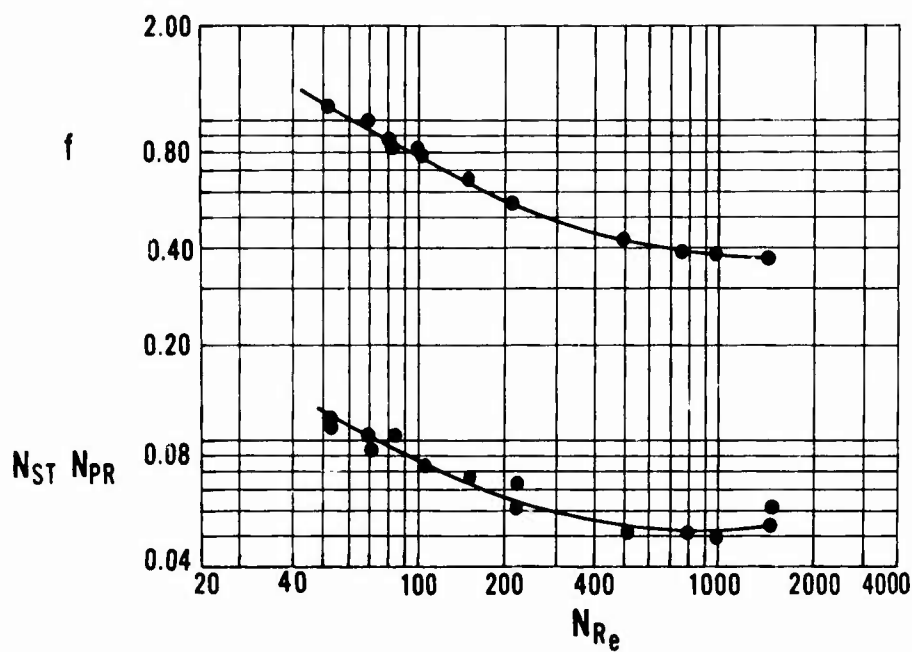
Figure 17. Stanton-Prandtl Number and Friction Factor Correlation for 40 x 40 x 0.0085 Wire Screen Matrix.



Frontal area	0.0726 ft. ²
Package thickness	0.879 in.
Mass of matrix	0.508 lb.
Number of screens	69
Screen material	Type 304 stainless steel
Porosity of matrix	0.838
Surface area/total volume	1,036 ft. ² /ft. ³
Layer thickness	0.015 in.
Density of screen material	490 lb./ft. ³
Screen specific heat	0.12 B.t.u./lb. - °F.
Hydraulic diameter	0.00322 ft.

Figure 18. Stanton-Prandtl Number and Friction Factor Correlation for 24 x 24 x 0.0075 Wire Screen Matrix.

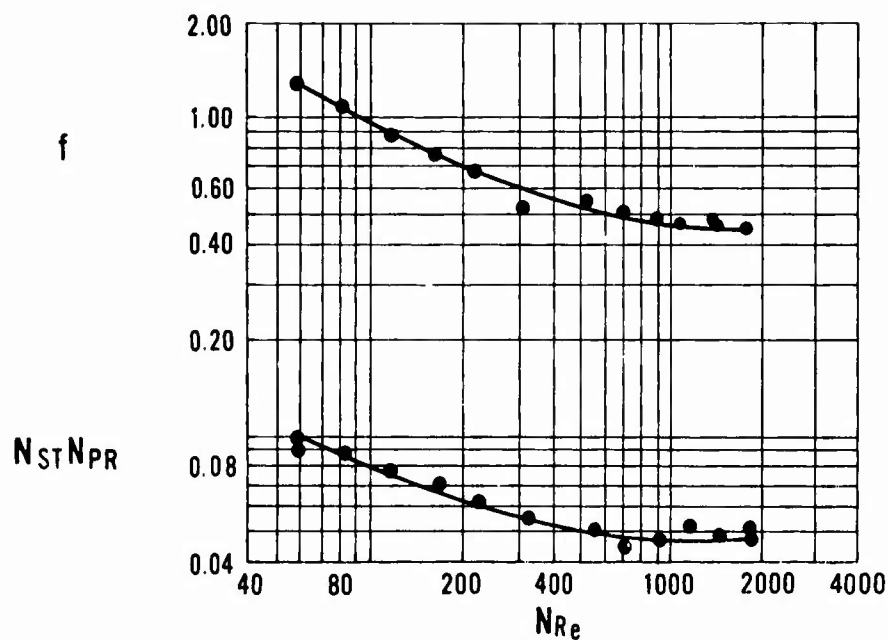
CONFIDENTIAL



Frontal area	0.08726 ft. ²
Package thickness	0.55 in.
Mass of matrix	0.402 lb.
Number of screens	71
Screen material	Type 304 stainless steel
Porosity of matrix	0.795
Surface area/total volume	2,345 ft. ² /ft. ³
Layer thickness	0.0085 in.
Density of screen material	490 lb./ft. ³
Screen specific heat	0.12 B.t.u./lb. - °F.
Hydraulic diameter	0.001355 ft.

Figure 19. Stanton-Prandtl Number and Friction Factor Correlation for 60 x 60 x 0.0040 Wire Screen Matrix.

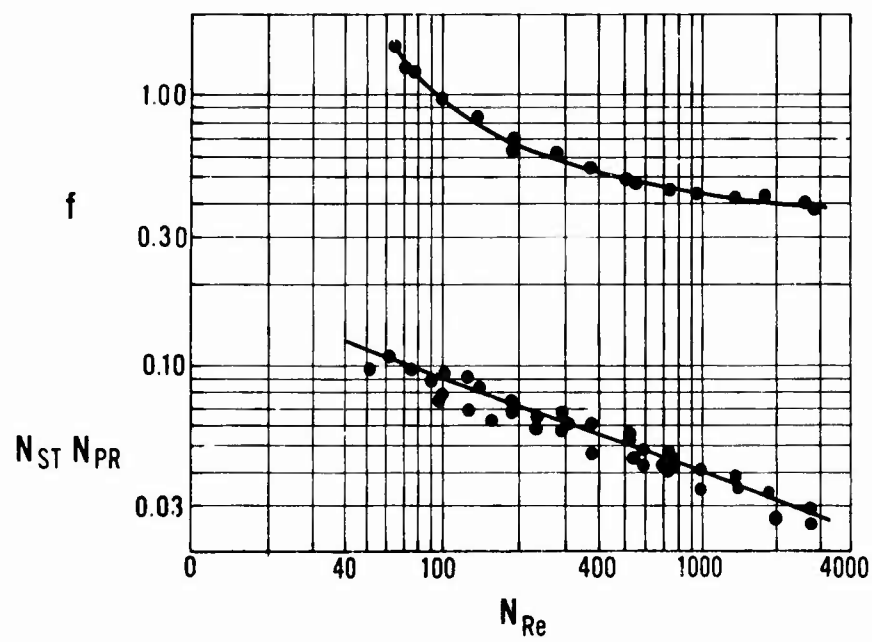
CONFIDENTIAL



Frontal area	0.08726 ft. ²
Package thickness	0.952 in.
Mass of matrix	0.966 lb.
Number of screens	68
Screen material	Type 304 stainless steel
Porosity of matrix	0.716
Surface area/total volume	2,100 ft. ² /ft. ³
Layer thickness	0.015 in.
Density of screen material	490 lb./ft. ³
Screen specific heat	0.12 B.t.u./lb. - °F.
Hydraulic diameter	0.001364 ft.

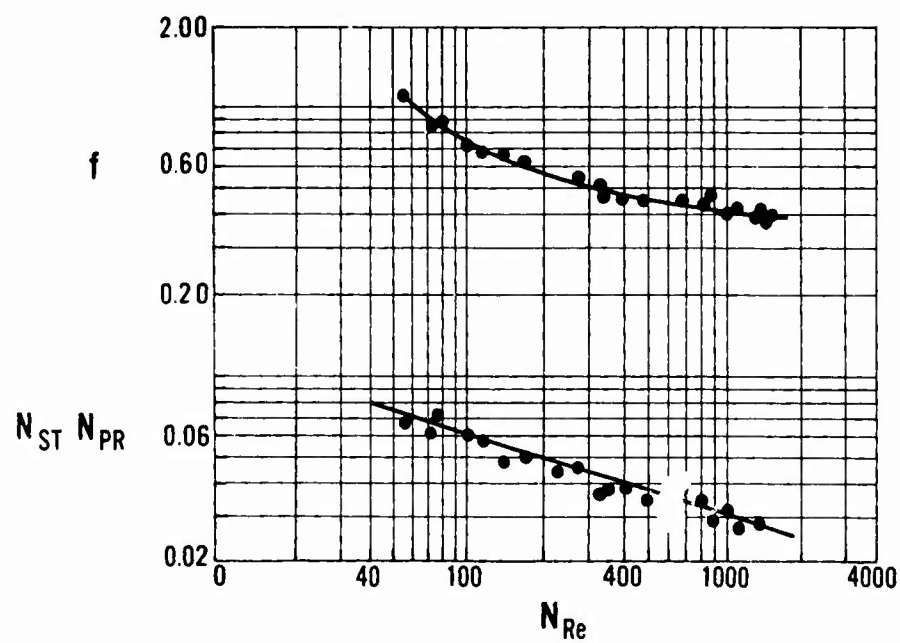
Figure 20. Stanton-Prandtl Number and Friction Factor Correlation for 60 x 60 x 0.0065 Wire Screen Matrix.

CONFIDENTIAL



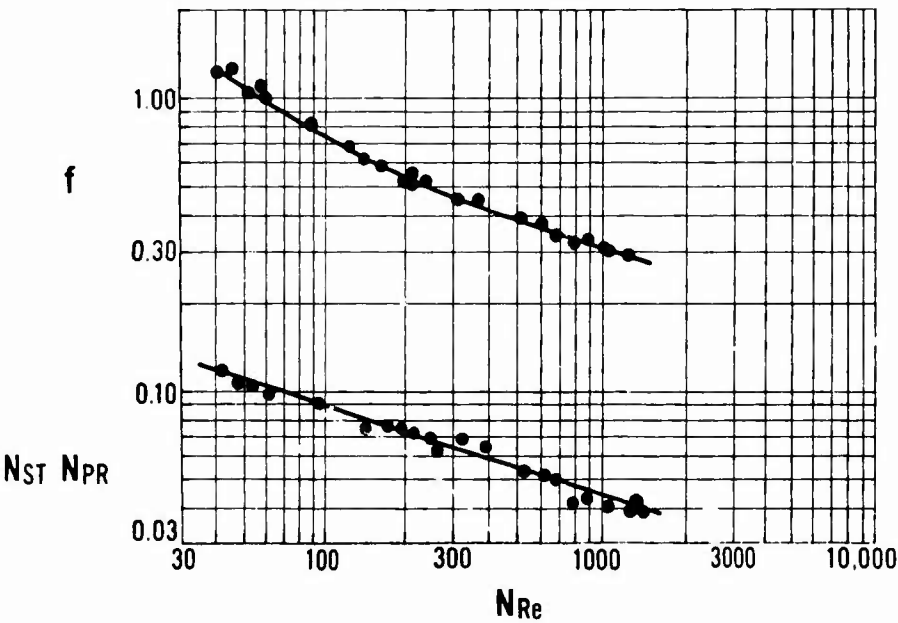
Frontal area	0.08726 ft. ²
Package thickness	1.44 in.
Mass of matrix	1.376 lb.
Number of screens	45
Screen material	Type 304 stainless steel
Porosity of matrix	0.732
Surface area/total volume	887 ft. ² /ft. ³
Layer thickness	0.0353 in.
Hydraulic diameter	0.00330 ft.

Figure 21. Stanton-Prandtl Number and Friction Factor Correlation for 24 x 24 x 0.0145 Wire Screen Matrix.



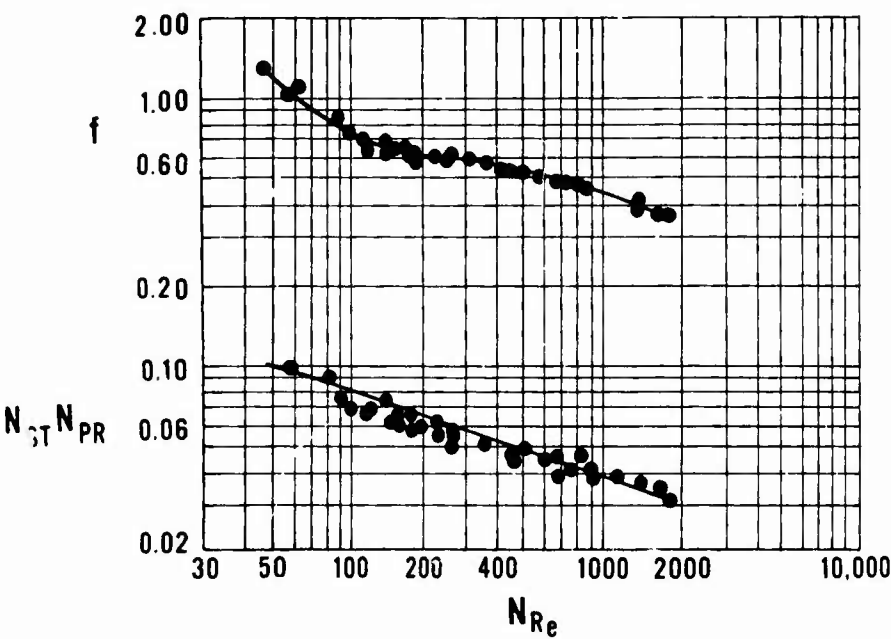
Frontal area	0.08726 ft. ²
Package thickness	0.674 in.
Mass of matrix	0.841 lb.
Number of screens	43
Screen material	Type 304 stainless steel
Porosity of matrix	0.650
Surface area/total volume	2,435 ft. ² /ft. ³
Layer thickness	0.0163 in.
Density of screen material	490 lb./ft. ³
Screen specific heat	0.12 B.t.u./lb. - °F.
Hydraulic diameter	0.001067 ft.

Figure 22. Stanton-Prandtl Number and Friction Factor Correlation for 60 x 60 x 0.0069 Wire Screen Matrix.



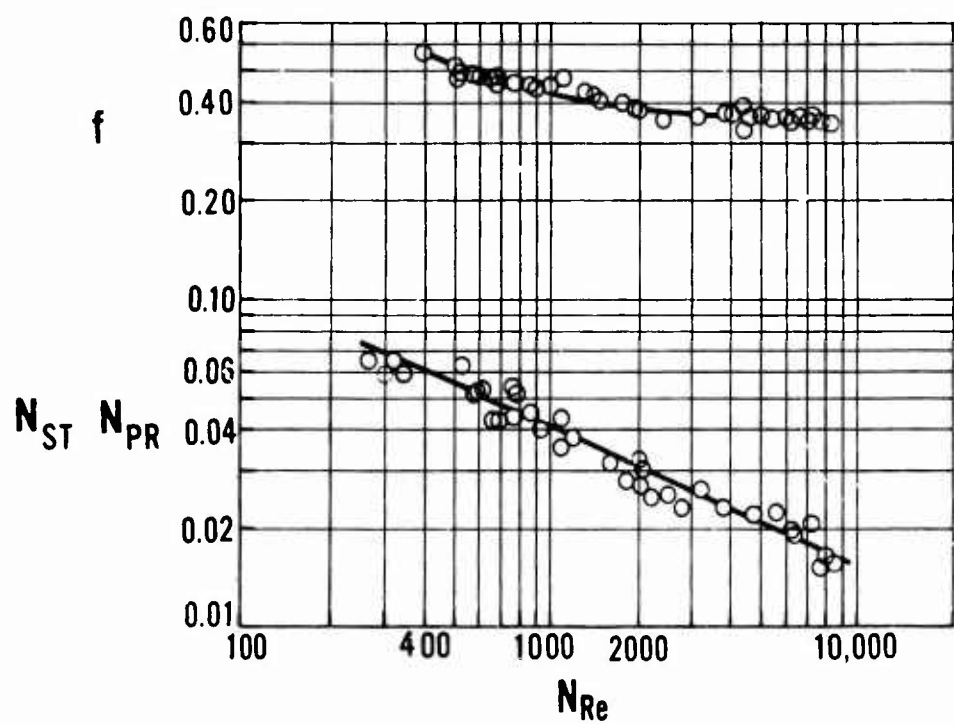
Frontal area	0.08726 ft. ²
Package thickness	0.565 in.
Mass of matrix	0.472 lb.
Number of screens	74
Screen material	Type 304 stainless steel
Porosity of matrix	0.765
Surface area/total volume	3,040 ft. ² /ft. ³
Layer thickness	0.0085 in.
Density of screen material	490 lb./ft. ³
Screen specific heat	0.12 B.t.u./lb. - °F.
Hydraulic diameter	0.001006 ft.

Figure 23. Stanton-Prandtl Number and Friction Factor Correlation for 80 x 80 x 0.0037 Wire Screen Matrix.



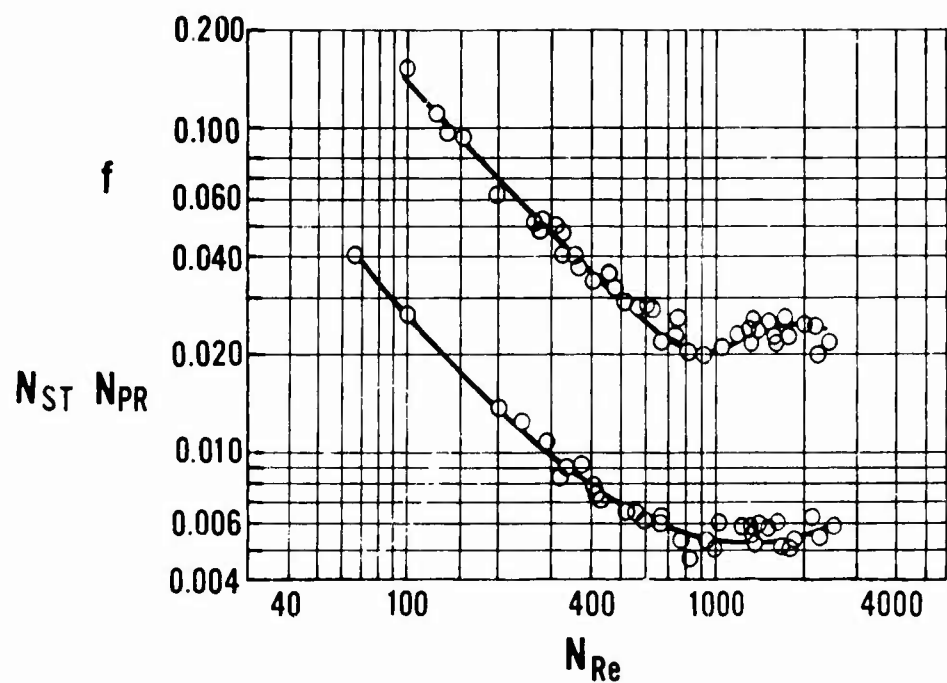
Frontal area	0.08726 ft. ²
Package thickness	0.704 in.
Mass of matrix	0.674 lb.
Number of screens	51
Screen material	Type 304 stainless steel
Porosity of matrix	0.7315
Surface area/total volume	2,220 ft. ² /ft. ³
Layer thickness	0.0146 in.
Density of screen material	490 lb./ft. ³
Screen specific heat	0.12 B.t.u./lb. - °F.
Hydraulic diameter	0.001320 ft.

Figure 24. Stanton-Prandtl Number and Friction Factor Correlation for 60 x 60 x 0.0058 Wire Screen Matrix.



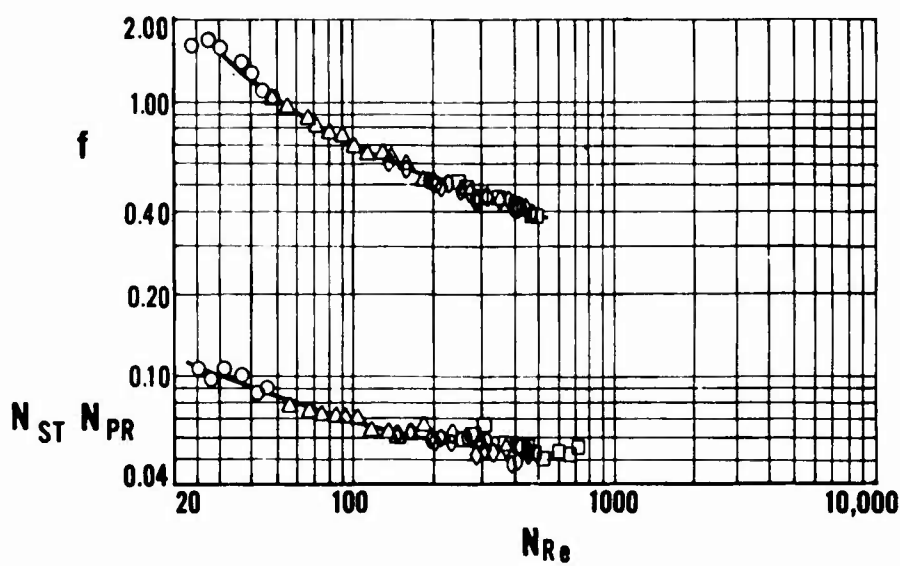
Frontal area	0.08726 ft. ²
Package thickness	3.377 in.
Mass of matrix	3.14 lb.
Number of screens	44
Screen material	Type 304 stainless steel
Porosity of matrix	0.739
Surface area/total volume	358 ft. ² /ft. ³
Layer thickness	0.0794 in.
Density of screen material	490 lb./ft. ³
Screen specific heat	0.12 B.t.u./lb. - °F.
Hydraulic diameter	0.00825 ft.

Figure 25. Stanton-Prandtl Number and Friction Factor Correlation for 10 x 10 x 0.0350 Wire Screen Matrix.



Frontal area	0.08600 ft. ²
Package thickness	2.500 in.
Mass of matrix	0.605 lb.
Matrix material	Corning 9690 CERCOR
Porosity of matrix	0.600
Surface area/total volume	1,400 ft. ² /ft. ³
Density of CERCOR	100 lb./ft. ³
CERCOR specific heat	0.20 B.t.u./lb. - °F.
Hydraulic diameter.	0.00171 ft.

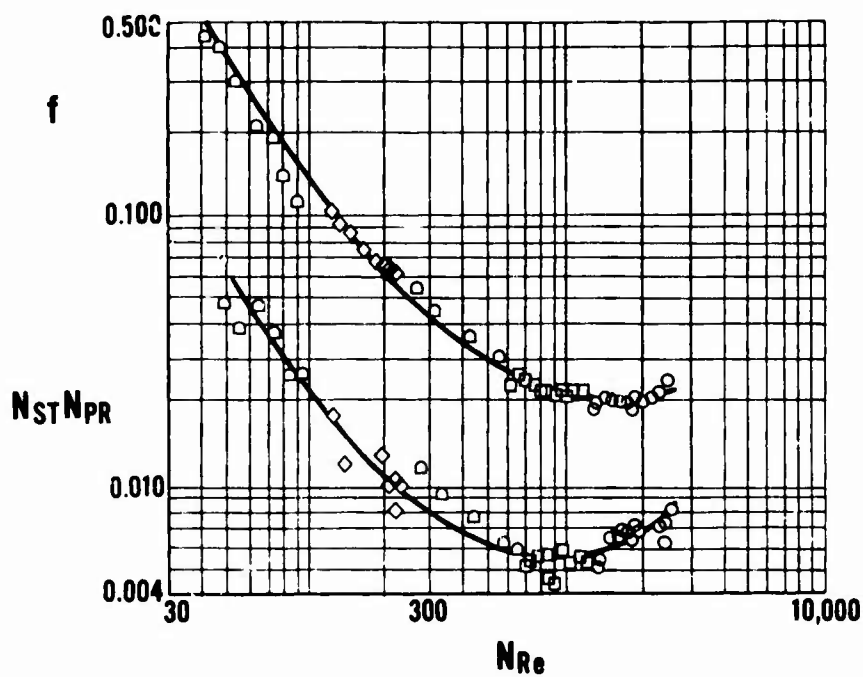
Figure 26. Stanton-Prandtl Number and Friction Factor Correlation for T-20-38 CERCOR Matrix.



Frontal area	0.08726 ft. ²
Package thickness	2.49 in.
Mass of matrix	0.943 lb.
Number of screens	656
Screen material	Type 304 stainless steel
Porosity of matrix	0.8938
Surface area/total volume	2,830 ft. ² /ft. ³
Layer thickness	0.0038 in.
Density of screen material	490 lb./ft. ³
Screen specific heat	0.12 B.t.u./lb. - °F.
Hydraulic diameter	0.001263 ft.

Figure 27. Stanton-Prandtl Number and Friction Factor Correlation for 60 x 60 x 0.0018 Wire Screen Matrix.

CONFIDENTIAL

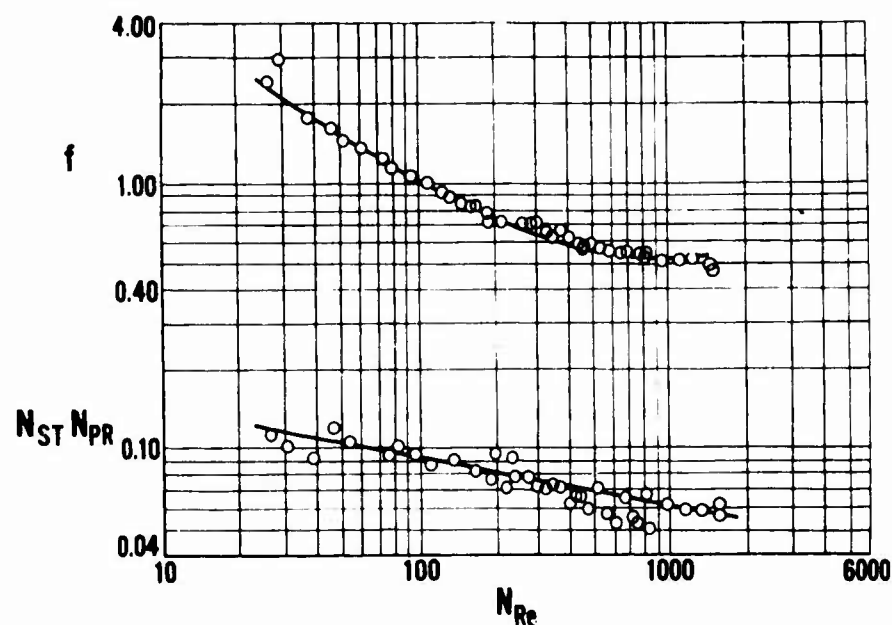


Frontal area	0.083 ft. ²
Package thickness	2.50 in.
Mass of matrix	0.685 lb.
Matrix material	Corning 9690 CERCOR
Porosity of matrix	0.600
Surface area/total volume	1,400 ft. ² /ft. ³
CERCOR specific heat	0.202 B.t.u./lb. - °F.
Hydraulic diameter.	0.00167 ft.

Figure 28. Stanton-Prandtl Number and Friction Factor Correlation for TC-20-38 Impregnated CERCOR Matrix.

CONFIDENTIAL

CONFIDENTIAL



Frontal area	0.08726 ft. ²
Package thickness	1.254 in.
Mass of matrix	1.23 lb.
Number of screens	77
Screen material	Type 304 stainless steel
Porosity of matrix	0.728
Surface area/total volume	2,140 ft. ² /ft. ³
Layer thickness	0.0149 in.
Screen specific heat	0.12 B.t.u./lb. - °F.
Hydraulic diameter	0.00136 ft.

Figure 29. Stanton-Prandtl Number and Friction Factor Correlation for 60 x 60 x 0.0061 Sintered Wire Screen Matrix.

CONFIDENTIAL

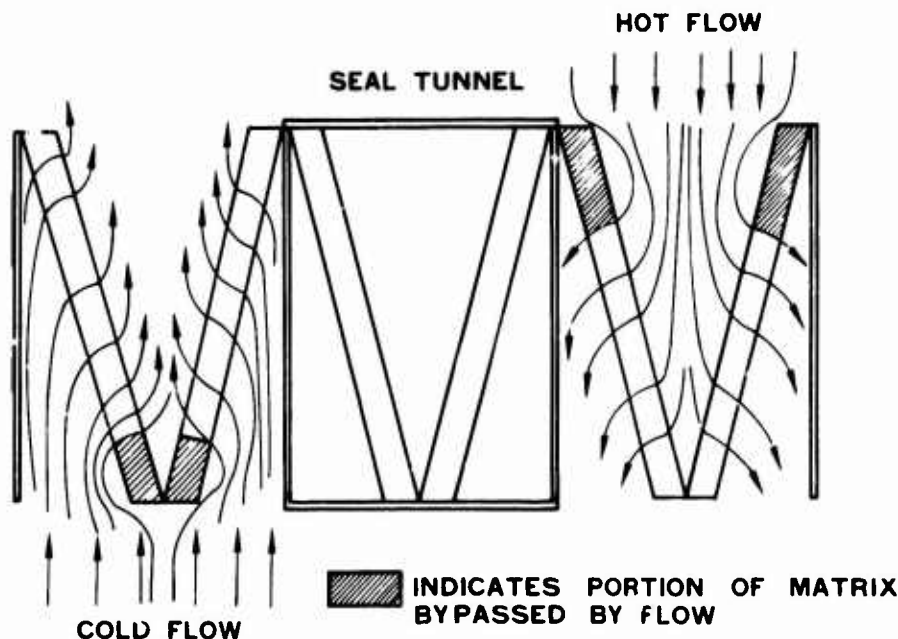


Figure 30. Local Flow Distortion of Early Matrices, Cross Section Through Torus.

The conclusion derived from this test was that the effective heat transfer area was substantially less than the physical screen area. Both the pressure loss and effectiveness data from regenerator tests verified this conclusion. To verify in the present program the theory that the loss of effective heat transfer area was caused by flow separation at the entrance of the matrix package, the matrix packages were reoperated by cutting away large areas of the front and back blockage plates. This configuration is shown schematically in the left-hand diagram of Figure 31. The matrix reoperation was designed to permit flow through the corners and thereby to provide a more uniform flow through the matrix in both flow directions.

Tests with this configuration showed improvement in both effectiveness and pressure loss, thus proving that the main problem was local flow disturbance.

Another demonstration-type matrix with further improved flow characteristics was constructed in this program. This matrix completely eliminated the front and back plates at the sacrifice of some frontal area. This configuration is shown schematically in Figure 31, center diagram. The purpose of this test was to demonstrate predicted performance of a matrix with optimum entrance flow conditions. If the data agreed with the prediction, it would then be possible to redesign the package more precisely to gain back the original design frontal area in the same package envelope (Figure 31, right-hand diagram).

CONFIDENTIAL

CONFIDENTIAL

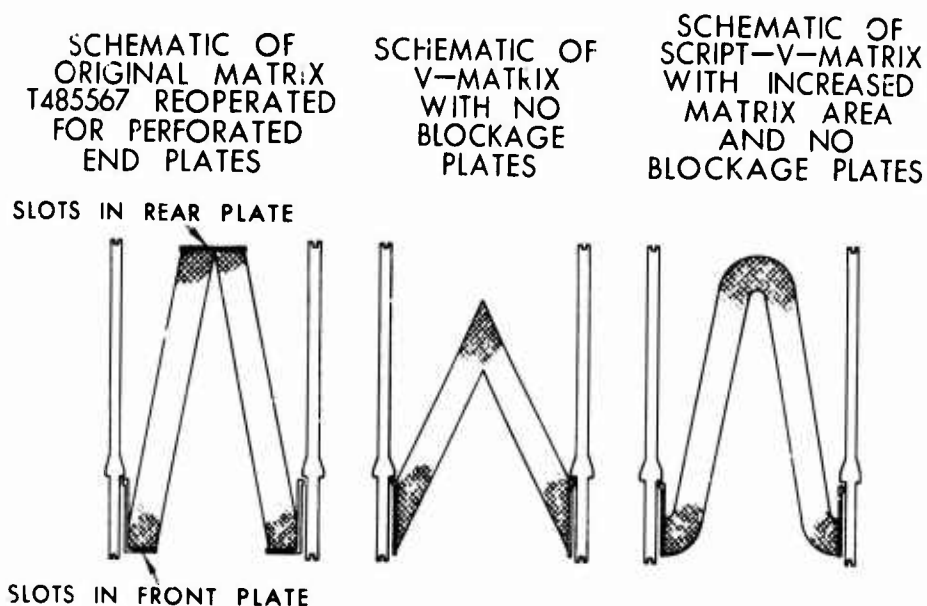


Figure 31. Schematics of Reoperated Vee Matrices.

Testing of this matrix indicated that the effectiveness and pressure data agreed closely with predicted values. It was concluded from this test that practically all of the heat transfer area was being utilized, whereas this was not true in the blunt-edge or perforated-edge configurations.

Method of Accomplishment

This early work defined the problem area but was not extensive enough to solve the fundamental flow distribution problem. Therefore, prior to this program, a simple, single-package flow rig, shown schematically in Figure 32, was fabricated to determine quantitatively the flow distribution through matrix packages. This rig was designed to determine the effects of the following variables on flow distribution:

1. Velocity of air entering package.
2. Angle which the matrix makes with the flow.
3. Relative matrix pressure loss.
4. Matrix thickness and package geometry.
5. Package entrance configurations.

CONFIDENTIAL

CONFIDENTIAL

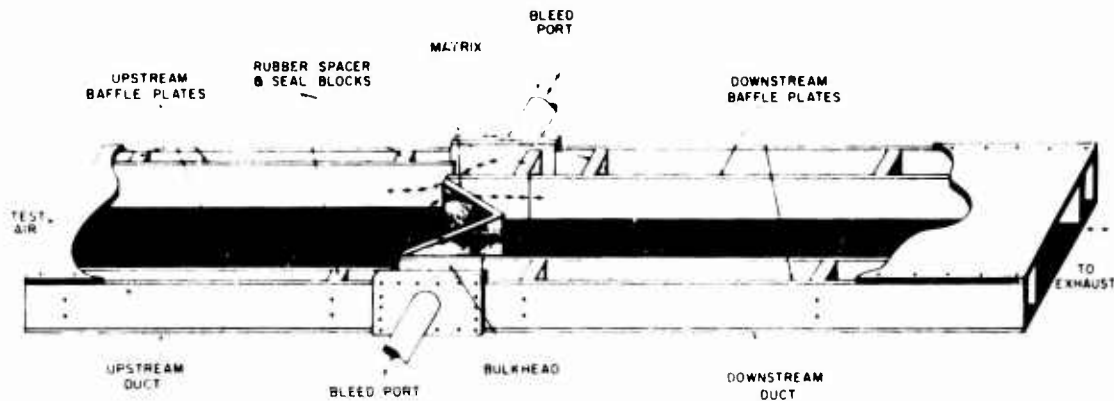


Figure 32. Matrix Airflow Rig Schematic.

An oil-graphite-plate technique of tracing streamlines was initially selected as a means of evaluating these variables. This technique was selected because earlier tests with pressure probes to determine the flow leaving the matrix showed that the results could not be duplicated because of the difficulties of measuring pressures in a turning stream. The oil-graphite plate technique involved placing a plate covered with a mixture of oil and graphite immediately upstream and downstream of the matrix at the midplane of the duct. As air was passed over the plate, the oil was carried downstream, leaving the graphite particles oriented in the direction of the flow, and thus indicating the flow streamlines. By measuring the total and static pressures in a known nonturning region, the flow streamlines could be traced from this point to the matrix face, and the mass velocity distribution through the matrix could be determined.

Description of Test Rig. The two-dimensional rig shown schematically in Figure 32 included the following features: (1) Two axially aligned rectangular ducts having cross-sectional dimensions of 5 x 10 inches, (2) two movable baffle plates in each duct to allow the duct width to be varied for any desired flow area, (3) a test section containing the matrix package, and (4) Teflon blocks to seal and position the baffle plates. The upstream baffle plates could be positioned to align with the leading edges of the matrix or to extend beyond the bulkhead to minimize duct wall boundary layer effects by bleeding a small percentage of the flow around the matrix. The bypass air was exhausted and measured in bleed ports provided in the test section. The top plate of each duct was removable to provide access within the duct.

CONFIDENTIAL

CONFIDENTIAL

The test section was constructed in a rectangular box configuration. The side plates of the test section, which contain bleed ports, were bolted to the sides of the ducts. Matrix packages could be readily installed and removed by removing the top plate only. The matrix packages were held within the test section by pins in the top and bottom plates.

Ports were provided in the side walls both upstream and downstream of the matrix for traversing with total and static pressure probes. Thermocouples were used to measure stream temperatures. A photograph of the rig after construction is shown in Figure 33.

Test Program. Since analytical studies have shown that a high ratio of frontal area to window area is required for a lightweight design, the matrix must be folded with small included angles. The test specimen planned for evaluation consisted of a 24-mesh, 0.0135-inch-wire-diameter sintered screen vee package (V-shaped) having hinged extremities, so that the included angle could be varied. Pending arrival of this test matrix, an existing V-shaped nonsintered matrix was modified for test. Tests were initiated on the modified matrix to establish the flow distribution within the matrix for included angles of 15° to 40° with a bulkhead-to-matrix spacing of 0.25 inch. The upstream sidewalls were extended 0.3 inch beyond the bulkhead to permit bleeding the boundary layer to simulate the adjacent

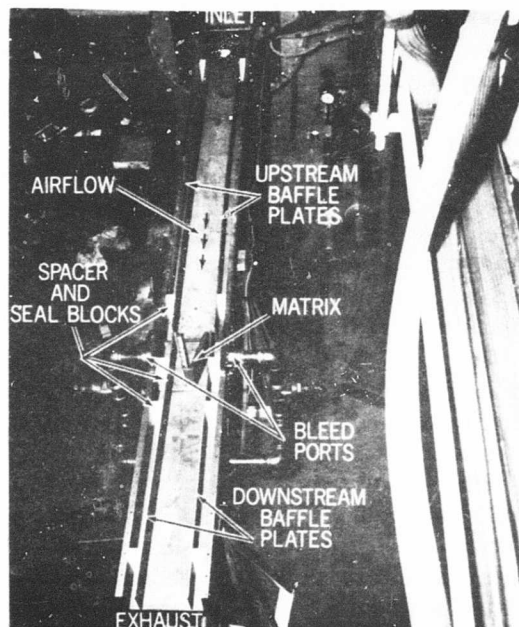


Figure 33. Matrix Airflow Rig.

CONFIDENTIAL

matrices in the actual regenerator. To evaluate flow distribution within the matrix, it was planned to measure total and static pressures upstream and downstream of the matrix in sections where the flow directions were known and where instrumentation would be straightforward. By tracing the streamlines formed by the oil-graphite coated plates to the matrix faces, the local mass velocity entering and leaving the matrix could be determined.

Flow Determination by Oil-Graphite Traces. The first oil-graphite traces with flow into the vee (Figure 34) showed a horseshoe-shaped vortex at the inlet blunt ends of the matrix on the upstream plate. The vortex made it difficult and questionable to determine quantitatively by the traces formed whether the flow was entering along the entire matrix or whether part of the matrix was flow starved. The downstream plate showed flow packing toward the outer walls. Examination of the streamlines on the upstream plates indicated secondary flows near the stagnation point of the matrix edges. To examine the validity of these results further, two test specimens, a flat plate and a cylinder having known flow distributions, were tested in a position normal to the flow. The same secondary flows were observed again (Figures 35 and 36), and the streamlines formed did not agree with free streams around tubes and plates, which were observed by other investigators using water or smoke visualization tests.

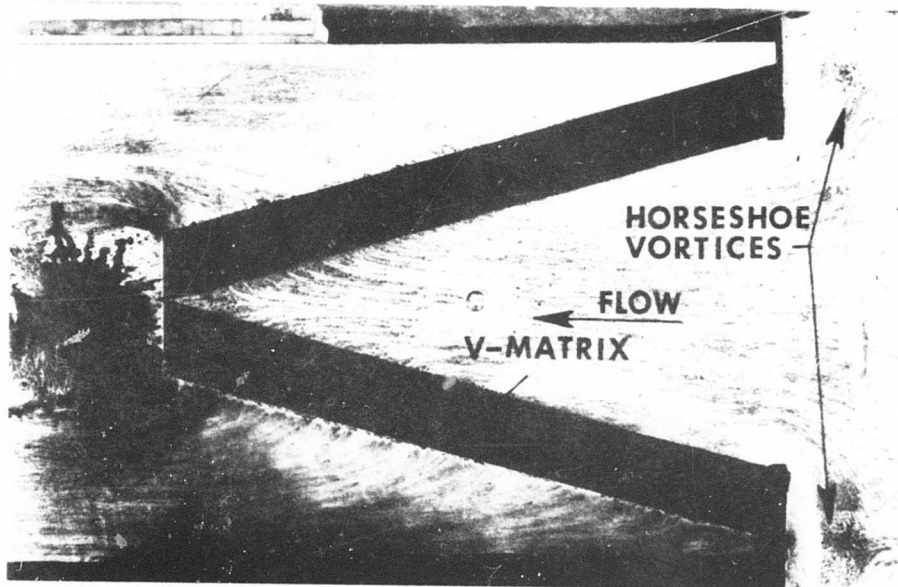


Figure 34. Oil-Graphite Traces on the 35° Vee Matrix.

CONFIDENTIAL

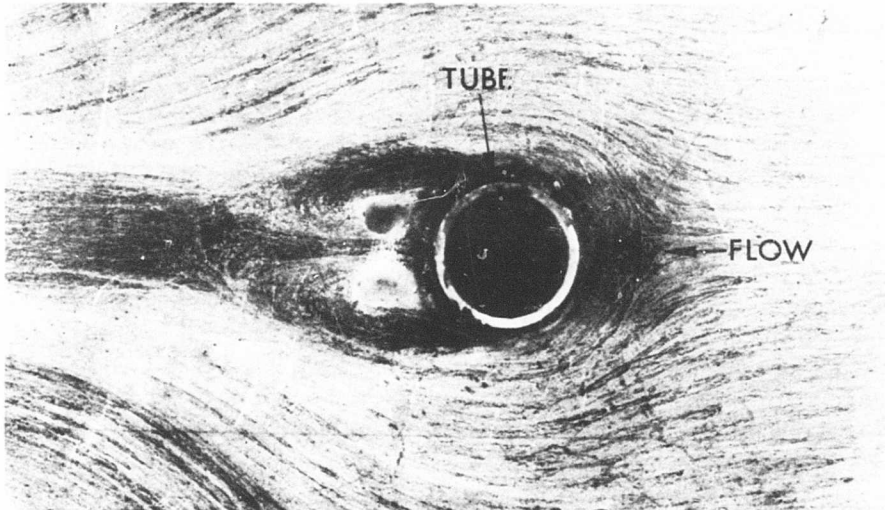


Figure 35. Oil-Graphite Traces and Flow Streamlines Around a Tube.

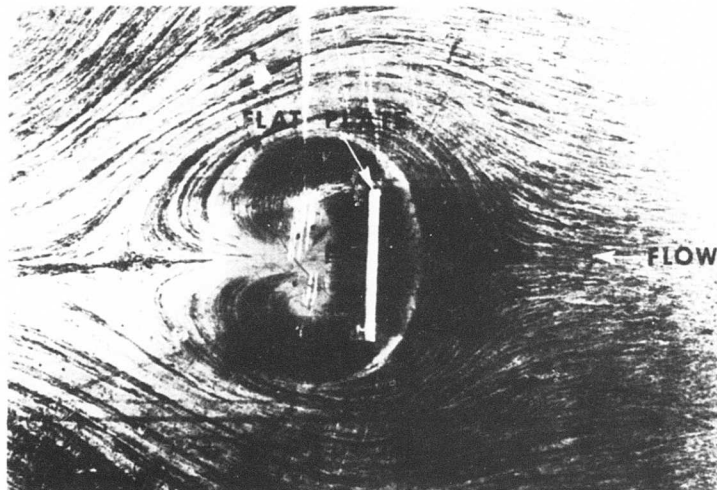


Figure 36. Oil-Graphite Traces and Flow Streamlines Around a Flat Plate.

CONFIDENTIAL

CONFIDENTIAL

Further tests were conducted on the flat plate test specimens with several inlet graphite plate lengths. By decreasing the plate length, the point of separation was seen to move closer to the plate specimen. Finally, a section of the oil-graphite plate immediately in front of the plate specimen was removed, and the streamlines formed resembled more closely those of a free stream around a flat plate normal to flow.

As a result of the above tests, the graphite plates were modified by removing sections of the plates ahead of all blunt edges of the vee matrix. Tests conducted with flow into the vee and with modified plates showed uniform flow entering the entire face of the matrix (Figure 37). However, regions of separation downstream of the matrix made it impossible to determine the mass flow distribution leaving the matrix by tracing the streamlines from the matrix face to the downstream pressure location (Figure 38). Provisions were then made to measure the total and static pressures immediately downstream of the matrix at a location ahead of the flow separation region indicated by the oil-graphite plate. An enlargement of one of the oil-graphite trace photographs was made to determine whether the streamlines could be traced from the new pressure measuring location. Examination of the enlarged photograph showed lines of flow disappearing into the bulkhead wall. It was evident from these photographs that the oil-graphite technique was not a suitable technique for determining flow distribution and that another technique should be sought.

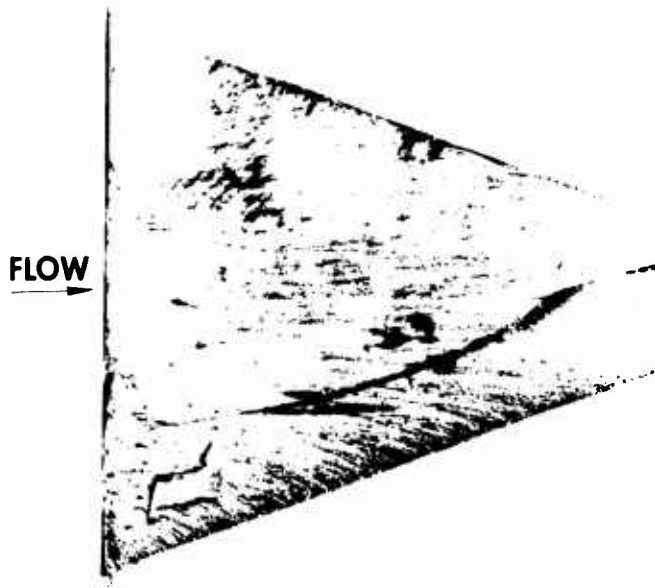


Figure 37. Oil-Graphite Traces and Flow Streamlines Entering Vee Matrix.

CONFIDENTIAL

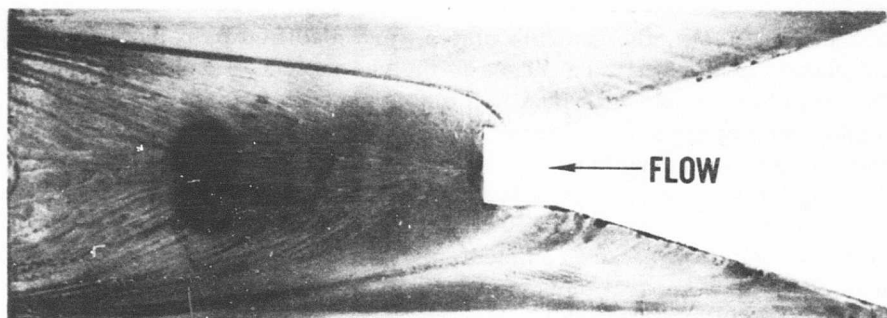


Figure 38. Oil-Graphite Traces and Flow Streamlines Leaving a 35° Vee Matrix.

Flow Determination by Channelization. The oil-graphite plates and pressure measurements indicated that the flow leaving the matrix was packing toward the outer walls. It was therefore decided to channel the flow to the pressure measuring location where the flow could be determined. A set of channels dividing the matrix frontal area into approximately five equal sections for both sides of a matrix having an included angle of 35° was constructed. In addition, the inlet oil-graphite plate was modified to incorporate static pressure taps so that flow distribution entering the matrix could be determined. Tests with the inlet plates extending beyond the bulkheads and in line with the leading edge of the matrix were conducted with flow into the vee. The results of the upstream total and static pressure measurements with the plates extended beyond the bulkhead showed slightly higher mass flows entering at each end of the matrix and uniform flows over the remainder of the matrix. Moving the sidewalls in line with the matrix edges resulted in more uniform flow entering the matrix. It was concluded that the flow entering the matrix was not a factor affecting flow distribution. The mass velocity leaving the matrix within each channel is shown in Figure 39; the average flow rate across the channels is represented by the dotted line. The flow measured within the channels agreed within 10 percent of the flow measured with the upstream orifice. Although the flow rate could be determined within the flow channels and the flow distribution through the matrix could be assessed, a large number of channels would be required to obtain the desired small incremental flow measurements along the matrix face. It was concluded that this method of measuring flow distribution was inadequate.

CONFIDENTIAL

CONFIDENTIAL

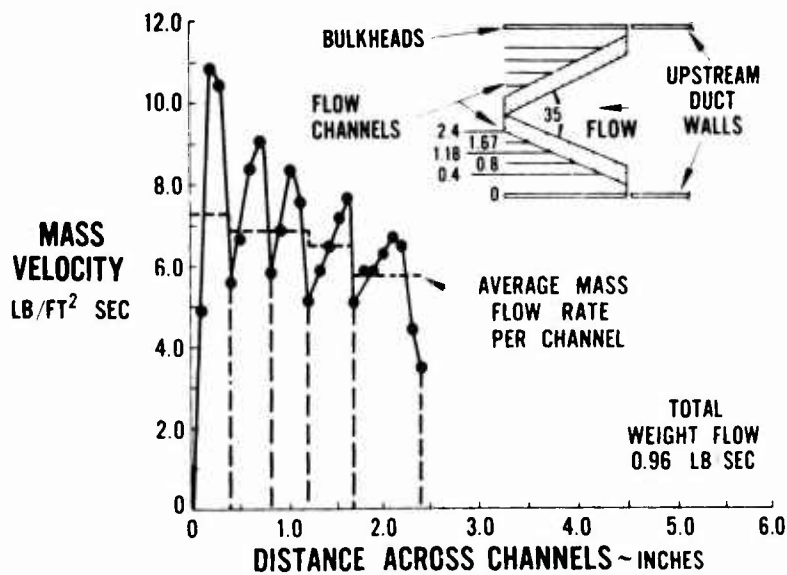


Figure 39. Mass Velocity Leaving Matrix Face Vs. Distance Across Channels (Flow Into the Vee).

Flow Determination Using Hot-Wire Anemometer. Tests were then conducted to evaluate a hot-wire anemometer technique for determining flow distribution through the matrix. Initially, hand traverse measurements were made along both matrix faces with flow in both directions to evaluate the technique. The results of these tests are shown in Figures 40 and 41. Figure 40 shows the mass velocity leaving the exit face of one side of the vee matrix with the flow direction entering the vee and two inlet configurations. The dotted curve represents the test conducted with the duct walls placed in line with the simulated bulkheads, which caused flow to separate over the blunt ends of the matrix. The solid curve represents the duct walls placed in line with the leading edges of the matrix. In both cases, the flow appears to be uniform over approximately 60 percent of the matrix and to be 25 percent higher near each end. The mass flow leaving the matrix measured by the anemometer probe was within 10 percent of the flow measured with the upstream orifice.

CONFIDENTIAL

CONFIDENTIAL

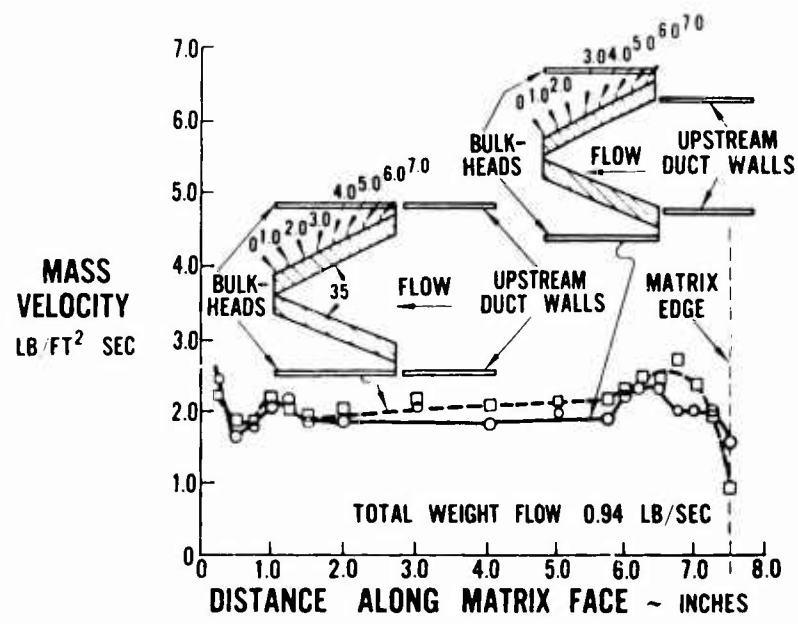


Figure 40. Mass Velocity Leaving Matrix Face Vs. Distance Along Matrix (Flow Into the Vee).

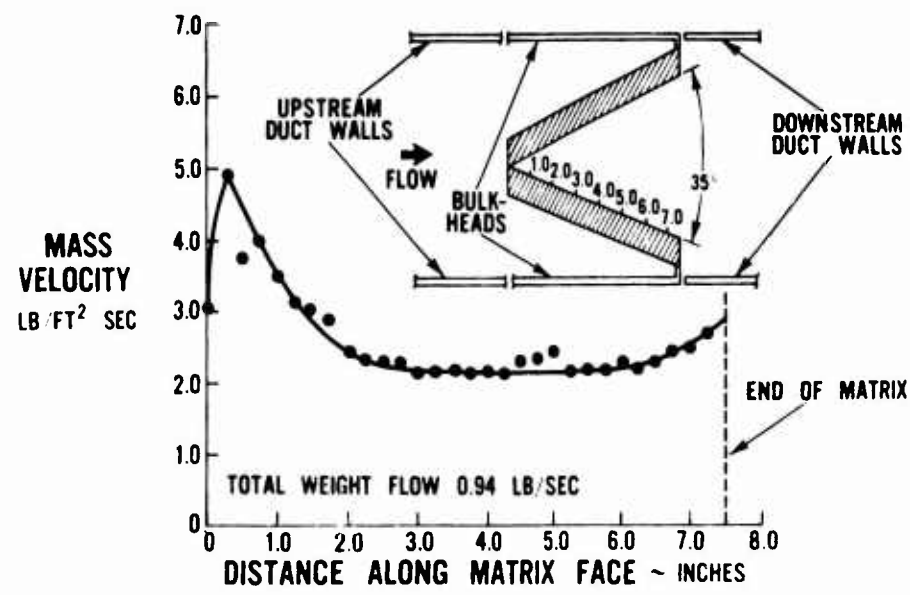


Figure 41. Mass Velocity Leaving Matrix Face Vs. Distance Along Matrix (Flow Over the Vee).

CONFIDENTIAL

CONFIDENTIAL

The mass velocity profile leaving the matrix with flow in the opposite direction (flow over vee) is shown in Figure 41. It appears from this graph that the flow was uniform over approximately the same area as was observed with the flow entering the vee. However, a large flow is indicated in the area where the two matrix sides join to form the vee. The integrated flow leaving the matrix was 24 percent higher than the flow as measured by the upstream orifice. The cause of the higher indicated weight flow was attributed to the positioning of the probe too far from the matrix face in a high-flow region. In this manner, the true flow leaving the matrix face was not being measured.

Since the anemometer probe traversing method appeared to be the best method for determining flow distribution through the matrix packages, design modifications to the airflow rig test section were made to incorporate a mechanical traversing mechanism (Figure 42) to provide a more accurate control of the matrix-to-probe distance and the traverse location. At this time the 24-mesh, 0.0135-inch-wire-diameter sintered screen vee matrix was received and incorporated into the rig. The screen was sintered to eliminate any possibility of screen bulging and interference with probe traversing. Each matrix was 7.6 inches long by 5 inches high; matrix thicknesses of 0.5, 1.0, and 1.5 inches were constructed. Figure 43 is a photograph of the 1.0-inch-thick screen matrix.

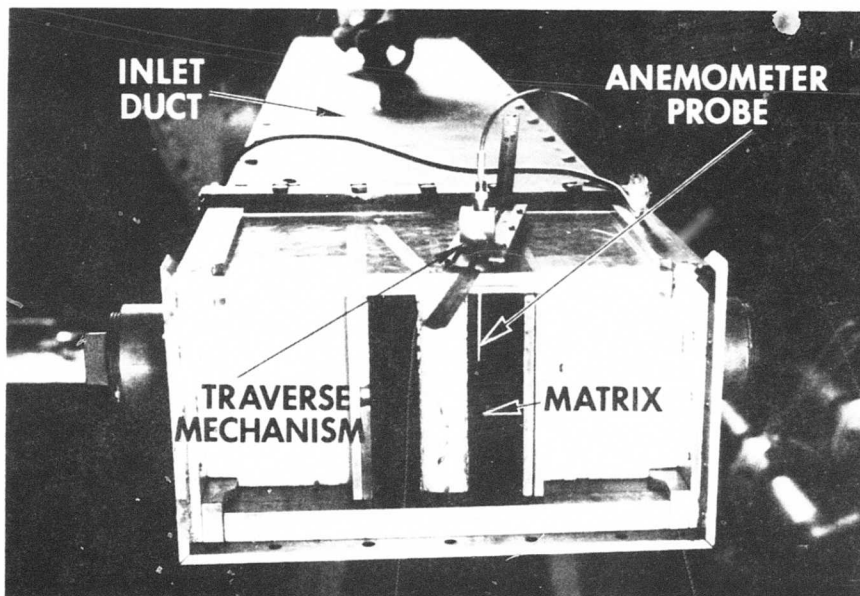


Figure 42. Hot-Wire Anemometer and 60 x 60 x 0.0058 Wire Screen Matrix, Airflow Rig.

CONFIDENTIAL

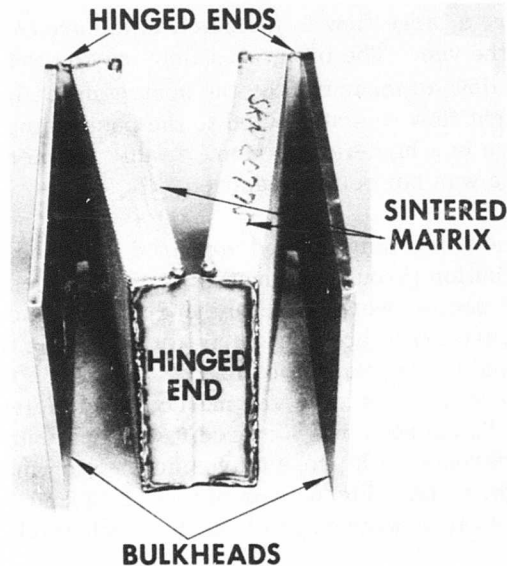


Figure 43. View of 24 x 24 x 0.0135 Matrix Package (1-Inch-Thick Screen).

Tests were conducted on the 0.5-inch-thick package with the improved traversing mechanism to evaluate the effects of entrance configurations. The entrance configurations consisted of the spacing between the matrix and the bulkheads, spacing between the two matrix sides at the junctions of the vee, and centerbodies for directing flow into and out of the matrix with flow in both directions. The tests were conducted at approximately the same Mach number as the exhaust gas side of the rotary regenerator. The first series of tests were conducted on a 15° matrix. The matrix configurations for this series of tests are shown in the appendix as configurations 1 through 20.

Results

In order that comparisons between the matrix configurations could be made and the variables which affect flow distribution could be assessed, the data were non-dimensionalized and are presented in Figure 44 for flow into the vee, and Figure 45 for flow over the vee. Examination of these figures indicates that

CONFIDENTIAL

CONFIDENTIAL

improvements in the flow distribution through approximately 18 percent of the matrix were obtained by optimizing the entrance configuration by:

1. Placing the upstream walls in line with the leading edges of the matrix (compare configuration 3 with configuration 1, Figure 44),
2. Using a nose piece over the blunt end of the vee when flowing over the vee (compare configuration 5 with configuration 4, Figure 45),
3. Eliminating the upstream gap when flowing in either direction (compare configuration 7 with configuration 3, Figure 44, and configuration 6 with configuration 5, Figure 45),
4. Increasing the length of the nosepiece attached to the blunt end of the vee when flowing over the vee (compare configuration 16 with configuration 5, Figure 45),
5. Adding a contoured centerbody which is designed to turn the flow into the matrix (compare configuration 13 with configuration 7, Figure 44, and configuration 15 with configuration 6, Figure 45).

Tests were conducted with an 11° wedge-shaped centerbody having no matrix-to-bulkhead gap (configuration 17) and having a contoured bulkhead (configuration 18). The resultant gap between matrix and the centerbody did not permit accurate measurement of the flow leaving the matrix. The overall pressure loss, however, is significantly higher with this centerbody.

Tests were also conducted with a diffuser inlet (configuration 19) and a diffuser inlet with an 11°-wedge centerbody (configuration 20) to diffuse and turn the flow into the matrix. The results (Figure 44) indicate that the diffuser inlet section (configuration 19) offers no improvements over the in-line walls (configuration 3). The addition of the centerbody (configuration 20) improved the local flow distribution near the leading edge of the matrix but did not improve the overall flow distribution through the matrix.

It appeared from the above tests that improvements in local flow distribution were realized by items 1 through 4 above. The use of contoured centerbodies improved flow distribution at the expense of high pressure loss. Utilizing these flow improvement factors, tests were continued to determine the effects of matrix angle (configurations 25 through 30), increased matrix flow length (configurations 31 and 32), higher pressure loss screen matrix

CONFIDENTIAL

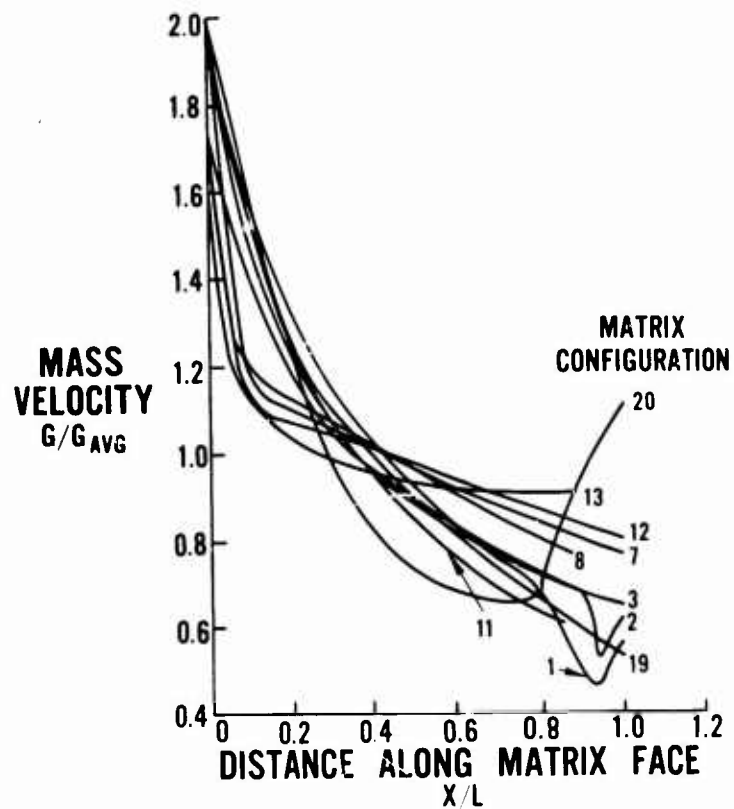


Figure 44. Normalized Mass Velocity Leaving Matrix Vs. Distance Along Matrix Face for Flow Into Vee, Configurations 1, 2, 3, 7, 8, 11, 12, 13, 19, and 20.

(configurations 35 and 36), and turning vanes (configurations 33, 34, 37, and 38) on flow distribution through the matrix package. The results of these tests are shown in Figures 46 through 55. Examination of these figures indicates that:

1. A significant improvement in flow distribution was realized by increasing the matrix angle from 15° to 20° , and a small improvement was realized as the angle was increased to 30° and 40° (Figures 46 and 47);

CONFIDENTIAL

CONFIDENTIAL

2. As the flow length was increased or a higher mesh screen matrix was utilized for higher pressure loss, the flow distribution through the matrix was improved (Figures 48, 49, 52, and 53);
3. Near-optimum flow distribution with the 15° and 30° matrix was obtained with the addition of turning vanes (Figures 50, 51, 54, and 55).

The flow distribution of the circumferential vee matrix package tested in Build 2 of the subscale test regenerator was determined to enable the maldistribution effects on regenerator performance to be assessed. The flow distribution through the package is shown in Figure 56. The analysis performed indicated that, for the flow distribution through the Build 2 package, 97 percent of the ideal effectiveness could be achieved. This series of tests was conducted at flow rates in each direction corresponding to the Reynolds numbers in the test regenerator, both with porous and nonporous matrix ends. These tests are designated as tests of configurations 21 through 24 in the Appendix.

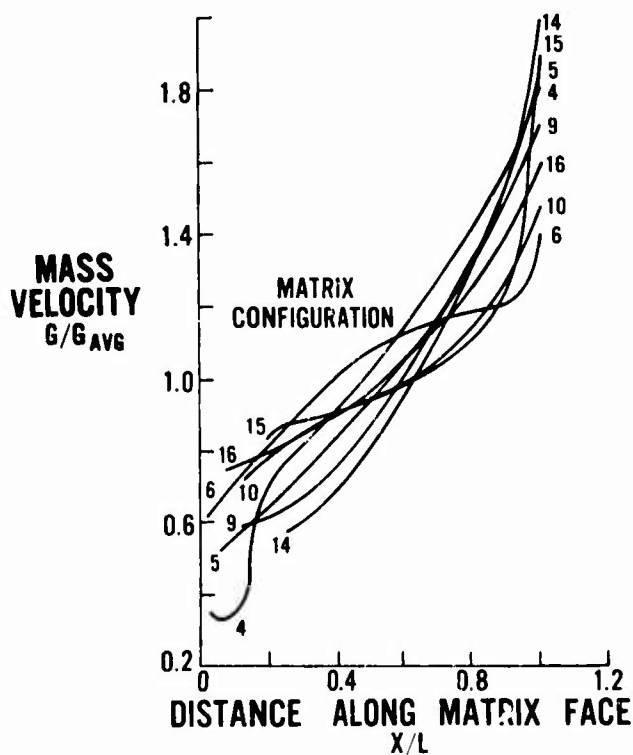


Figure 45. Normalized Mass Velocity Leaving Matrix Vs. Distance Along Matrix Face for Flow Over Vee, Configurations 4, 5, 6, 9, 10, 14, 15, and 16.

CONFIDENTIAL

CONFIDENTIAL

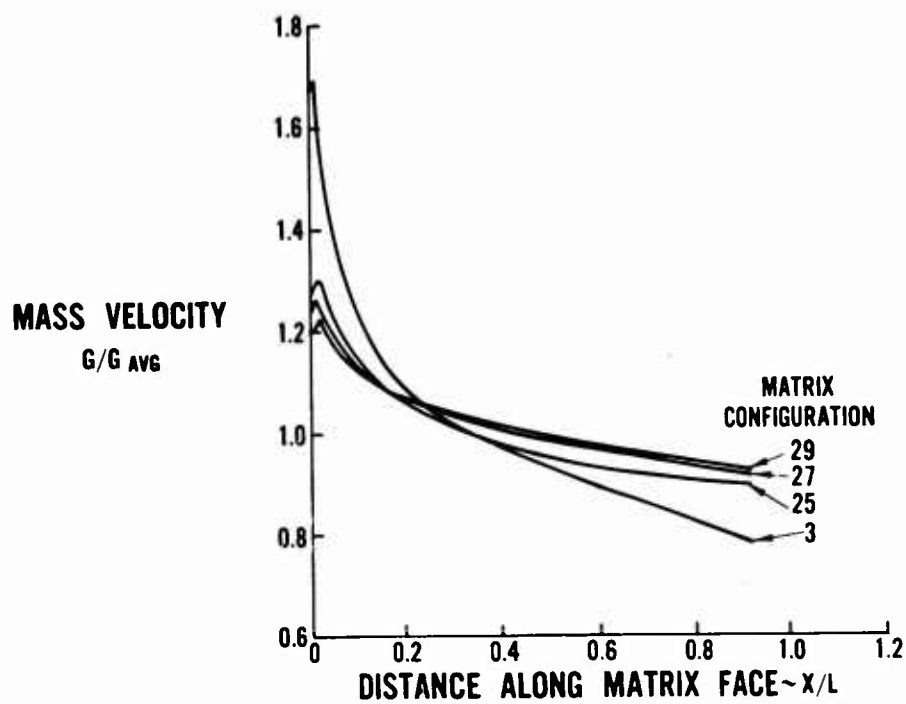


Figure 46. Normalized Mass Velocity Leaving Matrix Vs. Distance Along Matrix Face for Flow Into Vee, Configurations 3, 25, 27, and 29.

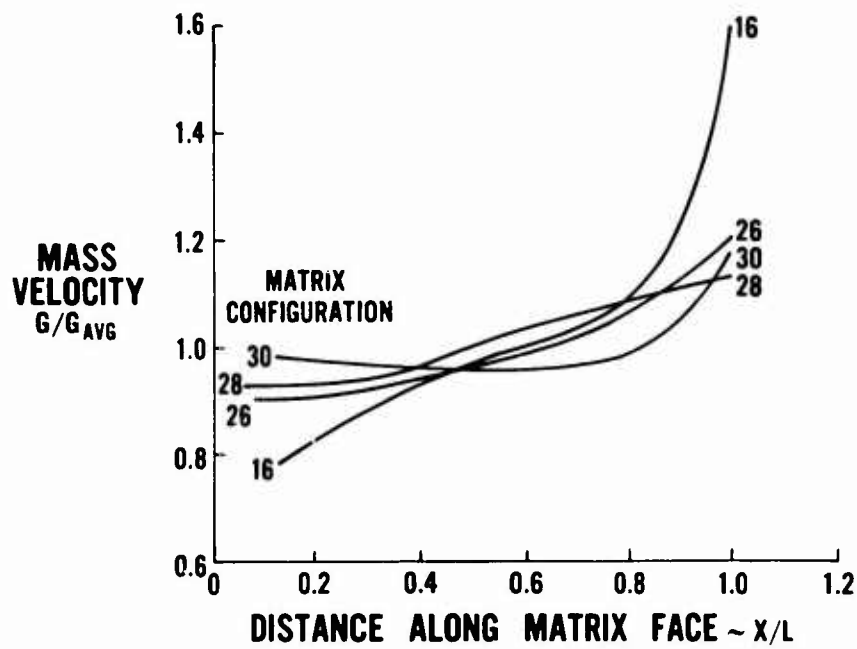


Figure 47. Normalized Mass Velocity Leaving Matrix Vs. Distance Along Matrix Face for Flow Over Vee, Configurations 16, 26, 28, and 30.

CONFIDENTIAL

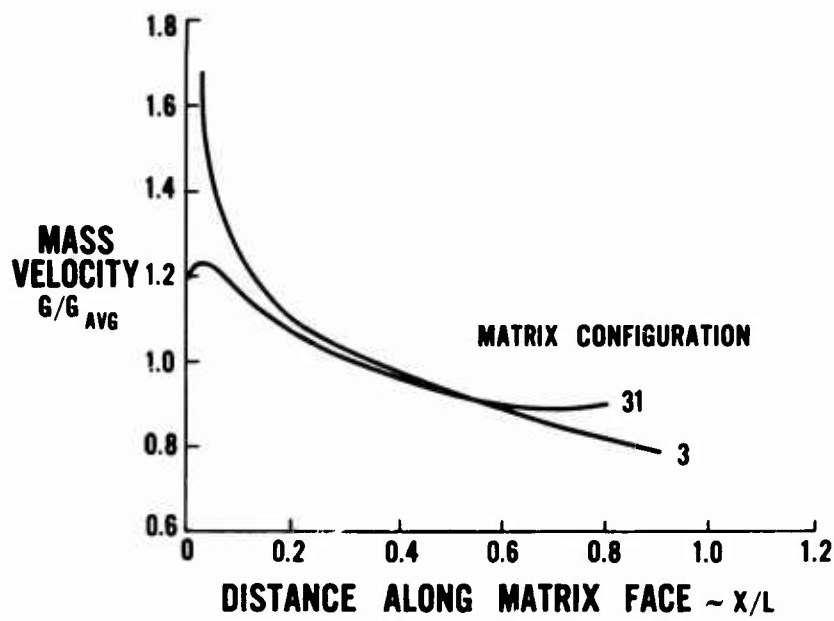


Figure 48. Normalized Mass Velocity Leaving Matrix Vs. Distance Along Matrix Face for Flow Into Vee, Configurations 3 and 31.

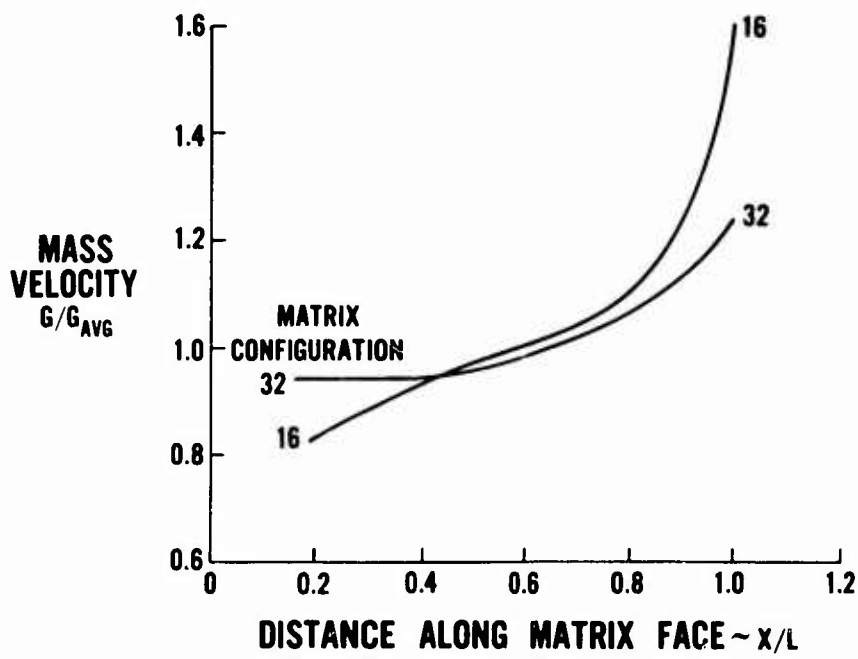


Figure 49. Normalized Mass Velocity Leaving Matrix Vs. Distance Along Matrix Face for Flow Over Vee, Configurations 16 and 32.

CONFIDENTIAL

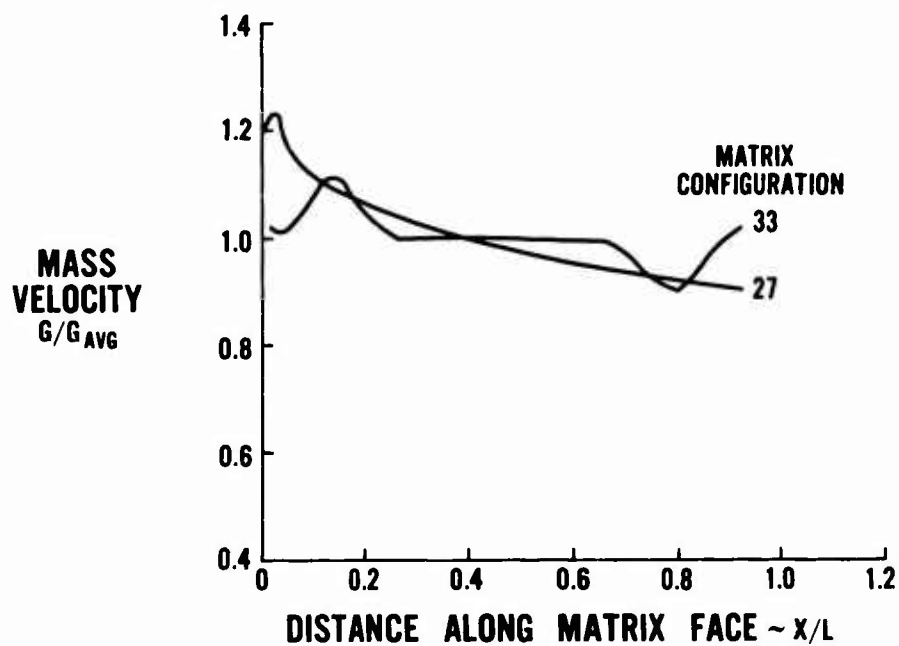


Figure 50. Normalized Mass Velocity Leaving Matrix Vs. Distance Along Matrix Face for Flow Into Vee, Configurations 27 and 33.

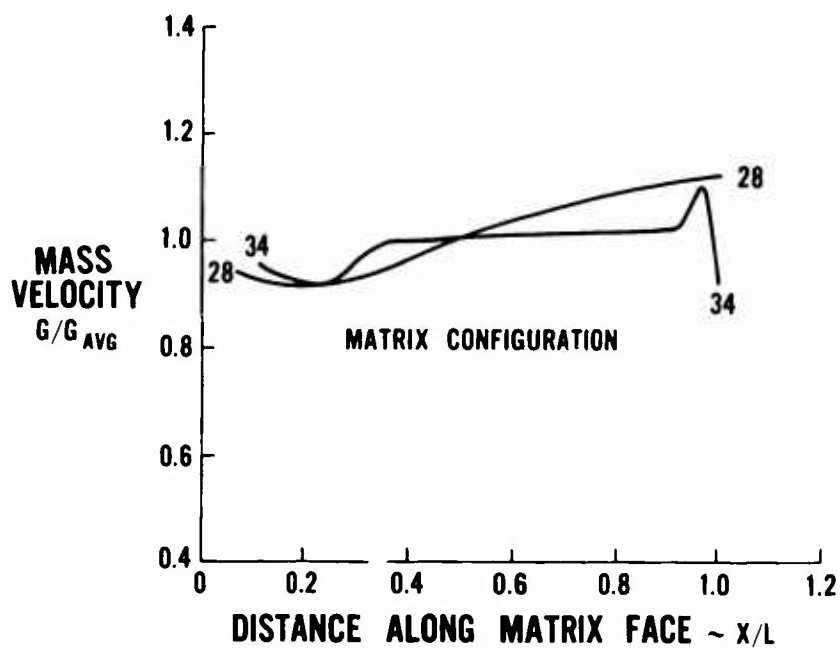


Figure 51. Normalized Mass Velocity Leaving Matrix Vs. Distance Along Matrix Face for Flow Over Vee, Matrix Configurations 28 and 34.

CONFIDENTIAL

CONFIDENTIAL

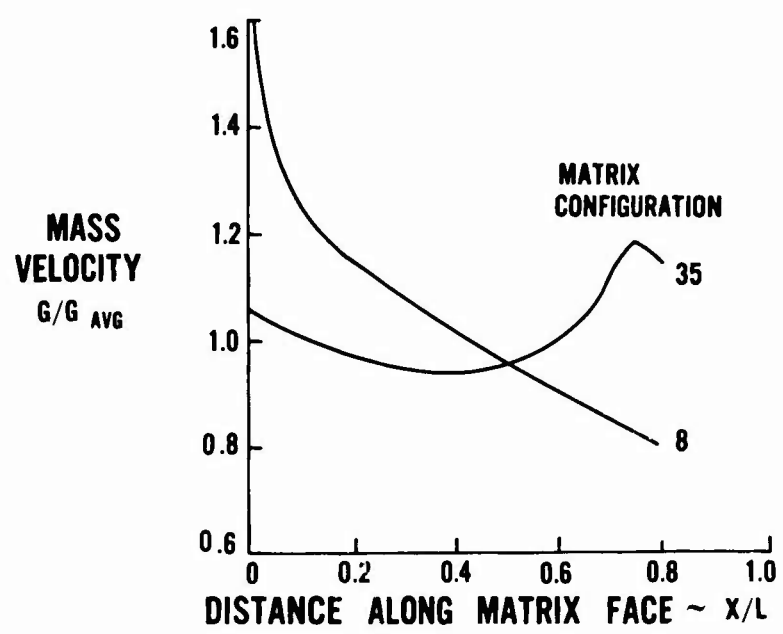


Figure 52. Normalized Mass Velocity Leaving Matrix Vs. Distance Along Matrix Face for Flow Into Vee, Matrix Configurations 8 and 35.

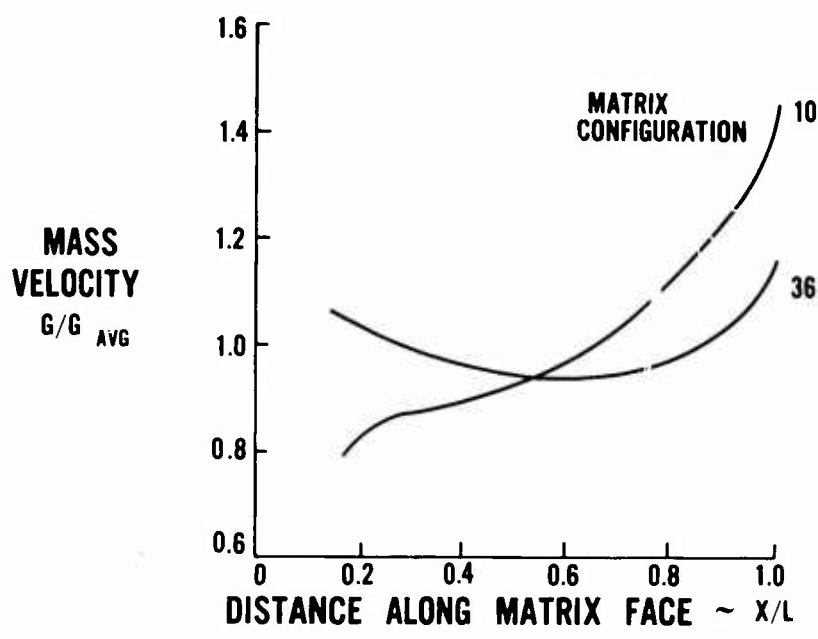


Figure 53. Normalized Mass Velocity Leaving Matrix Vs. Distance Along Matrix Face for Flow Over Vee, Matrix Configurations 10 and 36.

CONFIDENTIAL

CONFIDENTIAL

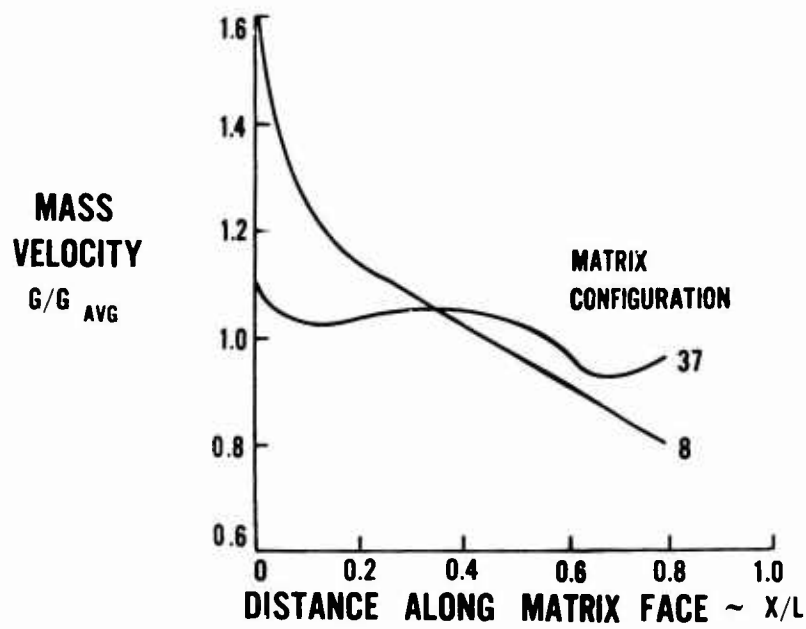


Figure 54. Normalized Mass Velocity Leaving Matrix Vs. Distance Along Matrix Face for Flow Into Vee, Matrix Configurations 8 and 37.

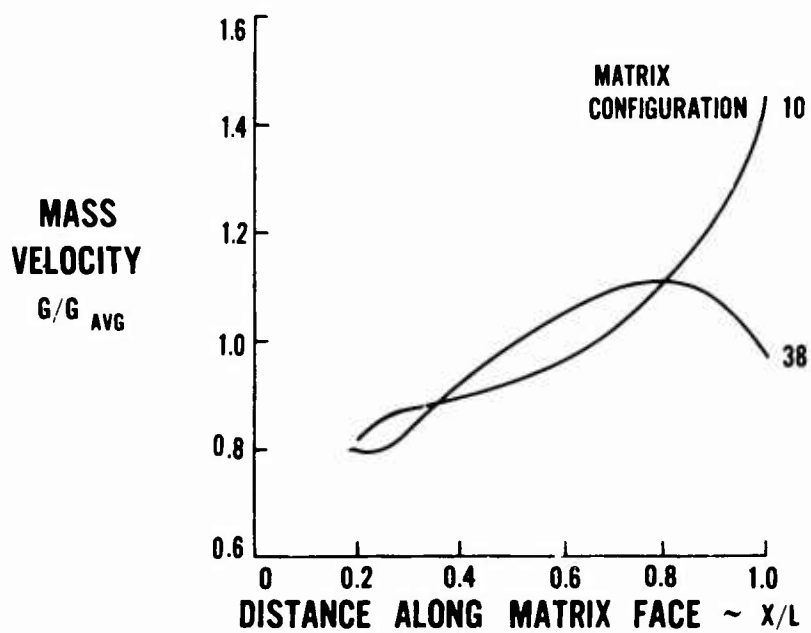


Figure 55. Normalized Mass Velocity Leaving Matrix Vs. Distance Along Matrix Face for Flow Over Vee, Matrix Configurations 10 and 38.

CONFIDENTIAL

CONFIDENTIAL

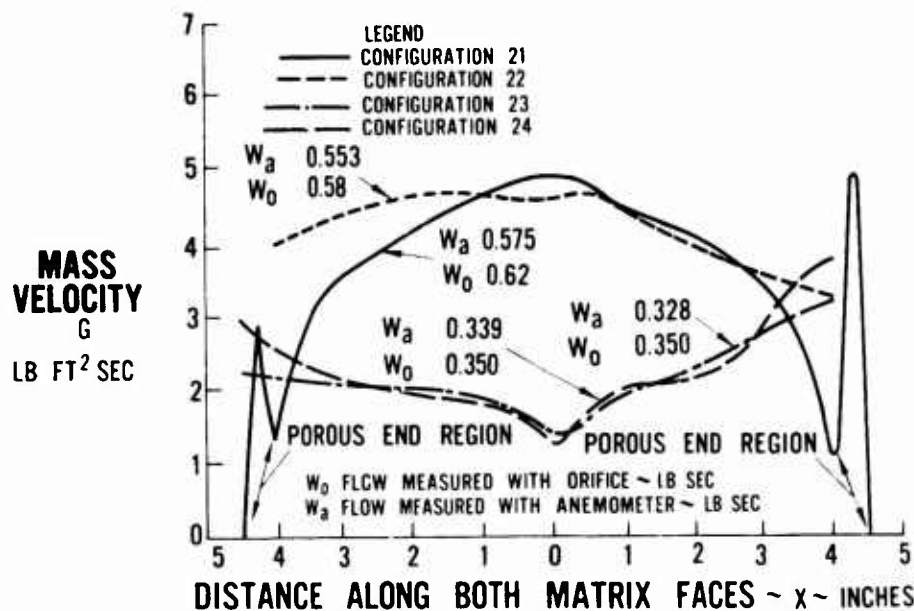


Figure 56. Mass Velocity Leaving Matrix Face Vs. Distance Along Matrix Face, Configurations 21 Through 24.

Compared to the blunt-end apex package of previous tests, the porous screen apex relieved the maldistribution in this region. The tests conducted with porous and nonporous or blunt ends revealed that the porous ends were detrimental to flow distribution in both flow directions because excess flow streams through the area of reduced flow length. The blunt-end matrix, which had less maldistribution, was tested in the regenerator.

Factors which improve flow distribution, with the exception of turning vanes or centerbodies, were incorporated in the high-effectiveness regenerator design. These factors included:

1. The addition of fairings in the compressor-to-regenerator and turbine-to-regenerator ducts to provide for in-line walls over the blunt ends,
2. The increased matrix angle from 16° to 18°, and
3. The elimination of all matrix gaps.

The high-effectiveness design matrix package was later flow tested (in Phase II) in the component rig to verify the desired flow distribution. Provisions were made in the design to incorporate turning vanes if required. The electron beam welding technique has been proven to be a satisfactory method of attaching the turning vanes to the sintered edges of the screen matrix.

CONFIDENTIAL

CONFIDENTIAL

MATRIX TESTS IN REGENERATOR

The existing regenerator rig tested under contract NOW 62-0636-f was used in this program as a subscale model.

The regenerator was used in performance loop tests to determine temperature effectiveness and pressure loss of candidate matrices and, in a separate facility, to determine total mass loss and leakage rates of each seal area.

The performance loop tests were an ideal method for evaluating data obtained from the component heat transfer and flow distribution tests of Contract Item 2 of Phase I; they also provided an ideal means for determining the accuracy of the rotary regenerator prediction system for future designs.

The ultimate goal of this portion of the program (matrix tests in regenerator, contract Item 3 of Phase II) was to demonstrate 85-percent temperature effectiveness with 7-percent regenerator pressure loss in the optimum matrix package at 1 pound per second airflow at 40 p.s.i.g., 400°F. compressor discharge air and 1050°F. turbine discharge gas.

METHOD OF ACCOMPLISHMENT

Description of Test Rig

The regenerator rig constructed prior to this program consists of two major assemblies. The rotor contains the matrix packages, rotary piston ring seals, torus inner diameter seals, and bearings. The housing consists of a structure to support the rotor and includes the toroid-shaped seal tunnels and inner diameter seal surfaces.

The rotor (see Figure 57), supported by two preloaded four-point contact bearings with rotating outer races, is driven through an integral 3:1 stepdown gearbox in the cold-side housing which mates with the ring gear of the rotor inner diameter. A rotating oil sump, sealed by face seals adjacent to the bearings and cooled by the bearing splash oil, is scavenged through two stand-pipes adjacent to the gearbox by means of external scavenge pumps.

The basic rotor (see Figure 58) consists of outer and inner rings with an integral gear; they form a truncated I-beam. The bulkhead is inserted into the pierced or slotted outer rim and is brazed to the rim. The piston ring seal grooves, machined into the bulkhead outer diameter, extend into the outer rim. The piston ring ends are contained by the mating surface of the bearing supports (see Figure 59), which are snapped into the inner diameter of the rotor and

CONFIDENTIAL

CONFIDENTIAL

are bolted at the ring gear location. The inner-diameter seal plate is integral with the bearing support. The axial location of the plate is controlled by chamfered mating surfaces on the reverse side of the seal plate at the outer diameter and the inner diameter of the rotor outer rim.

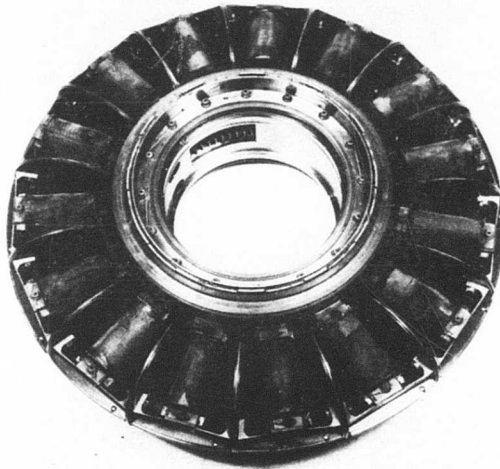


Figure 57. View Showing Cold Side of Rotor Assembly.

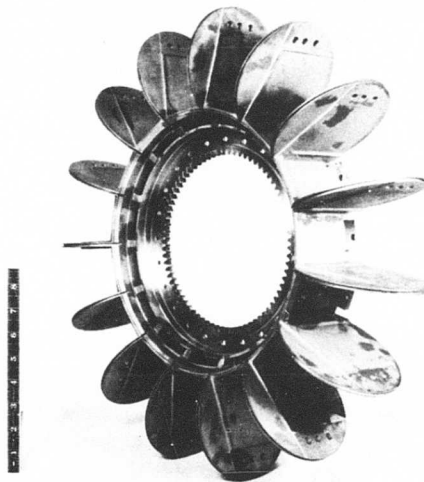


Figure 58. Regenerator Rotor Subassembly.

CONFIDENTIAL

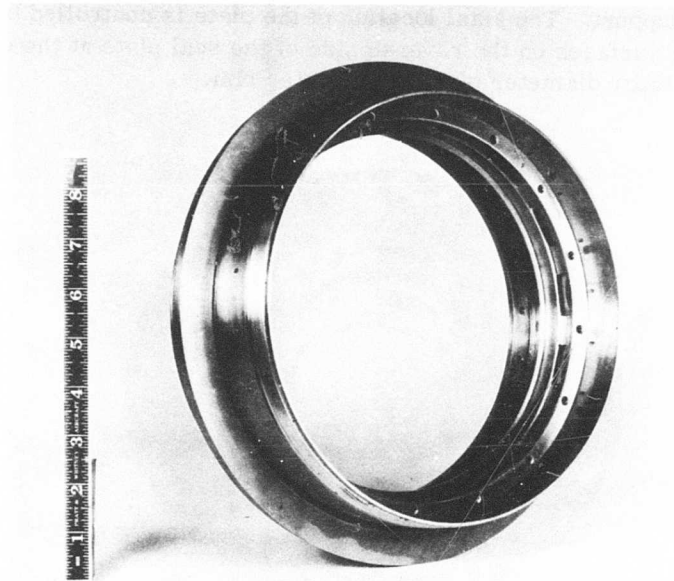


Figure 59. Regenerator Bearing Housing and Integral Seal Plate.

The piston rings, which rotate with the torus, are retained by three guiding surfaces when not in the two seal tunnels. These three surfaces, which include approximately 30° of arc on the stationary housing outer diameter and 5° of arc on each seal liner outer diameter, maintain piston ring circularity when not in the seal tunnels. The piston rings are led into and out of the tunnels by chamfers in the leading and trailing edges of each tunnel (see Figures 60 and 61). The chamfers prevent the rings from feeling the full pressure load until the rings are fully seated in each tunnel, and they relieve the pressure load before the ring is released on exit. The piston rings are under pressure load only while they are in the seal tunnels. The length of the tunnels is designed so that there is always a minimum of one active piston ring to prevent compressor discharge air from leaking into the low-pressure turbine discharge sector.

The all-metal spring-loaded circumferential segment seals on the outer diameter of the torus prevent matrix bypass leakage. These seals are lightly loaded by the pressure differential across the matrix external of the seal tunnels (see Figure 62). The outer-diameter segment seal holders are bolted to the bulkheads and transmit a portion of the bulkhead pressure loads.

CONFIDENTIAL

CONFIDENTIAL

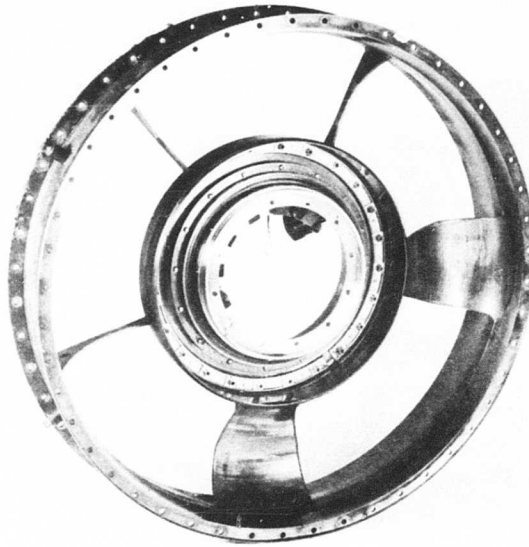


Figure 60. Hot Side of Regenerator Housing.

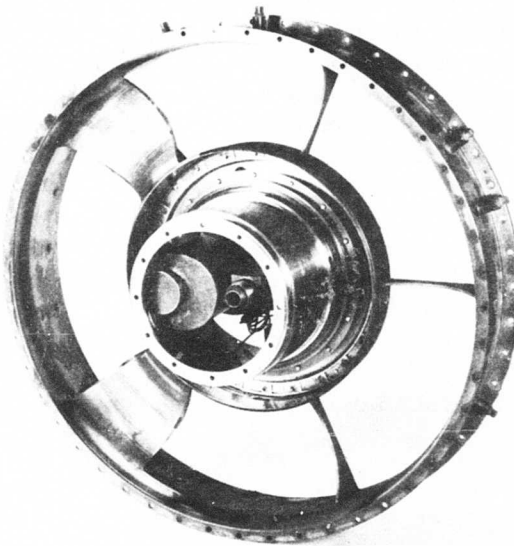


Figure 61. Cold Side of Regenerator Housing.

CONFIDENTIAL

CONFIDENTIAL

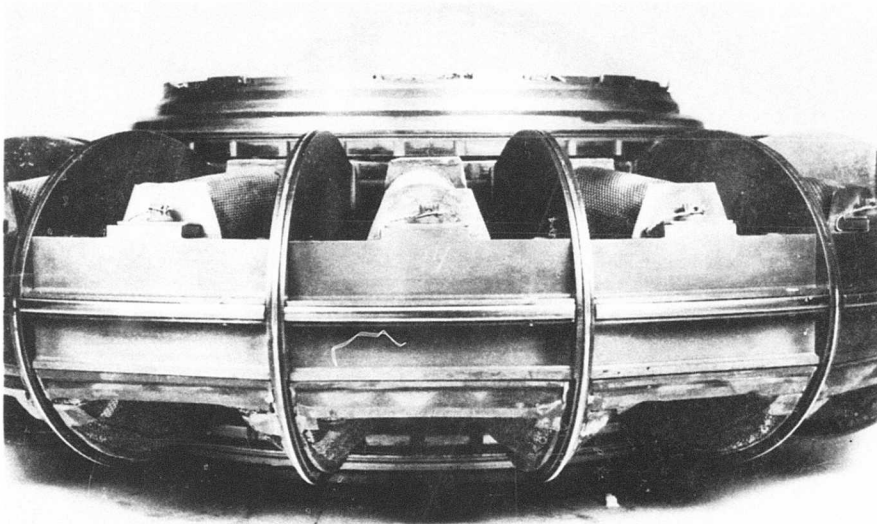


Figure 62. Regenerator Rotor Assembly.

At each side of the torus inner diameter are a pair of conically sprung split-ring carbon seals. The outermost seal of each pair is fully pressure relieved and serves only as a guiding member for the thrust washers and wave springs. The compartment formed between the bearing, sealed by a face seal, and the rotor is vented to compressor discharge air, which pressurizes the seals internally through holes in the bearing support housing. The ring seal against the rotor is the active seal; it feels the full pressure drop across that portion of the seal which is in the low-pressure sector, and it feels essentially zero pressure drop on that portion of the seal which is in the high-pressure sector. A ring seal, or its variation, is required in this area to minimize the direct tangential leak path at the rotor and housing intersection at the tunnel extremities. The face seals form the other boundary of the pressure cavity and seal the bearing lubrication oil from the gas stream. The seal is axially spring-loaded and is pressure-balanced to minimize wear. Air leakage through the face seal lip and the secondary piston ring seals force the oil to the scavenge side.

CONFIDENTIAL

CONFIDENTIAL

RESULTS

Build 1 Experimental Program

The purpose of the first test of the program was to establish a baseline performance calibration and to check out the facilities and instrumentation.

Existing heat transfer elements, radial vee matrices of 24 x 24 x 0.0135-inch-diameter screen mesh (Figures 63 and 64), were installed for this test. The matrix package geometry was such that the effective heat transfer area and matrix end effects (i.e., distribution and leakage) were not determined with component flow testing. Therefore, theoretical results are presented for the maximum flow area (2.229 square feet), which assumes full and uniform flow through the total frontal area, and for the minimum flow area (1.725 square feet), which eliminates area that is subjected to edge or end effects.

The seals for this first test were conically sprung one-piece carbon ring seals at the torus inner diameters, and face seals with the 16 torque pins and chrome-carbide coated piston rings for the torus bulkhead seals.

Seal leakage tests were conducted prior to the effectiveness performance tests to document the mass loss from the following areas as functions of pressure drop and regenerator speed:

1. Hot-side inner diameter seal plus face seal cavity.
2. Cold-side inner diameter seal plus face seal cavity.
3. Piston ring plus carryover.

This leakage calibration was performed by blanking off the high-pressure section on both sides of the regenerator, as illustrated in Figures 65 and 66. By pressurizing the compartment enclosed by these plates and seal cavities, pressurization of the regenerator in the engine was simulated.

Figure 67 shows that the total mass loss at 40 p.s.i.g. compressor discharge pressure and 40 r.p.m. regenerator speed is 17 percent of the regenerator engine mass flow based on 1 pound per second. One pound per second flow is equivalent to 800 standard cubic feet per minute.

The total mass loss at 80 p.s.i. pressure drop is 7 percent of the engine flow of 5 pounds per second, which is equivalent to 4000 standard cubic feet per minute.

CONFIDENTIAL

It should be noted that the seals in this build had none of the improvements determined from earlier component seal rig tests due to lead time of parts. The purpose of this build was to establish a baseline for regenerator leakage for later comparisons.

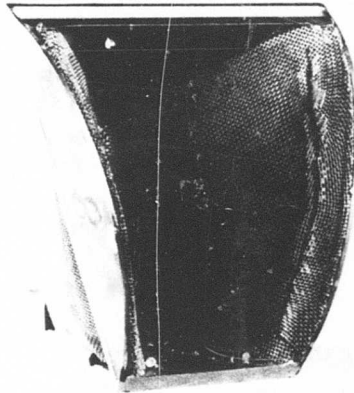


Figure 63. Hot-Side Inlet View of Straight Radial Vee Matrix.

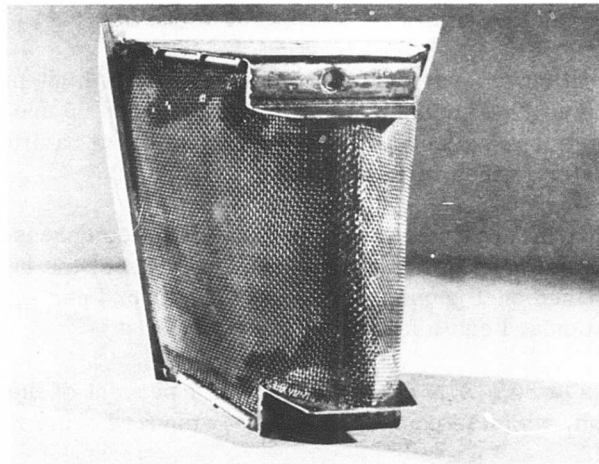


Figure 64. Cold-Side Inlet View of Straight Radial Vee Matrix.

CONFIDENTIAL

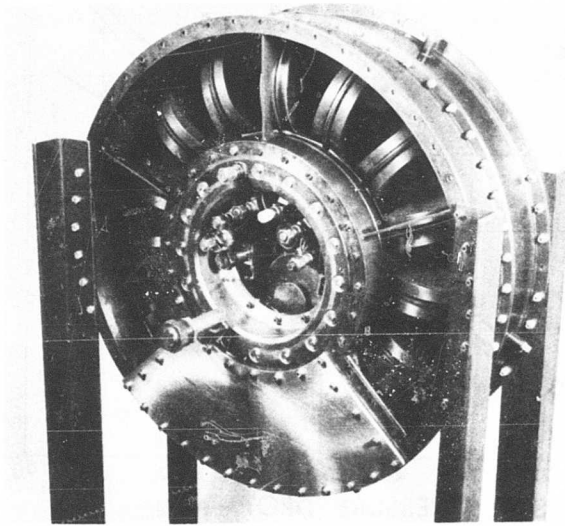


Figure 65. View of Regenerator Rig (Hot Side) With Blanking Plates Installed.

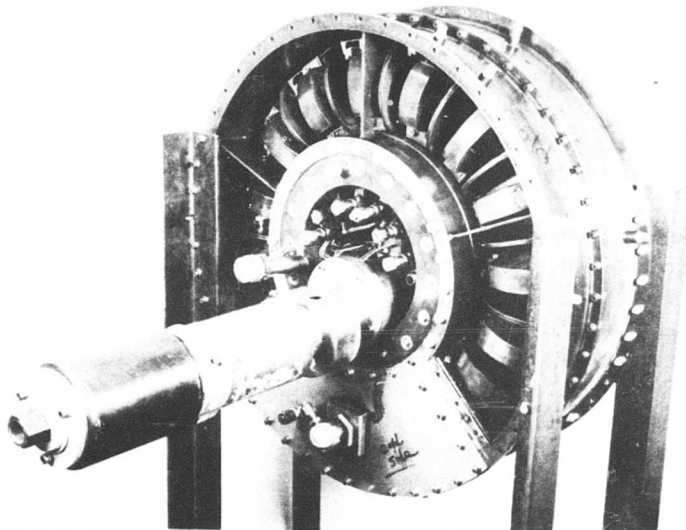


Figure 66. View of Regenerator Rig (Cold Side) With Pressurizing Boss on Blanking Plate; Rig Drive Motor Visible.

CONFIDENTIAL

CONFIDENTIAL

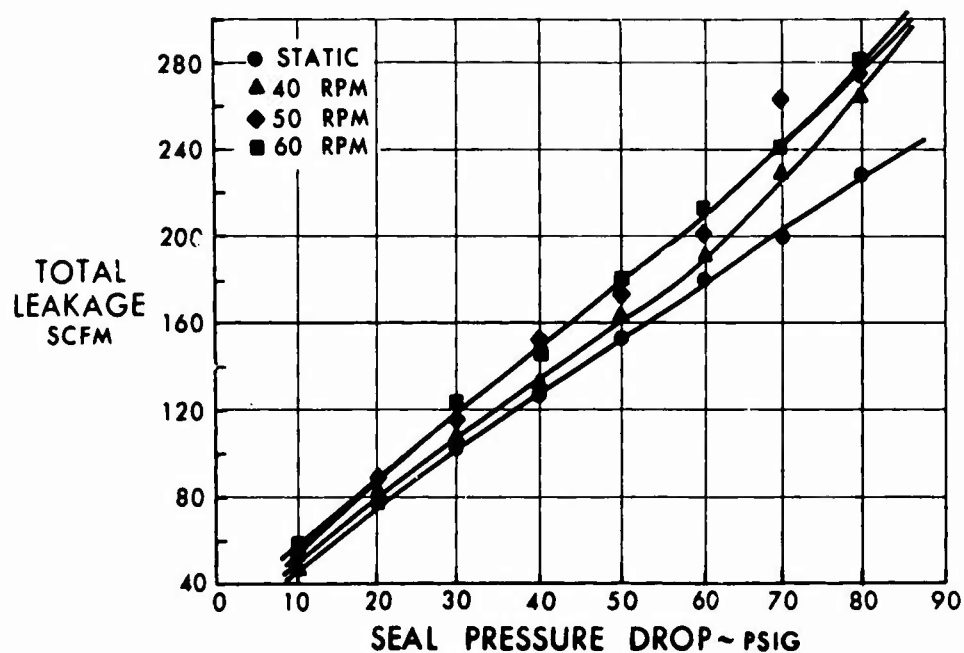


Figure 67. Baseline Calibration, Total Rotary Regenerator Leakage and Carryover.

Build 1 Analysis

Theoretical temperature effectiveness predictions were based on an empirical effectiveness relationship suggested by various investigators. The empirical effectiveness relation is limited to values of rotor-to-flowstream heat capacity ratios (C_R/C_C) greater than 1.5, since cycle studies invariably indicate that an optimum C_R/C_C exists in the region of 2.0. This results from the rotor carry-over-versus-effectiveness trades.

In Figures 68 and 69 are curves of temperature effectiveness as a function of airflow for constant rotor speed. The data fell approximately 3 to 8 percent below the theoretical results in the C_R/C_C region of 1.4 to 2.0. This discrepancy appears to be caused by nonuniform flow distribution through the matrix and leakage through the matrix ends.

Rig testing was conducted at relatively low rotor speeds due to problems encountered with the rotor drive system. Consequently, some of the data are at C_R/C_C values below the region of normal design and in the region where the empirical effectiveness relation is not applicable. The data in this region show less decrease in effectiveness than the correlation predicts. This trend was also noted during previous runs.

CONFIDENTIAL

CONFIDENTIAL

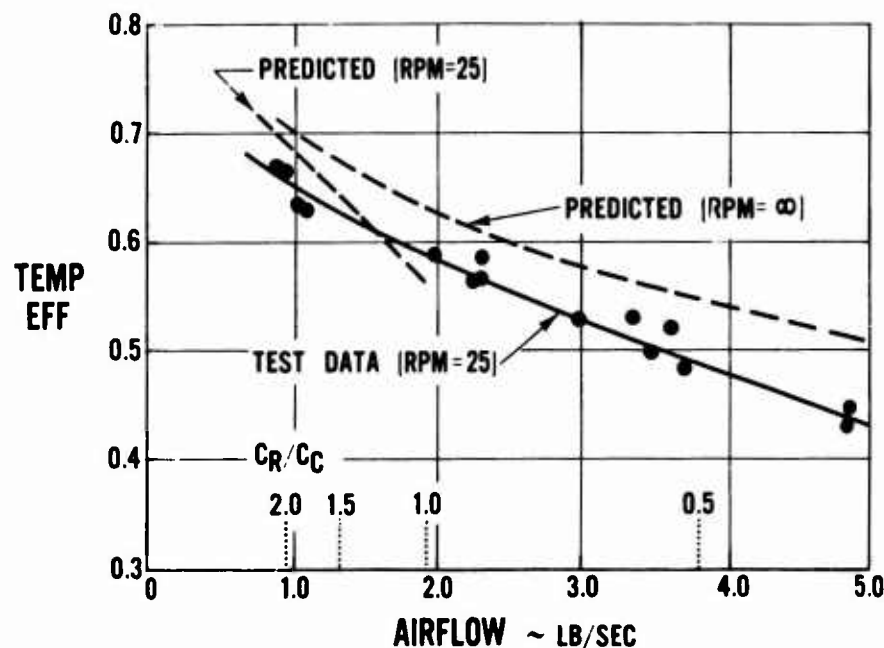


Figure 68. Temperature Effectiveness Vs. Airflow for Build 1 Regenerator With 24 x 24 Wire Screen Matrix; Prediction Based on 1.73 Square Feet of Frontal Area.

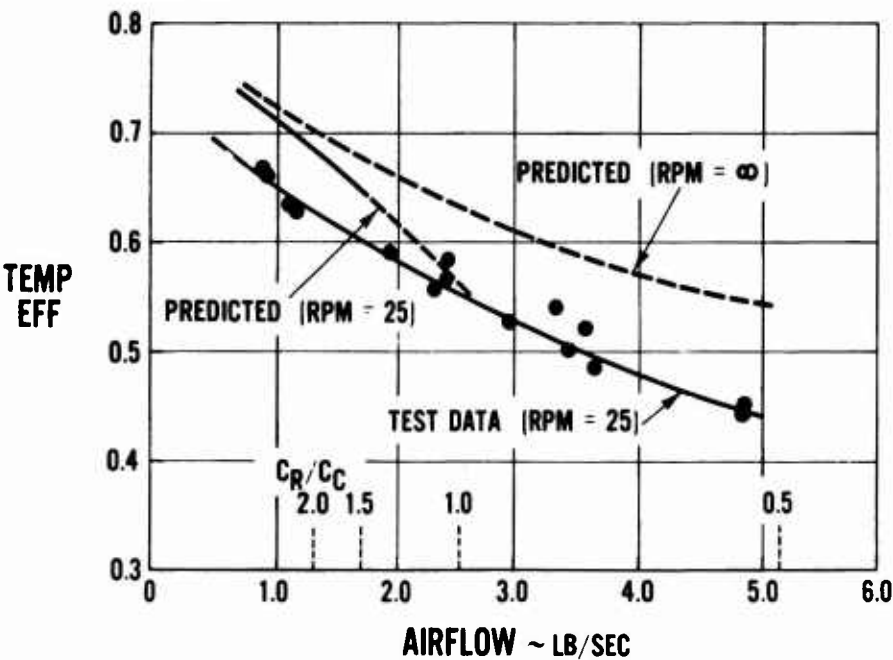


Figure 69. Temperature Effectiveness Vs. Airflow for Build 1 Regenerator Test Rig With 24 x 24 Wire Screen Matrix; Prediction Based on 2.23 Square Feet of Frontal Area.

CONFIDENTIAL

Attempts to operate the rotor at higher speeds resulted in unstable speed. Two calibrations that were obtained in the region of high speed are shown in Figure 70. Although the data indicated an increased effectiveness relative to the predicted values, the tendency was not observed during previous running. The increased effectiveness may have been due to error in the assumed test speed. Successive tests were accomplished with an improved drive system, which allowed better investigation of rotor speed effects.

Theoretical pressure losses were determined in a manner similar to that suggested by Kays and London (reference 5, page 21). Matrix package geometry and the associated end effects were handled in the same manner as they were in determining regenerator effectiveness.

Pressure loss is presented in Figures 71 and 72 as a function of flow parameter for the high- and low-pressure sides of the regenerator, respectively. The data agreed reasonably well with theoretical results based on the maximum flow area. Nonuniform flow distribution through the matrix caused increased pressure loss while leakage through the matrix ends caused a decrease in pressure loss. Test results indicated that the leakage effect dominated.

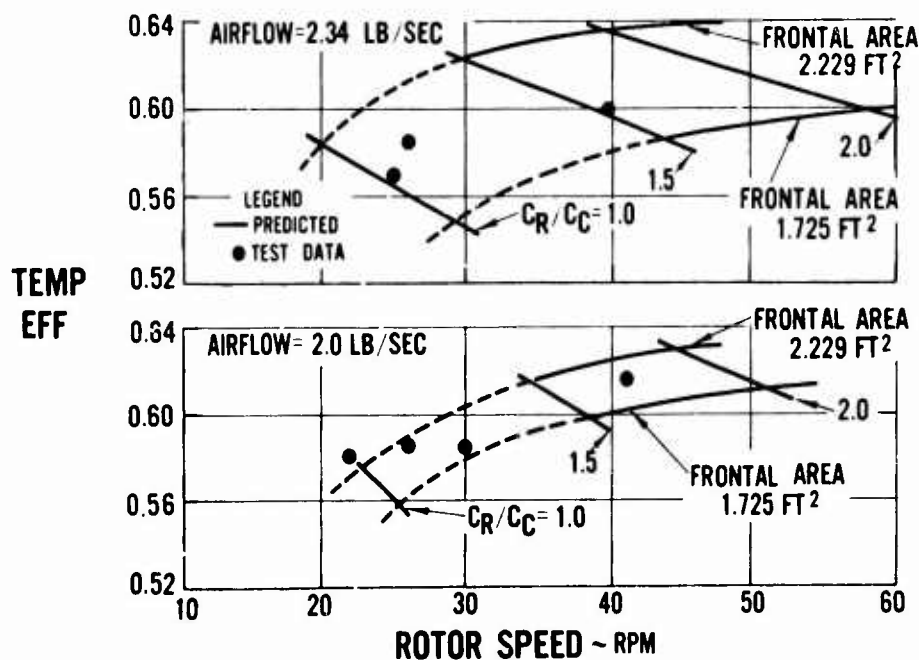


Figure 70. Temperature Effectiveness Vs. Rotor Speed for Build 1 Regenerator Test Rig.

CONFIDENTIAL

CONFIDENTIAL

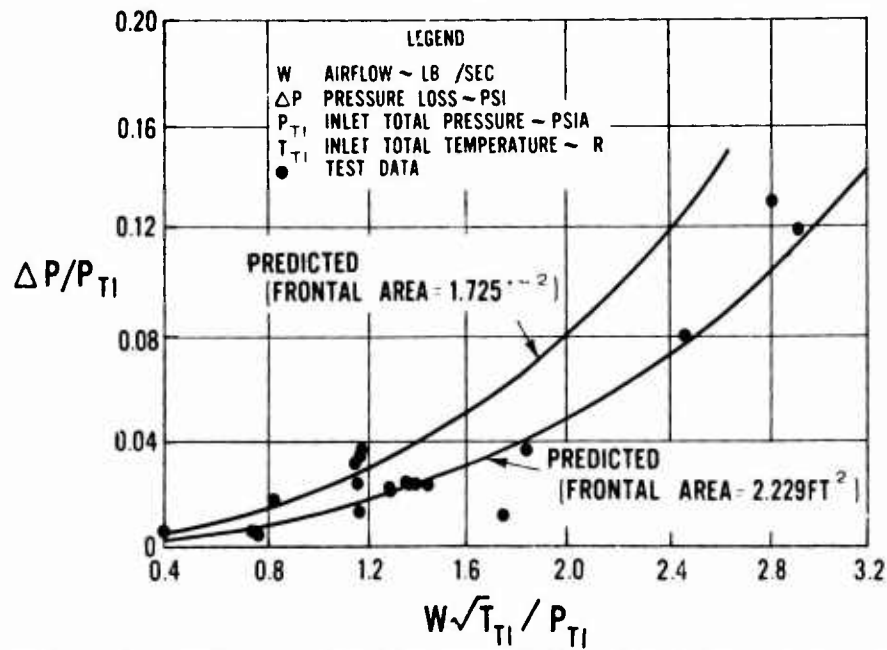


Figure 71. Pressure Loss Vs. Flow Parameter for Build 1, High-Pressure Side.

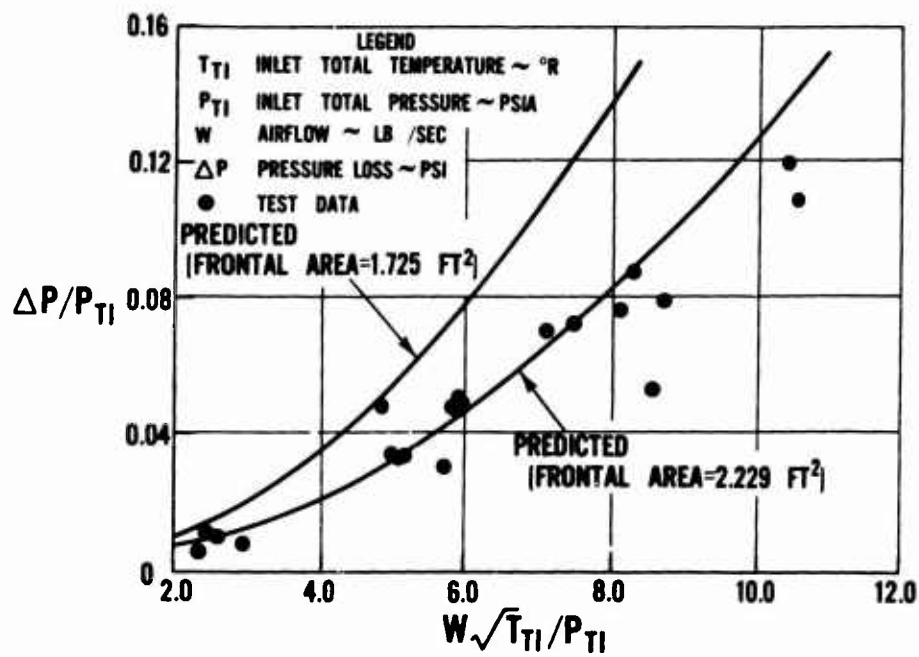


Figure 72. Pressure Loss Vs. Flow Parameter for Build 1, Low-Pressure Side.

CONFIDENTIAL

CONFIDENTIAL

Build 2 Experimental Program

The second test of the regenerator was a direct comparison of the circumferential vee matrix to the radial vee matrix of Build 1. Turning the apex of the vee angle 90° to a circumferential orientation reduced the flow distribution problem to two dimensions, since the angle of the matrix is constant at 33° . In the radial vee matrix, the included angle at the rotor was approximately 8° ; it opened to an angle of 30° at the outer diameter and thus increased the radial flow maldistribution. The circumferential vee matrix package, shown in Figures 73 through 75, had the same frontal area as the minimum frontal area (1.725 square feet) of the radial vee matrix; the screen thickness and mesh geometry were the same as for the Build 1 matrix.

Other advantages of the circumferential vee matrix are listed below.

1. Elimination of flow disturbances caused by mechanical attachments to the rotor.
2. Elimination of necessity to pierce matrix with tie rods on tie plates to absorb bulkhead loads for future flightweight torus designs.
3. Utilization of fairings in the stationary housings or ducts which reduced torus diameter and weight.
4. Ease of matrix package fabrication.

The seal arrangement for this build consisted of the single-stage segmented carbon seals on the torus inner diameter with compensated seal plates.

The oil face seals were modified by reducing the number of torque pins from 16 to 3 to allow the seal more freedom from sticking or hangup. The torus seals were the same chrome-carbide-coated piston rings.

The regenerator leakage calibration (Figure 76), compared to the baseline calibration of Build 1, revealed a 40- to 50-percent reduction in total regenerator leakage and a total mass loss of 4 percent at 80 p.s.i.g. based on 5 pounds per second flow.

CONFIDENTIAL

CONFIDENTIAL

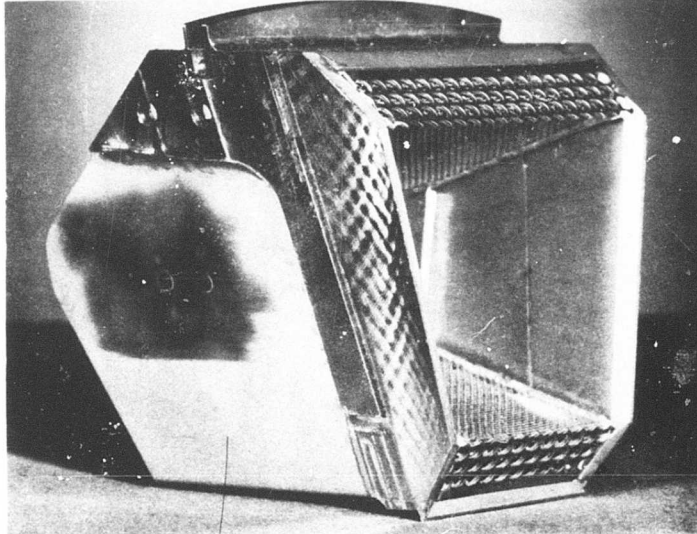


Figure 73. Build 2 Rotary Regenerator Circumferential Matrix Assembly With Integrated Rub Strip at Top of Matrix Package.

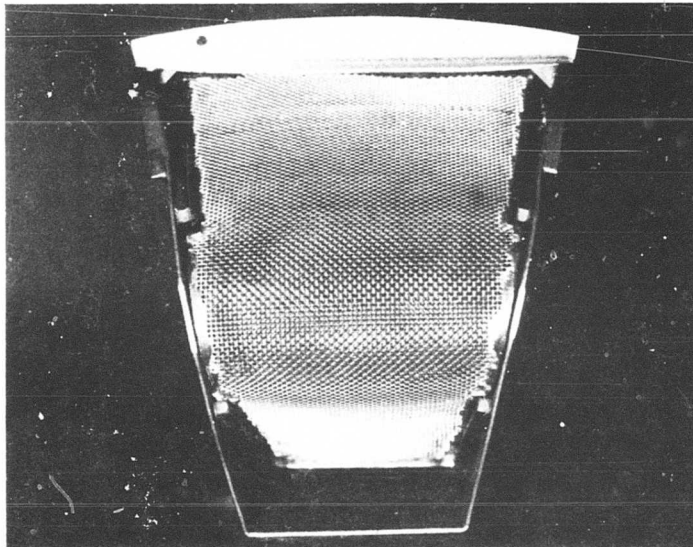


Figure 74. Build 2 Rotary Regenerator Circumferential Matrix Assembly Viewed From Cold Side of Vee Matrix; Screen Incorporates 24-Mesh, 0.0135-Inch-Diameter Wire.

CONFIDENTIAL

CONFIDENTIAL

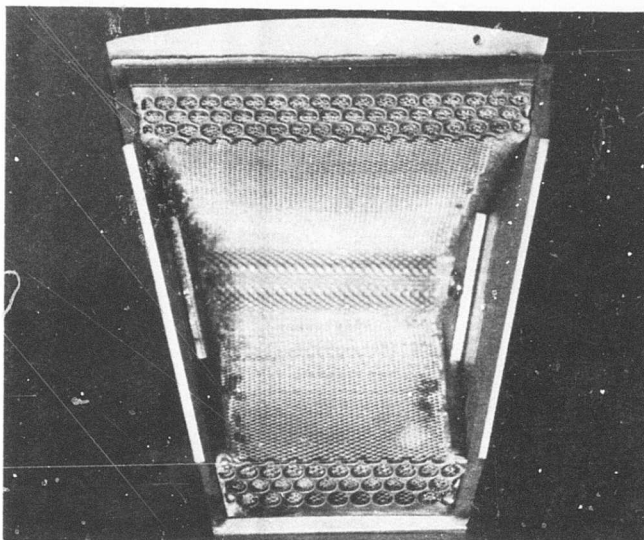


Figure 75. Build 2 Rotary Regenerator Circumferential Matrix Assembly Viewed From Hot Side of Vee Matrix; Screen Incorporates 24-Mesh, 0.0135-Inch-Diameter Wire.

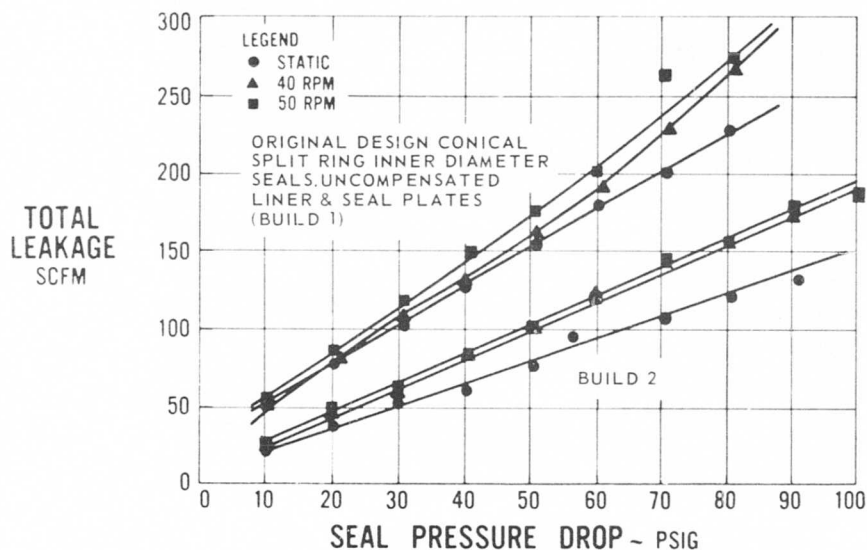


Figure 76. Leakage Calibration, Total Rotary Regenerator Leakage and Carryover.

CONFIDENTIAL

CONFIDENTIAL

The rig assembled with the circumferential vee matrix is shown in Figure 77, which is a view of the cold side and the hydraulic drive rotor which replaced the air motor drive of Build 1.

The positive-displacement-type hydraulic motor was a very satisfactory drive system which gave excellent speed control. The required power determined by test to drive this rig at T74 conditons was 0.5 horsepower.

The performance regenerator satisfactorily completed a 15-point test program (Table VI). During this program, the regenerator was exposed to simulated engine conditions for a continuous period of 8 hours. No operational problems were encountered during the test program.

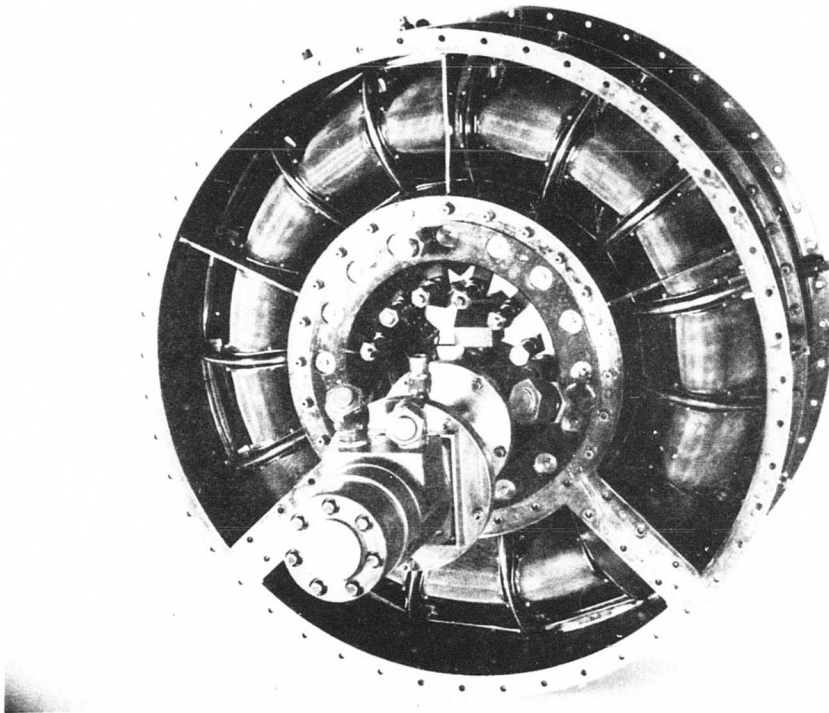


Figure 77. Rotary Regenerator Build 2 Viewed From Cold Side Showing Circumferential Vee Matrix Assemblies and Hydraulic Drive.

CONFIDENTIAL

TABLE VI
ROTARY RECENERATOR EFFECTIVENESS CALIBRATION PROGRAM

Airflow (lb./sec.)	Rotor Speed (r. p. m.)	Compressor Discharge Pressure (p. s. i. a.)	Turbine Discharge Pressure (p. s. i. a.)	Compressor Discharge Temp. (°F.)	Turbine Discharge Temp. (°F.)
1.8	25, 30, and 35 40 and 50	55.0 35.0	15.0	400	1050
1.5	30 and 35 40 and 50	55.0 35.0	15.0	400	1050
2.0	40 and 45 50 and 55	55.0 35.0	15.0	400	1050
2.5	50 and 55	35.0	15.0	400	1050

Build 2 Analysis

Theoretical performance and test data for Build 2, which incorporated the circumferential vee packages, are presented in Figures 78 through 83. The predicted results assume full and uniform flow through the matrix frontal area (1.725 square feet) with no axial leakage.

The circumferential vee package had less total heat transfer area than the radial vee packages of Build 1. However, the effective heat transfer area is comparable and well defined. For these reasons, the theoretical results are presented for only one matrix frontal area.

Temperature effectiveness is presented in Figures 78 and 79 as functions of airflow at constant rotor speed and in Figure 80 and 81 as functions of rotor speed at constant airflow. The measured effectiveness was approximately 5 percent below the predicted results throughout the range of rotor-to-flowstream heat capacity ratios (C_R/C_C) investigated. At low values of C_R/C_C (about 1.5) the measured effectiveness approached the predicted effectiveness. The discrepancy between the test data and the predicted results was caused by both nonuniform flow distribution and axial leakage.

CONFIDENTIAL

CONFIDENTIAL

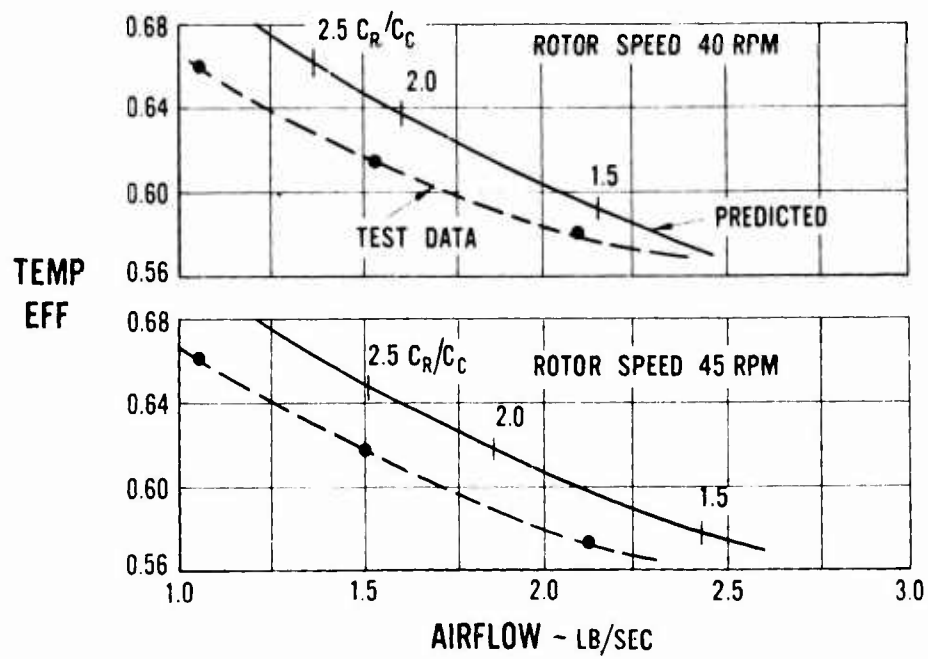


Figure 78. Temperature Effectiveness Vs. Airflow for Build 2 With 24 x 24 x 0.0135 Wire Screen Matrix and With Rotor Speeds of 40 and 45 R. P. M.

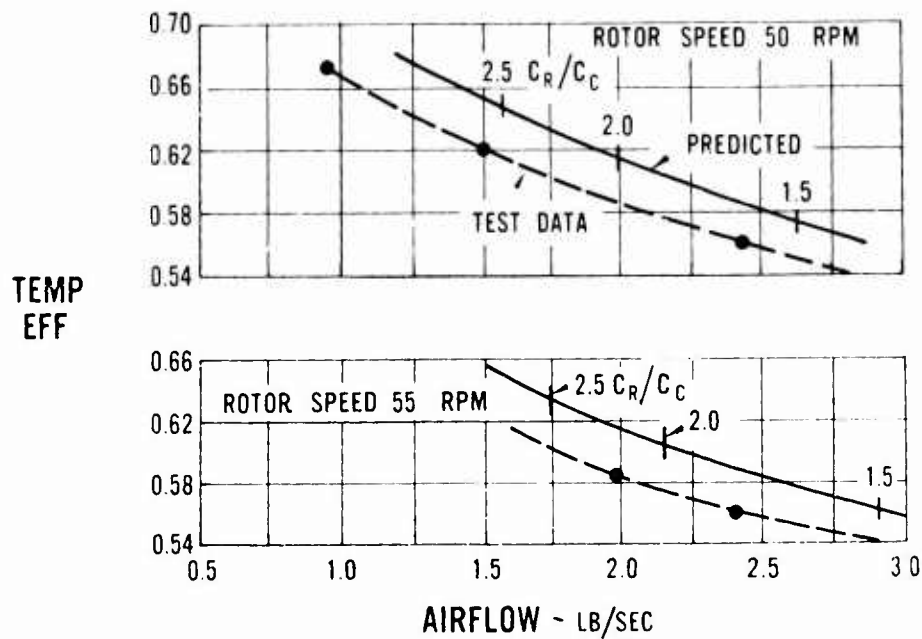


Figure 79. Temperature Effectiveness Vs. Airflow for Build 2 With 24 x 24 x 0.0135 Wire Screen Matrix and With Rotor Speeds of 50 and 55 R. P. M.

CONFIDENTIAL

CONFIDENTIAL

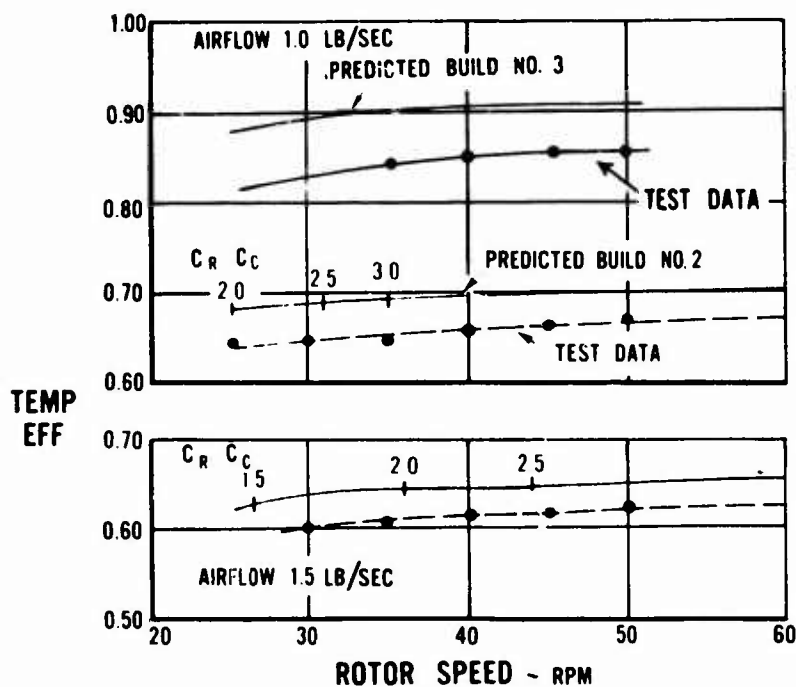


Figure 80. Temperature Effectiveness Vs. Rotor Speed for Builds 2 and 3 (1.0 and 1.5 Pounds per Second Airflow).

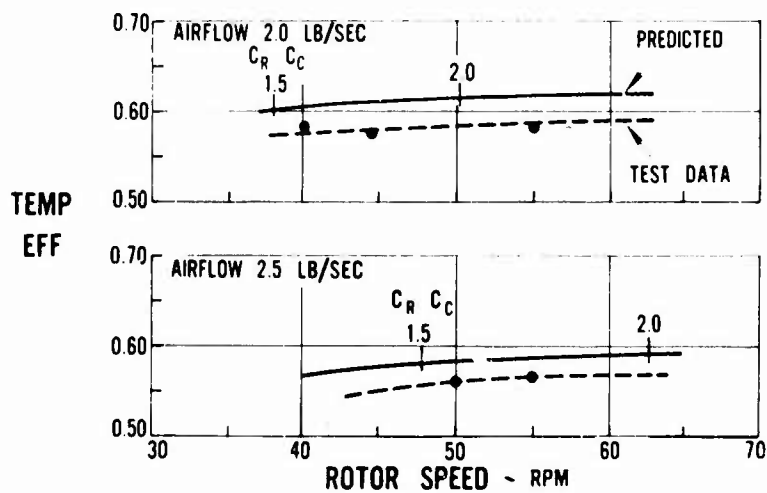


Figure 81. Temperature Effectiveness Vs. Rotor Speed for Build 2 (2.0 and 2.5 Pounds per Second Airflow).

CONFIDENTIAL

CONFIDENTIAL

Pressure loss is presented in Figures 82 and 83 as a function of flow parameter for the high- and low-pressure sides of the regenerator, respectively. The test data agreed reasonably well with the predicted results. Nonuniform flow distribution caused increased pressure loss. The test results indicated that leakage effects dominated. This trend was noted in the previous build where axial leakage occurred through the matrix ends.

Airflow distribution tests conducted in the component airflow rig (Figure 84) showed that the flow through this matrix did have a degree of nonuniformity. Since the component airflow tests revealed that the porous end regions caused a higher degree of maldistribution, the perforated plates on the matrix ends were covered.

The predicted temperature effectiveness based on the actual matrix flow distribution was 96.5 to 97.0 percent of the predicted effectiveness based on uniform flow distribution; the data were then within 2 percent of the corrected prediction. The 2-percent difference was attributed to bypass leakage, which was found upon posttest inspection to exist between the matrix package frame and screen element.

Although axial leakage existed and the circumferential vee packages contained less total heat transfer area than the radial packages used in the previous build, an improvement in performance was realized. This improvement was attributed to improved flow distribution associated with the circumferential package configuration.

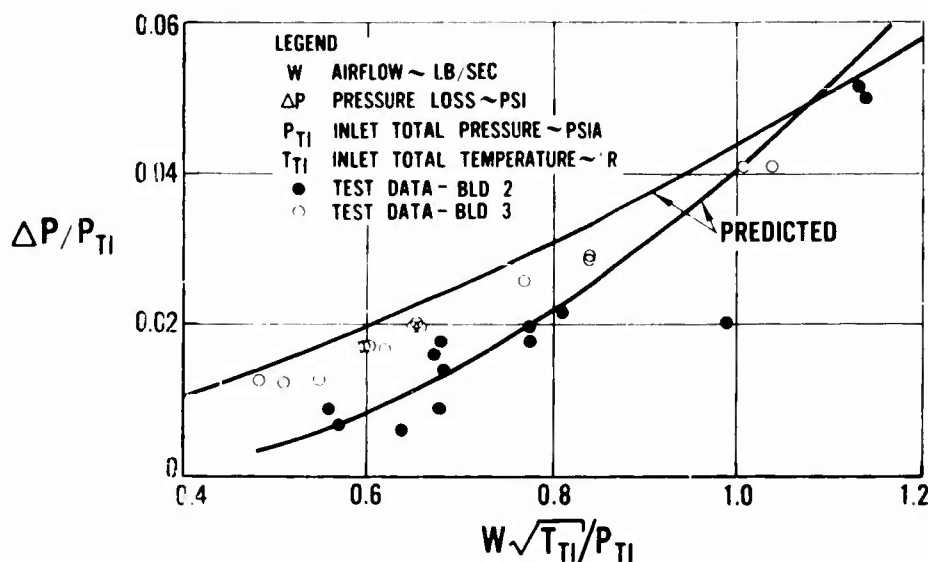


Figure 82. Pressure Loss Vs. Flow Parameter for Builds 2 and 3 (High-Pressure Side).

CONFIDENTIAL

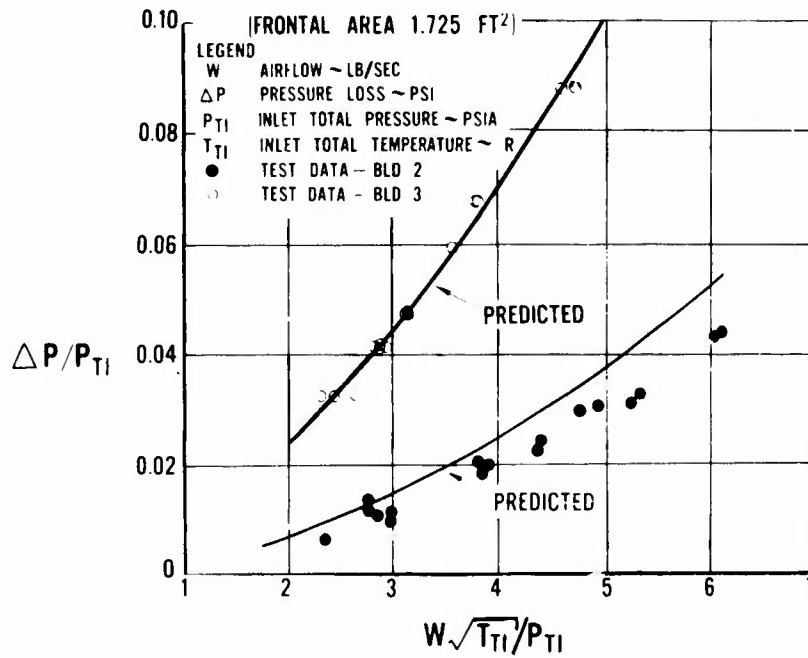


Figure 83. Pressure Loss Vs. Flow Parameter for Builds 2 and 3 (Low-Pressure Side).

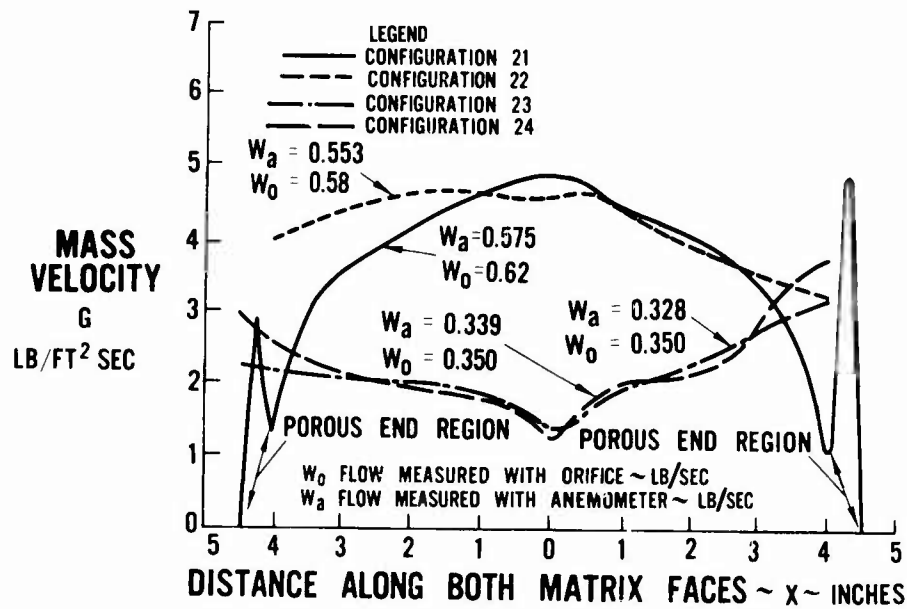


Figure 84. Mass Velocity Leaving Matrix Face Vs. Distance Along Matrix Face for Build 2.

CONFIDENTIAL

CONFIDENTIAL

Build 3 Experimental Program

The optimum circumferential vee matrix configuration was installed in Build 3 to obtain the 85-percent temperature effectiveness goal with 1 pound per second airflow at 40 p.s.i.g., 400°F. compressor discharge air, 1050°F. turbine discharge air, and 7-percent regenerator total pressure loss.

An analytical study to determine the theoretical performance of the circumferential vee matrix package for use in Build 3 of the existing regenerator rig was conducted. This study was based on the two most attractive matrices tested in the transient heat transfer rig. Both the 80 x 80 x 0.0037 and 60 x 60 x 0.0040 matrices satisfied the performance goals of 85-percent effectiveness and 7-percent pressure loss at 1 pound per second flow. However, the 60 x 60 x 0.0040 mesh required a considerably larger matrix thickness.

The predicted temperature effectiveness, matrix thickness, and rotor speed are presented in Figures 85 and 86 as a function of total regenerator pressure loss. Matrix thickness, carryover, rotor speed, and associated regenerator performance for a 6-percent total regenerator pressure loss are summarized in Table VII.

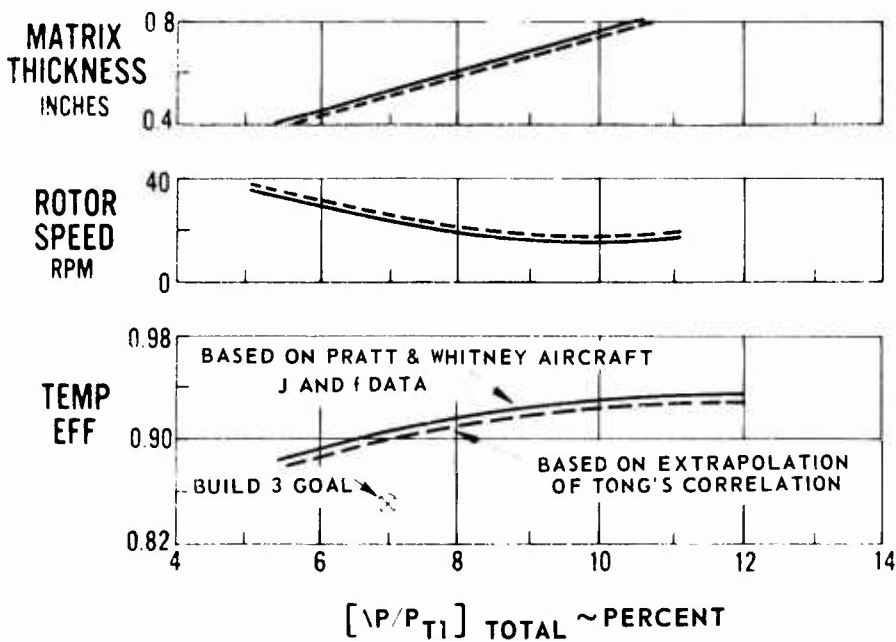


Figure 85. Predicted Ideal Regenerator Performance Vs. Regenerator Total Pressure Loss for 80 x 80 x 0.0037 Wire Screen Matrix (Frontal Area 1.73 Square Feet).

CONFIDENTIAL

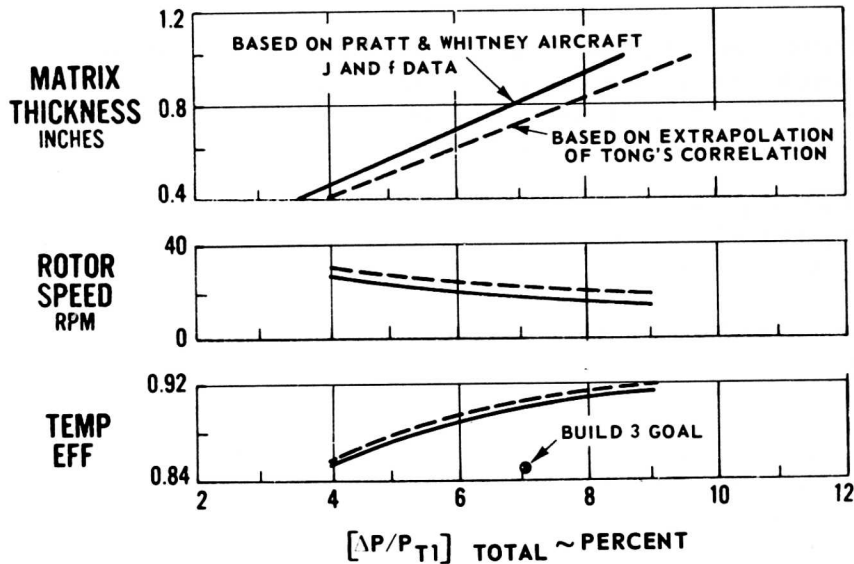


Figure 86. Predicted Ideal Regenerator Performance Vs. Regenerator Total Pressure Loss for 60 x 60 x 0.004 Wire Screen Matrix (Frontal Area 1.73 Square Feet).

TABLE VII
PREDICTED IDEAL HEAT TRANSFER CORE REQUIREMENTS AND
ASSOCIATED REGENERATOR PERFORMANCE FOR A 6-PERCENT
TOTAL PRESSURE LOSS ON BUILD 3

		Matrix Thickness (in.)	Rotor Speed (r.p.m.)	Total Carryover (lb./sec.)	Predicted Effectiveness (%)
80 x 80 x 0.0037	Pratt & Whitney Aircraft Data	0.45	28	0.0309	89.2
	Tong's Correlation	0.44	29	0.0315	89.0
60 x 60 x 0.004	Pratt & Whitney Aircraft Data	0.70	22	0.0237	89.0
	Tong's Correlation	0.62	25	0.0274	89.5

CONFIDENTIAL

CONFIDENTIAL

The theoretical performance for both matrices was approximately identical. However, the core thickness required for the 60 x 60 x 0.004 mesh was 55 percent larger than that required for the 80 x 80 x 0.0037 mesh.

As core thickness increases, the window area decreases. Hence, the airflow maldistribution, which is a function of window velocity, will be lower with the 80 x 80 x 0.0037 mesh matrix and will simulate more closely the inlet geometry of the matrix package for the new high-effectiveness regenerator. Therefore, the 80 x 80 x 0.0037 mesh, 0.45 inch thick, was installed in Build 3 for demonstrating the performance goal. As indicated in Table VII, this matrix theoretically will provide some margin in both effectiveness and pressure lost performance.

The theoretical pressure loss and temperature effectiveness were based on uniform flow distribution with no seal leakage or carryover. Heat transfer and frictional characteristics obtained from both the test data and the extrapolation of Tong's Correlation were utilized in the analysis.

The degree of leakage and carryover at the required operating conditions had negligible effect on the predicted performance. However, flow maldistribution can cause significant changes in both pressure loss and temperature effectiveness.

The more suitable matrix for demonstrating 85-percent temperature effectiveness and 7-percent total pressure loss was determined by package geometry and the associated flow distribution. Previous testing in Build 2 indicated the maldistribution losses for the circumferential V-shaped package to be approximately 3 percent with an additional 2-percent loss due to axial leakage.

In addition to the higher resistance screen to improve the matrix flow distribution, fairings were installed on the hot inlet side at the matrix blunt ends. It was estimated with these improvements that the net performance losses would be less than 4 percent in temperature effectiveness and a 1-percent increase in total pressure loss. On this basis, the predicted temperature effectiveness of the 0.45-inch-thick 80-mesh matrix was reduced to approximately 85 percent.

The seal arrangement for this build consisted of single-stage, segmented carbon seals at the torus inner diameter, chrome-carbide coated piston ring bulkhead seals, and modified face seals in the bearing compartment.

The single-stage segmented seals were modified to increase the width of the sealing lips from 0.040 inch to 0.100 inch.

CONFIDENTIAL

CONFIDENTIAL

A further reduction in mass loss was obtained as shown in Figure 87. The total mass loss at 80 p.s.i., based on 5 pounds per second airflow, was 3 percent, while at the T74 test-bed compression ratio mass loss was 2.5 percent of engine flow.

Build 3 Analysis

The final goal of this phase was achieved. The 85-percent temperature effectiveness with 1 pound per second airflow at 40 p.s.i.g., 400°F. compressor discharge air, and 1050°F. turbine discharge gas temperature was obtained with a total regenerator pressure loss of 4.6 percent. This total pressure loss was a 34-percent improvement over the contract limit.

The predicted performance and test data of Build 3 are shown in Figures 80, 82, and 83. Predicted performance assumed full and uniform flow through the matrix frontal area. Temperature effectiveness was based on the frontal area (1.725 square feet) common to both sides of the packages. The predicted pressure loss was based on the mean frontal area, which accounts for the script portion of the vee package.

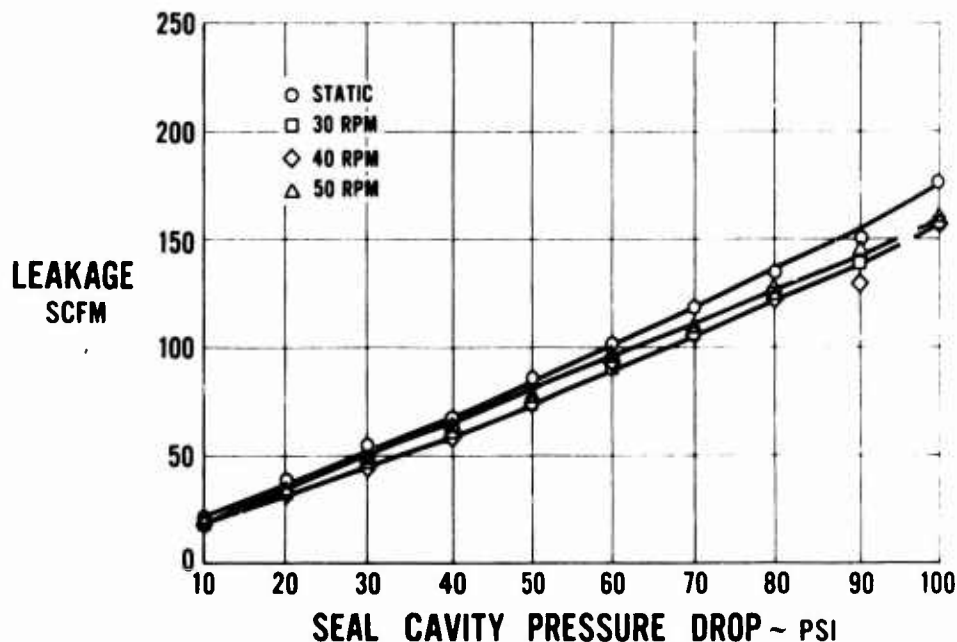


Figure 87. Build 3 Rotary Regenerator Total Mass Loss Vs. Seal Cavity Pressure Drop.

CONFIDENTIAL

CONFIDENTIAL

Temperature effectiveness is presented in Figure 80 as a function of rotor speed for a constant airflow. The measured effectiveness was 94.5 percent of the theoretical effectiveness throughout the range of rotor-to-flowstream heat capacity ratios investigated. This discrepancy was due primarily to nonuniform flow distribution and secondarily to axial bypass leakage.

The pressure loss data for the low-pressure stream agreed very well with the predicted loss. The high-pressure-side data were slightly lower; this was attributed to axial bypass leakage.

It was concluded from this test that the goals of the new flightweight regenerator design would be obtained.

CONFIDENTIAL

CONFIDENTIAL

INNER DIAMETER SEAL TESTS

The previous rotary regenerator program (Contract NOw 62-0636-f) conducted at Pratt & Whitney Aircraft revealed that the most critical seal area is at the torus inner diameter. The function of this seal area is to prevent leakage from the high-pressure sector of the regenerator flow path to the regenerator bearing compartment from which leakage air is dumped overboard. This seal is larger in diameter than most gas turbine mainshaft rubbing seals and is loaded non-uniformly, since one sector is in the low-pressure gas side while the remaining sector is in the high-pressure air side of the regenerator.

To ensure a positive seating force for the carbon, cold compressor discharge air is introduced between two seal rings. This pressurizing air causes the pressure drop across the sector in the high-pressure side to be approximately zero and that in the low-pressure side to be approximately equal to the compressor discharge pressure minus exhaust pressure.

In addition, the carbon seal intersects the bulkhead piston ring seals; to minimize leakage at this intersection, a ring seal (or its variation) featuring a closely controlled outer diameter rubbing surface positions the seal in relation to the piston rings.

Experience prior to this contract indicated that the leakage of these seals is much higher than expected in comparison with smaller diameter mainshaft engine seals. The suspected causes of this excessive leakage are:

1. Seal plate coning, whereby high pressure causes the plates to dish and disrupt normal radial seal contact,
2. Seal liner coning, whereby high pressure causes the liner to distort normal outer diameter circumferential seal contact.

Previous experience also indicates that metal-to-metal seal contacts are feasible because of the low rubbing speed in the regenerator. This attractive feature raises the possibility that an all-metal inner diameter seal with its inherent ruggedness would be a logical replacement for previously used carbon seals.

The purpose of the work on inner diameter seals tests (Contract Item 4 Phase I) were:

1. To determine the feasibility of an all-metal inner diameter seal,

CONFIDENTIAL

CONFIDENTIAL

2. To determine the cause of excessive leakage of typical carbon ring seals in regenerators, and
3. To determine acceptable alternate designs incorporating fixes.

A leakage goal of 10 standard cubic feet per minute at 100 p.s.i. pressure drop was established for the inner diameter component seal tests to meet the leakage requirements of the high-effectiveness regenerator.

METHOD OF ACCOMPLISHMENT AND RESULTS

Carbon Seal Tests

The first phase of the seal program was devoted to the determination of coning effects with the large-diameter carbon ring seals and the elimination of these effects to reduce seal leakage to the design goal.

An existing seal rig was assembled with available segmented carbon seals. The rig as shown in Figures 88 and 89 simulates the torus inner diameter seal location except for the nonuniform pressure loads. Figure 88 shows the assembly with conically sprung one-piece carbon ring seals with the simulated rotor seal plate on the left and the stationary housing which represents the seal liner of the regenerator housing. High-pressure air is introduced into the rig (see Figure 89) through the end cover; both seals are pressurized through holes in the hub and spacer between the seals. Pressure sensors and temperature probes are located in the pressure cavity in close proximity to the seals. Air leakage is measured with calibrated float-type rotometers and corrected for static pressure at the rotometer.

The first test was to establish a baseline leakage and to eliminate extraneous leakage paths at the rig flanges and at all stand connections. The segmented carbon seal of the first test is shown in Figure 90. This seal has five segments with interlocking lapped joints. Each segment has independent axial and radial springs.

The baseline calibration repeated the data of tests in the previous program (Contract NOw 62-0636-f), where leakage of 75 to 80 standard cubic feet per minute at 100 p.s.i. pressure drop was obtained, as shown in Figure 91.

The suspected cause of the extremely high leakage was coning or deflection of the seal plate and/or liner. A method was devised to compensate for this suspected deflection whereby a tapered surface was machined into the sealing surfaces of each part so that proper seal lip contact would be maintained under loading.

CONFIDENTIAL

CONFIDENTIAL

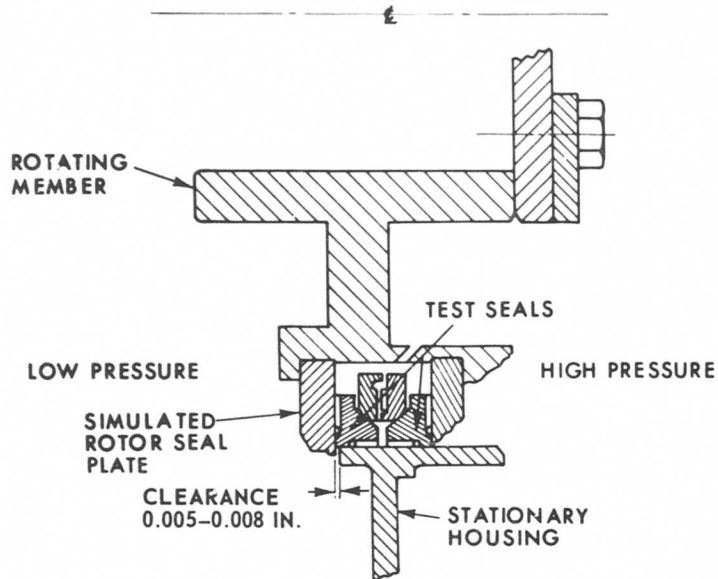


Figure 88. Torus Inner Diameter (I.D.) Ring Seal Rig Schematic.

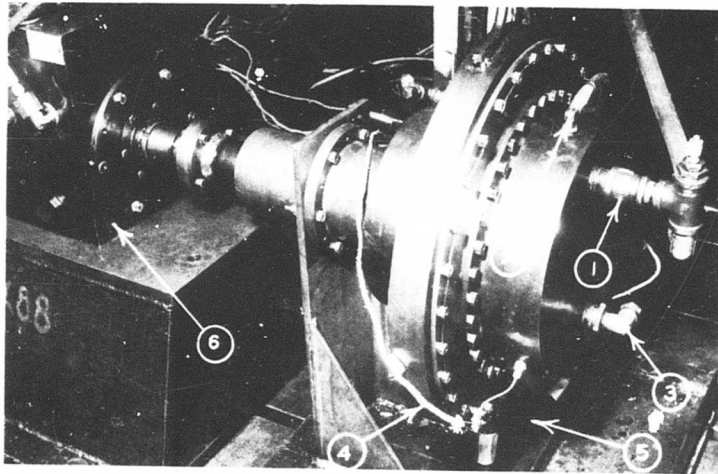


Figure 89. Regenerator I.D. Ring Seal Test Installation Showing (1) Air Supply to Seal, (2) Pressure Sensing Line, (3) Seal Bleed, (4) Air Temperature Probes, (5) Rig Oil Scavenge Line, and (6) 3.4-to-1 Gearbox.

CONFIDENTIAL

CONFIDENTIAL



Figure 90. Regenerator I. D. Ring Seal, Segmented Carbon, With Axial and Radial Spring Loading.

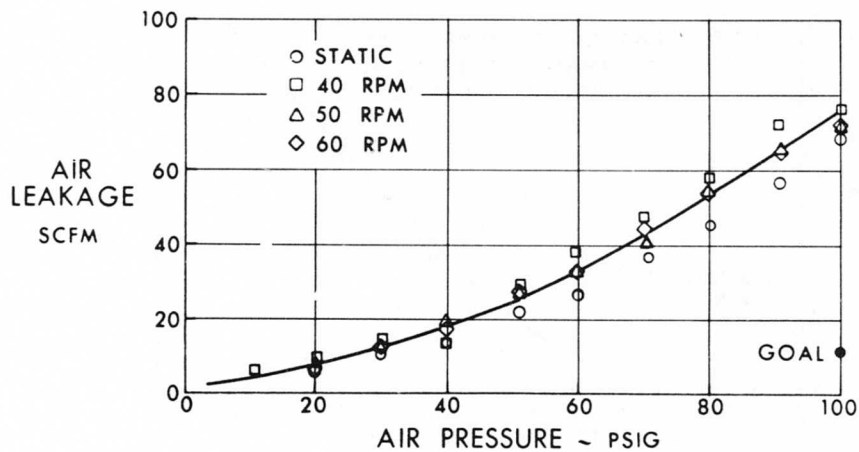


Figure 91. Regenerator I. D. Seal Leakage Calibration, Segmented Single-Ring Carbon Seal with Uncompensated Seal Plate and Liner.

CONFIDENTIAL

CONFIDENTIAL

The same segmented carbon seal when tested with tapered or the compensated seal plate and liner had a leakage of one-third the leakage goal, as shown in Figure 92.

A series of tests was conducted to determine whether the seal plate deflection or liner deflection had the major effect on leakage. These tests were run with both the segmented carbon seal and the conically sprung one-piece carbon seal. The latter seal arrangement consisted of two conically sprung one-piece split carbon ring seals in tandem. Axial and radial seating forces were applied to the seal by means of a wave spring acting through the corical surfaces of the thrust washers and inner surfaces of both ring seals. The components of this seal configuration are shown in Figure 93, and the assembly is shown in Figure 94.

The results of these tests revealed that seal plate deflection had the major effect on leakage and that the liner or regenerator housing deflection had little effect. With conically sprung seals, the leakage at 100 p.s.i. with uncompensated seal plate and compensated liner was 105 standard cubic feet per minute. The same seals with both compensated seal plate and liner had a leakage of 12 standard cubic feet per minute, as shown in Figure 95. Previous tests with the same type seal with uncompensated seal plate and liner resulted in leakages of 130 standard cubic feet per minute at 100 p.s.i. The test series with the segmented carbon seals had the same comparative results (Figure 96). Table VIII summarizes the test series.

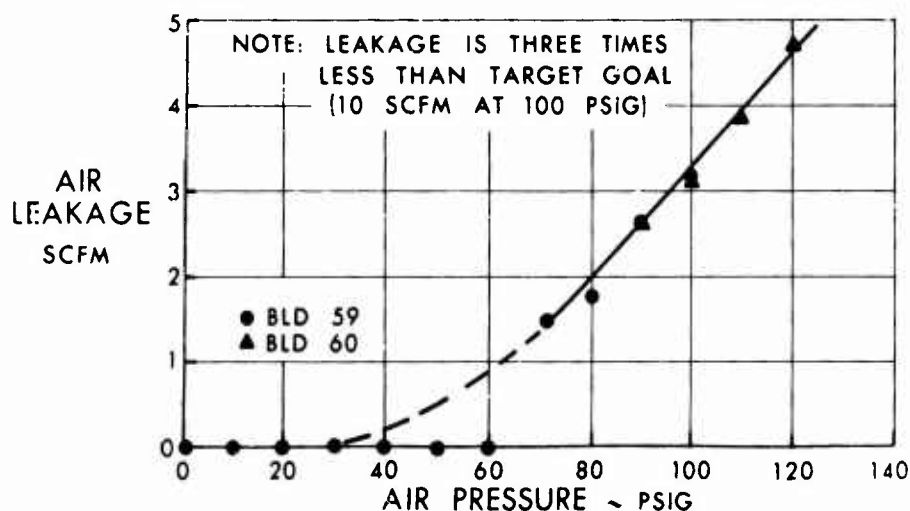


Figure 92. Regenerator I.D. Seal Leakage Calibration, Single-Ring Segmented Carbon Seal With Compensated Plate and Liner (Ambient Air Temperature).

CONFIDENTIAL

CONFIDENTIAL

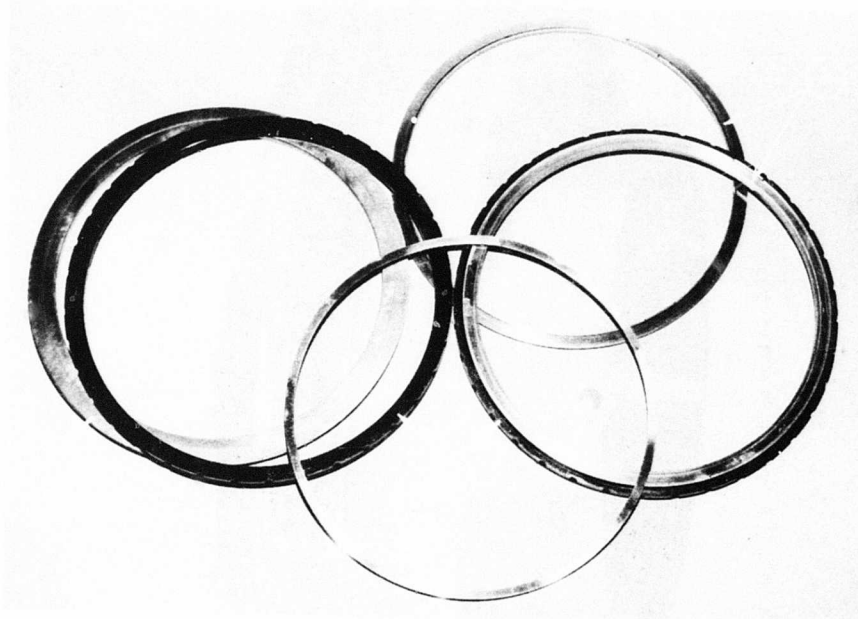


Figure 93. Regenerator I.D. Seal, Split One-Piece Conically Sprung Ring Seals Disassembled, Showing (1) Untapered Seal Plate, (2) Conical Carbons, (3) Wavy Spring Washer, and (4) Thrust Plates.

To investigate the effect of liner deflection further, the segmented carbon seal with two different tapers machined into the outer diameter surfaces of the seal was tested with the same compensated seal plate and uncompensated liner. As seen in Figures 97 through 100, there was no significant change in leakage with a change in outer diameter taper.

Incorporation of tapered surfaces is not the ideal method of compensating for seal plate deflection, since at only one pressure load are the mating surfaces of the seal and seal plate in full contact. This partial contact of the seal lip would result in high wear and an ultimate increase in seal leakage. In addition, maintaining manufacturing controls and lapped polished surfaces is difficult with the tapered surfaces. A practical approach to minimize seal plate deflection is to use seal plates which have acceptably low distortion.

CONFIDENTIAL

CONFIDENTIAL

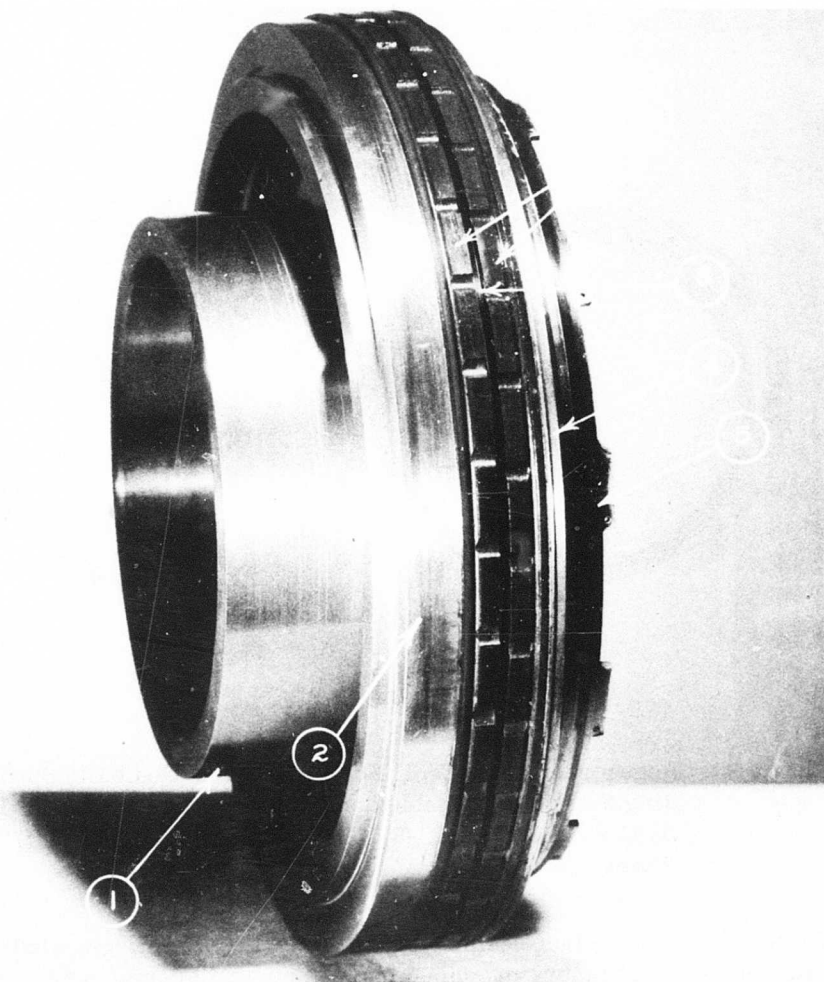


Figure 94. Regenerator I.D. Seal, Split One-Piece Conically Sprung Ring Seals Assembled, Showing (1) Hub, (2) Tapered Seal Plate, (3) Conical Carbons, (4) Untapered Seal Plate, (5) Locking Nut, and (6) Wavy Spring Washer.

CONFIDENTIAL

CONFIDENTIAL

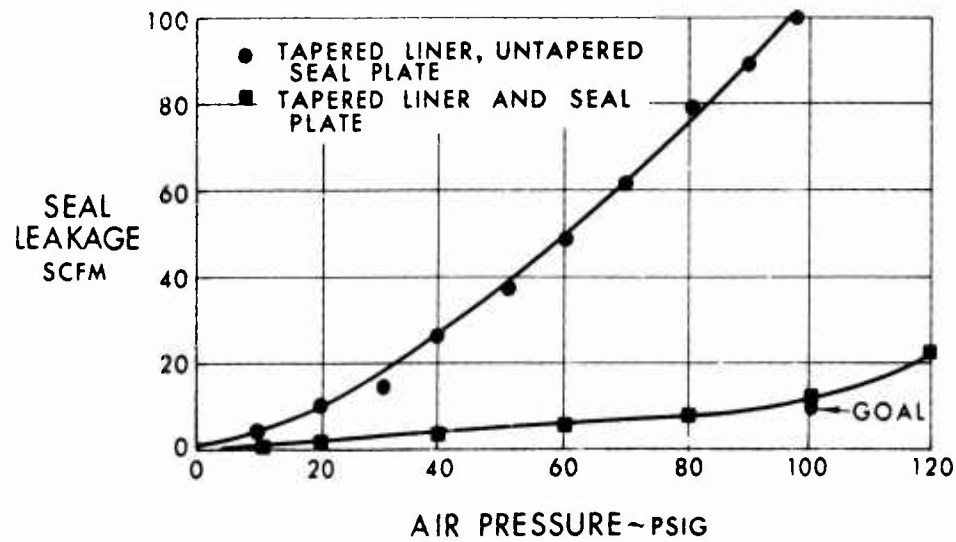


Figure 95. Regenerator I.D. Seal Leakage Calibration, Split One-Piece Conically Sprung Ring Seals (Ambient Air Temperature).

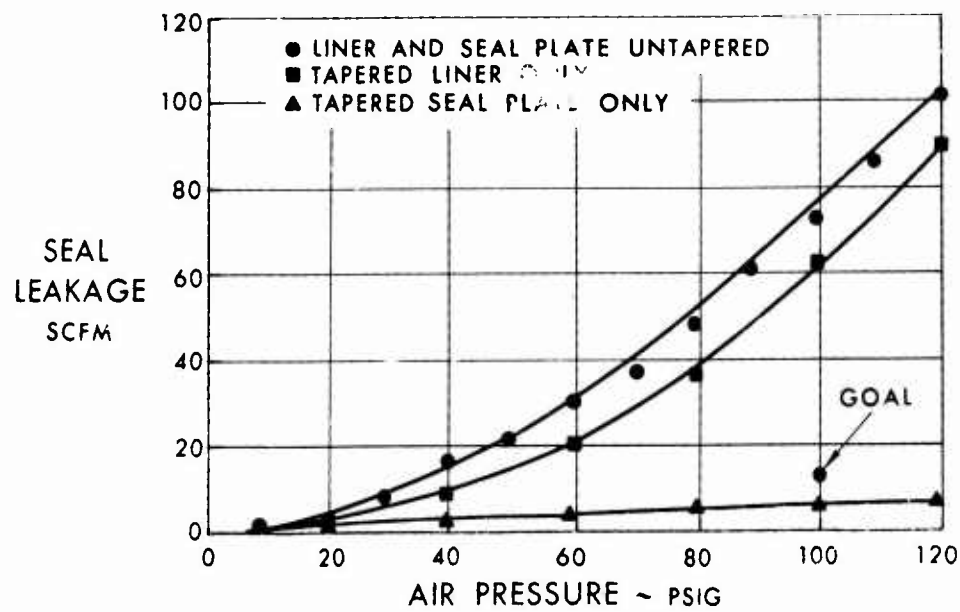


Figure 96. Regenerator I.D. Seal Leakage Calibration, Single-Ring Segmented Carbon Seal (Ambient Air Temperature).

CONFIDENTIAL

CONFIDENTIAL

TABLE VIII

COMPARISON OF INNER DIAMETER SEAL TEST RESULTS

Configuration	Liner	Plate	Leakage at 100 p. s. i. (SCFM)
Segmented Package Seal	Coned	Coned	75.0
Segmented Package Seal	Compensated	Coned	63.0
Segmented Package Seal	Coned	Compensated	5.0
Segmented Package Seal	Compensated	Compensated	3.0
Conically Sprung One- Piece Ring Seal	Coned	Coned	130.0
Conically Sprung One- Piece Ring Seal	Compensated	Coned	105.0
Conically Sprung One- Piece Ring Seal	Compensated	Compensated	12.0

The conically sprung carbon ring seals and seal plates of three thicknesses were tested to determine the required seal plate thickness to minimize this deflection. As shown in Figure 101, the 0.750-inch-thick seal plate had the lowest leakage. Also, there was very little increase in effective leakage area with pressure drop, as shown in Figure 102. It is also noted from this figure that there was a consistent leak path in all three tests which caused higher leakage rates than in previous tests. To maintain a direct comparison of the effect of seal plate thickness on leakage, this constant rig leak was not repaired.

The 0.750-inch-thick seal plate was lightened by removing material from the area of the least bending moment at the seal plate outer diameter. A radius was cut on the reverse side of the plate to maintain the 0.750-inch thickness at the inner diameter and a 0.500-inch thickness at the outer diameter (Figure 103). This seal plate was tested with the conically sprung one-piece carbon ring seal with a 15- and a 28-pound spring force. As seen in Figure 104, the seal performance was in close agreement with the tapered or compensated seal plate test in Figure 95, which had the same seal arrangement and spring load.

CONFIDENTIAL

CONFIDENTIAL

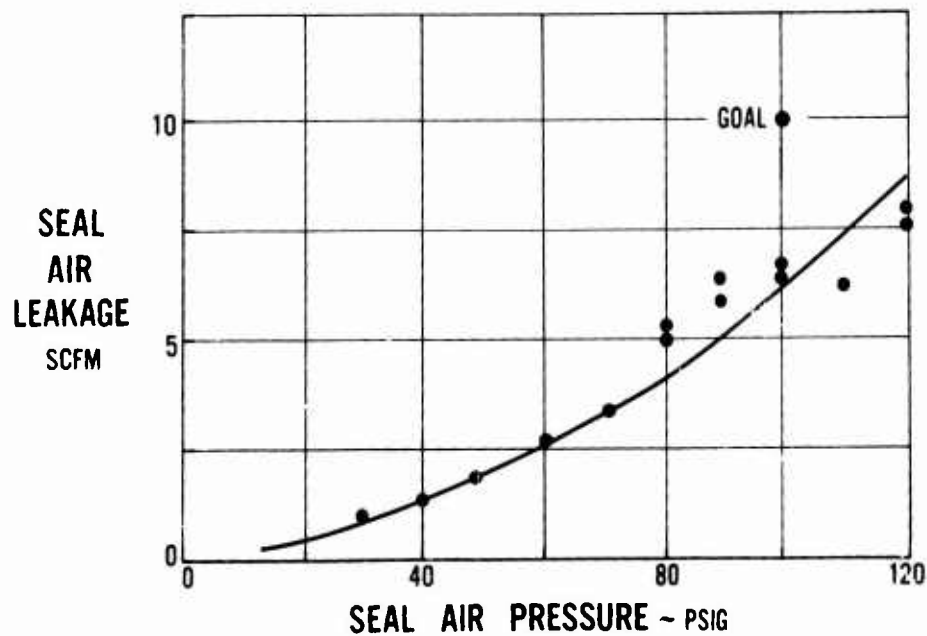


Figure 97. Regenerator I.D. Seal Leakage Calibration, Single-Ring Segmented Carbon With Outer Diameter (O.D.) Seal Taper No. 1 and Compensated Plate and Uncompensated Liner; 500°F. Air Temperature.

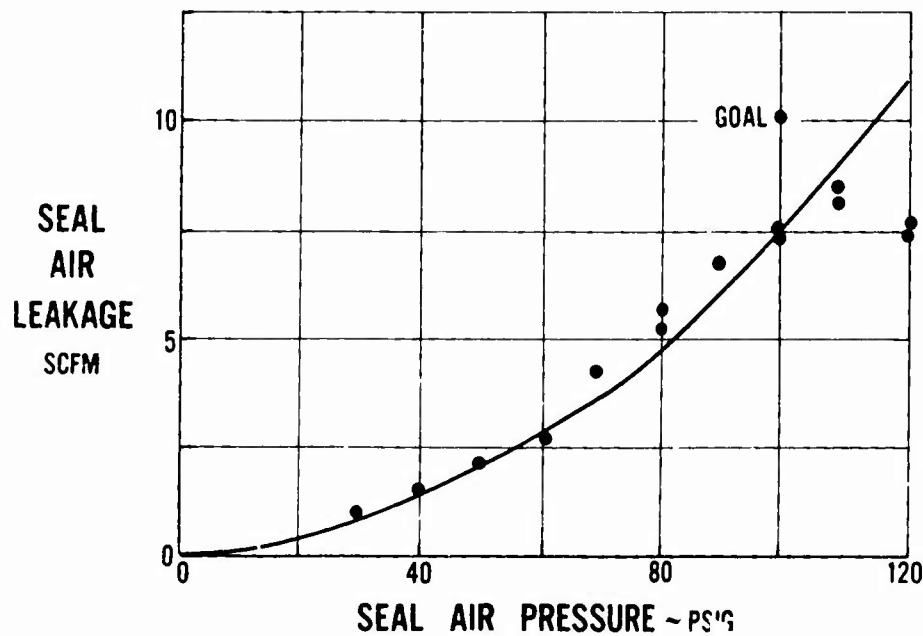


Figure 98. Regenerator I.D. Seal Leakage Calibration, Single-Ring Segmented Carbon With O.D. Seal Taper No. 1 and Compensated Plate and Uncompensated Liner; Ambient Air Temperature.

CONFIDENTIAL

CONFIDENTIAL

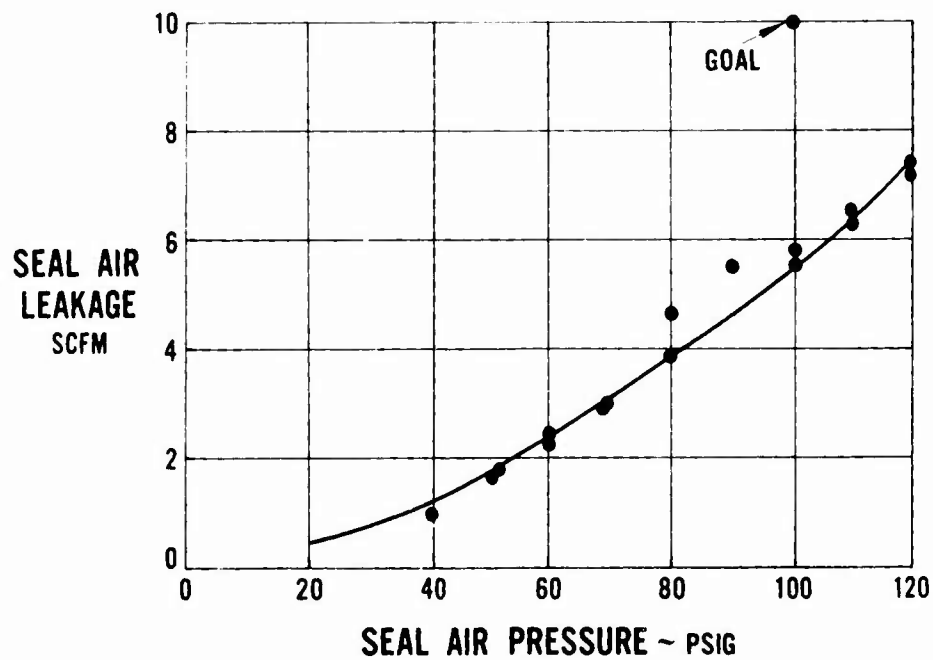


Figure 99. Regenerator I.D. Seal Leakage Calibration, Single-Ring Segmented Carbon With O.D. Seal Taper No. 2 and Compensated Plate and Uncompensated Liner; 500°F. Air Temperature.

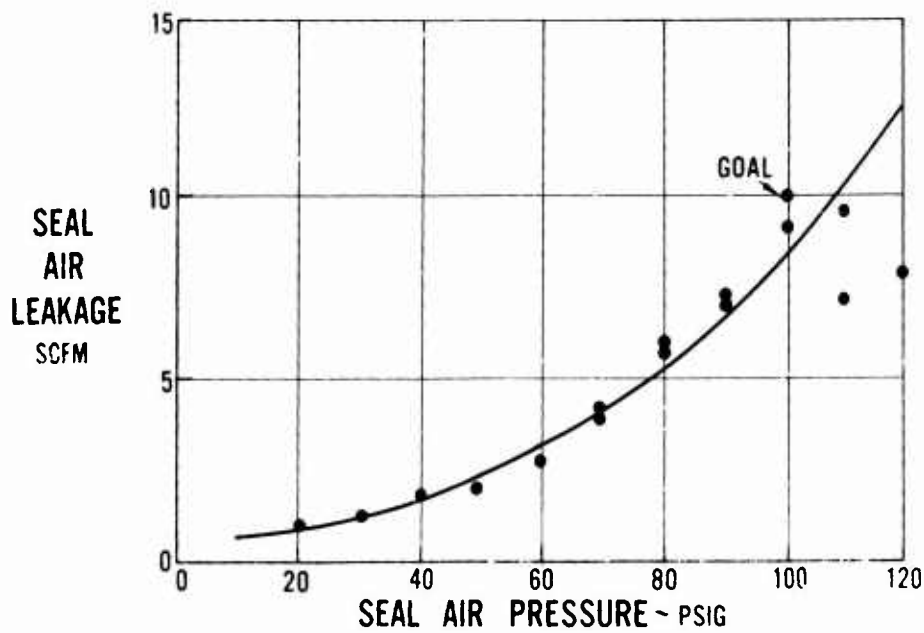


Figure 100. Regenerator I.D. Seal Leakage Calibration, Single-Ring Segmented Carbon With O.D. Seal Taper No. 2 and Compensated Plate and Uncompensated Liner; Ambient Air Temperature.

CONFIDENTIAL

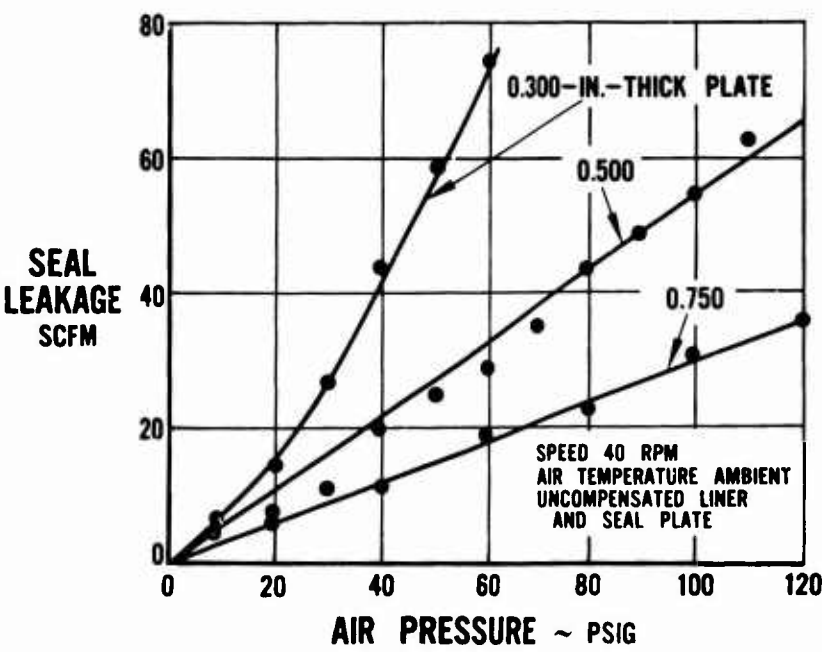


Figure 101. Regenerator I.D. Seal Leakage Calibration, Split One-Piece Conically Sprung Ring Seals With Three Levels of Seal Plate Thickness.

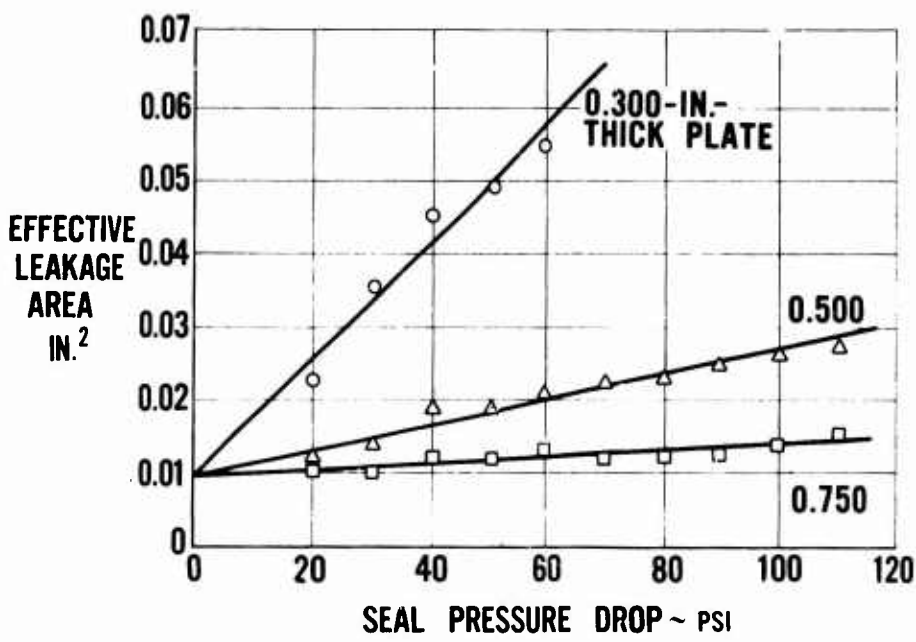


Figure 102. Leakage Area Vs. Seal Pressure Drop.

CONFIDENTIAL



Figure 103. Regenerator I.D. Seal Plate Showing Weight Reduction Scheme.

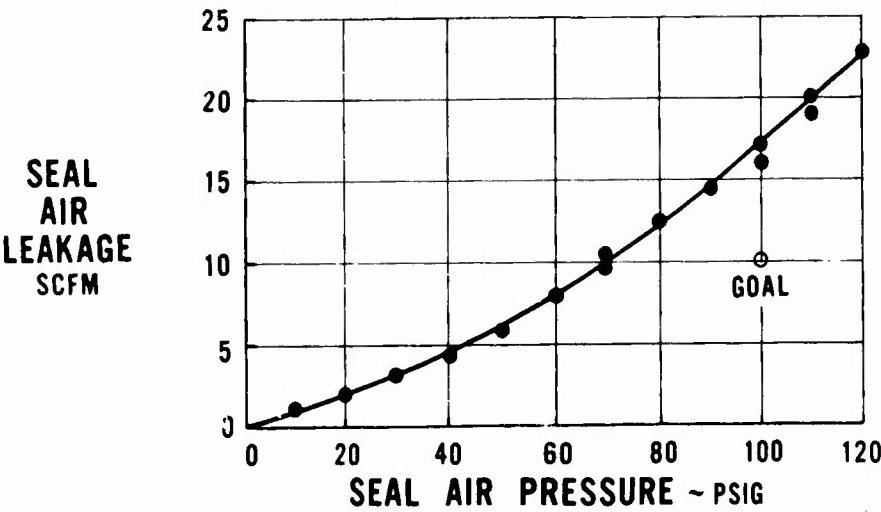


Figure 104. Regenerator I.D. Seal Leakage Calibration, Conically Sprung One-Piece Carbon Ring Seal, Ambient Air Temperature, 15-Pound Spring Load (Seal Plate 0.75 Inch Thick at Inner Diameter, 0.5 Inch Thick at Outer Diameter).

CONFIDENTIAL

The leakage rate was below the goal at seal operating temperature in the regenerator (see Figure 105). An increase to a 28-pound spring force resulted in leakage of less than the 10-SCFM goal for both ambient and operating temperature, as seen in Figures 106 and 107.

In addition to the segmented carbon ring seal and the conically sprung one-piece carbon ring seal arrangement, both of which met the design goal, a segmented double carbon ring seal in tandem (Figures 108 and 109) was tested. This seal could potentially reduce total regenerator leakage by 30 percent, since both rings are seals and since pressurization of an auxiliary face seal is not required. The ambient air temperature seal leakage test was conducted with an uncompensated seal plate and liner. The test results shown in Figure 110 revealed the leakage to be twice the goal. At operating temperature (Figure 111) the leakage was slightly above the goal. The same seal was then tested with the compensated seal plate and was slightly above the leakage goal at ambient (Figure 112) and one-half the 10-SCFM goal at normal operating temperature (Figure 113). At the conclusion of the tests with carbon seals there were three configurations that would meet or excel the design leakage goal for the high-effectiveness toroidal regenerator.

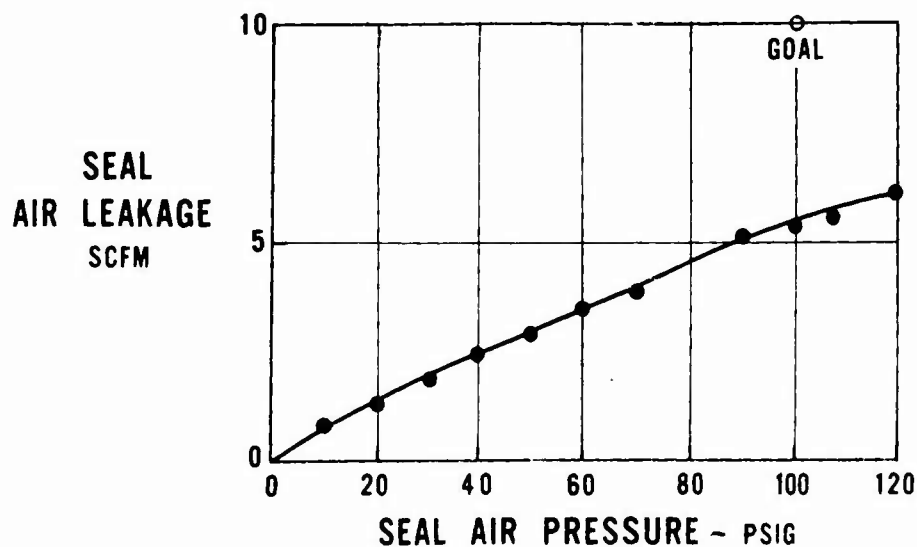


Figure 105. Regenerator I.D. Seal Leakage Calibration, Conically Sprung One-Piece Carbon Ring Seal, 500°F. Air Temperature, 15-Pound Spring Load (Seal Plate 0.75 Inch Thick at Inner Diameter, 0.5 Inch Thick at Outer Diameter).

CONFIDENTIAL

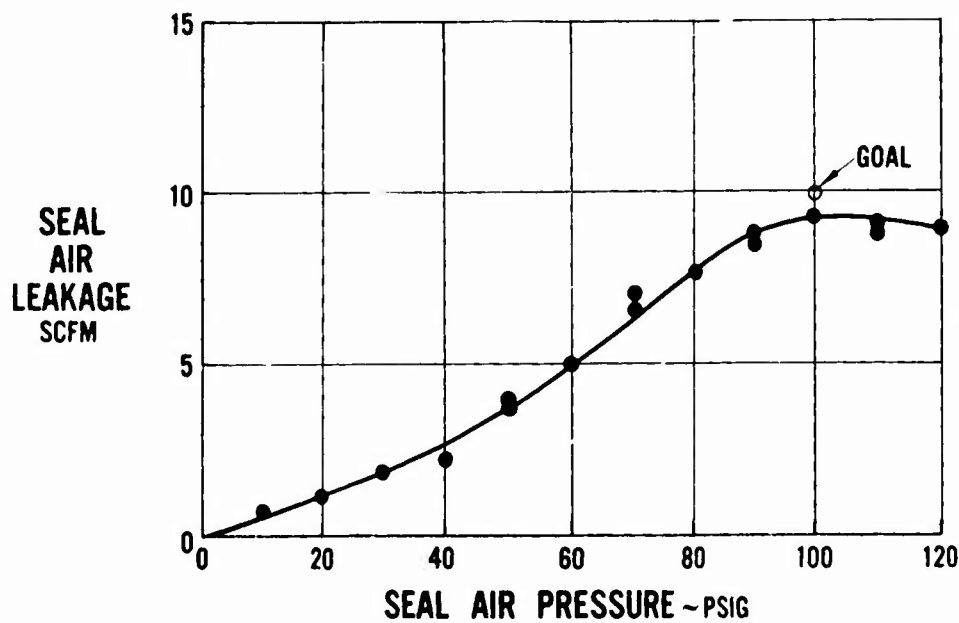


Figure 106. Regenerator I.D. Seal Leakage Calibration, Conically Sprung One-Piece Carbon Seal Ring, Ambient Air Temperature, 28-Pound Spring Load (Seal Plate 0.75 Inch Thick at Inner Diameter, 0.5 Inch Thick at Outer Diameter).

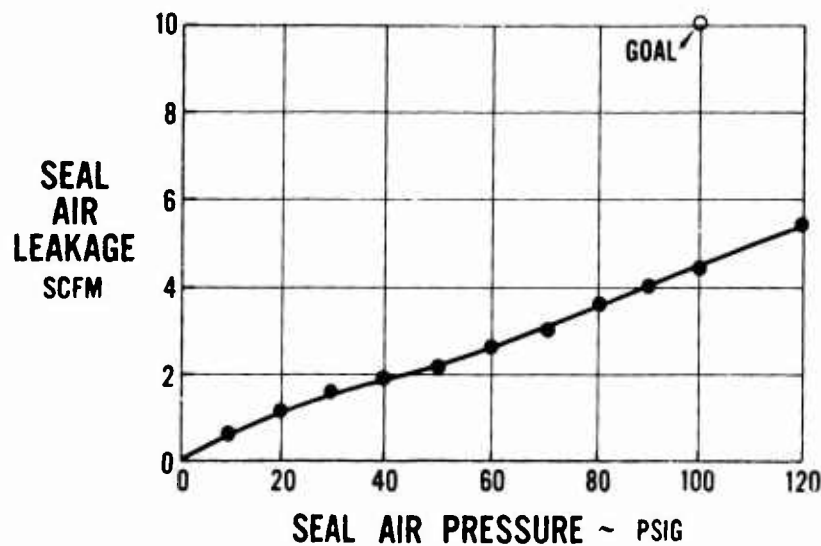


Figure 107. Regenerator I.D. Seal Leakage Calibration, Conically Sprung One-Piece Carbon Ring Seal, 500°F. Air Temperature, 28-Pound Spring Load (Seal Plate 0.75 Inch Thick at Inner Diameter, 0.5 Inch Thick at Outer Diameter).

CONFIDENTIAL

CONFIDENTIAL

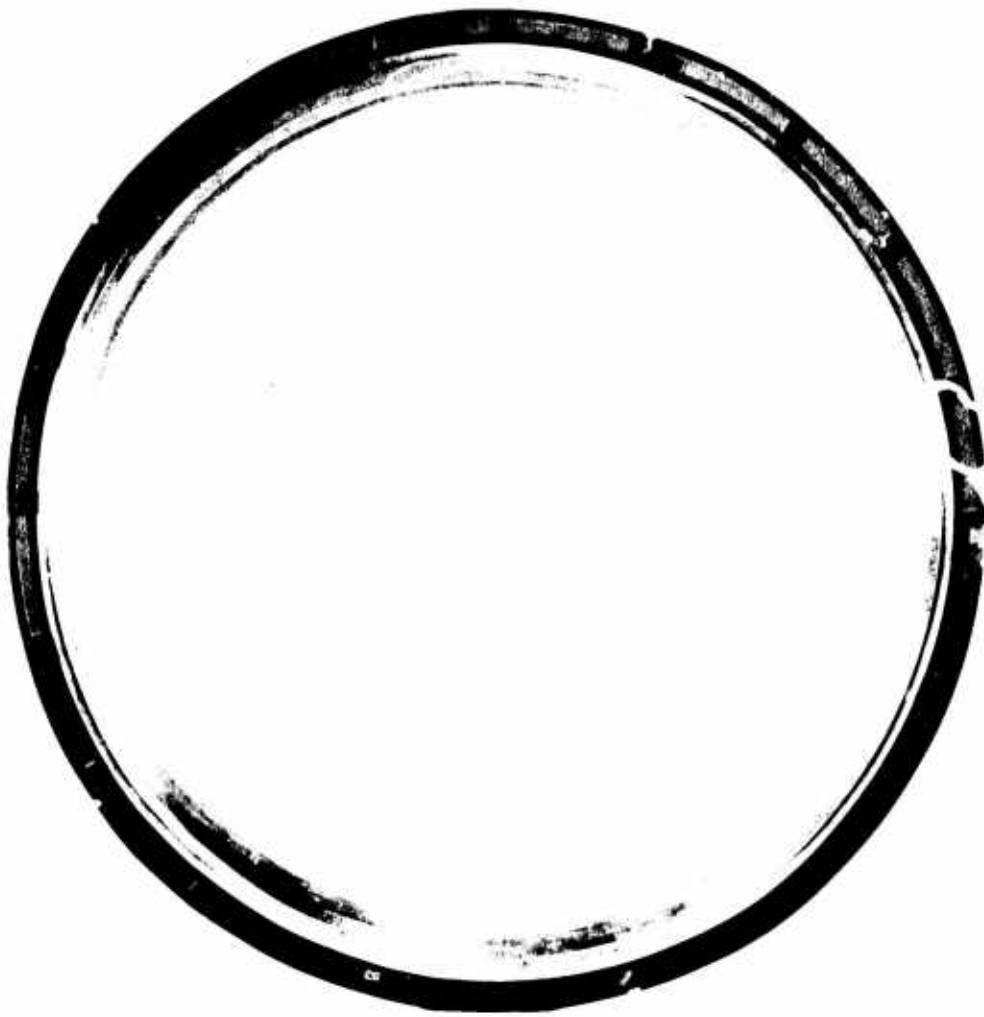


Figure 108. Axial View of Regenerator I.D. Ring Seal, Back-to-Back Segmented Carbon Seal.

CONFIDENTIAL

CONFIDENTIAL

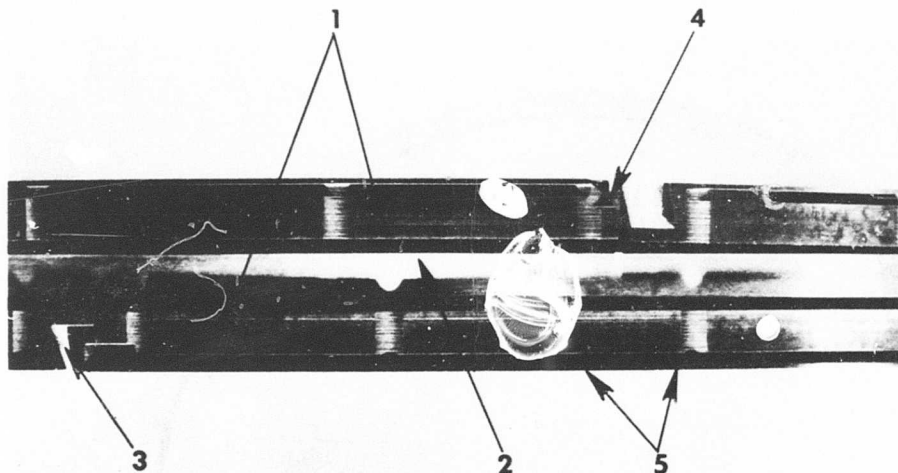


Figure 109. Edge View of Regenerator I.D. Ring Seal, Back-to-Back Segmented Carbon Seal, Showing (1) Carbon Segments, (2) Thrust Plates, (3) Step Joint, (4) Damaged Step Joint, and (5) Sealing Lips, Axial and Radial.

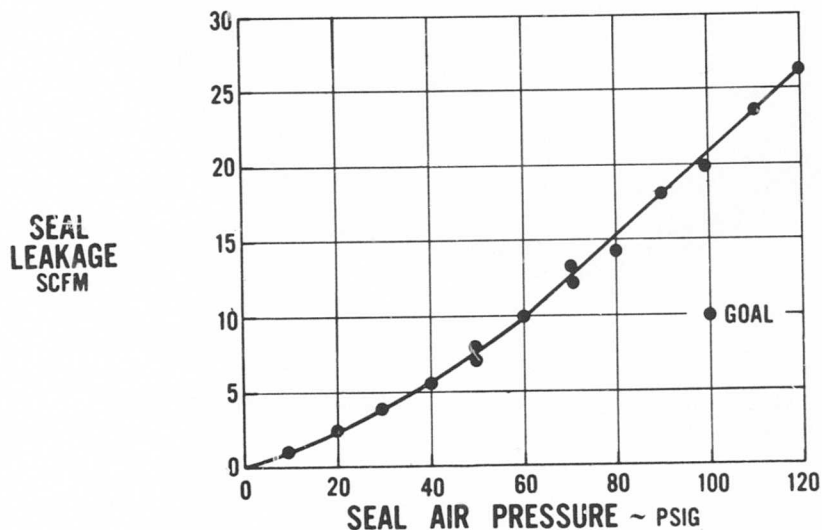


Figure 110. Regenerator I.D. Seal Leakage Calibration, Back-to-Back Segmented Carbon Seal With Uncompensated Seal Plate and Liner; Ambient Air Temperature.

CONFIDENTIAL

CONFIDENTIAL

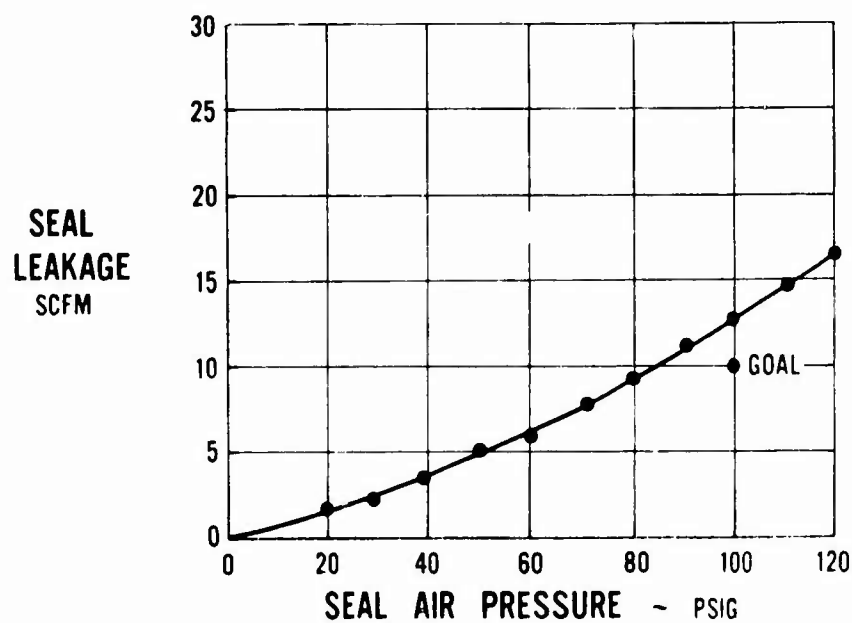


Figure 111. Regenerator I.D. Seal Leakage Calibration, Back-to-Back Segmented Carbon Seal With Uncompensated Seal Plate and Liner; 500°F. Air Temperature.

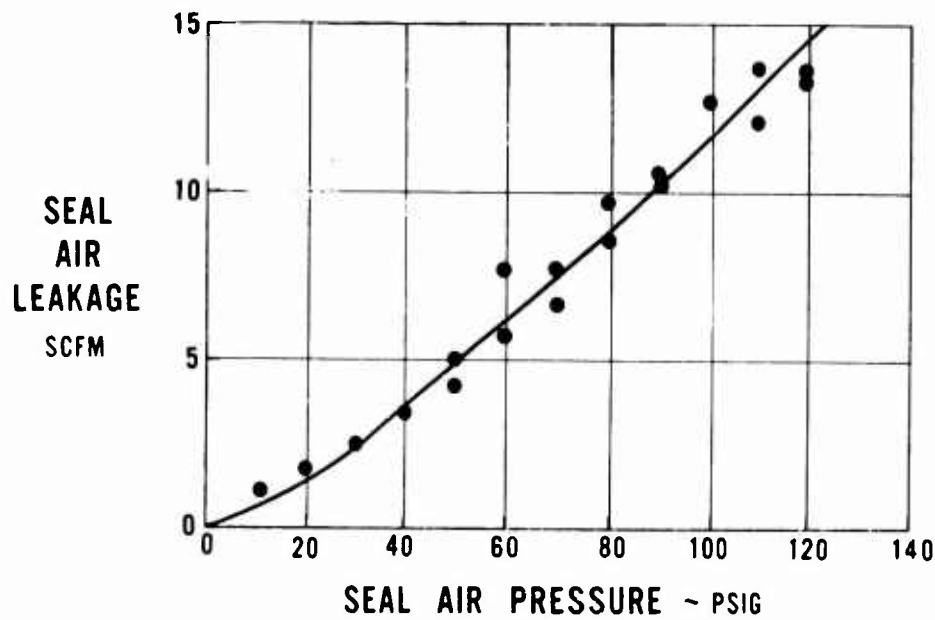


Figure 112. Regenerator I.D. Seal Leakage Calibration, Back-to-Back Segmented Carbon Seal With Compensated Seal Plate and Uncompensated Liner; Ambient Air Temperature.

CONFIDENTIAL

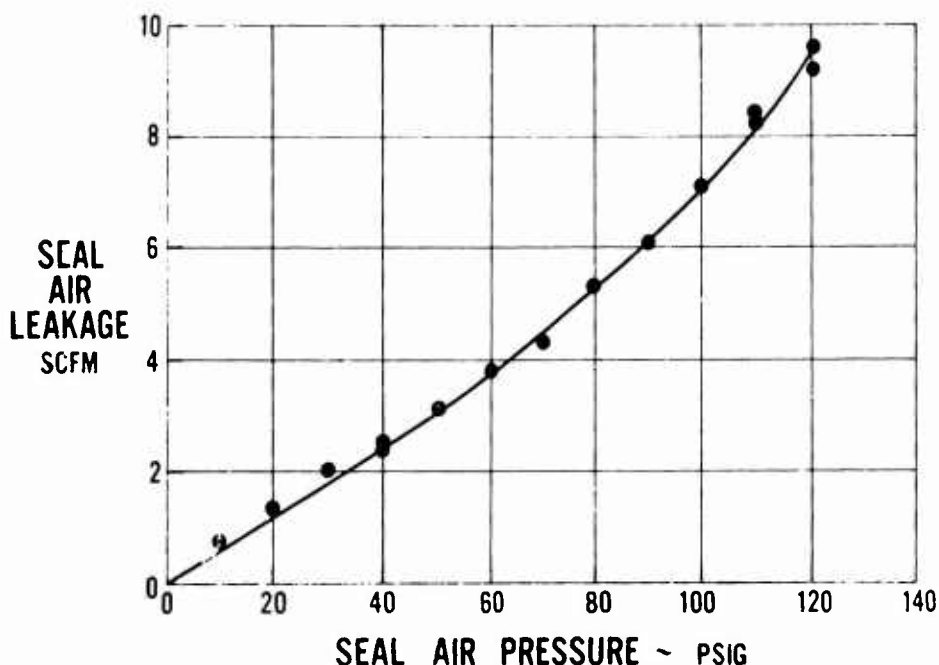


Figure 113. Regenerator I.D. Seal Leakage Calibration, Back-to-Back Segmented Carbon Seal With Compensated Seal Plate and Uncompensated Liner; 500°F. Air Temperature.

An overload endurance test was conducted on the segmented carbon seal and compensated seal plates with 500°F. air at 100 p.s.i. pressure and 60 r.p.m. speed for a period of 107 hours. Seal leakage was less than the design goal for about 90 hours (Figure 114). Then it increased slowly to slightly above the goal. Examination of the carbon after test indicated very little erosion or wear. However, two deep scratches were observed in the sealing lip of the carbon. These were probably caused by dirt particles in the air supply. The severity of this test far exceeded normal regenerator operation, thus fully qualifying this type inner diameter ring seal and material combination in the regenerator design.

All-Metal Seal Tests

Concurrent with the carbon seal development program, an all-metal seal program was undertaken. The all-metal seal is attractive for several reasons. It potentially has high durability, low leakage, and low wear characteristics. The use of metal-to-metal seal contacts was demonstrated in the previous regenerator program with the torus bulkhead piston ring seals. In addition, all-metal seals can be made in very large sizes, whereas for some carbon grades size is limited by the molding press capacity to form the seal. Large-diameter carbon seals of certain materials can be made economically only by forming segments.

CONFIDENTIAL

CONFIDENTIAL

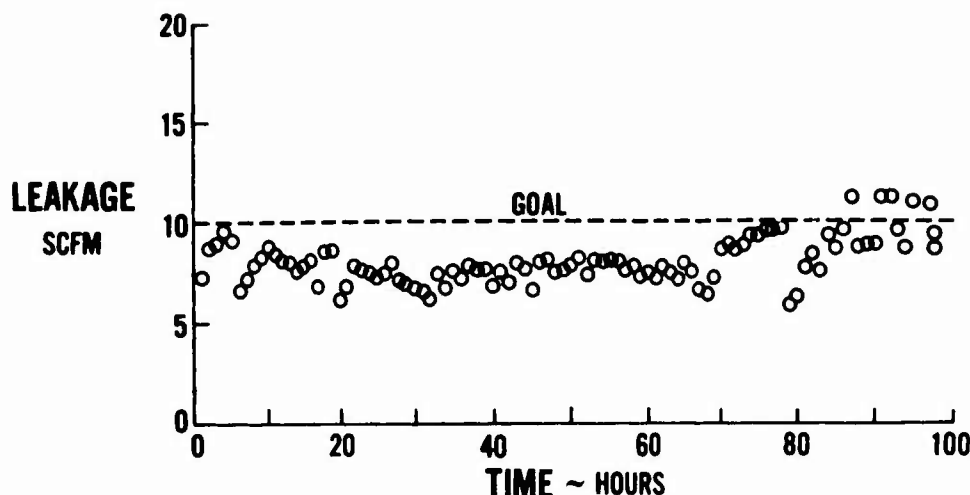


Figure 114. Regenerator I.D. Seal Leakage Vs. Endurance Time, Segmented Single-Ring Carbon Seal With Compensated Seal Plate and Uncompensated Liner.

As seen in Figure 115, the interlocking joint of the segmented seal is fragile and requires extreme care during regenerator assembly to prevent breakage.

Two basic configurations of an all-metal seal design were tested in Phase I. These were the simplex type and the wave spring design. The simplex seal configuration is shown in Figures 116 and 117. This seal resembled a wide piston ring seal with sealing surfaces on each end at the outer diameter. An axial spring force was built into the seal by removing material from the cylindrical section to produce a series of beams which when deflected under load produce a restoring seating force. The radial force was built into this seal similar to a piston ring by making an oversize split ring which was then compressed and ground to the gage sealing diameter. The effect of this split on the axial spring force was not predictable and had to be evaluated by test.

The second basic all-metal seal configuration tested was also similar to a two-stage piston-ring-type seal. This seal is shown in Figures 118 and 119. The assembly consisted of two wide split piston rings located back-to-back with the sealing lip on each end of the outer diameter. The axial sealing force was initially supplied by a continuous wave washer but was later modified by splitting the wave washer. The radial force was machined into each ring in the same manner as the simplex seal.

CONFIDENTIAL

CONFIDENTIAL

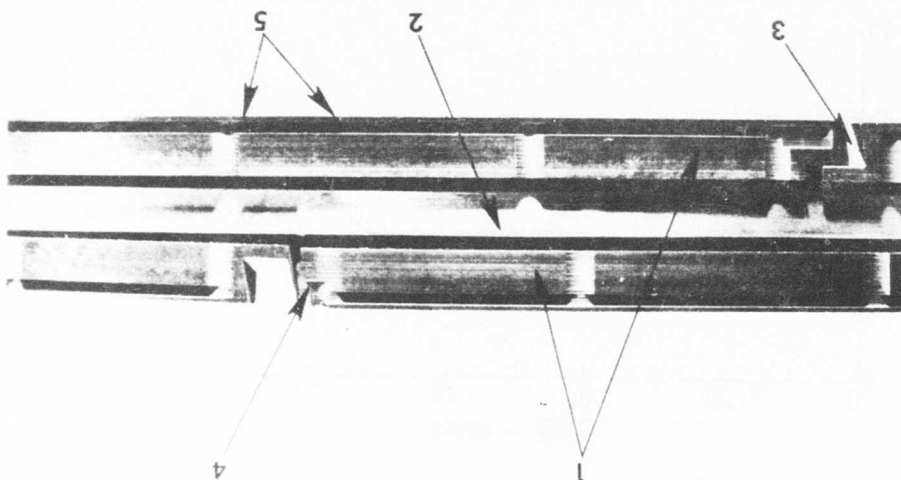


Figure 115. Edge View of Regenerator I.D. Ring Seal, Back-to-Back Segmented Carbon Seal, Showing (1) Carbon Segments, (2) Thrust Plates, (3) Step Joint, (4) Damaged Step Joint, and (5) Sealing Lips, Axial and Radial.



Figure 116. Regenerator I.D. Ring Seal, All-Metal Simplex Seal.

CONFIDENTIAL

CONFIDENTIAL

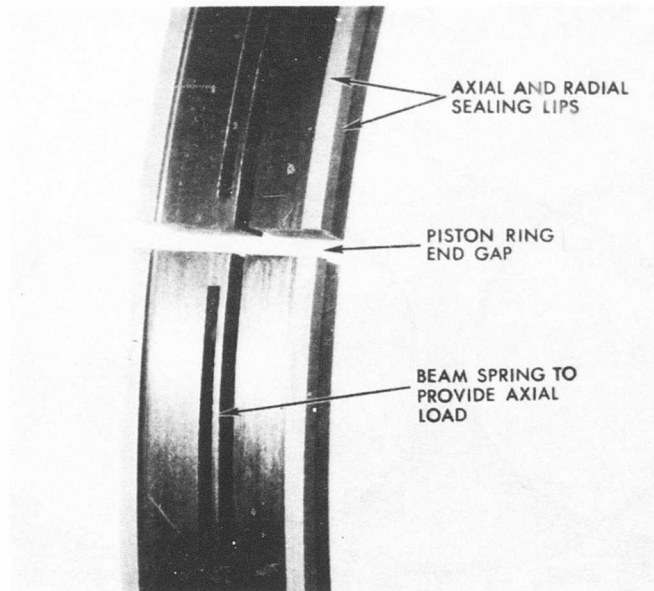


Figure 117. Regenerator I.D. Ring Seal, All-Metal Simplex Seal Showing Axial and Radial Sealing Lips, Piston Ring End Gap and Beam Spring.

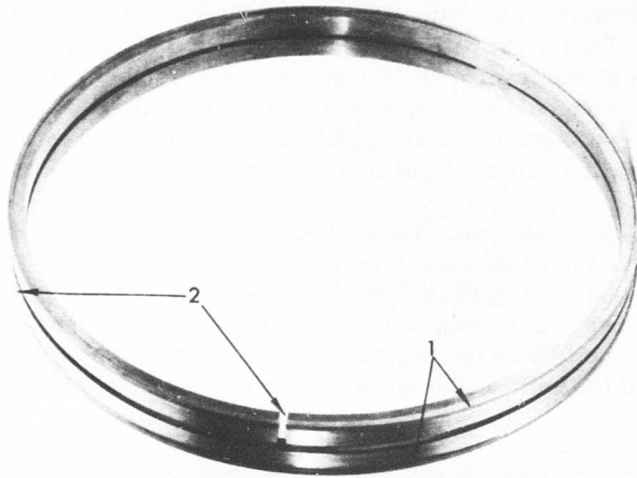


Figure 118. Regenerator I.D. Ring Seal, All-Metal Split Ring Seal Showing (1) Sealing Lips and (2) Staggered Joints.

CONFIDENTIAL

CONFIDENTIAL

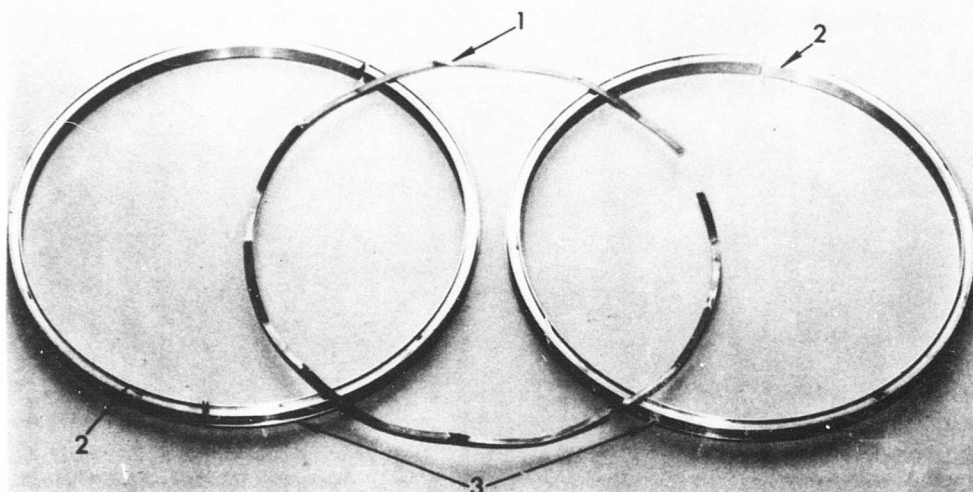


Figure 119. Regenerator I.D. Ring Seal, All-Metal Split Ring Seal Showing (1) Wave Washer Spring, (2) Groove for Wave Washer, and (3) Sealing Lip.

The third all-metal seal configuration was a modification to the basic all-metal wave spring seal. This modification added an internal radial wave spring contained in a channel on the inner diameter of the seal assembly. The radial sealing force could then be varied by replacing the internal radial wave spring. This allowed testing of several combinations of axial and radial forces by simply replacing wave springs. This seal is shown in Figure 120.

The first all-metal seal test was conducted with the simple back-to-back piston-ring-type seal with a continuous axial wave spring. The results of this test (Figure 121) show that once the high radial stiffness was overcome by pressure load, the seal did meet the leakage goal. The high radial stiffness of this particular design was due to both the continuous wave washer, which restricted the radial movement of the split piston rings, and to the thick radial section of the piston rings.

The same type seal, but with reduced radial web thickness seal rings to increase radial flexibility, was calibrated; leakage was not appreciably affected, as shown in Figures 122 and 123 at two different spring loadings. High-pressure loads were still required to overcome the radial stiffness.

CONFIDENTIAL

CONFIDENTIAL

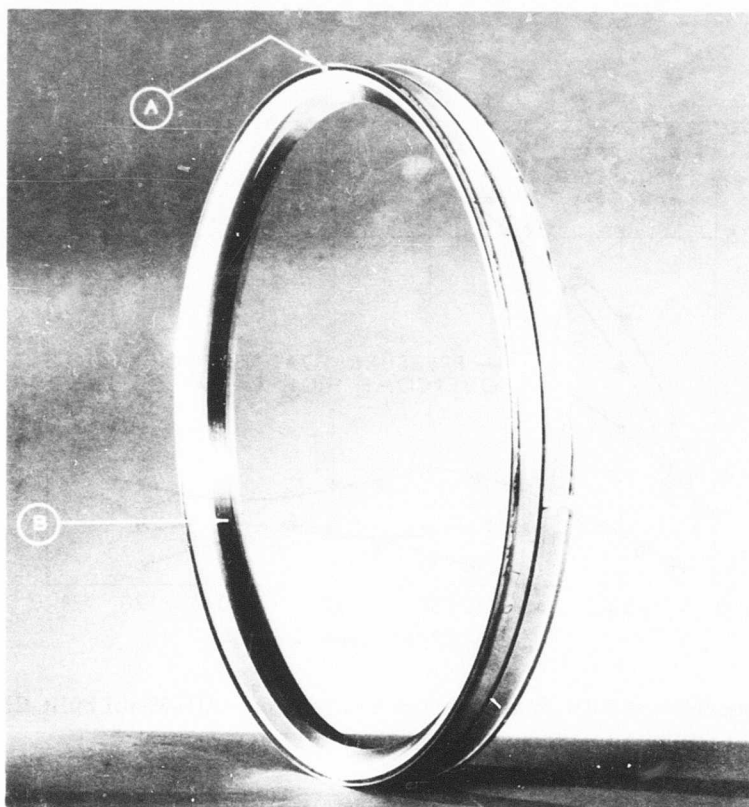


Figure 120. Regenerator I.D. Ring Seal, All-Metal Split Ring Seal With Radial Springing Showing Staggered Gaps at A and C Retaining Ring B.

This seal was further modified by splitting the wave spring seal, as shown in Figure 119, to increase radial flexibility. An antirotation pin was installed tight in one ring and loose in the opposite seal ring to allow for radial movement but to prevent relative rotation. The split wave spring was prevented from turning by the same pin. This was required to prevent wave washer or reverse-side seal wear. The leakage curve of this test had the characteristic shape of a flexible seal (see Figure 124), although the leakage was above the goal. Although the seal leakage was excessive at the design point, leakage could be reduced by further increasing the radial load.

Five simplex-type all-metal seals were tested. The radial loads were varied from 1.0 to 3.5 pounds and the axial loads from 5.5 to 12.5 pounds. All seals were calibrated with ambient air, compensated seal plates, and an

CONFIDENTIAL

CONFIDENTIAL

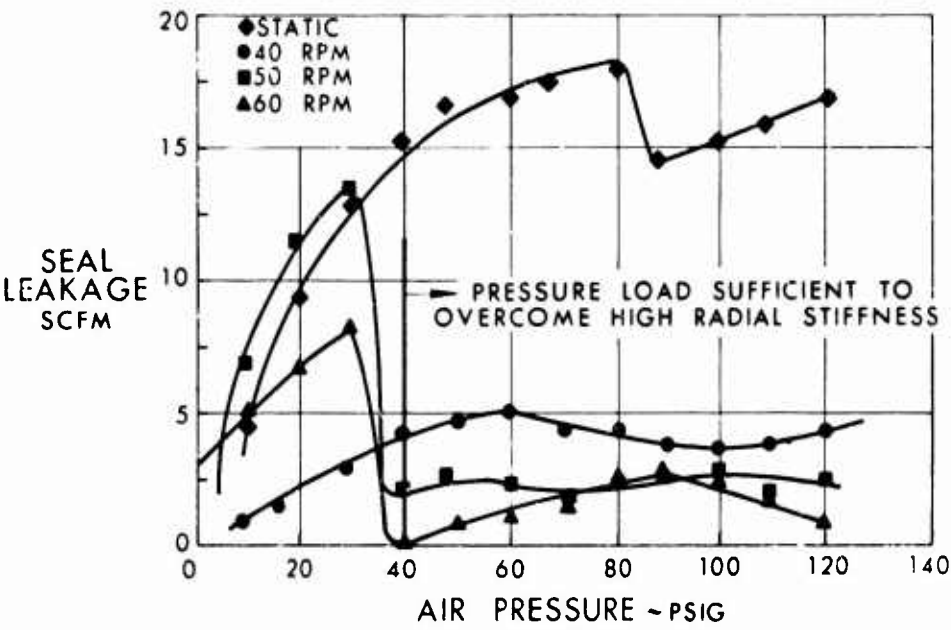


Figure 121. Regenerator I.D. Seal Leakage Calibration, All-Metal Split Ring Seal (Ambient Air Temperature).

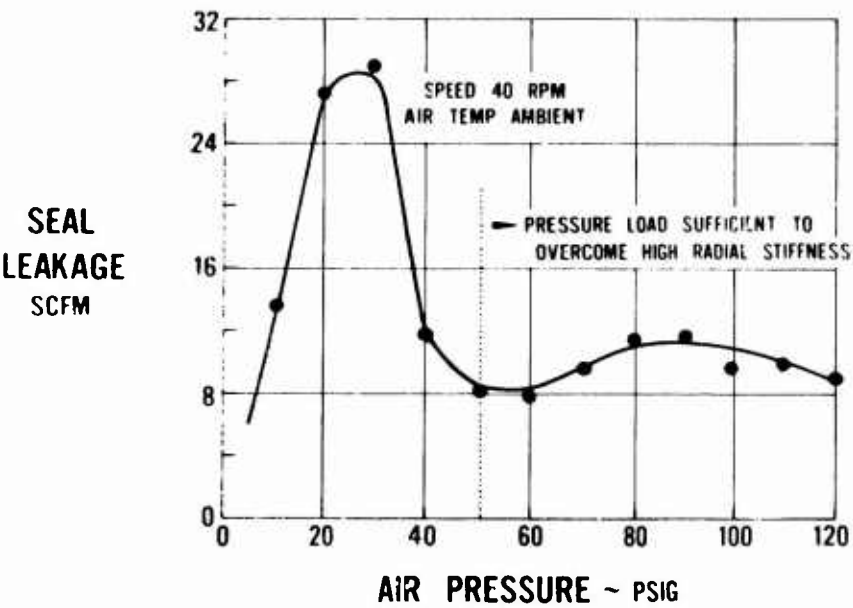


Figure 122. Regenerator I.D. Seal Leakage Calibration, All-Metal Split Ring Seal With Reduced Web Thickness and Uncompensated Seal Plate and Liner (Ambient Air Temperature).

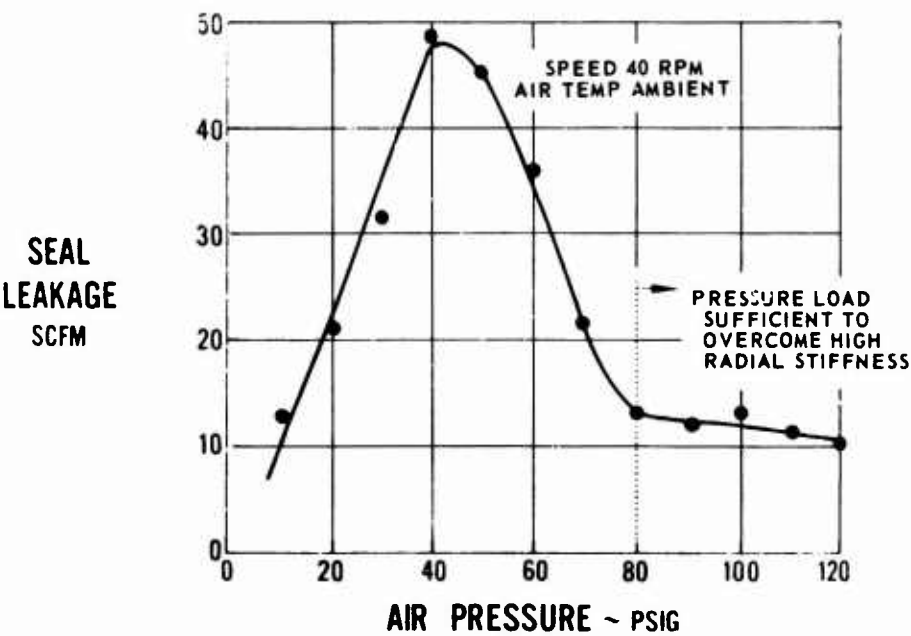


Figure 123. Regenerator I.D. Seal Leakage Calibration, All-Metal Split Ring Seal With Reduced Web Thickness and Uncompensated Seal Plate and Liner (Ambient Air Temperature).

uncompensated liner. A typical leakage calibration is shown in Figure 125; it has the characteristic shape of a flexible seal and is very similar to that of the last wave spring seal tested (Figure 124). The leakage of this seal could also be brought within the design goal with the correct combination of axial and radial loads.

The axial and radial wave spring metal seal shown in Figure 120 was used to determine the combination of axial and radial spring force required to meet the design leakage goal. The results of tests on six combinations of spring forces are shown in Table IX.

CONFIDENTIAL

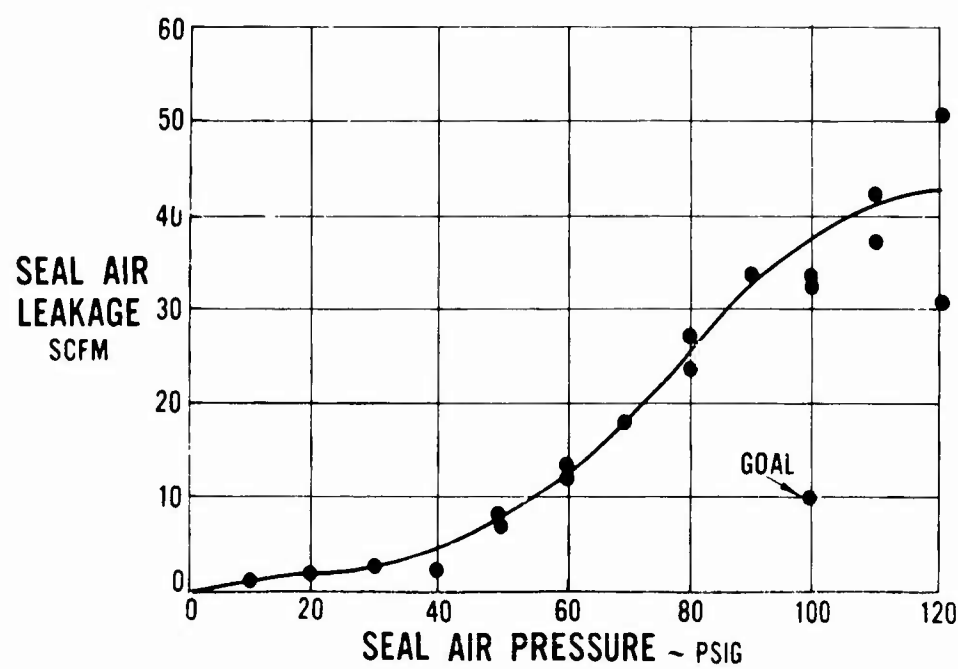


Figure 124. Regenerator I.D. Seal Leakage Calibration, All-Metal Split Ring Wave Spring Seal With Compensated Seal Plate and Uncompensated Liner.

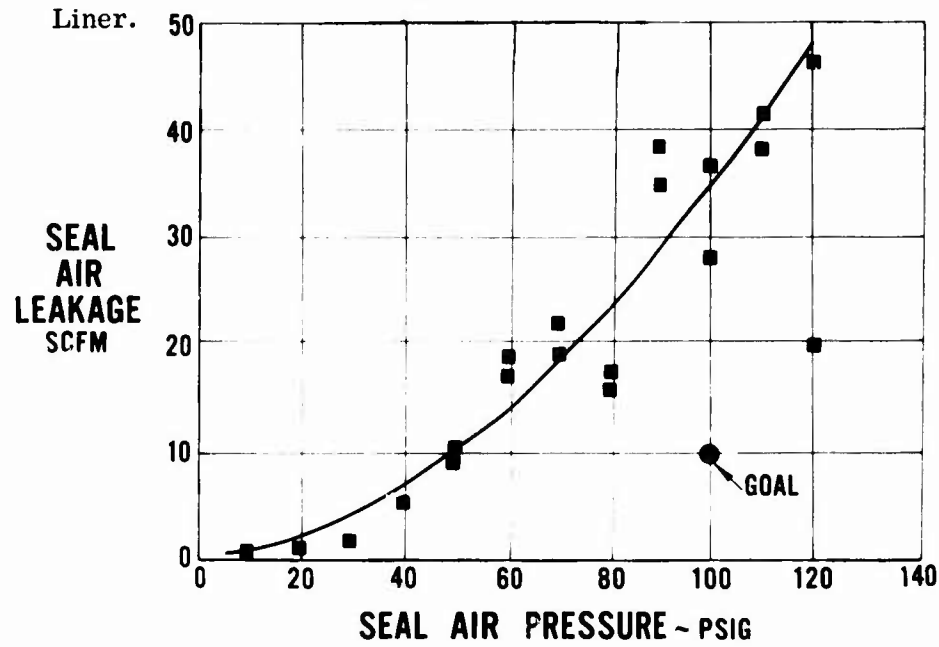


Figure 125. Regenerator I.D. Seal Leakage Calibration, All-Metal Simplex Seal With Compensated Seal Plate and Uncompensated Liner.

CONFIDENTIAL

CONFIDENTIAL

TABLE IX
ALL-METAL SEAL SPRING LOAD TESTS

Axial Load (lb)	Radial Load (lb.)	Leakage at 100 PSIG SCFM
15	20	10
10	10	12
15	6	6
20	8	5
25	10	6
30	12	12

CONCLUSIONS

As a result of 38 inner diameter seal tests in a seal rig and 6 tests in a toroidal rotary regenerator, the following conclusions have been reached.

1. Seal plate coning was the cause of excessive leakage (over 100 standard cubic feet per minute at 100 p.s.i.) in seals tested prior to this program.
2. Adequate seal plate thickness can prevent seal plate coning.
3. Three carbon seal designs met or exceeded the leakage target:
 - a. One-piece split carbon ring seals with a spring load applied through conical seats.
 - b. Segmented carbon ring seals with axial and radial spring loading.
 - c. Segmented back-to-back carbon ring seals with axial and radial spring loading.

CONFIDENTIAL

4. The all-metal seal concept is feasible for regenerator inner diameter seals; three configurations tested have development potential for this application.
5. Seal endurance tests with carbon seals at overspeed and overload conditions demonstrated long seal overhaul life.
6. Leakage did not significantly increase with running time.

CONFIDENTIAL

CONFIDENTIAL

FULL SCALE REGENERATOR DESIGN

Contract Item 5 of Phase I required the design of the high-effectiveness light-weight regenerator. In addition, the integration of the regenerator with the T74 test bed required design modifications to the T74 engine. The main areas requiring modification were the compressor scroll, burner, power turbine, and ducts. The compressor scroll, power turbine, and ducts must deliver uniform temperature and flow profiles to the regenerator and burner with minimum pressure loss and weight. The present standard T74 burner was redesigned to accept higher inlet temperature. This redesign required changes in cooling louvers and in the burner hole pattern.

REGENERATOR DESIGN

Determination of Regenerator Size

Upon completion of the design-point T74 test-bed performance and parametric cycle performance studies, an analytical study was conducted to establish the optimum matrix, frontal area, and flow length. These geometric dimensions established the overall size of the regenerator needed to obtain the performance goal.

This preliminary study based on the radial vee concept of matrix packaging resulted in a regenerator of the following size:

Rotor outer diameter	35.5 in.
Tunnel diameter	8.0 in.
Active matrix frontal area	8.8 ft. ²
Total frontal area	10.0 ft. ²
Matrix thickness	0.55 in.
Bulkhead thickness	0.30 in.
Number of bulkheads	16
Number of active matrix packages	14
Gas side angle	245°
Air side angle	70°
Total tunnel angle (2 tunnels)	45°
Average matrix vee angle	26.6°
Minimum matrix vee angle	21.0°
Screen mesh	60 x 60 x 0.0059
Matrix weight	62.5 lb.
Porosity	0.725
Inlet fairing gap	0.30 in.
Rotor speed	20 r.p.m.

CONFIDENTIAL

Preliminary regenerator-engine arrangements aimed at a minimum total weight were sketched, and relative weight estimates were made. All schemes were unacceptable for flightweight designs, and a major effort was placed on reducing the regenerator diameter. Since the circumferential package concept offered many advantages over the radial vee package, a series of preliminary sketches was made to determine the matrix arrangement for the given torus diameter. A comparison of these package arrangements is shown in Figures 126 through 129. Figure 126 shows the radial vee package with a smaller included matrix angle at the torus inner diameter than at the outer diameter, which creates a three-dimensional flow problem. The circumferential vee matrix shown in Figure 127 did not have sufficient frontal area. The Z-matrix package had the required frontal area, but, by the addition of one more leg to form a W-package and the addition of 1 inch to the bulkhead diameter, the regenerator outer diameter was reduced from 35.5 inches to 28 inches and the inner diameter was reduced from 19.5 to 10.0 inches. This reduction of the regenerator diameter allowed a flightweight regenerator design. The reduced inner diameter resulted in a 50-percent reduction of the inner diameter seal leakage. The inner diameter seals are smaller than those of the existing regenerator rig.

The final regenerator geometry was as follows:

Rotor	28.1 in.
Tunnel diameter	9.0 in.
Total frontal area	8.66 ft. ²
Matrix thickness	0.7 in.
Equivalent bulkhead thickness	0.3 in.
Number of bulkheads	14
Number of active matrix packages	12
Gas side angle	240°
Air side angle	68.6°
Total tunnel angle	51.4°
Screen mesh	60 x 60 x 0.004
Matrix weight	58 lb.
Matrix vee angle	18°
Porosity	0.81
Rotor speed	20 r. p. m.

The circumferential W-package concept permitted a greater flow length matrix than the radial vee and still maintained a reasonable included angle for good flow distribution. This concept changed the optimum matrix to the 60 x 60 x 0.004 screen mesh.

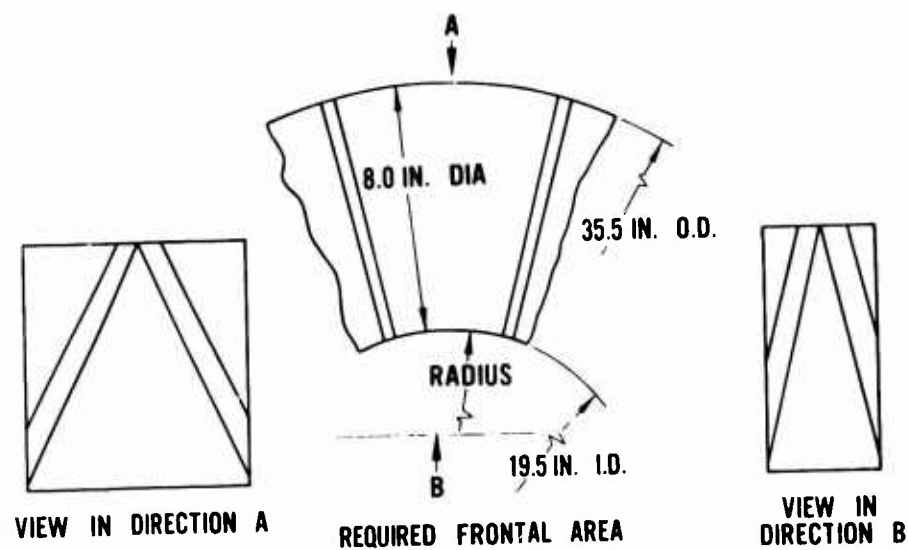


Figure 126. Radial Vee Matrix Arrangement.

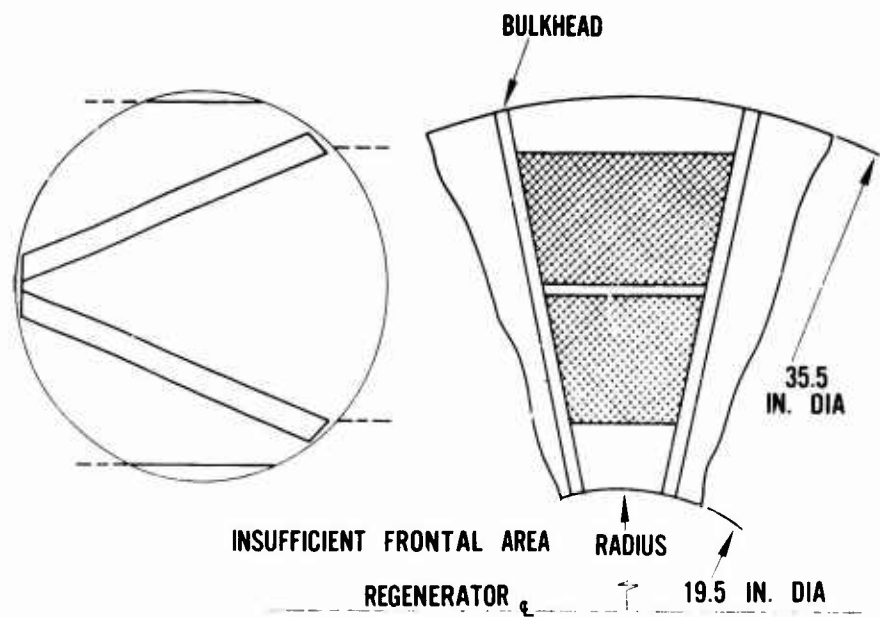


Figure 127. Circumferential Vee Matrix Arrangement.

CONFIDENTIAL

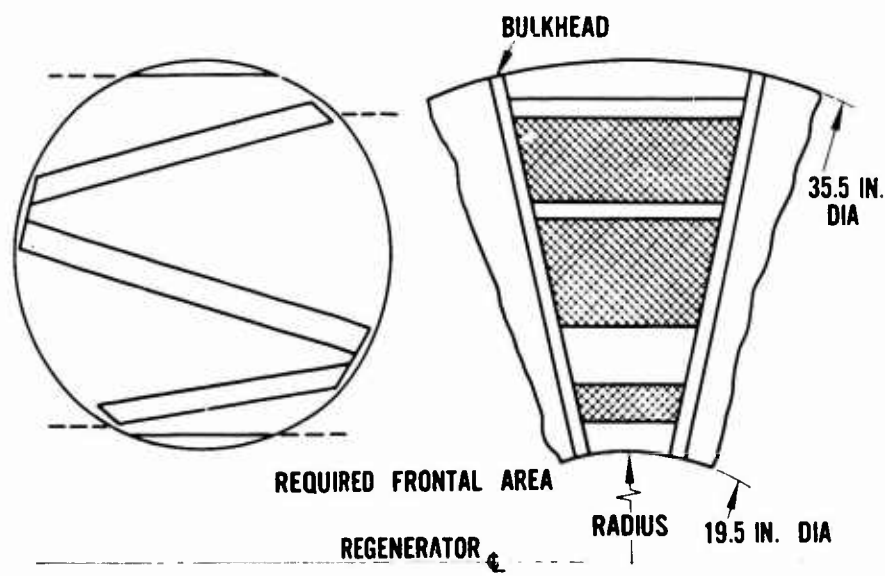


Figure 128. Circumferential Z-Matrix Arrangement.

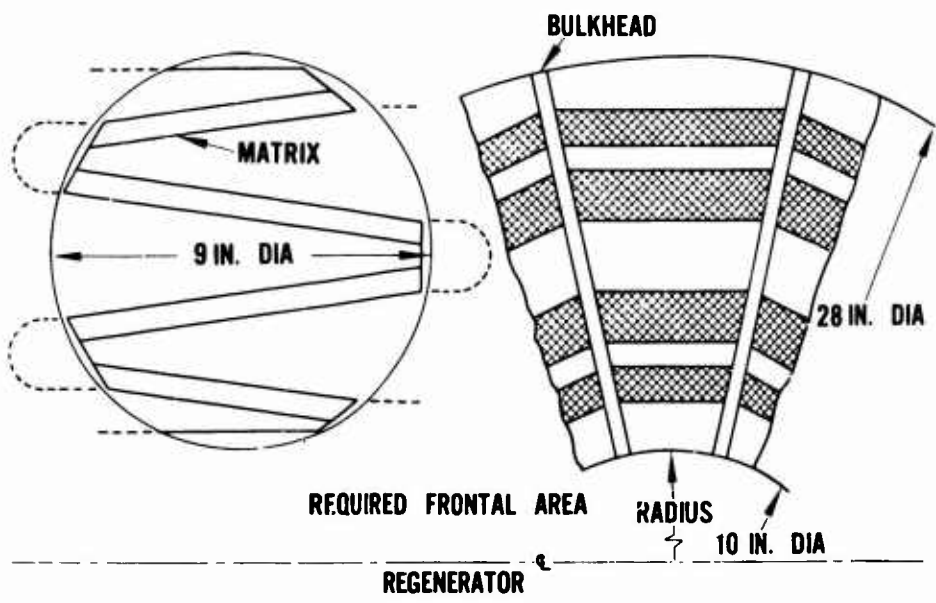


Figure 129. Circumferential W-Matrix Arrangement.

CONFIDENTIAL

Discussion of the Regenerator Design

The heat transfer elements and general configuration were decided during the sizing studies. The details of fabrication, attachment, and sealing arrangements were completed.

The W-shaped matrix is fabricated from 60 x 60 x 0.004 screen mesh. Approximately 90 layers of screen are riveted together, forming a semirigid subassembly which can be handled easily and clamped for edge grinding to final size.

End plates are electron beam welded to the edge of the screen pack. The matrix screen packs are fixtured to locate the screen such that a constant window-area-to-frontal-area ratio is maintained. Side plates are electron beam welded to the edge of the screen, and the ends of the side and end plates are fusion welded. This fabrication will result in minimum distortion and a clean, unplugged screen matrix. The matrix package is assembled into two units: an outer vee and an inner vee section. This is necessary for assembly in the rotor. The end plate of the screen element at the rotor inner diameter is extended to form a blockage plate to prevent axial leakage through the inner diameter. The extended end plate also mechanically attaches the lower vee portion of the matrix to the rotor.

The top vee matrix end plate is extended and bolted to an integral outer diameter segmented seal holder and bulkhead tie plate. The hard-coated, spring-loaded, segmented outer diameter seal, which prevents bypass leakage, is air-loaded by the pressure drop across the matrix.

A major improvement in rotor bulkhead design and tie rod configuration was conceived in order to permit lower rotor weight with no loss in structural integrity. This concept utilized thin chordal tension plates at the bulkhead midspan and outer diameter which link adjacent bulkheads through hinged joints. Since the hinged joints allow only tension loads to be transmitted, the tie plates are much thinner than equivalent tie rods. In addition to being lighter, the thin plates and hinge joints cause a minimum of flow disturbance along the matrix face. The tension plates also allow a major weight reduction in bulkhead design. Since the plates distribute the pressure load more uniformly than the rods, a waffle-type bulkhead which reduced the original bulkhead weight by 50 percent could be used.

To compensate for the tolerance accumulation between the bulkhead and the rotor, classified pins are used in the hinged joints. This allows interchangeability of all parts. The tie plates and matrix are installed in the rotor with a certain class pin. At the installation of the final pin, a certain mismatch

CONFIDENTIAL

will be realized. This distance is measured and compensated by changing to another class pin in several locations to distribute the load over several bulkheads.

In addition to the seals at the inner attachment and outer diameter segmented seal, which prevent bypass leakage, an all-metal seal is located on the hot side at the junction of the top and bottom half of the matrix. This spring seal prevents bypass leakage at the joint. There are spring seals in the bulkheads to prevent bypass leakage through the gap formed between the matrix side plates and bulkheads.

Hard-coated piston rings are used as bulkhead seals. As in the existing rig, the bulkhead spacing and tunnel length are designed so that a minimum of one active seal is in each seal tunnel to prevent compressor discharge leakage into the low-pressure gas side. Each edge of the tunnels is chamfered to allow the piston rings to be seated prior to sealing and to release the pressure load before the ring is released on exit from the tunnel. To maintain ring circularity and control, hard-coated guide surfaces are machined into the torus outer diameter and at the ring end gap on both sides of the outer surface of the torus inner diameter seal housing.

A mockup of the matrix package, rotor, and housing section which demonstrates the design concepts mentioned is shown in Figures 130 through 133.

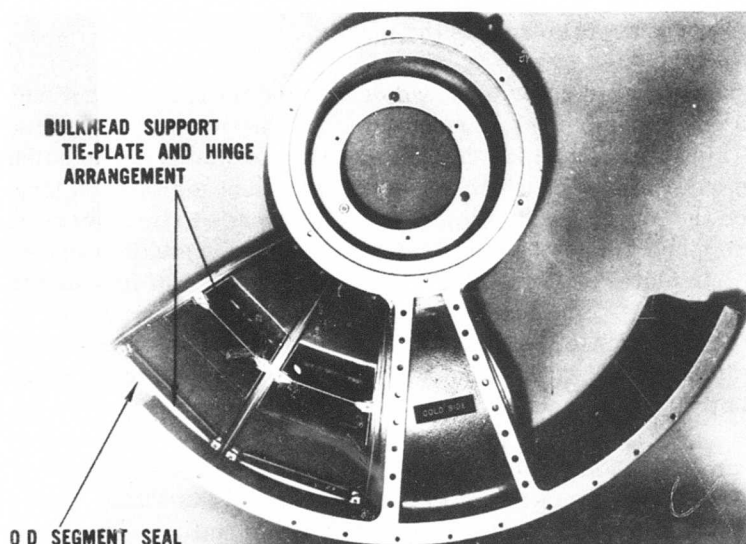


Figure 130. Model of Regenerator Section, Cold Side.

CONFIDENTIAL

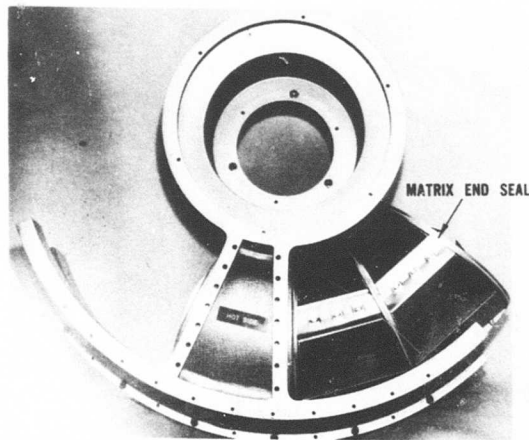


Figure 131. Model of Regenerator Section, Hot Side.

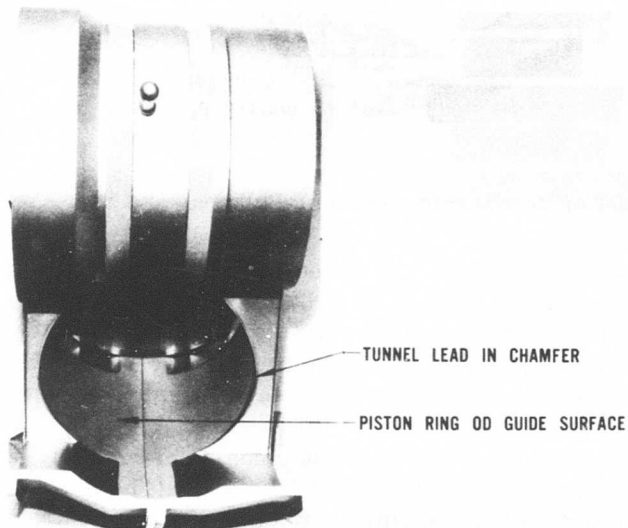


Figure 132. Model of Regenerator Section, Tunnel Area Showing (1) Tunnel Lead-In Chamfer and (2) Piston Ring O.D. Guide Surface.

The rotor is a one-piece construction to which the bulkheads are bolted. This was done to eliminate brazed joints, to prevent distortion, and to allow interchange of component parts.

CONFIDENTIAL

CONFIDENTIAL

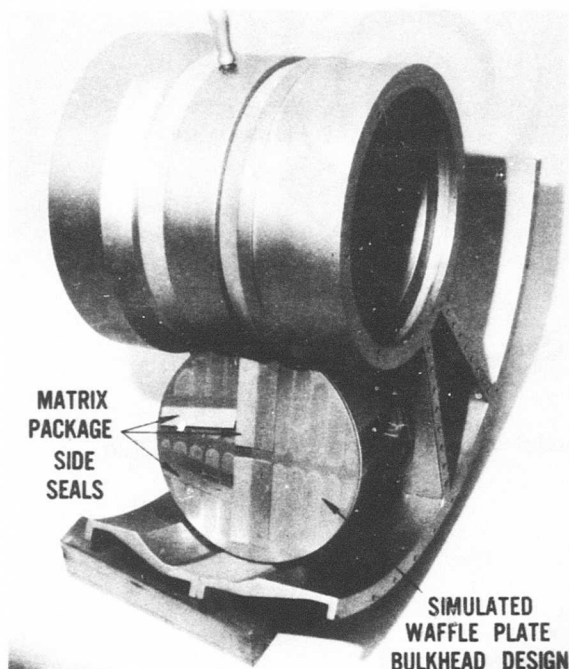


Figure 133. Model of Regenerator Section, Bulkhead and Seal Area.

Rectangular dead-ended holes are machined into the outer diameter of the rotor. Between these holes are located axial slots into which the tab extensions of the bulkheads fit. The tab extensions are attached to the rotor with two through-bolts. The rectangular holes permit clearance for the through-bolts and provide platform bosses to which the lower matrix half is attached.

The torus inner diameter seal arrangement consists of conically sprung one-piece carbon seals with 0.750-inch-thick seal plates at the inner diameter which are scalloped to 0.300 inch at the outer diameter. The seals are pressurized internally by the compressor discharge air through holes in the seal liner of the housing on the cold side. This same air is vented to the hot-side seals through holes in the rotor and seal plate to pressurize the seals similar to the cold-side seals. The relatively cool pressurizing air scrubs that portion of the rotor adjacent to the bearing, keeping the rotor cool and maintaining the design bearing fits.

Analytical studies which showed that the rotor can be supported by a single four-point-contact ball bearing were completed. The elimination of one

CONFIDENTIAL

CONFIDENTIAL

bearing (previous regenerator rig had two bearings) allowed the inner case to be shortened (lower weight), reduced oiling and scavenging requirements, and reduced oil heat rejection. This study included radial loading caused by a pressure difference acting on the rotor and moment loading caused by the matrix pressure drops.

The single bearing is lubricated by jet. Oil slots on the inner diameter of the hub allow the oil that passes through the bearings to be returned to the scavenge side. The scavenge oil passes through drain holes in the hub at the drive gear location to the single oil sump located at the regenerator cold side. The scavenge tube is located in the low-pressure cold side and is attached to an external scavenge system for the test-bed engine program.

The bearing lubrication oil is prevented from entering and being trapped in the hot-side ring seal compartment by means of a close-clearance baffle and pressure-balanced face seal. Air leakage through the face seal also forces the oil to the scavenge side.

The rig drive is essentially a right-angle-drive gear system. The original rig design had a spur gear driving through a gearbox located at the torus housing inner diameter. The concept of a right-angle drive through the side of the housing wall permits the location of the regenerator to be at a smaller diameter, since the local gearbox on the inner diameter was eliminated. A hydraulic positive displacement motor, using oil as the working fluid (similar to the motor tested on the existing rig), is located behind one of the cold-side seal tunnels. The estimated power requirement is less than 1 horsepower at maximum test-bed engine pressure and speed. A test-stand mounted pump was used later during performance test to power the regenerator motor.

The regenerator housings are designed to the same concept as the existing rig. The housings form the structure to support the rotor and to establish the gas and air flow passages as generated by the toroidal seal tunnels and all the stationary seal surfaces. The seal surfaces in the hot areas are hard-coated. The inner diameter seal surface on the cold side is chromium-plated.

REGENERATOR TEST-BED ARRANGEMENT

The finalized regenerator test-bed arrangement is shown in Figure 134. This arrangement is a representative method of integrating a toroidal rotary regenerator with an engine. Although there may be better arrangements for the powerplant, the regenerator itself represents a lightweight configuration in size, performance, and construction detail.

CONFIDENTIAL

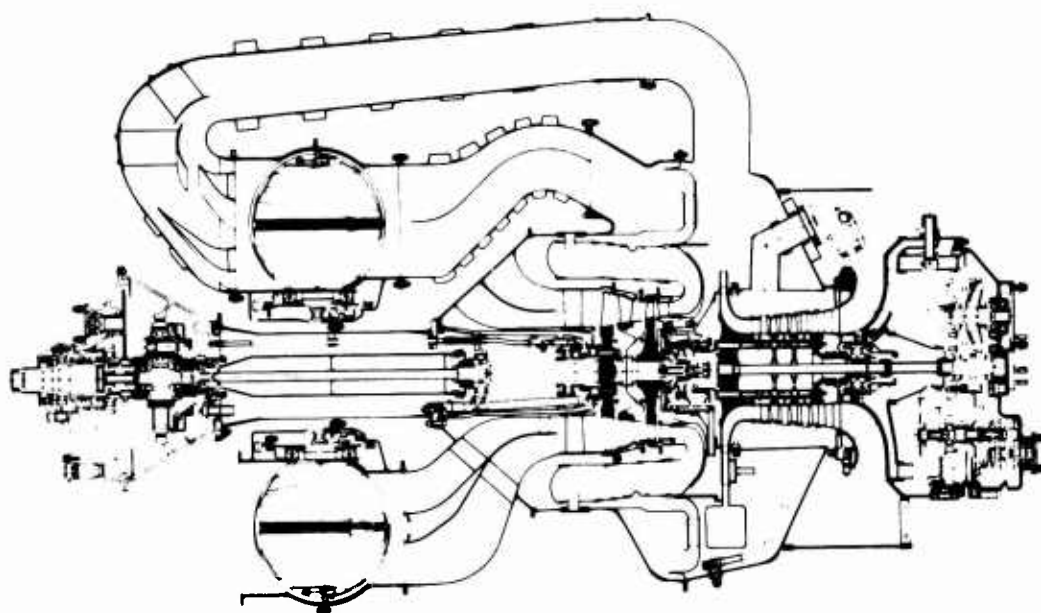


Figure 134. Regenerator on T74 Test Bed.

Construction of a full scale mockup was completed to verify sufficient accessibility of engine and duct flanges (Figures 135 through 137). This arrangement features an extended free turbine drive shaft so that the regenerator can be placed at the smallest diameter behind the main reduction gearbox. In addition to being the lightest configuration studied, this method has the lowest duct pressure losses, leaves ample space for drive shaft coupling, and allows access to the standard T74 engine mounts.

Air is delivered from the radial compressor stage to a square-cross-section collector scroll, which is housed within a structural pressurized case. This scroll guides the compressor air to an elbow outlet for delivery to the regenerator inlet. The delivery duct was made to sweep out radially prior to turning through the 90° on the engine top dead center position to reduce the stresses in the structural case. A bellows located at the junction of the compressor delivery elbow and the regenerator delivery duct absorbs the growth changes due to the difference in thermals between this relatively cool duct and the hot sections of the engine. The air is then turned and diffused in the transition section with the correct area ratio to provide uniform flow distribution to the regenerator. A flow model of this duct was made and was later tested at the engine flow parameter to ensure that an acceptable flow profile will be obtained and to determine the duct pressure loss.

CONFIDENTIAL

CONFIDENTIAL

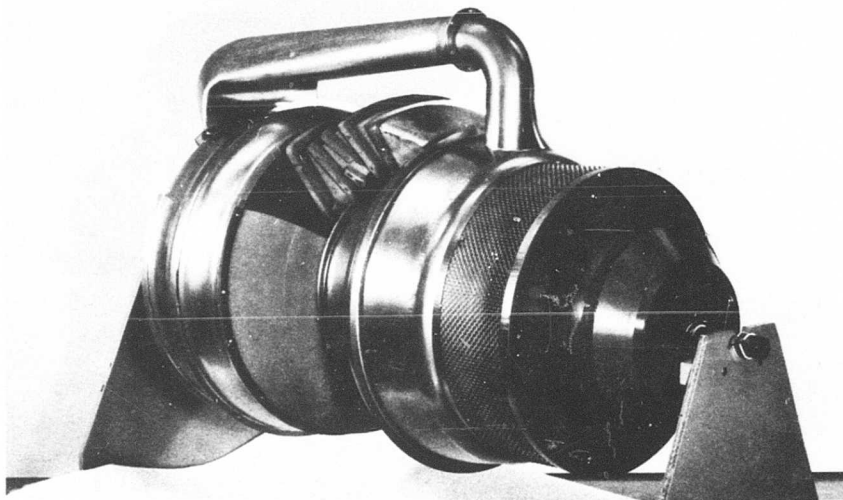


Figure 135. Regenerator Test-Bed Mockup, Engine Inlet Three-Quarter View.

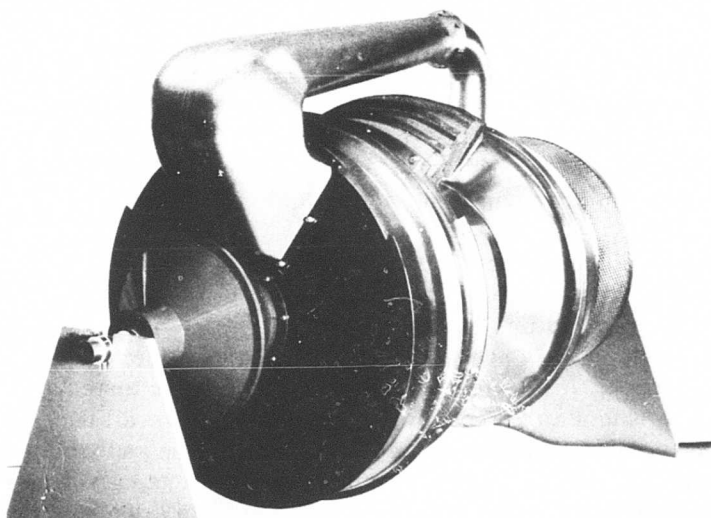


Figure 136. Regenerator Test-Bed Mockup, Regenerator Exhaust Three-Quarter View

CONFIDENTIAL

CONFIDENTIAL

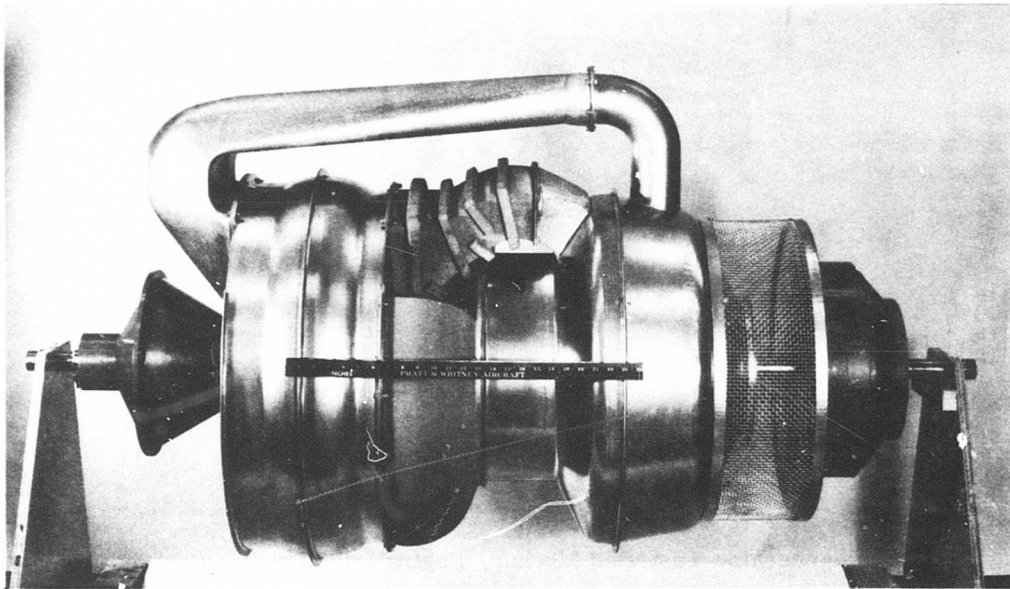


Figure 137. Regenerator Test-Bed Mockup, Side View

The compressor air absorbs the heat from the matrix and is delivered through a duct which has added top hot stiffeners to an elliptical inlet of the burner entry scroll. A mixing baffle in the regenerator-to-inlet-burner duct was provided to deliver the air to the burner with a maximum temperature profile of 50° . Turning vanes in the burner entry port guide the air into the burner scroll.

The swirl angle from the power turbine is removed by guide vanes in the turbine exhaust collector to the regenerator inlet case. The flow separators, which provide the proper diffusion rate and turning, also provide good inlet configurations for the matrix package in the inlet burner duct and the compressor delivery duct. A flow model of this duct was later tested at the engine flow parameter to obtain an acceptable flow profile and overall duct pressure loss. This duct is also a structural member of the engine and isolates the engine loads from the regenerator. The turbine exhaust gas gives up its heat to the matrix as it passes through the regenerator and is exhausted through the exhaust case, which has a single exhaust port offset to the side to mate with the exhaust collector of the test stand.

CONFIDENTIAL

CONFIDENTIAL

Critical speed analysis has shown that the power turbine extension shaft is acceptable. Extensions for the power turbine bearing oil and scavenge tubes were provided so that no changes in normal bearing oiling or scavenging were required.

Optimization studies of the power turbine area were completed with the blade angle restaggered 2° closed relative to the nominal design angle. The power turbine was matched to run at 9 percent above the nominal design speed, which will result in a 24° swirl angle.

The compressor turbine vanes were opened 0.25° relative to the nominal design angle to provide optimum matching.

The T74-style compressor was selected for this design because of the advanced development with this component and an overall compressor efficiency of 78 percent up to the scroll at the regenerator match point.

An initial burner can configuration was developed on an empirical basis for the test-bed engine. Water flow visualization tests, followed by tests performed in a standard T74-style rig, achieved a good exit temperature profile of 60°F . from root to tip at the turbine entry annular. No carbon deposits or local skin hot spots occurred. The radial temperature profile was obtained by a vortex generator in the primary zone, which allowed accurate adjustment of downstream mixing.

The estimated weight of the regenerator, including the flightweight rotor, housings, and rig-type drive, is 260 pounds. The major regenerator component weights are as follows:

Bearings and seals with inner structure	42 lb.
Regenerator housings	72
Regenerator rotating parts, including matrix	132
Regenerator drive	14
Total flange-to-flange regenerator weight	260 lb.

This is the most sophisticated flightweight toroidal rotary regenerator designed within the present state of the art of sealing and uniform flow distribution methods.

All seal arrangements of the design have demonstrated in the component rigs and the existing regenerator rig that the leakage goal and seal life will be obtained. Airflow tests of matrix configurations in the component rig have demonstrated that the matrix package designed will have the required flow distribution to attain the performance goal.

CONFIDENTIAL

To remain within the scope of this program in both time and cost, a regenerator test-bed integration concept was designed. The test-bed integration approaches flightweight regenerator design with only minor modifications to the basic engine. The estimated component weights of the modification parts are as follows:

Turbine-exhaust-to-regenerator case	36 lb.
Regenerator-to-burner-scroll duct	14
Compressor-scroll-to-regenerator duct	<u>20</u>
Total duct weight	70 lb.
Power turbine shaft extension	13 lb.
Compressor and burner scroll with T74 modifications	<u>57</u>
Total engine modification weight	70 lb.

CONFIDENTIAL

SUPPORTING STUDIES

LEAKAGE EFFECTS ON EFFECTIVENESS

An analytical study to determine the extent of each discrete leakage path and its effect on regenerator performance was completed during this program. Leakage, inherent in rotary regenerators, decreases engine cycle performance by allowing high-pressure air to bypass the burner and turbine and by decreasing regenerator effectiveness. Prior to this program, existing rotary regenerator design systems treated all leakage as one quantity and assessed regenerator and cycle performance penalties on this basis. The purpose of this study was to present a method of evaluating the effect of leakage on overall regenerator temperature effectiveness.

Method of Accomplishment

Toroidal rotary regenerator leakage can be categorized by axial and tangential leakage. The major types of leakage, shown schematically in Figure 138, are listed below.

1. Axial leakage (outer diameter seal leakage)
2. Tangential leakage (before or after passing through matrix)
 - a) Carryover
 - b) Bulkhead piston ring seal leakage
 - c) Inner diameter seal leakage

Axial leakage in either the high-pressure or the low-pressure stream influences the effectiveness of both sides of the regenerator. When axial leakage occurs in both high- and low-pressure streams, the change in effectiveness (due to axial leakage) for either side of the regenerator is a function of the higher leakage only. This results from a lower heat capacity in the stream with the higher leakage.

The assumptions used in deriving the relationships between leakage and effectiveness are as follows:

1. The specific heat of the gas is constant.
2. The Reynolds number based on the matrix flow area is constant.

CONFIDENTIAL

3. The leakage and the stream vehicle, which receives the leakage, mix completely.

Results

The individual effects of axial and tangential leakage on effectiveness are shown in Figures 139 through 141. The overall effect of the leakage on effectiveness is approximated by multiplying the individual effectiveness ratios obtained from these three figures.

For the regenerator designed under Contract Item 5 of Phase I, which has a predicted mass loss of 3 percent (1 percent seal leakage, 2 percent carryover), the overall effect using this method is less than a 1-percent loss of ideal effectiveness. This approximate method agrees within 0.11 percent of the exact solution which treats all leakages simultaneously.

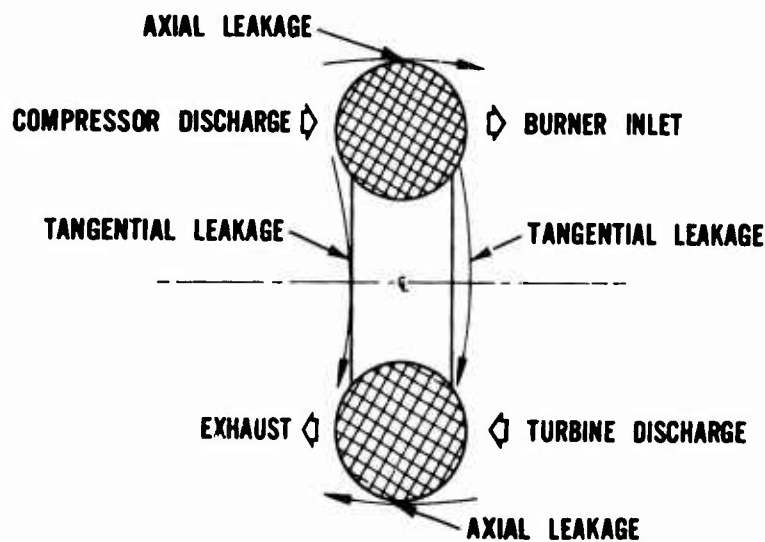


Figure 138. Toroidal Rotary Regenerator Leakage Flow System Schematic.

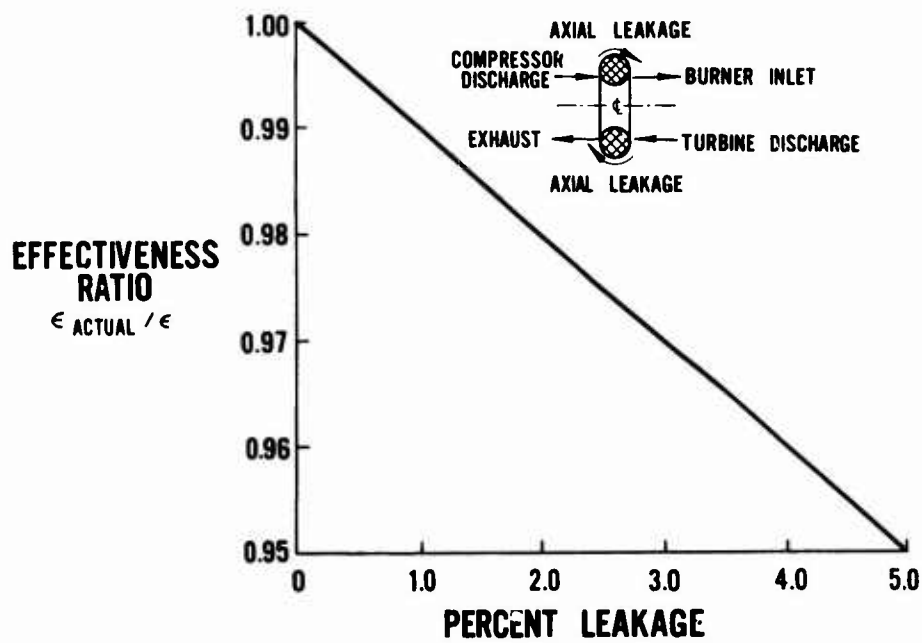


Figure 139. Regenerator Effectiveness Ratio Vs. Percent Leakage for Axial Leakage.

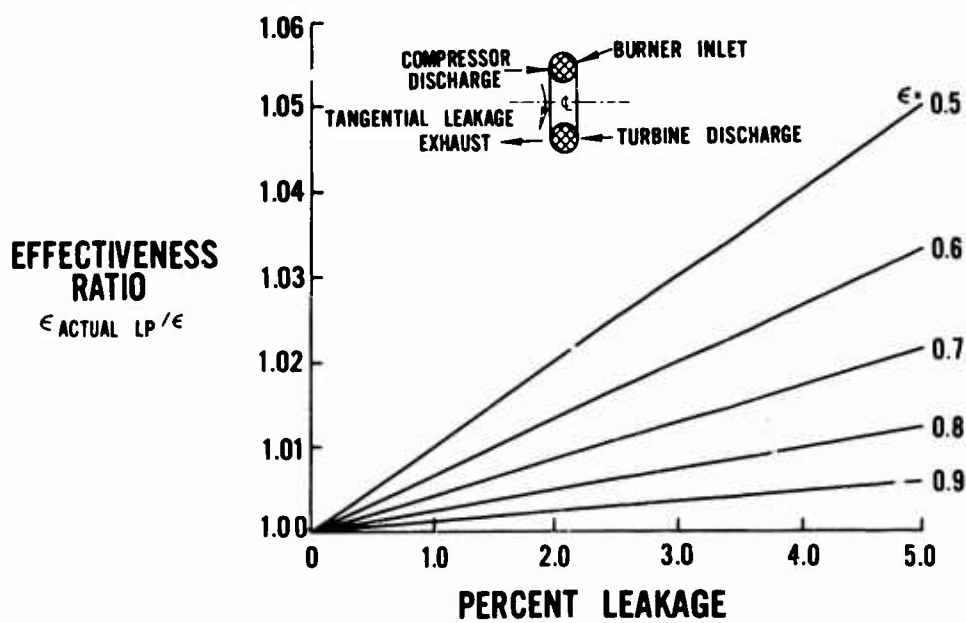


Figure 140. Regenerator Effectiveness Ratio Vs. Percent Leakage for Tangential Leakage Bypassing Matrix, Burner, and Turbine.

CONFIDENTIAL

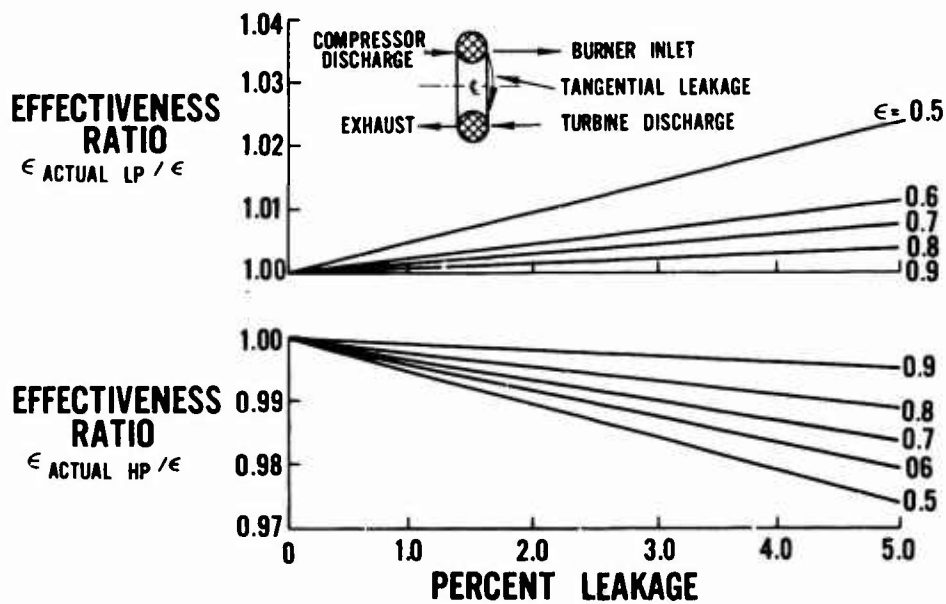


Figure 141. Regenerator Effectiveness Ratio Vs. Percent Leakage for Tangential Leakage Bypassing Burner and Turbine.

REGENERATIVE T74 CYCLE ANALYSIS

Design Point Selection

Cycle studies were performed to determine the optimum design-point operating conditions for the regenerative T74 required to meet the 0.40 pound of fuel per horsepower-hour SFC goal with a toroidal rotary regenerator. The following design point parameters were used in this study:

Altitude	Sea Level
Ambient temperature	59° F
Compressor efficiency	78.5%
Combustion efficiency	98%
Gas generator turbine efficiency	87%
Power turbine efficiency	86.7%
Regenerator effectiveness	85%
Total mass loss	3%
Total flow system pressure loss	15%

CONFIDENTIAL

The results of this study (Figures 142 and 143) indicate that the optimum compressor pressure ratio is in the range of 5:1 to 6:1 and that a turbine inlet temperature of 1850° to 1900° F. is required to demonstrate the target goal of 0.40 pound per horsepower-hour specific fuel consumption.

On the basis of this study, a compression ratio of 5.25 and a turbine inlet temperature of 1900° F. were selected as the sea level design point for test-bed engine matching.

Part Power Operation

A cycle analysis was performed to predict part-load SFC as a function of power level. The results of this study are shown in Figure 144 together with the performance of the standard nonregenerative T74. This study shows that with the regenerator the SFC is about 40 percent lower at full power and is about 50 percent lower at part power. It should be noted that these performance levels are with fixed-geometry turbines and compressor and that no regenerator bypass is required at the maximum-power operating point.

The component performance used in this study is based on standard T74 components. The variations of component performance with power level are shown in Figures 145 through 147 for the compressor, Figures 148 and 149 for the turbines, and Figure 150 for the regenerator. The predicted fuel flow and flow system pressure loss are shown in Figure 151.

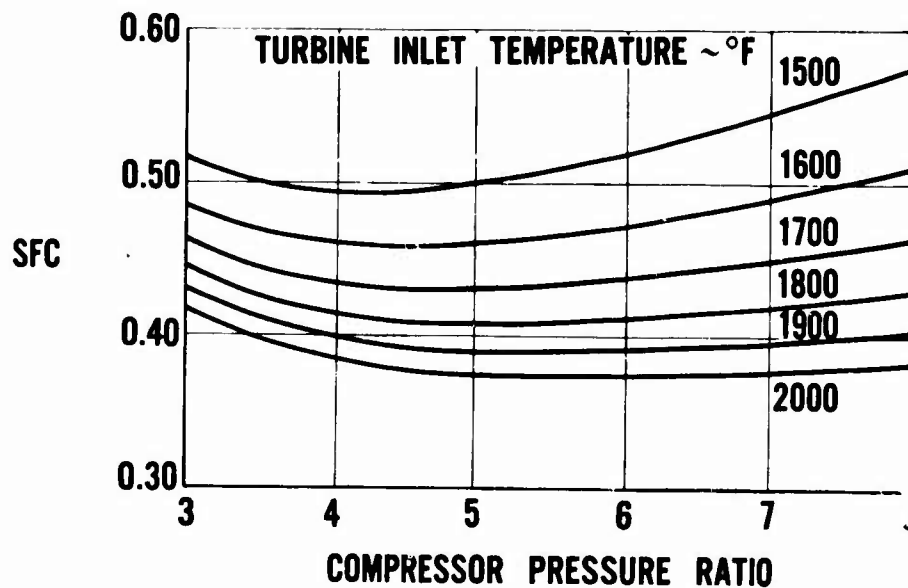


Figure 142. Predicted Design-Point SFC Performance, Gas Turbine Powerplants With Toroidal Rotary Regenerators.

CONFIDENTIAL

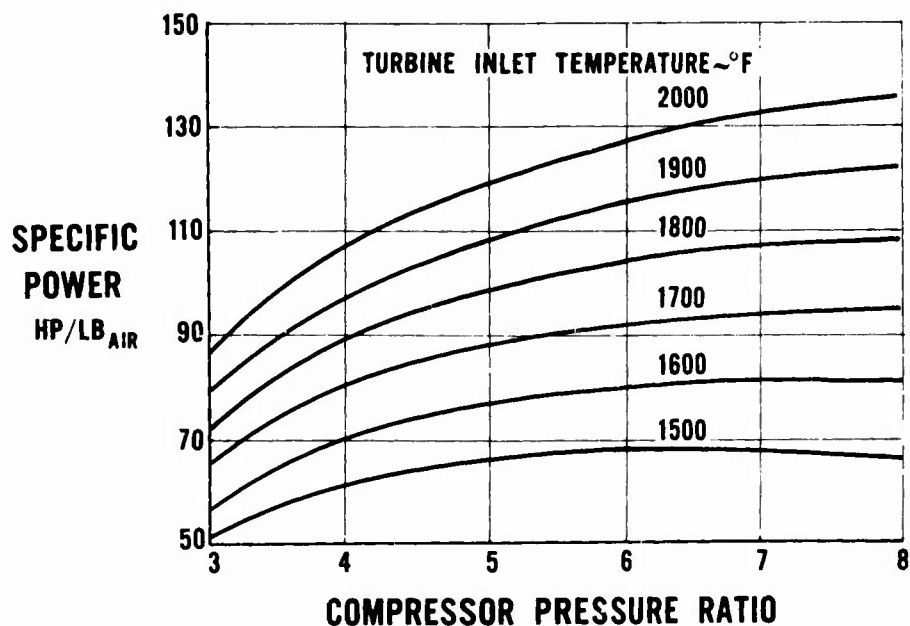


Figure 143. Predicted Design-Point Specific Power Performance, Gas Turbine Powerplants With Toroidal Rotary Regenerators.

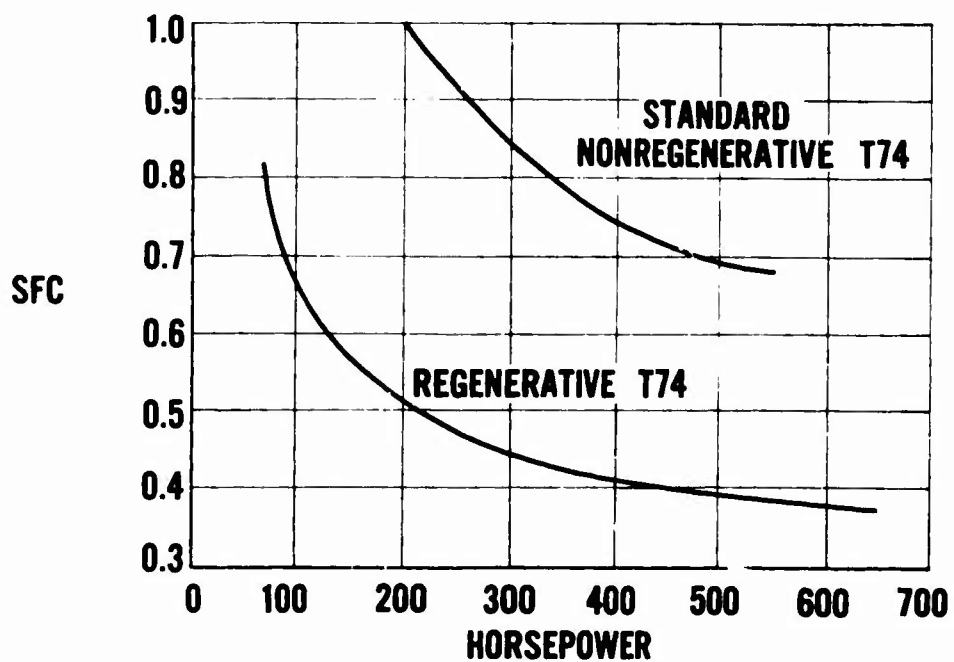


Figure 144. Predicted Specific Fuel Consumption, Regenerative T74 Powerplant.

CONFIDENTIAL

CONFIDENTIAL

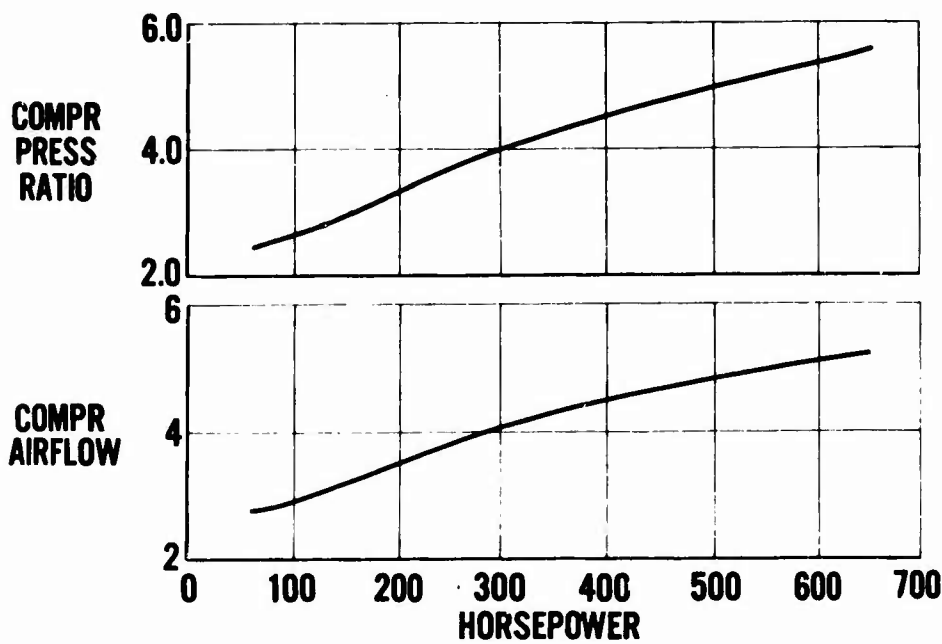


Figure 145. Predicted Compressor Airflow and Compressor Pressure Ratio, Regenerative T74 Powerplant.

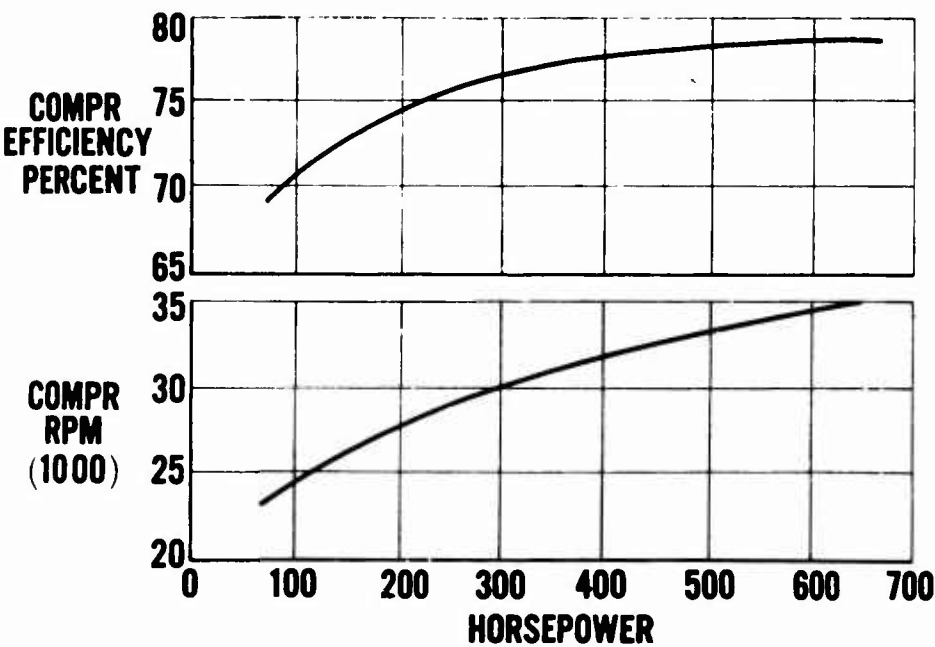


Figure 146. Predicted Compressor Efficiency and Compressor Speed, Regenerative T74 Powerplant.

CONFIDENTIAL

CONFIDENTIAL

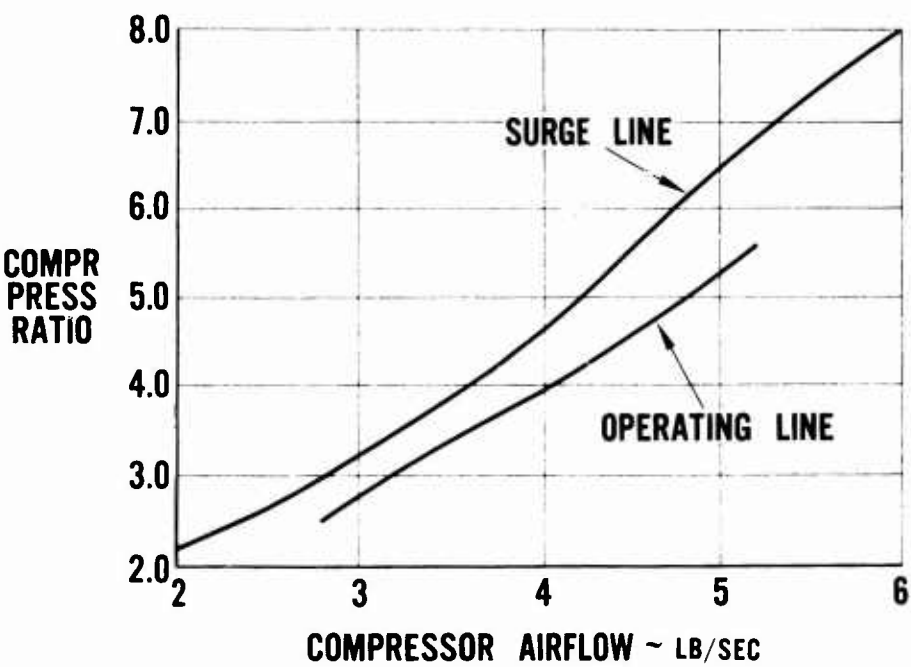


Figure 147. Compressor Operating Line, Regenerative T74 Powerplant.

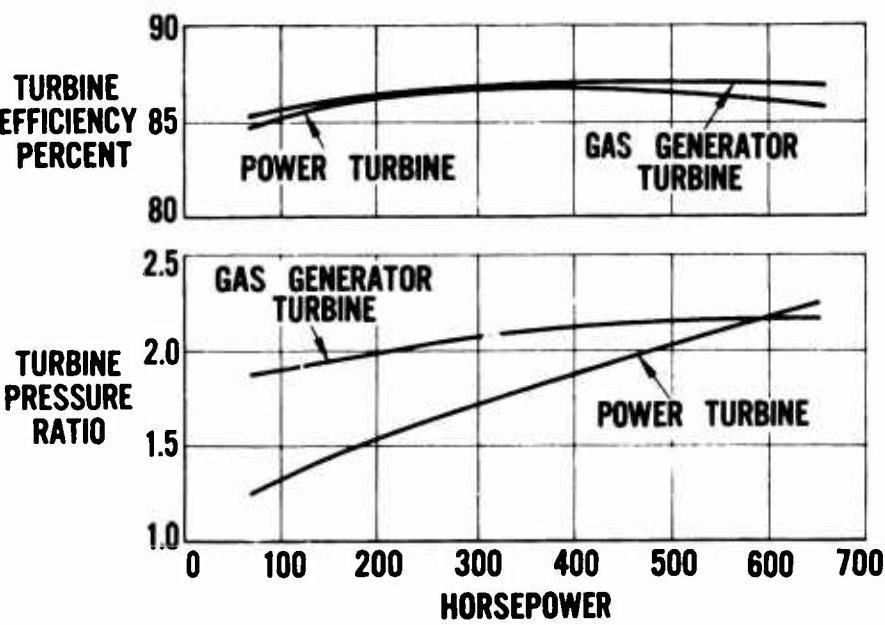


Figure 148. Predicted Turbine Efficiency and Turbine Pressure Ratio, Regenerative T74 Powerplant.

CONFIDENTIAL

CONFIDENTIAL

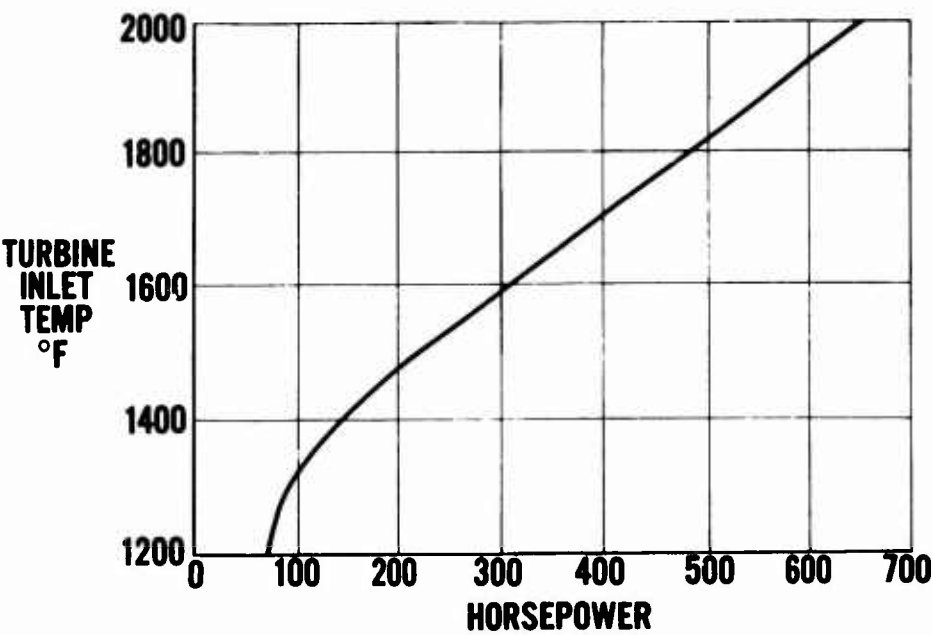


Figure 149. Predicted Turbine Inlet Temperature, Regenerative T74 Powerplant.

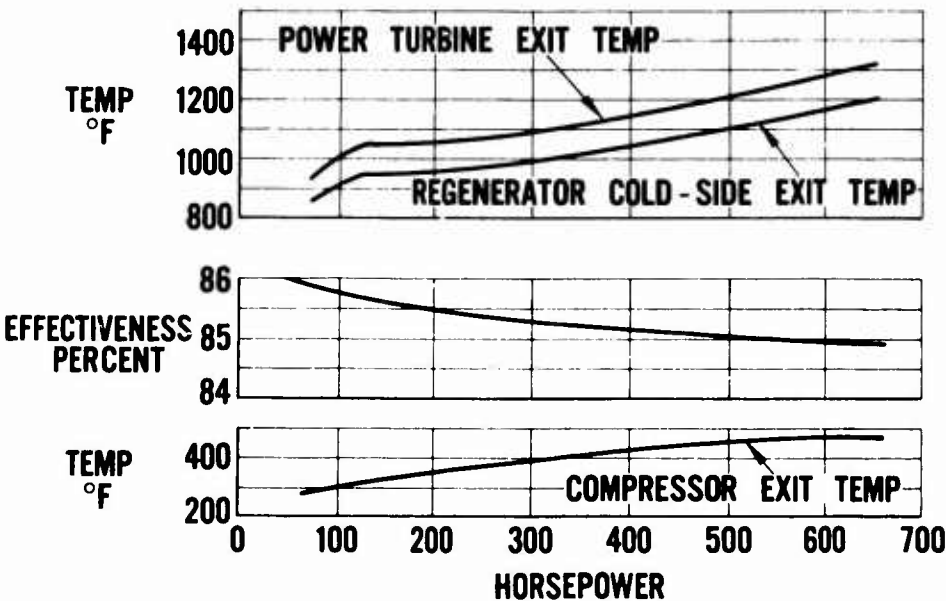


Figure 150. Predicted Regenerator Performance, Regenerative T74 Powerplant.

CONFIDENTIAL

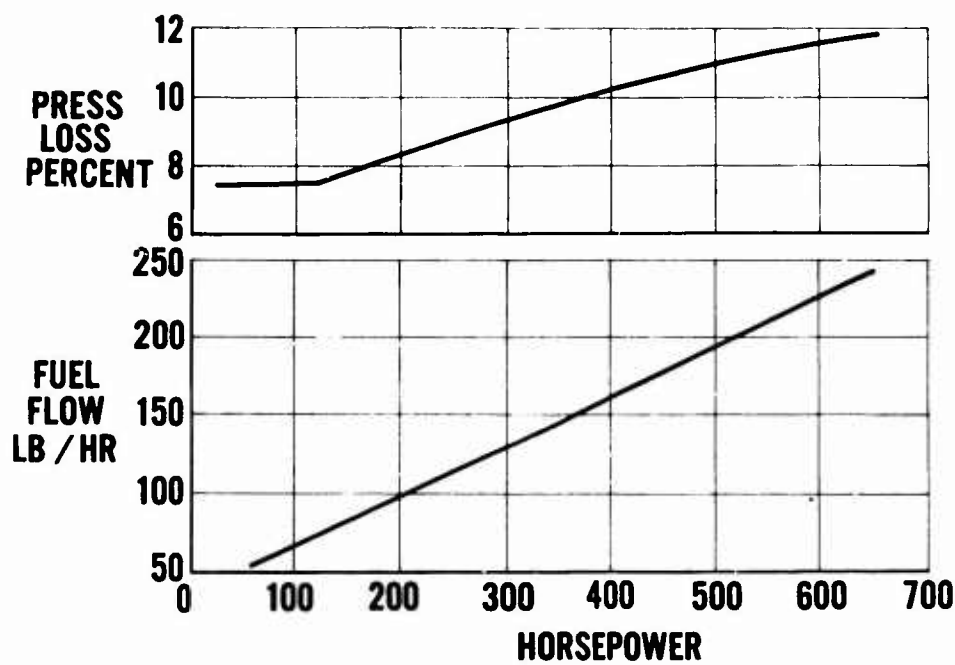


Figure 151. Predicted Fuel Flow and Flow System Pressure Loss, Regenerative T74 Powerplant.

Component Performance Trades

An analytical study was performed to assess the effects of variations in component performance on cycle performance. The nominal operation point used in this study is defined as follows:

Compressor pressure ratio	5.25
Compressor efficiency	78.5%
Turbine inlet temperature	1900° F.
Gas generator turbine efficiency	87.0%
Power turbine efficiency	86.7%
Regenerator effectiveness	85.0%
Total mass loss	3.0%
Total flow system pressure loss	15.0%
Specific fuel consumption	0.39

CONFIDENTIAL

The effects of small changes in mass loss, pressure loss, and regenerator effectiveness on engine specific fuel consumption are shown in Figure 152; the effects of the compressor and turbine efficiencies on the specific fuel consumption are shown in Figure 153. The effects of small changes in mass loss and pressure loss on shaft power are shown in Figure 154; the effects of compressor and turbine efficiencies on power are shown in Figure 155.

MATRIX CLOGGING

Experience prior to this program in determining the clogging characteristics of woven screen matrices is summarized below.

<u>Mesh</u>	<u>Type Flow</u>	<u>Results</u>
24 x 24	Cyclic	No clogging in 500 hours
24 x 24	Unidirectional	Gradual clogging in 27 hours
24 x 24	Unidirectional	Sudden clogging at 140 hours
50 x 50	Cyclic	Completed 100 hours with no clogging
50 x 50	Unidirectional	Gradual clogging until flow restricted at 4 hours
100 x 100	Cyclic	Pressure loss increased 1 inch Hg in 5 hours but was erratic, indicating intermittent clogging and cleaning
100 x 100	Unidirectional	Clogged within 1 hour

The analytical studies completed under Contract Item 1 of Phase I indicated that the optimum matrix for the T74 regenerator was between the 50 x 50 mesh, which did not clog, and the 100 x 100 mesh, which showed intermittent clogging in previous tests.

In order to verify that the matrix with optimum or near-optimum heat transfer properties would not be susceptible to clogging from normal burner deposits, the matrix clogging loop was reactivated; the three candidate matrices for performance tests in the subscale regenerator under Contract Item 3 were evaluated with cyclic flow for 100-hour periods.

CONFIDENTIAL

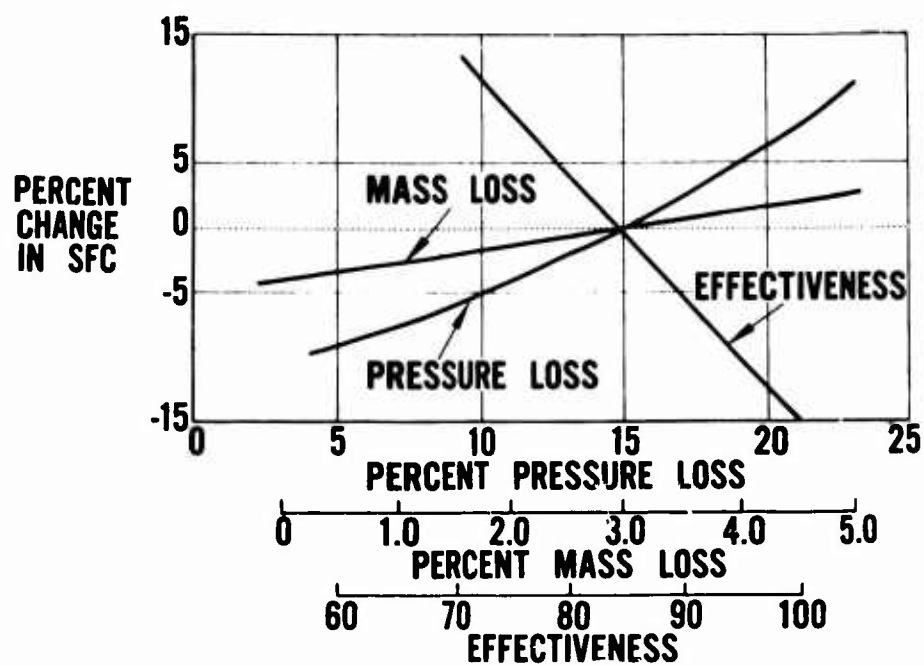


Figure 152. Predicted Design Point Trades, Regenerative T74 Powerplant.

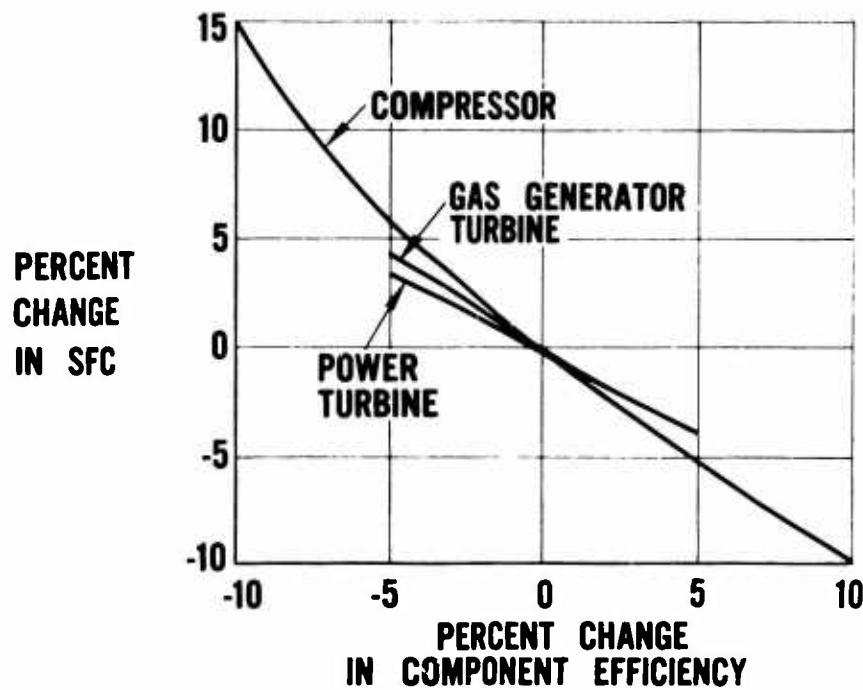


Figure 153. Predicted Design Point Trades, Regenerative T74 Powerplant.

CONFIDENTIAL

CONFIDENTIAL

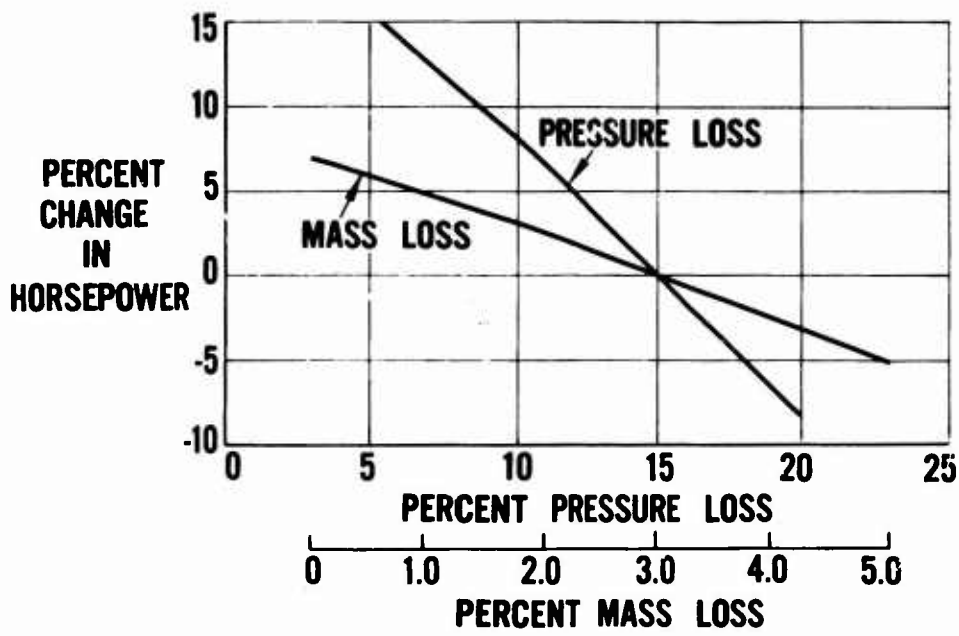


Figure 154. Predicted Design Point Trades, Regenerative T74 Powerplant.

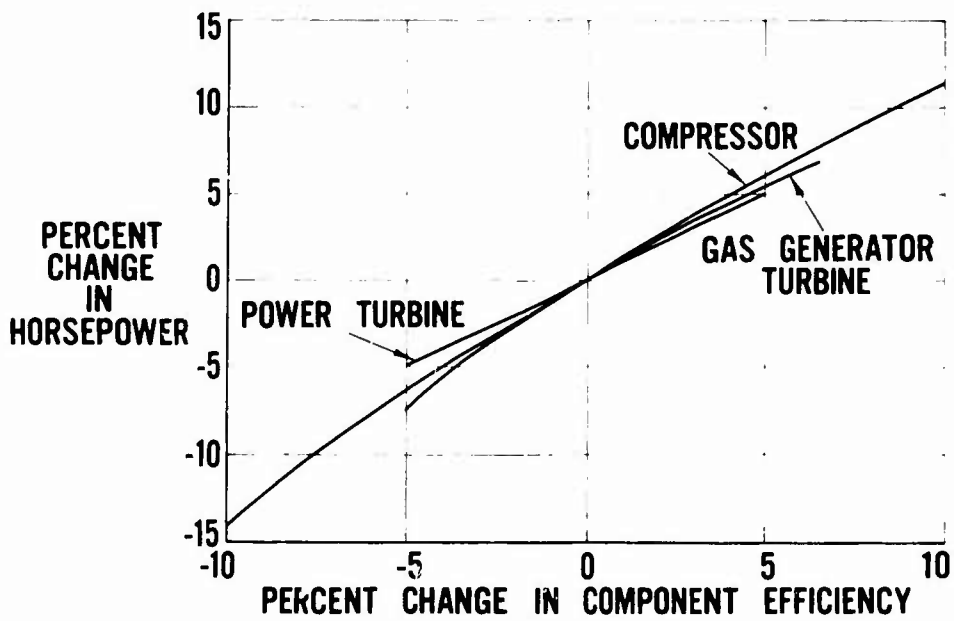


Figure 155. Predicted Design Point Trades, Regenerative T74 Powerplant.

CONFIDENTIAL

CONFIDENTIAL

Method of Accomplishment

An existing matrix clogging loop rig, shown schematically in Figure 156, was reactivated and assembled on the stand (Figure 157). This rig was used in a previous program to determine the self-cleaning characteristics of 24 x 24 x 0.014 mesh wire screens.

The test specimen was a circular disk of approximately 30 square inches frontal area. At an airflow of about 1800 pounds per hour, the velocities through the screen closely approximated those in the regenerator.

The test program consisted of repeated 1-minute cycles with 40 seconds of simulated hot flow at 1200° F. and 20 seconds reverse ambient flow. These times simulated the relative dwell time in the hot and cold sectors of the actual regenerator. In order to avoid the complexities of two air supplies, a system of valves was employed to obtain reverse cyclic flow.

Results

Three 100-hour cyclic endurance tests were completed on the 80 x 80 x 0.0044, the 60 x 60 x 0.0044, and the 60 x 60 x 0.0065 screen matrices to determine clogging characteristics. At the completion of the cyclic program, there was no indication of matrix clogging, as shown in Figures 158 through 162. The matrix specimen pressure drop remained essentially constant at 2.2 inches of

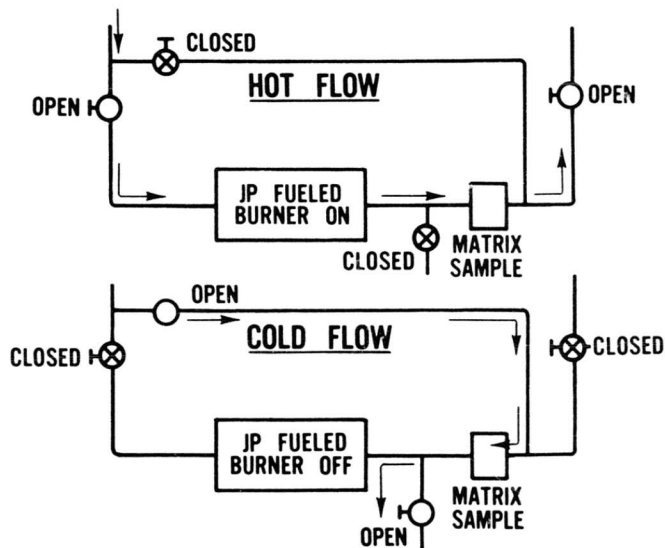


Figure 156. Matrix Clogging Loop Schematic.

CONFIDENTIAL

mercury through the 60 x 60 x 0.0044 matrix, 4.2 inches of mercury through the 80 x 80 x 0.0044 matrix, and 2.1 inches of mercury through the 60 x 60 x 0.0065 matrix.

Unidirectional clogging tests with 1200° F. products of combustion at 1800 pounds per hour flow were conducted on three candidate specimens. The continuous operation tests were conducted for 100 hours. Light clogging was observed on all specimens (see Figures 163 through 168). However, there was no screen penetration and no observed increase in the matrix pressure drop over this time period.

As a result of this testing, the following conclusions were reached: (1) With cyclic flow, as in the toroidal regenerator, screen matrices as fine as 80 x 80 mesh (0.725 porosity) will not clog, and (2) with unidirectional flow these screens will eventually clog but the rate of clogging is sufficiently slow that engine operation with a damaged (nonrotating) torus will not seriously hamper engine operation.

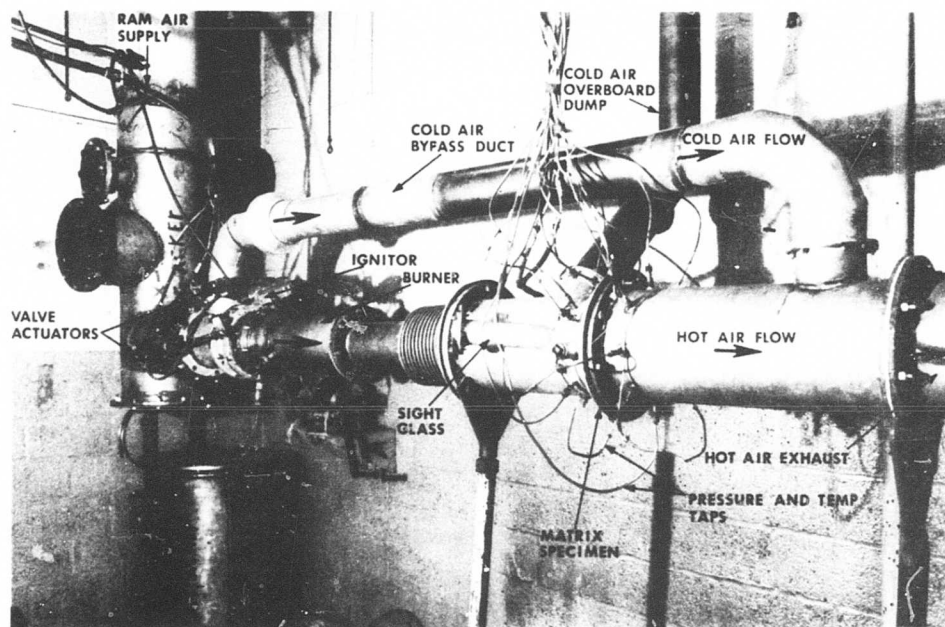


Figure 157. Matrix Clogging Loop Rig.

CONFIDENTIAL

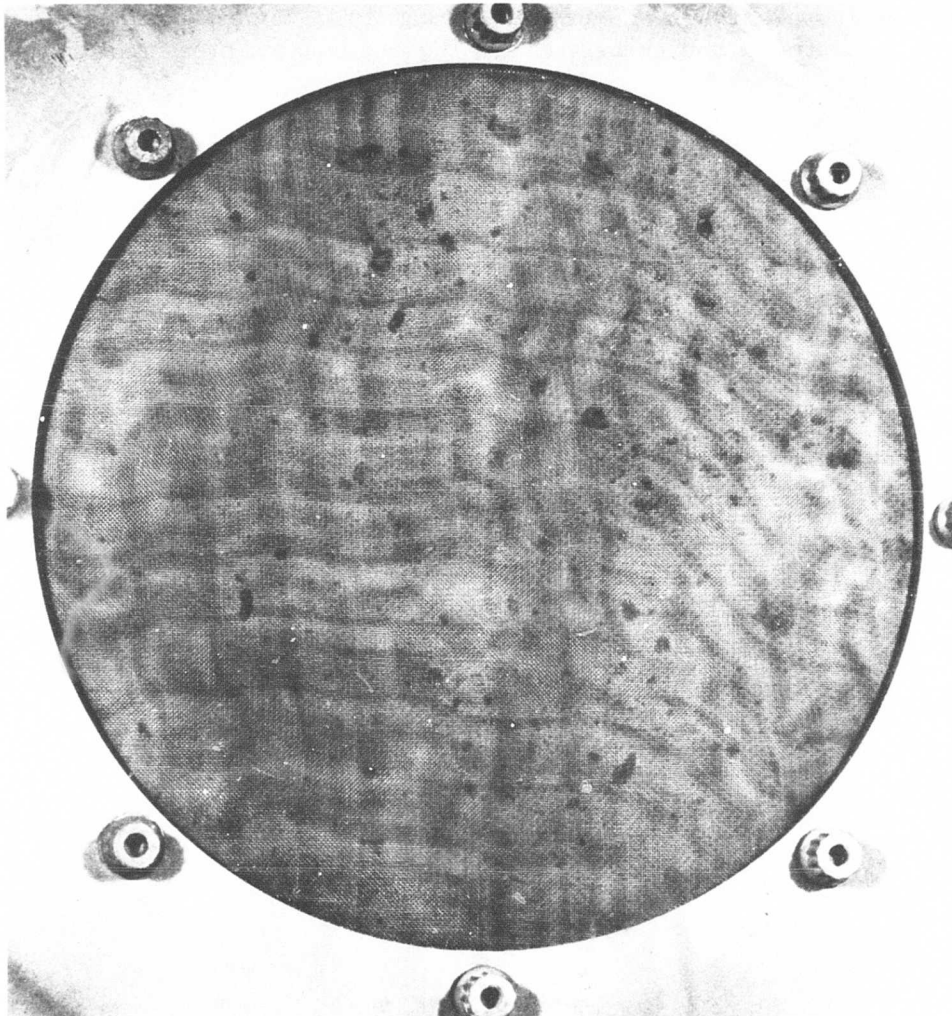


Figure 158. Hot Side of Regenerator Matrix Clogging Test Specimen (Screen 60 x 60 x 0.0044) After 100 Hours of Hot- and Cold-Air Cycling (1800 Pounds per Hour Airflow and 1200°F. Air Temperature).

CONFIDENTIAL

CONFIDENTIAL

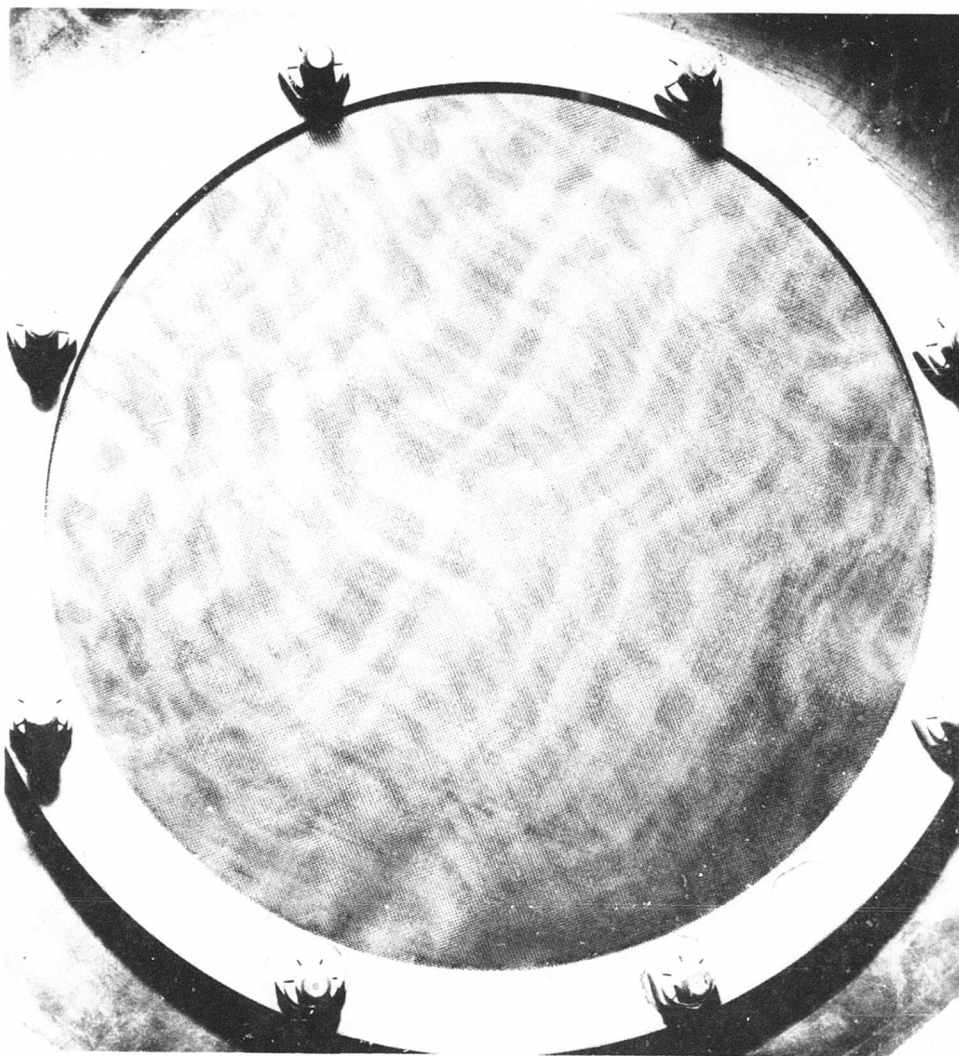


Figure 159. Cold Side of Regenerator Matrix Clogging Test Specimen (Screen 60 x 60 x 0.0044) After 100 Hours of Hot- and Cold-Air Cycling (1800 Pounds per Hour Airflow and 1200°F. Air Temperature).

CONFIDENTIAL

CONFIDENTIAL

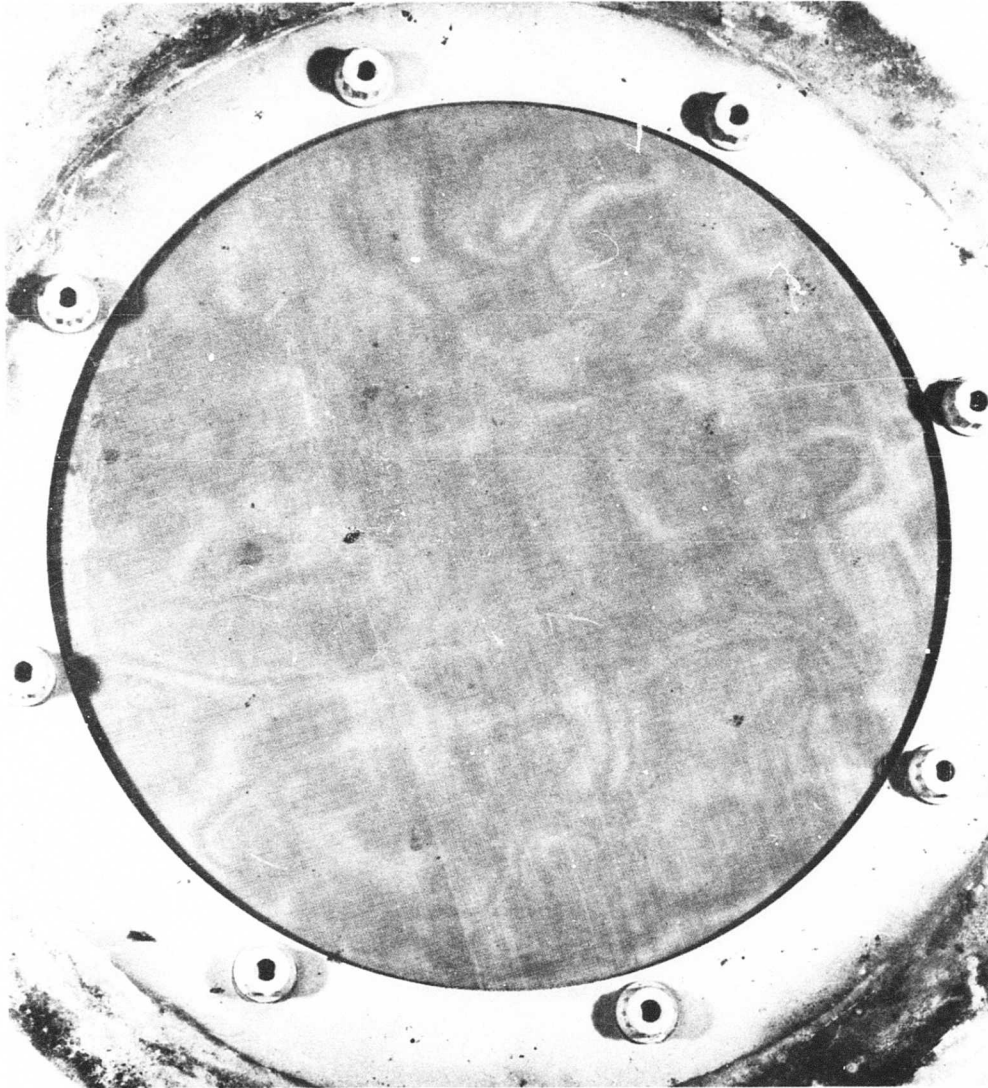


Figure 160. Hot Side of Regenerator Matrix Clogging Test Specimen (Screen 80 x 80 x 0.0044) After 100 Hours of Hot- and Cold-Air Cycling (1800 Pounds per Hour Airflow and 1200°F. Air Temperature).

CONFIDENTIAL

CONFIDENTIAL

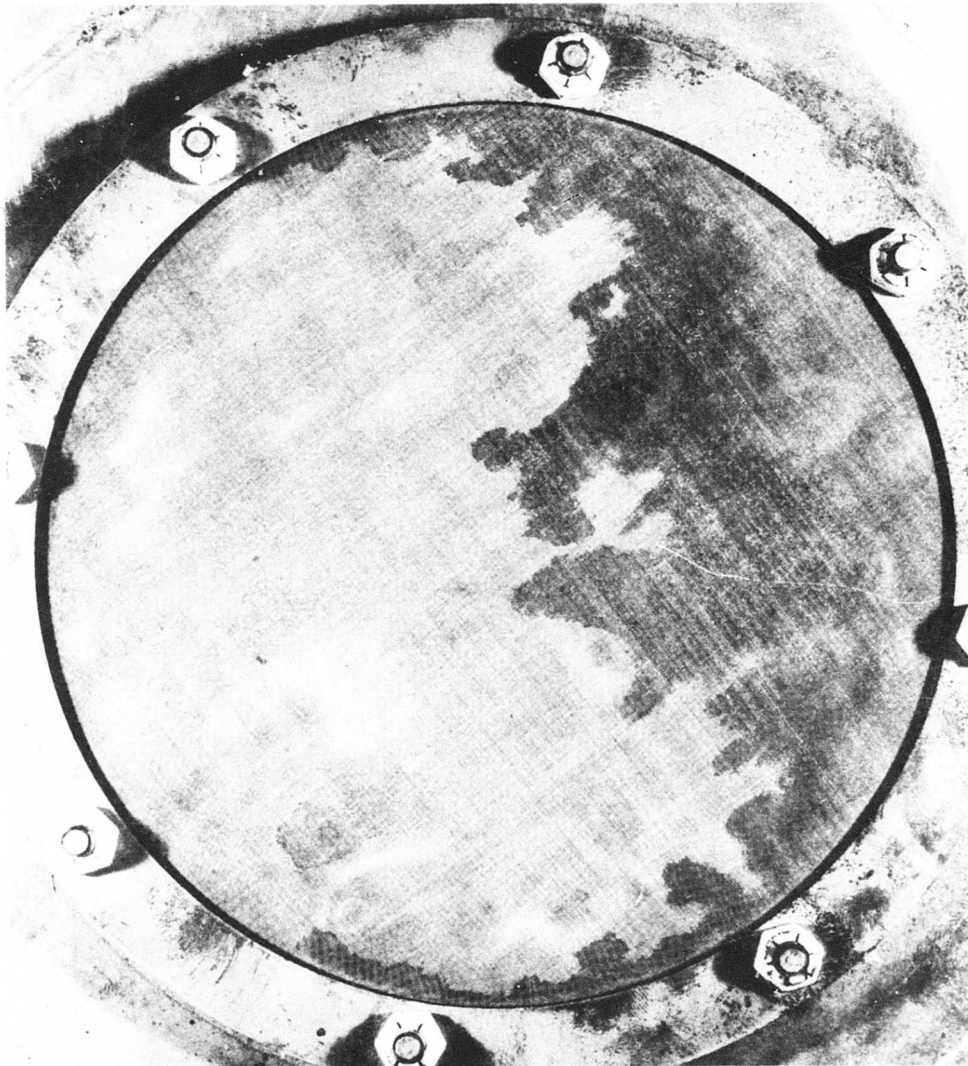


Figure 161. Cold Side of Regenerator Matrix Clogging Test Specimen (Screen 80 x 80 x 0.0044) After 100 Hours of Hot- and Cold-Air Cycling (1800 Pounds per Hour Airflow and 1200°F. Air Temperature).

CONFIDENTIAL

CONFIDENTIAL

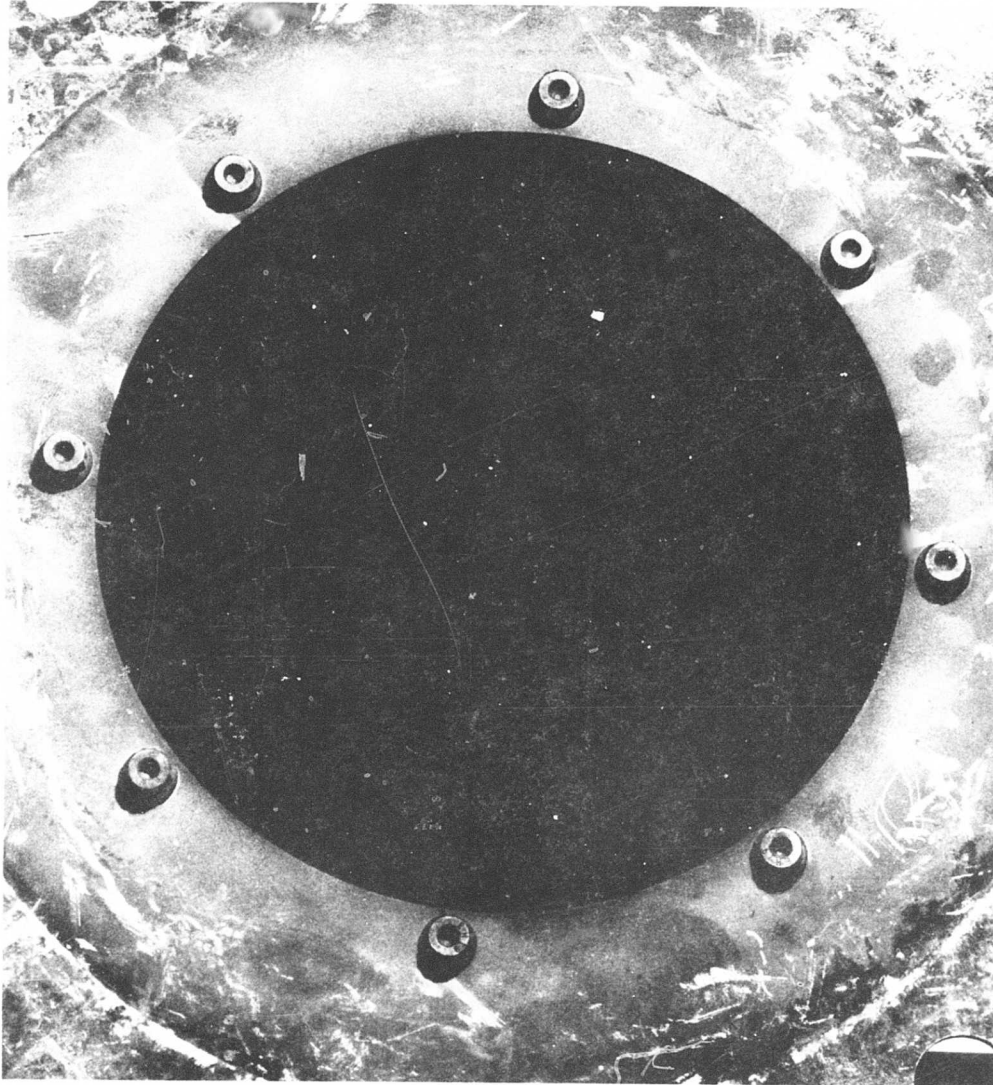


Figure 162. Hot Side of Regenerator Matrix Clogging Test Specimen (Screen 60 x 60 x 0.0065) After 100 Hours of Hot- and Cold-Air Cycling Endurance Test (1800 Pounds per Hour Airflow and 1200°F. Air Temperature).

CONFIDENTIAL

CONFIDENTIAL

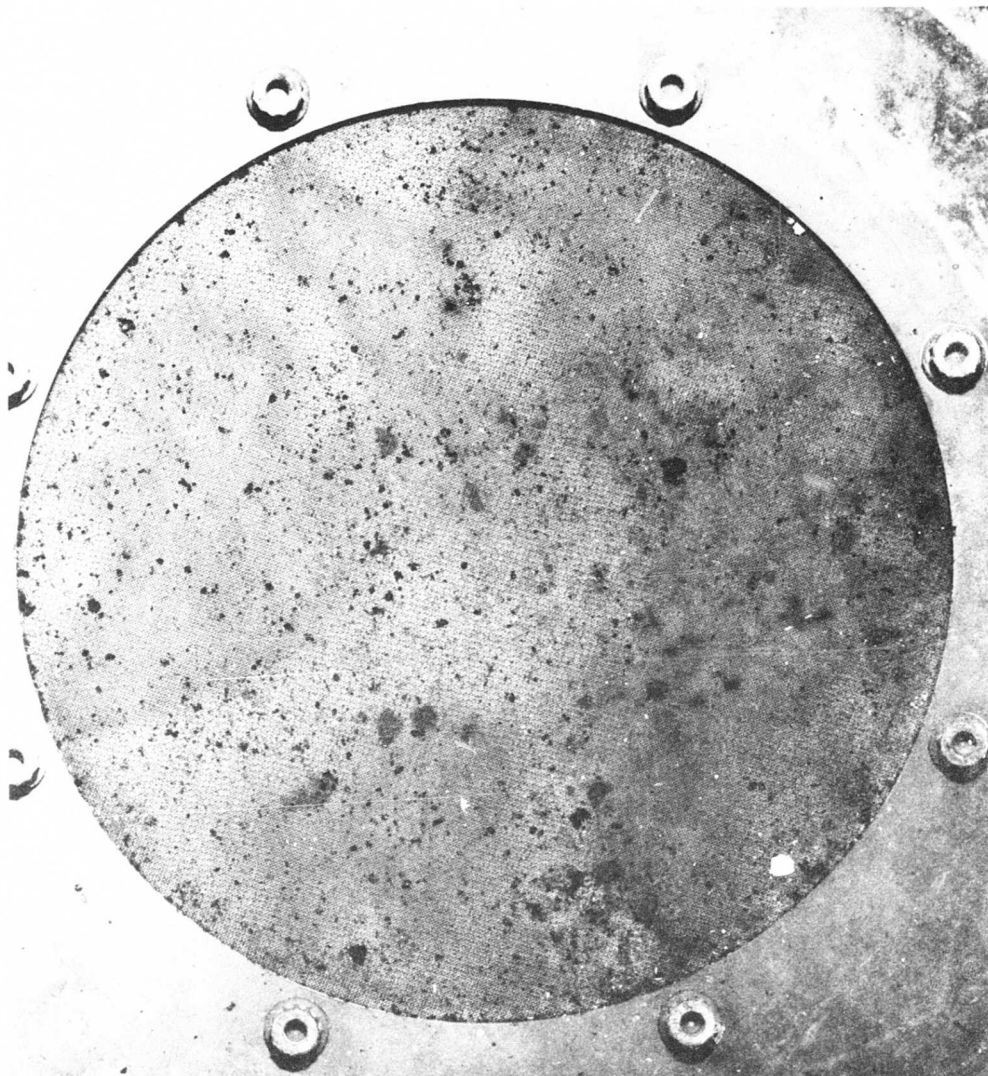


Figure 163. Hot Side of Regenerator Matrix Clogging Test Specimen (Screen 60 x 60 x 0.0065) After 100 Hours of Unidirectional Operation at 1800 Pounds per Hour Airflow and 1200°F. Air Temperature.

CONFIDENTIAL

CONFIDENTIAL

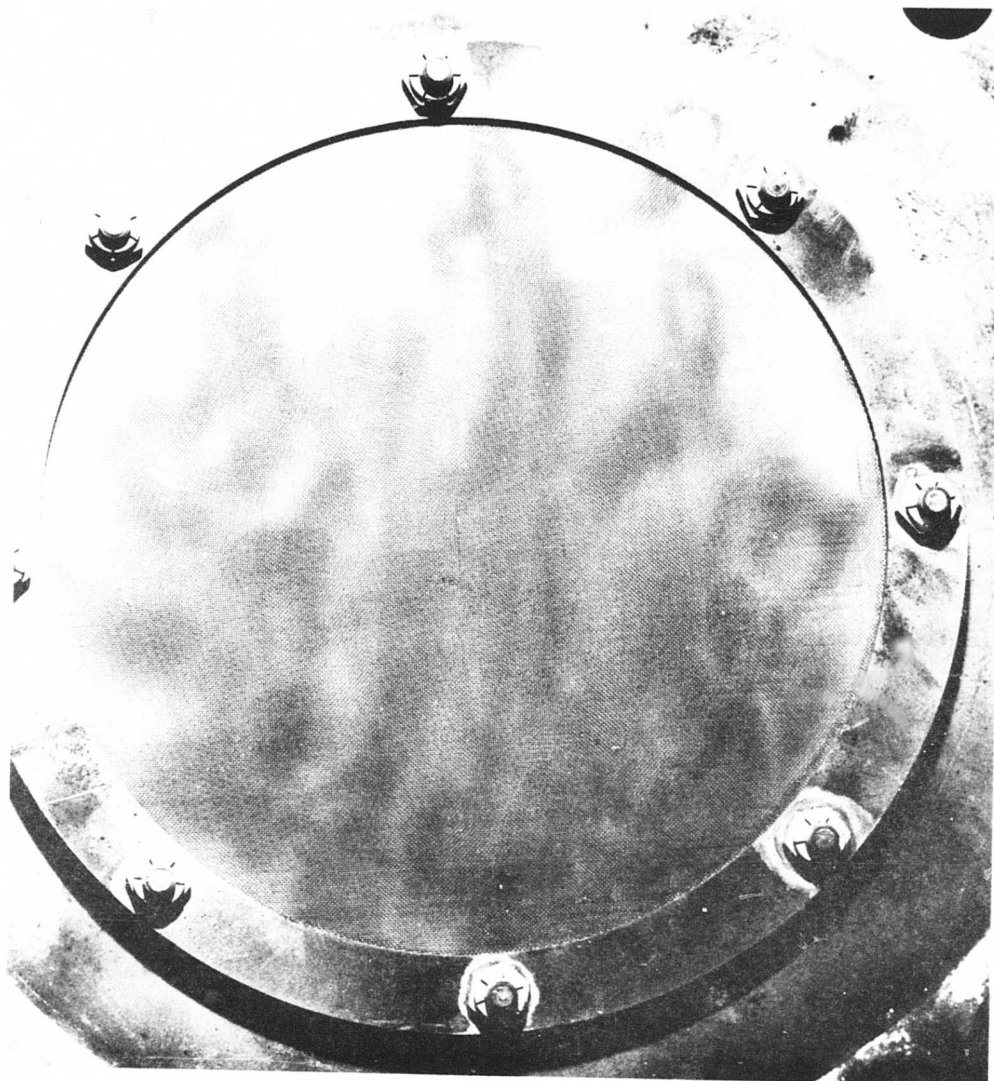


Figure 164. Cold Side of Regenerator Matrix Clogging Test Specimen (Screen 60 x 60 x 0.0065) After 100 Hours of Unidirectional Operation at 1800 Pounds per Hour Airflow and 1200°F. Air Temperature.

CONFIDENTIAL

CONFIDENTIAL

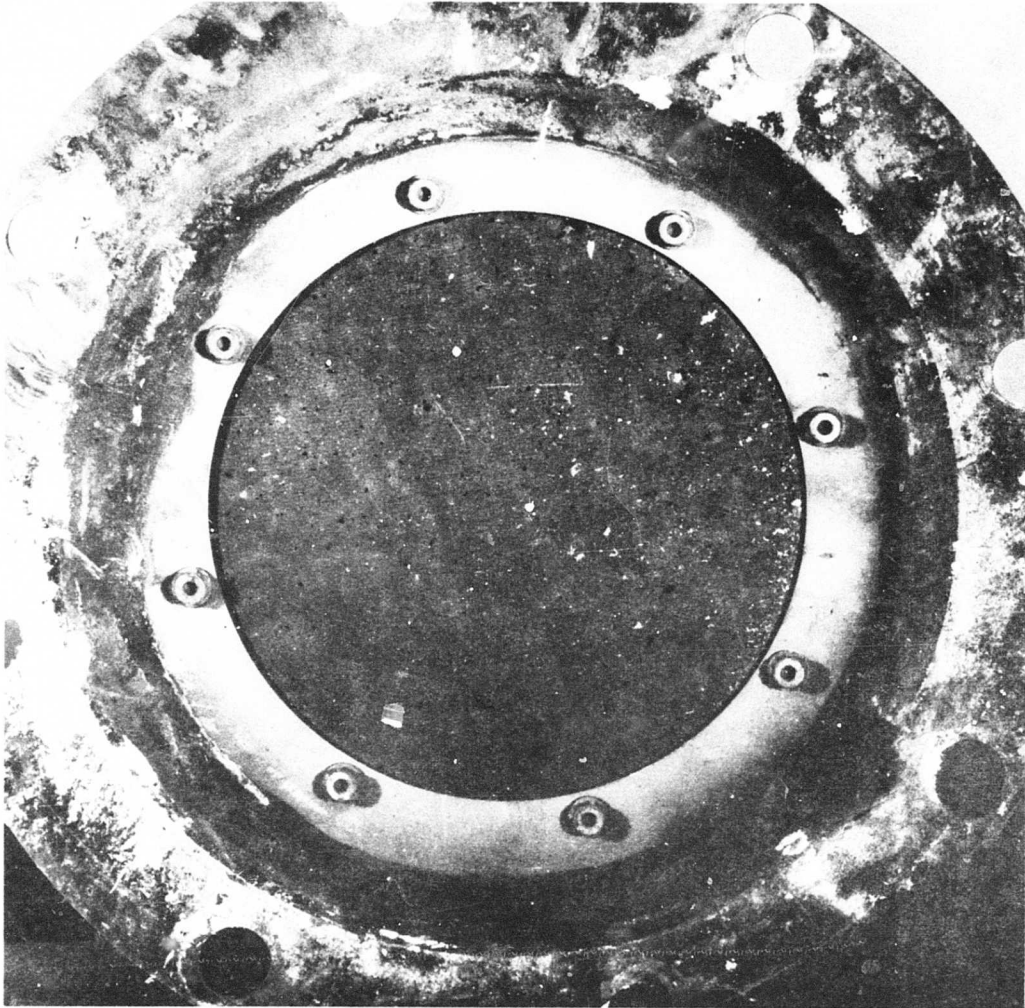


Figure 165. Hot Side of Regenerator Matrix Clogging Test Specimen (Screen 80 x 80 x 0.0044) After 100 Hours of Unidirectional Operation at 1745 Pounds per Hour Airflow and 1200° F. Air Temperature.

CONFIDENTIAL

CONFIDENTIAL

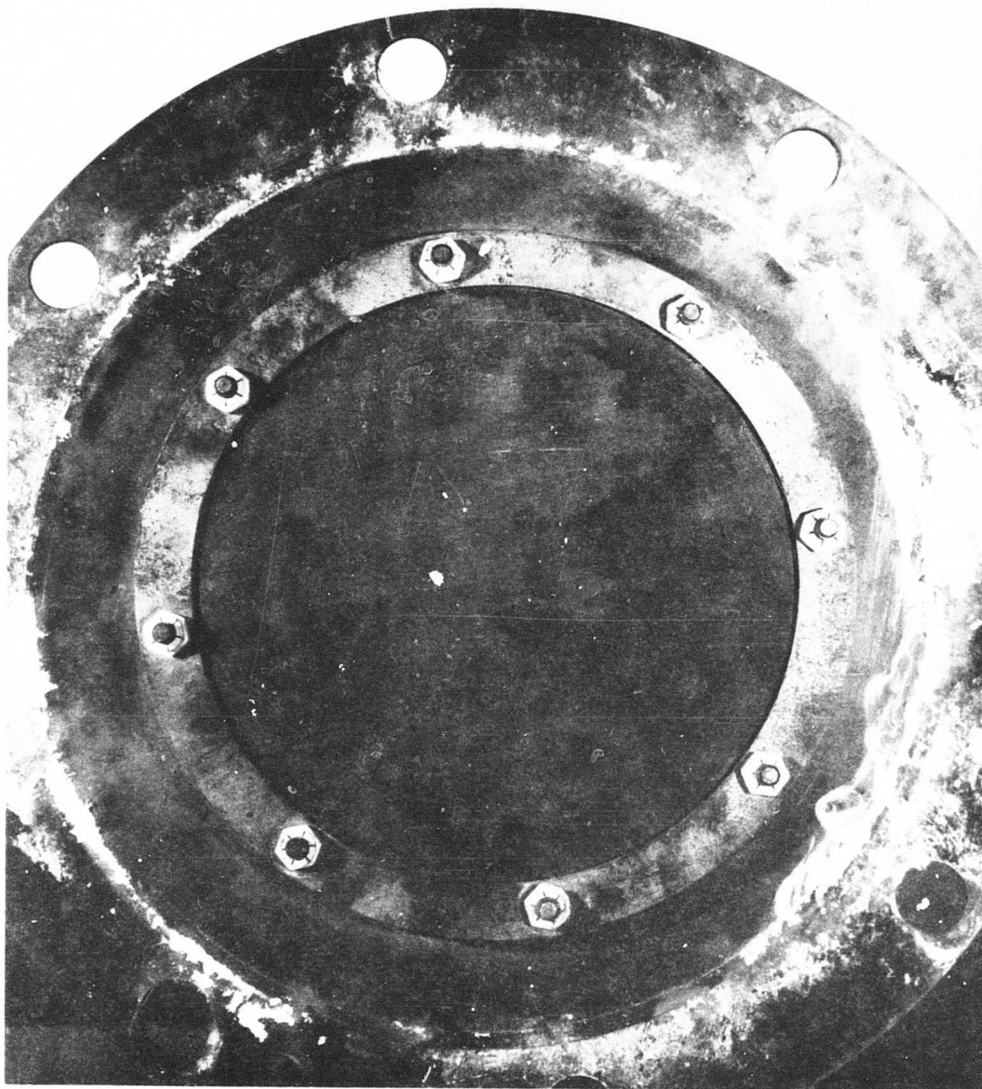


Figure 166. Cold Side of Regenerator Matrix Clogging Test Specimen (Screen 80 x 80 x 0.0044) After 100 Hours of Unidirectional Operation at 1745 Pounds per Hour Airflow and 1200° F. Air Temperature.

CONFIDENTIAL

CONFIDENTIAL

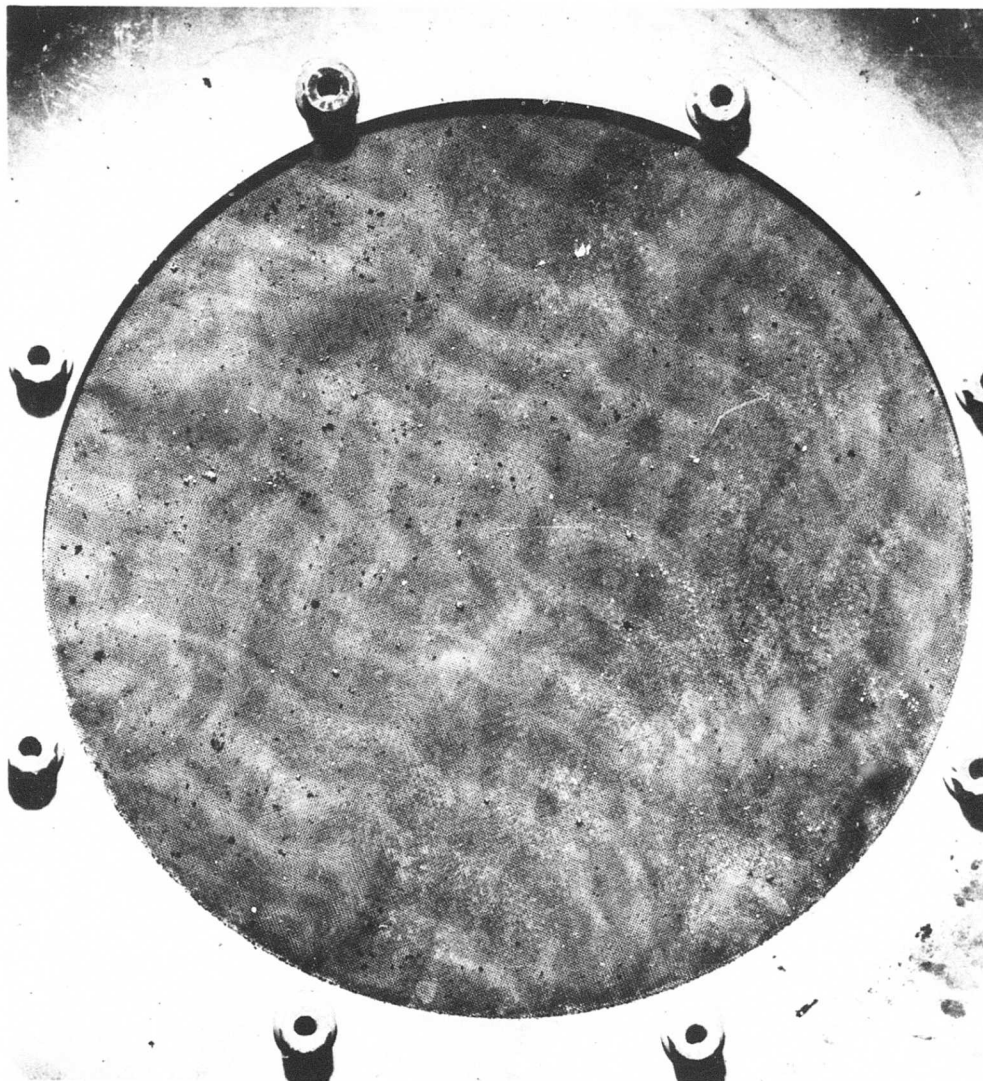


Figure 167. Hot Side of Regenerator Matrix Clogging Test Specimen (Screen 60 x 60 x 0.0044) After 100 Hours of Unidirectional Operation at 1745 Pounds per Hour Airflow and 1200°F. Air Temperature.

CONFIDENTIAL

CONFIDENTIAL

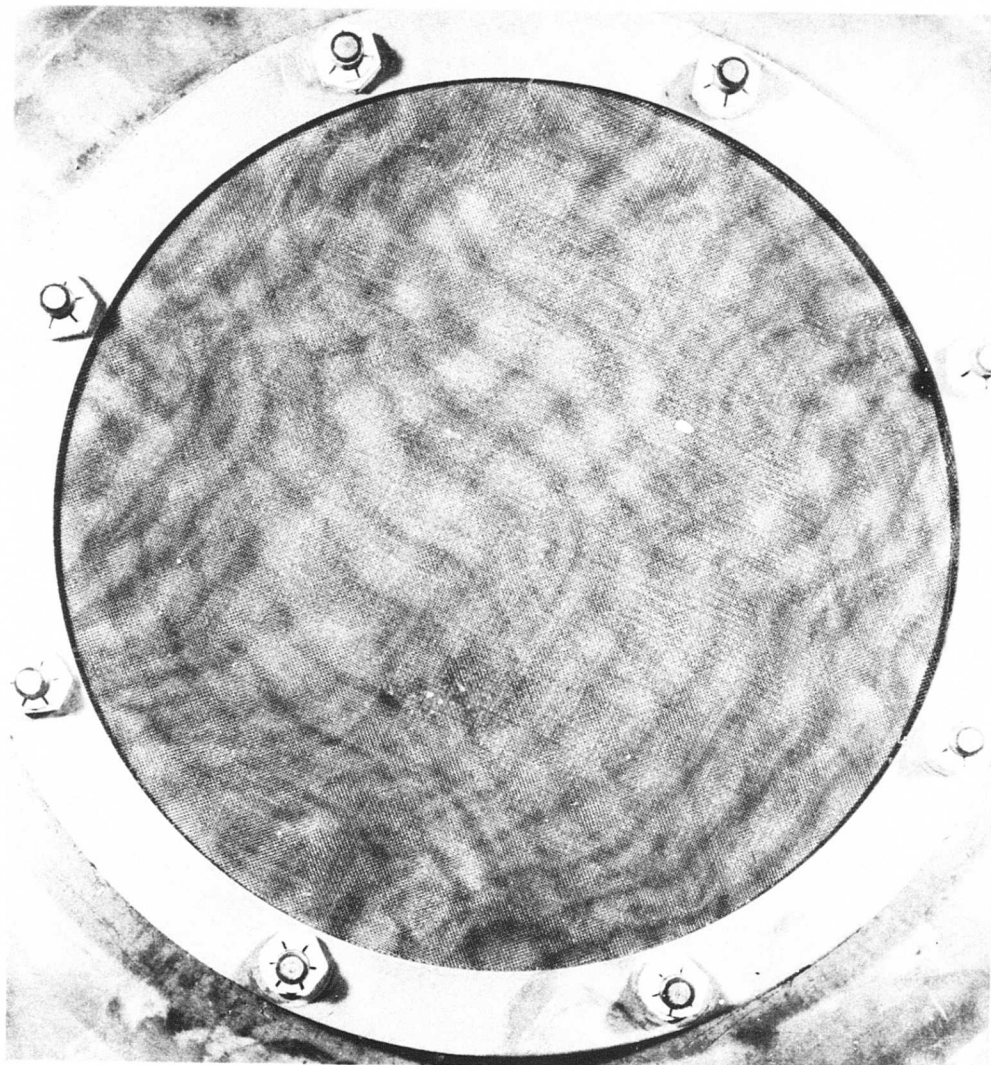


Figure 168. Cold Side of Regenerator Matrix Clogging Test Specimen (Screen 60 x 60 x 0.0044) After 100 Hours of Unidirectional Operation at 1745 Pounds per Hour Airflow and 1200°F. Air Temperature.

CONFIDENTIAL

CONFIDENTIAL

CONCLUSIONS

The following conclusions, based on the analytical and experimental investigations conducted during Phase I of the program, have been reached:

1. The target T74 engine performance of 0.40 pound of fuel per horsepower-hour specific fuel consumption can be demonstrated with a lightweight toroidal rotary regenerator.
2. The target regenerator performance of 85-percent effectiveness, 2-percent leakage, and 6-percent pressure loss can be demonstrated with a 28-inch diameter torus at 5 pounds per second airflow.
3. The optimum matrix for the T74 lightweight regenerator is a wire screen matrix of 60 wires per inch, 0.0040-inch-wire-diameter packages.
4. The 60-mesh, 0.0040-inch-wire-diameter matrix will not foul or clog from burner deposits during cyclic flow conditions which exist in the regenerator.
5. The heat transfer and friction factor characteristics determined experimentally in this program for 16 matrix cores extend the range of design information required for future lightweight regenerator designs.
6. The circumferentially folded matrix package has both performance and structural advantages over the radially folded matrix.
7. Uniform matrix flow distribution was demonstrated on packages simulating those in the lightweight regenerator design.
8. The leakage goal of 10 standard cubic feet per minute at 100 p. s. i. drop for the most critical seal (inner diameter of torus) was satisfied by three different types of carbon seals.
9. Seal endurance tests at overspeed and overload conditions demonstrated long seal overhaul life and no performance deterioration.
10. The feasibility of three different types of all-metal inner diameter seals was demonstrated, but additional refinement is required before these configurations can be used in regenerators.

CONFIDENTIAL

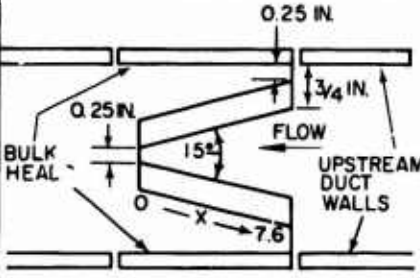
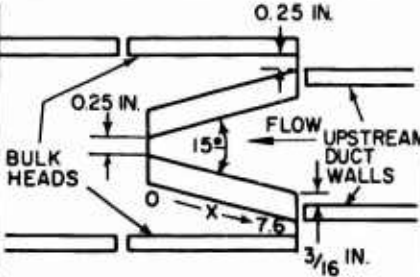
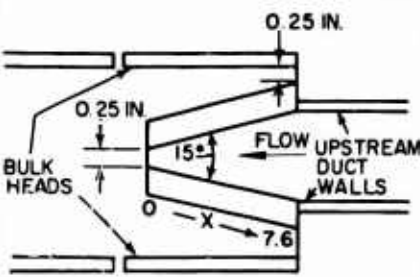
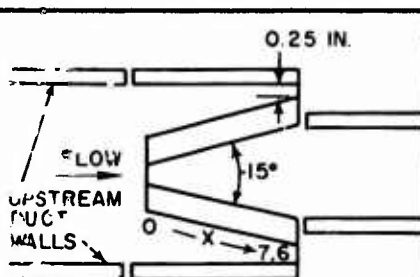
BIBLIOGRAPHY

1. Briggs, D. C., and London, A. L., The Heat Transfer and Flow Friction Characteristics of Five Offset Rectangular and Six Plain Triangular Plate-Fin Heat Transfer Surfaces, TR-49, Department of Mechanical Engineering, Stanford University, Stanford, California, November 1960.
2. Coppage, J. E., Heat Transfer and Flow Friction Characteristics of Porous Media, TR-16, Department of Mechanical Engineering, Stanford University, Stanford, California, December 1952.
3. Howard, C. P., Heat Transfer and Flow Friction Characteristics of Skewed Passage and Glass-Ceramic Heat Transfer Surfaces, TR-59, Department of Mechanical Engineering, Stanford University, Stanford, California, October 1963.
4. Kays, W. M., "The Basic Heat Transfer and Flow Friction Characteristics of Six Compact High Performance Heat Transfer Surfaces", Transactions of the American Society of Mechanical Engineers, Series A, Volume 82, January 1960, pp. 27-34.
5. Kays, W. M., and London, A. L., Compact Heat Exchangers, McGraw-Hill Book Company, Toronto, Ontario, 1958.
6. London, A. L., "Compact Heat Exchangers", Mechanical Engineer, Volume 86, Number 5, May 1964, pp. 47-51.
7. London, A. L., "Compact Heat Exchangers", Mechanical Engineer, Volume 86, Number 6, June 1964, pp. 31-34.
8. Regenerator Core Module Thermal Tests--T-600 Engine, Solar Engineering Report ER-1221, AD 290234, Solar Division of International Harvester Company, San Diego, California, 18 April 1962, Revision A, 25 October 1962.
9. Tong, L. S., and London, A. L., "Heat Transfer and Flow Friction Characteristics of Woven-Screen and Cross-Rod Matrices", Transactions of the American Society of Mechanical Engineers, Volume 79, October 1957, pp. 1558-1570.

CONFIDENTIAL

APPENDIX

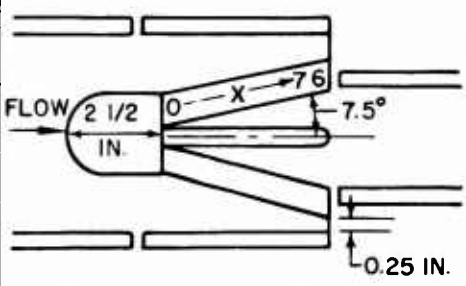
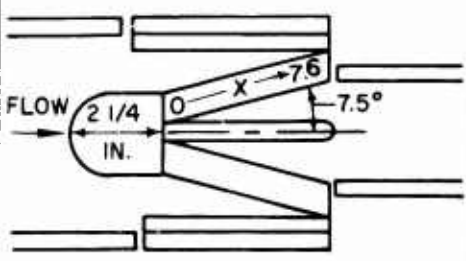
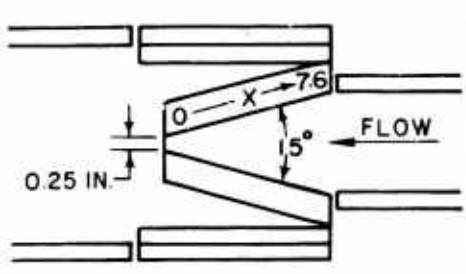
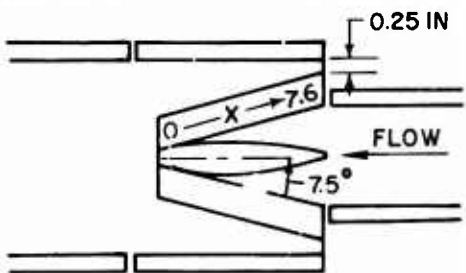
REGENERATOR MATRIX CONFIGURATIONS TESTED IN THE MATRIX AIRFLOW RIG

CONFIGURATION NO.	CONFIGURATION	TEST PURPOSE
1		EFFECT OF INLET CONFIGURATION WITH FLOW INTO VEE
2		EFFECT OF INLET CONFIGURATION WITH FLOW INTO VEE
3		EFFECT OF INLET CONFIGURATION WITH FLOW INTO VEE
4		EFFECT OF INLET CONFIGURATION WITH FLOW OVER VEE

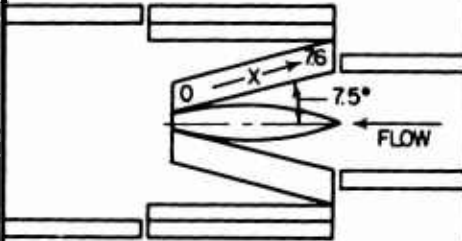
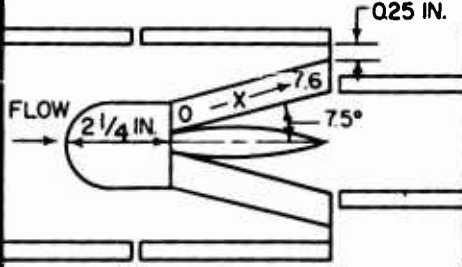
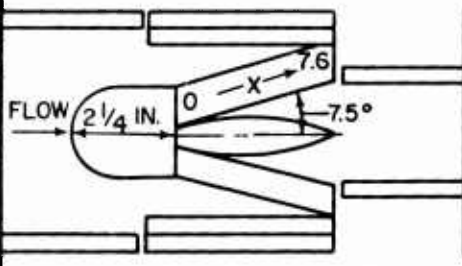
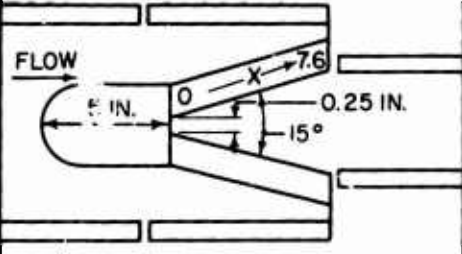
CONFIDENTIAL

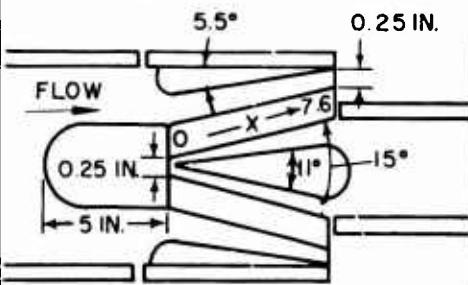
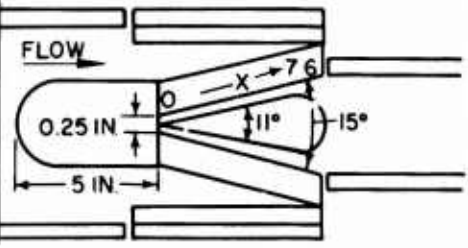
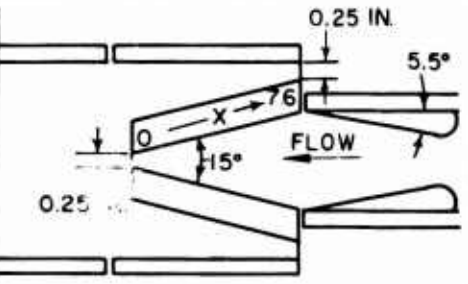
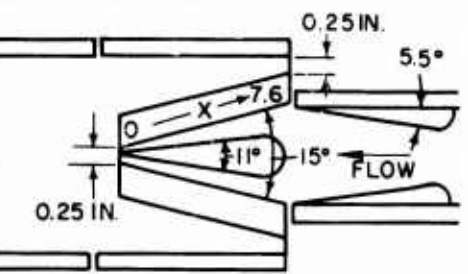
CONFIGURATION NO.	CONFIGURATION	TEST PURPOSE
5		EFFECT OF INLET CONFIGURATION WITH FLOW OVER VEE
6		EFFECT OF MATRIX-TO-BULKHEAD GAP WITH FLOW OVER VEE
7		EFFECT OF MATRIX SIDES JUNCTION GAP WITH FLOW INTO VEE
8		EFFECT OF NO GAPS WITH FLOW INTO VEE

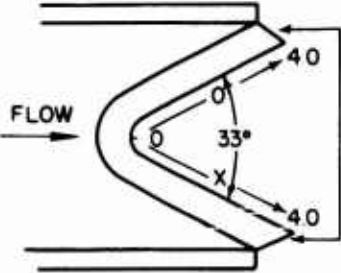
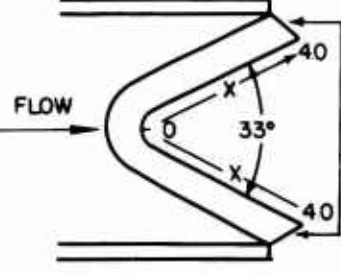
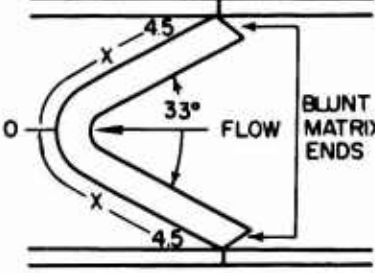
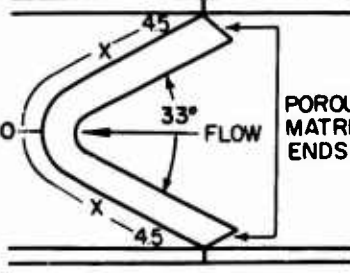
CONFIDENTIAL

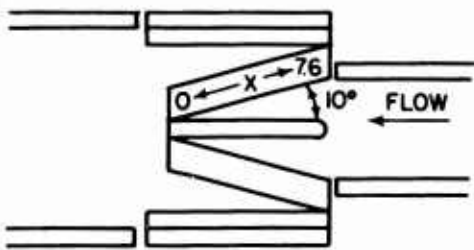
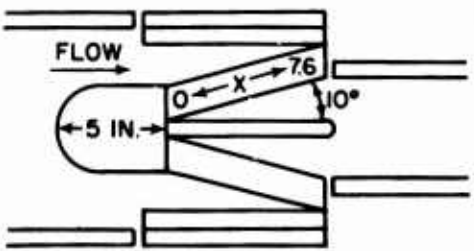
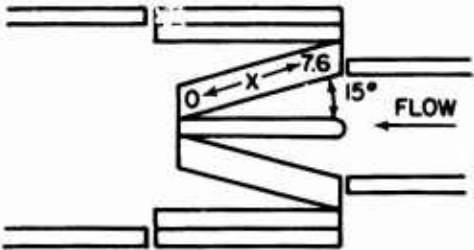
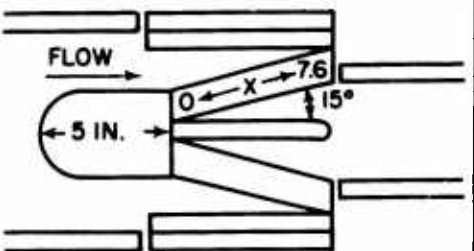
CONFIGURATION NO.	CONFIGURATION	TEST PURPOSE
9		EFFECT OF MATRIX SIDES JUNCTION GAPS WITH FLOW OVER VEE
10		EFFECTS OF NO GAPS WITH FLOW OVER VEE
11		EFFECT OF NO MATRIX-TO-BULKHEAD GAP WITH FLOW INTO VEE
12		EFFECT OF CONTOURED CENTERBODY WITH FLOW INTO VEE

CONFIDENTIAL

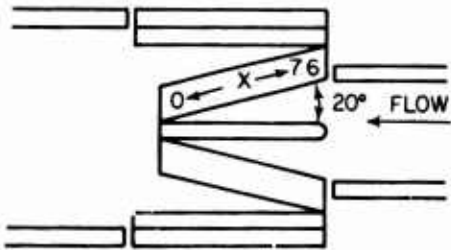
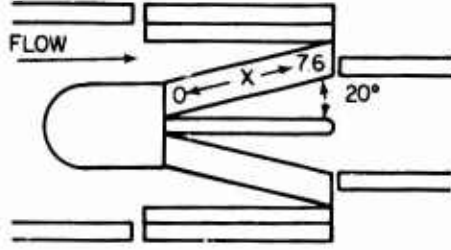
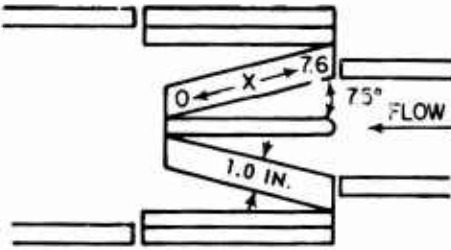
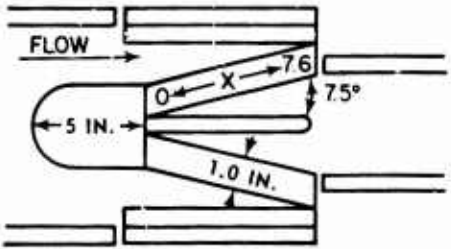
CONFIGURATION NO.	CONFIGURATION	TEST PURPOSE
13		EFFECT OF CONTOURED CENTERBODY AND NO MATRIX-TO-BULKHEAD GAP WITH FLOW INTO VEE
14		EFFECT OF CONTOURED CENTERBODY WITH FLOW OVER VEE
15		EFFECT OF CONTOURED CENTERBODY AND NO MATRIX-TO-BULKHEAD GAP WITH FLOW OVER VEE
16		EFFECT OF LONGER NOSE PIECE WITH FLOW OVER VEE

CONFIGURATION NO.	CONFIGURATION	TEST PURPOSE
17		EFFECT OF 11° WEDGE-SHAPE CENTER-BODY AND WEDGE-SHAPE SIDEWALLS WITH FLOW OVER VEE
18		EFFECT OF 11° WEDGE-SHAPE CENTER-BODY AND NO MATRIX-TO-BULKHEAD GAP WITH FLOW OVER VEE
19		EFFECT OF INLET CONFIGURATION WITH FLOW INTO VEE
20		EFFECT OF INLET CONFIGURATION AND 11° CENTERBODY WITH FLOW INTO VEE

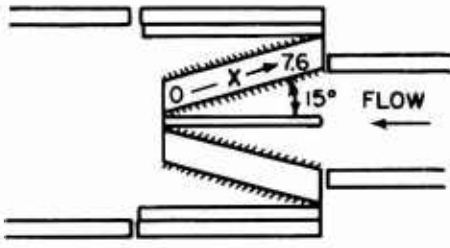
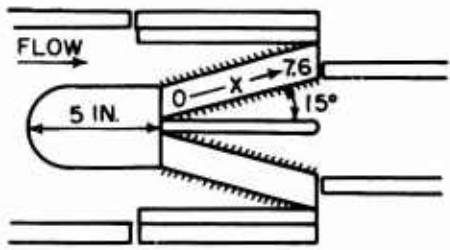
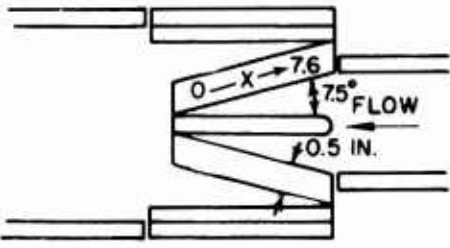
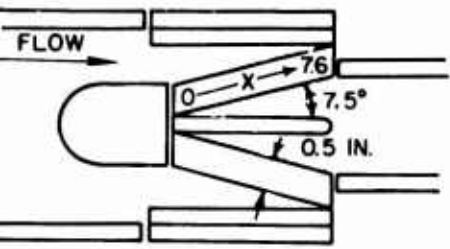
CONFIGURATION NO.	CONFIGURATION	TEST PURPOSE
21	 <p>POROUS MATRIX ENDS</p>	BUILD 2 REGENERATOR CIRCUMFERENTIAL V-PACKAGE POROUS MATRIX ENDS WITH FLOW OVER VEE
22	 <p>BLUNT MATRIX ENDS</p>	BUILD 2 REGENERATOR CIRCUMFERENTIAL V-PACKAGE BLUNT MATRIX ENDS WITH FLOW OVER VEE
23	 <p>BLUNT MATRIX ENDS</p>	BUILD 2 REGENERATOR CIRCUMFERENTIAL V-PACKAGE BLUNT MATRIX ENDS WITH FLOW INTO VEE
24	 <p>POROUS MATRIX ENDS</p>	BUILD 2 REGENERATOR CIRCUMFERENTIAL V-PACKAGE POROUS MATRIX ENDS WITH FLOW INTO VEE

CONFIGURATION NO.	CONFIGURATION	TEST PURPOSE
25		EFFECT OF MATRIX ANGLE WITH FLOW INTO VEE
26		EFFECT OF MATRIX ANGLE WITH FLOW OVER VEE
27		EFFECT OF MATRIX ANGLE WITH FLOW INTO VEE
28		EFFECT OF MATRIX ANGLE WITH FLOW OVER VEE

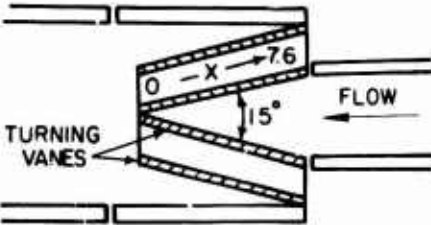
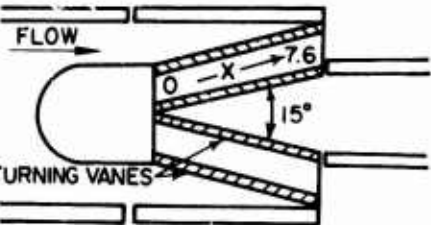
CONFIDENTIAL

CONFIGURATION NO.	CONFIGURATION	TEST PURPOSE
29		EFFECT OF MATRIX ANGLE WITH FLOW INTO VEE
30		EFFECT OF MATRIX ANGLE WITH FLOW OVER VEE
31		EFFECT OF INCREASED FLOW LENGTH WITH FLOW INTO VEE
32		EFFECT OF INCREASED FLOW LENGTH WITH FLOW OVER VEE

CONFIDENTIAL

CONFIGURATION NO.	CONFIGURATION	TEST PURPOSE
33		EFFECT OF TURNING VANES WITH FLOW INTO VEE
34		EFFECT OF TURNING VANES WITH FLOW OVER VEE
35		EFFECT OF HIGHER MESH, HIGHER PRESS. LOSS SCREEN MATRIX WITH FLOW INTO VEE (60-MESH 0.006-IN.-DIA. SCREENS)
36		EFFECT OF HIGHER MESH, HIGHER PRESS. LOSS SCREEN MATRIX WITH FLOW OVER VEE (60-MESH 0.006-IN.-DIA. SCREENS)

CONFIDENTIAL

CONFIGURATION NO.	CONFIGURATION	TEST PURPOSE
37		EFFECT OF INLET AND EXIT TURNING VANES WITH FLOW INTO VEE
38		EFFECT OF INLET AND EXIT TURNING VANES WITH FLOW OVER VEE

Unclassified

Security Classification

DOCUMENT CONTROL DATA - R & D		
(Security classification of title, body of abstract and indexing annotation must be entered when the overall report is classified)		
1. ORIGINATING ACTIVITY (Corporate author) Pratt & Whitney Aircraft Division United Aircraft Corporation East Hartford, Connecticut 06108		2a. REPORT SECURITY CLASSIFICATION Confidential
		2b. GROUP 4
3. REPORT TITLE SMALL GAS TURBINE ENGINE COMPONENT TECHNOLOGY, REGENERATOR DEVELOPMENT, PHASE I, PRELIMINARY COMPONENT TESTING AND REGENERATOR DESIGN (U)		
4. DESCRIPTIVE NOTES (Type of report and inclusive dates) Final report, May 1964 to May 1965		
5. AUTHOR(S) (First name, middle initial, last name) Spaight, Harry A., and Selfors, Henry J.		
6. REPORT DATE October 1967	7a. TOTAL NO. OF PAGES 190	7b. NO. OF REFS 9
8a. CONTRACT OR GRANT NO. DA-44-177-AMC-181(T)	8b. ORIGINATOR'S REPORT NUMBER(S) USAAVLABS Technical Report TR 67-34	
8c. PROJECT NO. Task 1M121401D14413	8d. OTHER REPORT NO(S) (Any other numbers that may be assigned this report) PWA-2942	
10. DISTRIBUTION STATEMENT Each transmittal of this document outside the Department of Defense must have prior approval of U. S. Army Aviation Materiel Laboratories, Fort Eustis, Virginia 23604.		
11. SUPPLEMENTARY NOTES		12. SPONSORING MILITARY ACTIVITY U. S. Army Aviation Materiel Laboratories Fort Eustis, Virginia 23604
13. ABSTRACT This report describes the work accomplished during the 12-month Phase I portion of a 32-month program for the advancement of toroidal rotary regenerator technology for small gas turbine engines. The regenerator component work included analytical and experimental evaluation of candidate heat transfer surfaces where previous data did not exist; experimental determination of matrix airflow distribution and corrective measures; and refinement of seal system components, including all-metal inner diameter seals. The optimum matrix and seal configurations determined from these component tests were evaluated in an existing regenerator which was run at conditions simulating small gas turbine operation. As a result of these component investigations, major improvements in regenerator technology were made and were incorporated into the design of a flight-weight high-effectiveness toroidal rotary regenerator designed during Phase I. (U)		

DD FORM 1473

REPLACES DD FORM 1473, 1 JAN 64, WHICH IS OBSOLETE FOR ARMY USE.

Unclassified

Security Classification

Unclassified

Security Classification

14. KEY WORDS:	LINK A		LINK B		LINK C	
	ROLE	WT	ROLE	WT	ROLE	WT
Toroidal Rotary Regenerator Lightweight Regenerator Regenerative Gas Turbine Engine PT6 (T74) Gas Turbine Engine High Performance Engine Heat Exchanger Wire-Screen Matrix Heat Transfer						

Unclassified

Security Classification

SUPPLEMENTARY

INFORMATION

AD-387211

ERRATA

USAAVLABS Technical Report 67-34

"Small Gas Turbine Engine Component Technology
Regenerator Development" (U)

"Phase 1, Preliminary Component Testing
and Regenerator Design" (U)

October 1967

The distribution statement on the cover, on the title page, and in block 10 of DD Form 1473 should be changed to read:

In addition to security requirements which apply to this document and must be met, each transmittal outside the Department of Defense must have prior approval of US Army Aviation Materiel Laboratories, Fort Eustis, Virginia 23604.